Ionic Mobility In Stuffed-Silica Minerals

Thesis

Ionic Mobility in Stuffed-Silica Minerals

A thesis presented to The Open University for the degree of Doctor of Philosophy

Alison Jones B.Sc.(Hons)

Department of Earth Sciences,

The Open University

July 2001

Abstract

Using a combination of dielectric spectroscopy and atomistic computer simulation techniques, the dynamical behaviour of loosely bound cations in the stuffed-silica minerals nepheline, yoshiokaite and β-eucryptite has been investigated. The investigation has been extended to include the feldspar minerals albite, K-feldspar and anorthite.

The low-frequency dielectric properties of all of the minerals have been investigated from room temperature to 1100 K. At each temperature, the dielectric constant, conductivity and dielectric loss were determined over a range of frequencies from 100 Hz to 10 MHz. At high temperatures distinct Debye-type relaxation processes were observed, from which activation energies were determined for each system studied. In order to rationalise these data, in the context of actual ionic mobility mechanisms, atomistic simulation techniques were used to elucidate the mechanisms and energetics of cation migration. Good correlation between experimentally determined and calculated energy barriers has been demonstrated. The results obtained from computer modelling confirm the nature of the processes responsible for the observed dielectric behaviour. Furthermore, they reveal the importance of framework relaxation effects in the facilitation of ion migration within a structure.

This study demonstrates that short-range ionic mobility in framework silicates can be described using conventional (Debye-type) activated "hopping" models. A detailed interpretation of the mechanism of these processes has been possible by a combination of dielectric spectroscopy and computer modelling techniques. By

applying the methods used here to a variety of mineral systems, it should be possible to develop a comprehensive body of transferable data relating structural aspects of framework minerals to the systematic prediction of ion migration mechanisms and energetics.

Acknowledgements

Firstly I should like to thank my supervisors at The Open University, Dr. David Palmer, of the Department of Earth Sciences, and Dr. Michael Mortimer, of the Department of Chemistry, for all their help and advice. David and Mike have been constant sources of encouragement throughout my time at The Open University. I am also indebted to Dr. Saiful Islam, of the Department of Chemistry at the University of Surrey, for his invaluable help and continued interest in my work. The numerous discussions with Saiful regarding computer modelling have allowed me to pursue a new technique, and to develop an interest in an area I had not previously considered. I would like to thank Dr. Elaine Moore, who first introduced me to computer modelling, and Dr. Mark Welch of the Natural History Museum for his assistance with the high temperature XRD and for providing me with samples of nepheline and K-feldspar.

I am also grateful to Dr. Peter Heaney and Dr. Hongwu Xu for providing me with a crystal of β–eucryptite; to Mike Henty for the sample of albite and to Dr. Michael Carpenter for the sample of anorthite. Thanks must also go to Professor James Kirkpatrick for the yoshiokaite, which he synthesised 25 years previously. The helpful discussions regarding its synthesis were useful, but the problem of melting platinum crucibles was one problem which we failed to resolve!

I would like to thank the Heads of the Earth Sciences and Chemistry Departments for the use of the facilities within the departments. Thanks also to Dr. Andy Tindle for assistance with the electron microprobe analyses and to Naomi Williams for teaching me how to use the electron microscope.

I gratefully acknowledge receipt of a bursary from the Mineralogical Society of Great Britain which allowed me to attend the AGU Spring Meeting 2000 in Washington D.C., and the financial assistance from the Mineralogical Society of America to attend a short course on Transformation Processes in Minerals in Cambridge.

Finally, I have to say a special thank you to my husband, David, for his support and encouragement throughout the past three years.

Contents

Chapter 5

Yoshiokaite

Chapter 6

β-eucryptite

Chapter 7

The Feldspars

Chapter 8

Conclusions

List of Figures

Chapter 2

Dielectric spectroscopy

Chapter 3

Computer simulation methods

Chapter 4

Nepheline

Chapter 5

Yoshiokaite

Chapter 6

β-eucryptite

Chapter 7

The Feldspars

Chapter 8

Conclusions

Chapter 1

Introduction

Contents

1.1 Introduction

Ionic mobility in minerals is fundamentally linked to the mechanisms of processes such as diffusion, exsolution, phase transitions, weathering and mineral reactions. A real understanding of these processes on a macroscopic scale can only be achieved if these minerals are studied using techniques that are sensitive to behaviour on a microscopic scale. The framework structures of silica polymorphs provide the common structural basis for a wide variety of technological and geological materials. Aluminosilicate framework structures with mobile channel ions residing in cages and channels have therefore been chosen for a diffusion study. Some of the highest ionic mobilities are observed in framework aluminosilicate minerals, of which the framework behaviour has been extensively documented (Carpenter, 1988; Dove et al., 1993a; Hayward et al., 2000). However, the nature of the interaction of the framework with the channel ions is less well understood (Downs et al., 1996). By studying model framework structures with variable channel ion content, the interaction of different ions in well characterised frameworks and the mechanisms of ionic mobility can be investigated on a microscopic scale.

1.2 Stuffed-Silica Minerals

The term "stuffed derivatives" was first used by Buerger (1954) to describe phases which comprise a silica framework topology with alkali or alkaline earth cations "stuffed" into framework cavities, with appropriate substitution of silicon by aluminium in order to maintain the charge balance. The exact nature of the stuffing species is determined by the framework geometry as well as the degree of Al/Si substitution and different framework distortions around the stuffing cations can lead

to a variety of derivative structures. In some of these structures the cations will be accommodated in sites which form part of a channel structure within the aluminosilicate framework, such as nepheline (Hahn and Buerger, 1954) and kalsilite (Perotta and Smith, 1965); in others, such as carnegieite (Withers and Thompson, 1993) and chkalovite (Simonov et al., 1976), the constraints of the framework geometry mean that the cations will be effectively trapped in cavities.

Stuffed-silica minerals (Palmer, 1994) are ideal candidate materials for studying ionic mobility in framework structures. In this investigation, a large part of the work was carried out on nepheline, a Na- and K-stuffed derivative of tridymite with a well defined channel structure. Using a combination of dielectric spectroscopy and computer simulation techniques, the mechanism for the short range ionic mobility of sodium ions in nepheline was determined. This approach was then developed in the study of other stuffed-silica derivatives. These were yoshiokaite, a calcium-stuffed derivative of tridymite and β-eucryptite, a lithium-stuffed derivative of β-quartz. It would have been extremely useful to include the mineral kalsilite, a potassium stuffed derivative of tridymite, in the investigation. Unfortunately there were no single crystals of kalsilite available.

To extend this work to include more geologically-important minerals, another group of framework aluminosilicates, the feldspars, have been investigated. The feldspars possess certain structural similarities to stuffed-silica phases, in that they comprise an aluminosilicate framework of corner sharing Si- and Al–tetrahedra with a range of cations in large structural cavities. However, as there is no clear diffusion pathway within the feldspar structure, they have provided the opportunity to develop the techniques used for nepheline in a system where the ion migration pathways are much less clearly defined.

1.3 Ion Diffusion Processes

Movement of ions through crystal lattices is an underlying, microscopic control behind important geological processes. An understanding of ionic mobility is also an essential prerequisite to the interpretation of solid-state chemical interactions, such as the behaviour of ions within microporous materials and fast ion conduction in superionic conductors. The ability to predict diffusion properties, including activation energies, for a given crystal structure, would provide intrinsic constraints in the modelling and prediction of geological phenomena and aid the interpretation of the controlling mechanisms of fast-ion transport in solid-state conductors (Tyburczy and Fisler, 1995; Wittingham, 1975).

A recent study carried out on the coordination of Na and K atoms in low albite and microcline (Downs et al., 1996) suggests strong interactions between mobile species, such as alkali cations, and the surrounding framework. In order to investigate this, it is necessary to first establish a more precise picture of ionic mobility at a microscopic level. Traditional diffusion data derived from bulk samples may be misleading, averaging over multiple diffusion processes (e.g. small scale site hopping, longer range tunnelling, or movements along twin/grain boundaries), and do not give any transferable data of physical significance. A more focused approach is to combine knowledge of the local crystal structural environment with highly specific spectroscopic probes, e.g. dielectric spectroscopy or NMR spectroscopy, which are able to characterise ionic mobility over a range of length scales and measure activation energies for discrete diffusion mechanisms.

Ionic transport in crystalline solids may occur by a process of activated hopping or correlated motion of ions along a channel. In both cases an energy barrier has to be

overcome. This is the measured activation energy for the process and it is this that is the principal determinant of rate in diffusion processes. Short-range mobilities can be satisfactorily described by an activated hopping model (Debye, 1929; Ohgushi and Kazuhide, 1998). Although the energy required to overcome the barrier comes from the thermal motion of the atoms, the probability of this happening at any time will depend on, among other things, the number of defects (e.g. vacancies) in the crystal and the distance between sites. Longer-range mobility in channel structures is more likely to occur by a correlated motion of ions along a channel (Alpen et al., 1977; Barrer and Saxon-Napier, 1962). This is the mechanism by which bulk conduction occurs in superionic conductors.

In the present work, ionic mobility has been probed using a combination of dielectric spectroscopy (Palmer, 1995; Palmer et al., 1997) and computer modelling techniques (Catlow and Price, 1990; Islam, 2000). Low-frequency dielectric spectroscopy provides a structural probe for measuring the behaviour of loosely-bound channel ions in framework minerals, as only the mobile charged species respond to the relatively-low frequency (< 10MHz) electric fields. Static lattice simulations have been used to test possible diffusion pathways and thereby provide an insight into the mechanistic details of the ion migration processes observed using dielectric spectroscopy.

1.4 Crystal Chemical Systematics

The first attempts at simplifying relationships in the physical behaviour of crystals were based on the principles of crystal chemistry developed by Linus Pauling (1960). Pauling reduced the complexities of inorganic structures to a set of "rules" of

reasonable simplicity which could be used in a predictive capacity. These rules are not always obeyed, but they provide a useful general guide to the coordination of ions and to the kinds of polyhedral linkages that are, and are not, possible in crystal structures. Although Pauling's rules had to be modified to include structures which were not necessarily ionic, they could nevertheless be usefully applied to a wide range of inorganic structures. Pauling's rules are not directly related to the present work, however, they provide an illustration of how *systematic* behaviour may be used to aid the understanding and interpretation of physical and structural phenomena.

One of the aims of this study is to identify how crystal chemical and structural aspects of minerals might influence diffusion rates in aluminosilicates. By taking into account structural data on framework geometry (e.g. presence of channels/cavities) and the nature of the inter-framework stuffing species, such a study should reveal systematic structural behaviour which could be used in a predictive capacity. These investigations will allow comparison of the mobility patterns of ions of differing size and charge in similar framework structures, and therefore provide an improved understanding of ionic mobility, at the atomic level, in framework silicates.

Chapter 2

Dielectric Spectroscopy

Contents

2.1 Dielectric materials

Dielectric materials are electrical insulators and possess high dielectric strength; that is they can withstand high voltages without undergoing degradation and becoming electrically conducting. They also have low dielectric loss, so that in an alternating field the loss of electrical energy, which is dissipated as heat, is minimised. Application of an electric field across a dielectric leads to a polarisation of charge within the material. However, no long range motion of ions or electrons is involved and the polarisation disappears when the electric field is removed.

In this chapter, a description of the dielectric theory and experimental methods used in this work are presented. More substantial descriptions of dielectric theory are described elsewhere (Harrop, 1973; Huebner and Dillenburg, 1995; Nover et al., 1992; Omar, 1975; Poole and Farach, 1971; West, 1984).

2.1.1 Perfect dielectric materials

Dielectric properties can be defined with reference to the behaviour of the material in a parallel plate capacitor. For a perfect dielectric material, the capacitance, C (F), is defined as:

$$C = \frac{\varepsilon_o \varepsilon' A}{d} \tag{2.1}$$

where ε' is the dielectric constant or relative permittivity of the dielectric material, ε_o is the permittivity of free space, 8.854×10^{-12} Fm^{-1}, A (m^2) is the area of the plates and d (m) is the separation of the plates (Figure 2.1). A capacitor such as this, containing a perfect dielectric material, does not conduct a direct current: as the plates accumulate charge the current will decrease exponentially, so that the capacitor impedes the flow of current. This is shown in Figure 2.2 (a).

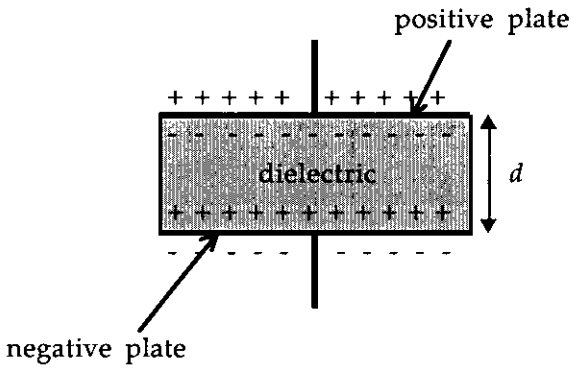

Figure 2.1 Dielectric material between a parallel plate capacitor.

With a potential difference , V (V), between the plates, the quantity of charge, Q (C) stored by the capacitor is given by the equation:

$$Q = CV \tag{2.2}$$

The quantity of charge which can be stored therefore depends on the dielectric constant of the dielectric medium and at time t the charge stored by the capacitor is given by:

$$Q = Q_m - Q_m\exp(-t/CR) \tag{2.3}$$

where Q_m is the maximum charge and R (Ω) is the circuit resistance.

A typical plot of charge versus time for a capacitor is shown in Figure 2.2(b).
In a d.c. supplied circuit, a capacitor obeys Ohm's law; under a.c. it impedes the flow of current by an amount that varies with frequency, f (Hz). The a.c. equivalent of resistance R (Ω) is defined as the impedance Z (Ω). In the simplest case of a perfect dielectric, $R = \infty$ and

$$Z = \frac{1}{\omega C} \tag{2.4}$$

where ω is the angular frequency ($\omega = 2\pi f$).

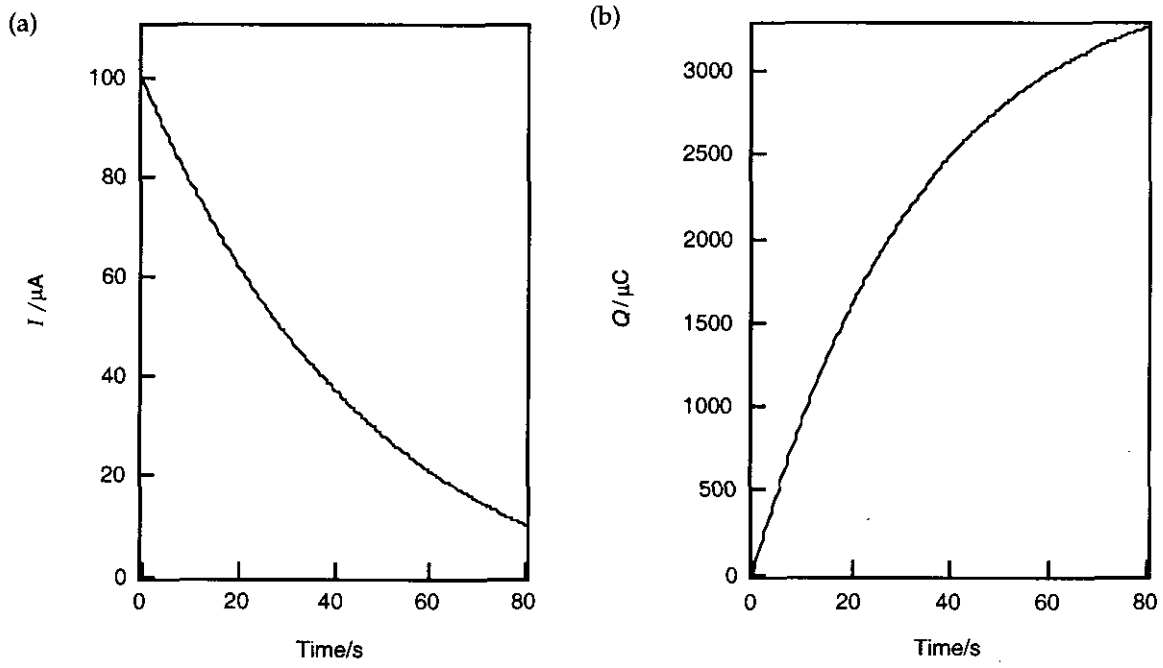

Figure 2.2 Typical plots of (a) I; (b) Q, against charging time for a capacitor.

2.1.2 Real dielectric materials

Any real dielectric material conducts electricity to some small extent when a d.c. voltage is applied across it. This can be modelled by a parallel circuit containing a resistance, R, and capacitance, C, as shown in Figure 2.3, where C is a perfect capacitor, as described above, and R represents an ideal resistor, i.e. one having no capacitive or inductive parts.

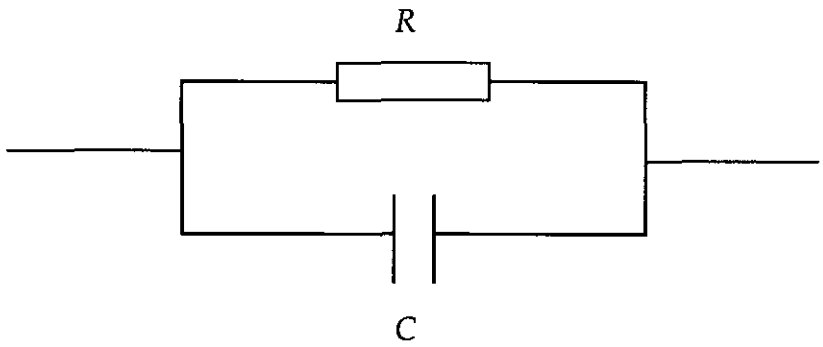

Figure 2.3 The defined equivalent circuit of a real dielectric.

The d.c. conductance, G (S), of the circuit is given by:

$$G = \frac{\sigma A}{d} = \frac{1}{R} \tag{2.5}$$

where σ is the conductivity (Sm^{-1}) of the dielectric.

2.1.3 Polarisation and polarisability

The magnitude of the dielectric constant for a material depends on the degree of polarisation, or charge displacement, that can occur in a dielectric material. When such a material is subjected to an electric field, there is a tendency for the positive and negative charges (i.e. nuclei, electrons or ions) within the material to be displaced relative to one another so that the overall system acquires an electric dipole moment. The polarising species within the dielectric approximates to a dipole with equal and opposite electrical charges $+e$ and $-e$ separated by a distance d (Figure 2.4).

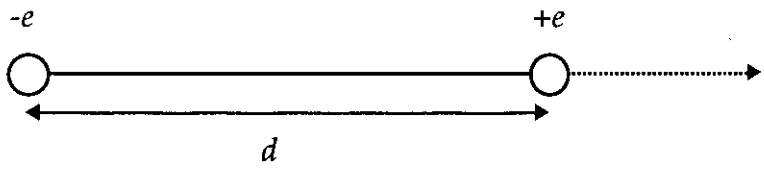

Figure 2.4 A simple dipole, showing the direction of the dipole moment.

The magnitude of the dipole moment, m, is given by:

$$m = ed \tag{2.6}$$

and the polarisability, α_d, of this dipole is defined by:

$$\mathbf{m} = \alpha_d \mathbf{E}_{loc} \tag{2.7}$$

where $\mathbf{m}$ is the dipole moment induced by the local (internal) electric field $\mathbf{E}_{loc}$. It should be noted that the local field is the field acting at the dipole and is not necessarily the same as the external applied field.

The polarisation, P, of a crystal is the induced dipole moment per unit volume. Thus,

$$\mathbf{P} = N_v \mathbf{m}_{\text{induced}} \tag{2.8}$$

where $\mathbf{m}_{\text{induced}}$ is the induced dipole moment per formula unit and N_v is the number of formula units per unit volume. (It is assumed that all the molecular dipole moments lie in the same direction.) If there are several different ions within a crystal formula unit, then the resultant polarisation is expressed as the sum over all the ions in the formula unit:

$$\mathbf{P} = N_v \underbrace{\sum_{i=1}^{n} \alpha_i}_{\alpha_{\text{tot}}} \mathbf{E}_{\text{loc}} \tag{2.9}$$

where α_{tot} is the polarisability. The polarisation of the crystal can therefore be expressed as:

$$\mathbf{P} = N_v \alpha_{\text{tot}} \mathbf{E}_{\text{loc}} \tag{2.10}$$

The polarisability of a complex mineral can therefore be expressed as the sum of the polarisabilities of the constituent ions in one formula unit.

The applied electric field, $\mathbf{E}$, is generally not the same as the local field, $\mathbf{E}_{\text{loc}}$, acting on a dipole in a unit cell. This local field is usually larger than the applied field because of the cumulative effect of all the other dipoles in the crystal. By considering the electrical field at the centre of a charged sphere, it is possible to derive the Lorentz equation, which relates the local electric field to the applied field:

$$\mathbf{E}_{\text{loc}} = \mathbf{E}\left(\frac{\varepsilon' + 2}{3}\right) \tag{2.11}$$

In fact this is only valid for mutually-interacting infinitely small dipoles in a cubic crystal, however it is a useful relation which, as will be seen later, is widely used.

The electrical flux density, $\mathbf{D}$, given by:

$$\mathbf{D} = \varepsilon_o \varepsilon' \mathbf{E} \tag{2.12}$$

is a measure of the extent to which the surroundings modify the applied electric field and is numerically equal to surface charge per unit area (Cm^{-2}). The polarisation, **P**, is equal to the difference between the bound surface charge and that for a vacuum:

$$\mathbf{P} = \mathbf{D} - \varepsilon_o \mathbf{E} \tag{2.13}$$

therefore,

$$\mathbf{P} = (\varepsilon' - 1)\varepsilon_o \mathbf{E} \tag{2.14}$$

The term $(\varepsilon' - 1)$ is the dielectric susceptibility, χ, so that

$$\varepsilon' = (1 + \chi) \tag{2.15}$$

It is possible to identify several different contributions to polarisability which occur over different frequency ranges as described below:

(i) *Electronic polarisability* consists of the displacement of the electrons in an atom relative to the nucleus under the influence of an electric field. This type of polarisation occurs within every dielectric solid and it occurs at very high frequencies, typically in the ultra-violet range (>EHz, 10^{18} Hz).

(ii) *Ionic polarisability* arises from the relative displacement or separation of anions and cations in a solid. It is the principal source of polarisation in an ionic crystal and occurs at microwave to infra-red frequencies (GHz - PHz, 10^9 - 10^{15} Hz).

(iii) *Dipolar polarisability* arises as a result of reorientation of permanent electric dipoles in materials such as H_2O or HCl . This occurs at audio to radio frequencies (kHz - MHz, 10^3 - 10^6 Hz) in solids, but at higher frequencies (radio - microwave, MHz – GHz, 10^6 – 10^9 Hz) in liquids and gases.

(iv) *Paraelectric polarisability* is caused by a cation in a "sloppy" fit between large anions. It occurs in crystalline solids, such as barium titanate, $BaTiO_3$, at microwave to infra-red frequencies (GHz – PHz, 10^9 – 10^{15} Hz).

(v) *Ferroelectric polarisability* occurs in ionic solids which have a permanent polarisation on account of a cooperative shift of some of the atoms in a given direction. For example, below 120°C the Ti^{4+} ion in barium titanate, $BaTiO_3$, undergoes a displacement of about 0.1 Å relative to its anionic neighbours, giving rise to electric dipoles that exist in the absence of an electric field. A solid which is ferroelectric will become paraelectric above a certain characteristic temperature: the Curie point, T_c. Above this temperature the amplitude of thermal vibrations is strong enough to prevent the formation of an ordered electric dipole array.

(vi) *Interfacial polarisability* occurs when charges (ions or electrons) accumulate at edges or intercrystalline boundaries. This takes place at extremely low frequencies (<1Hz).

2.1.4 Frequency dependence of real dielectrics

In an oscillating electric field, dipoles in a system tend to follow the field, flipping back and forth as the field reverses its direction during each cycle. The value of the dielectric constant varies with the frequency of the applied electric field and at certain frequencies energy is absorbed and is dissipated as heat within the dielectric. When an alternating field, E , is applied, there is a frequency dependent alternating current which does not reach its maxima and minima at the same time as the voltage, i.e. it leads in phase. At low frequencies the current leads the voltage by exactly 90°; this is the behaviour of an ideal dielectric because the energy losses due to the Joule heating are zero, i.e. the product $I \times V = 0$. As the frequency is raised, the ionic polarisations can no longer keep up with the alternating field and the current now leads the voltage by an angle $(90 - \delta)$ as shown in Figure 2.5.

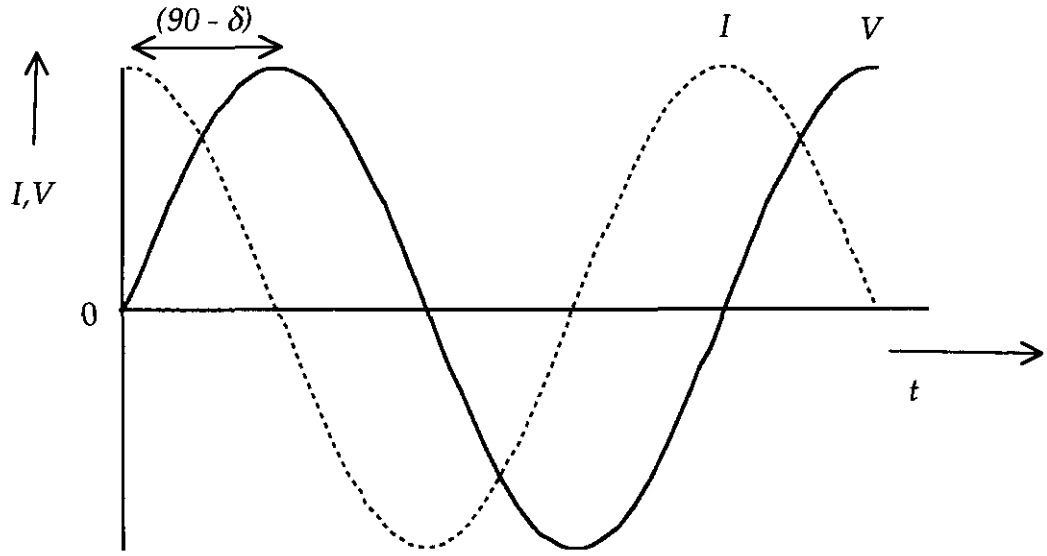

Figure 2.5 Time dependence of current, I, and applied voltage, V.

This current, I, is given by:

$$I = j\omega CE \tag{2.16}$$

where $j = \sqrt{-1}$ and ω is the angular frequency.

The current, I, passing through a resistor under an applied voltage, V, is given by Ohm's Law:

$$I = \frac{V}{R} \tag{2.17}$$

and is independent of frequency. Therefore, the magnitude of the total impedance, Z, of a real dielectric is given by:

$$\frac{1}{Z} = \frac{1}{R} + j\omega C \tag{2.18}$$

If the phase angle, $\theta = (90 - \delta)$, represents the angle by which the current waveform leads the voltage waveform, then equation 2.18 can be represented by a complex diagram (Figure 2.6).

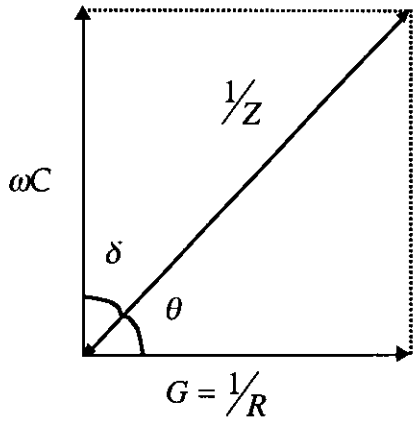

Figure 2.6 Complex diagram showing the electrical response of a dielectric.

2.2 Dielectric theory

2.2.1 Dielectric loss

When the frequency of the applied field is such that the ionic polarisations can no longer keep up with the field and the current leads the voltage by $(90 - \delta)$, the current now has a component $I\sin\delta$ that is in phase with the voltage. This gives rise to dissipation of heat, i.e. dielectric losses. If a general permittivity is defined such that:

$$\varepsilon^* = \varepsilon' - j\varepsilon'' \tag{2.19}$$

where ε' is the real part of ε^* and is equivalent to the measured dielectric constant; ε'' is the loss factor and is a measure of the conductance or dielectric losses in the material. The complex capacitance, C^* of a real dielectric can be expressed as:

$$C^* = \varepsilon^* C_0 = \frac{\varepsilon^* \varepsilon_0 A}{d} \tag{2.20}$$

The impedance, Z, of a real capacitor is therefore given by:

$$Z = \frac{1}{j\omega C^*} = \frac{1}{j\omega C_0[\varepsilon' - j\varepsilon'']} \tag{2.21}$$

where C_0 is a constant.

It follows from equation 2.18 that:

$$Z = \frac{R}{1 + j\omega CR} \tag{2.22}$$

and so by combining equations 2.21 and 2.22 and equating real and imaginary parts:

$$\frac{1}{R} + j\omega C = j\omega C_0(\varepsilon' - j\varepsilon'') = j\omega C_0\varepsilon' + \omega C_0\varepsilon'' \tag{2.23}$$

giving:

$$\varepsilon' = \frac{C}{C_0} \tag{2.24}$$

and:

$$\varepsilon'' = \frac{1}{\omega C_0 R} = \frac{G}{\omega C_0} \tag{2.25}$$

With reference to Figure 2.6 it follows that:

$$\tan\delta = \frac{1}{\omega CR} = \frac{\varepsilon''}{\varepsilon'} = \frac{G}{\omega C} = \frac{\sigma}{\omega\varepsilon'\varepsilon_0} \tag{2.26}$$

The equivalent circuit defined for a real capacitor contains a resistor and conduction through it must always therefore cause Joule heating. It can be seen from Figure 2.6 that $\sin\delta$ is a measure of the resistive impedance and hence is proportional to the heat dissipated or energy absorbed. Since most dielectric materials have very little conduction, $\tan\delta < 0.5$ and $\sin\delta \approx \tan\delta$. Therefore the energy absorbed is proportional to $\tan\delta$, the dielectric loss.

Measurement of $\tan\delta$ or ε'' as a function of frequency of the applied field can therefore be used as a measure of the energy absorbed by polarising species in a dielectric material. If the dielectric response of the material is measured as a function of frequency, it is found that there are regions of increased dielectric loss and sharp drops in the permittivity at certain frequencies, known as *dispersion regions* (Figure 2.7). These rapid changes in dielectric constant suggest that for each of the frequencies at which they occur, one of the polarisation mechanisms "switches off" because it can no longer keep in step with the applied field.

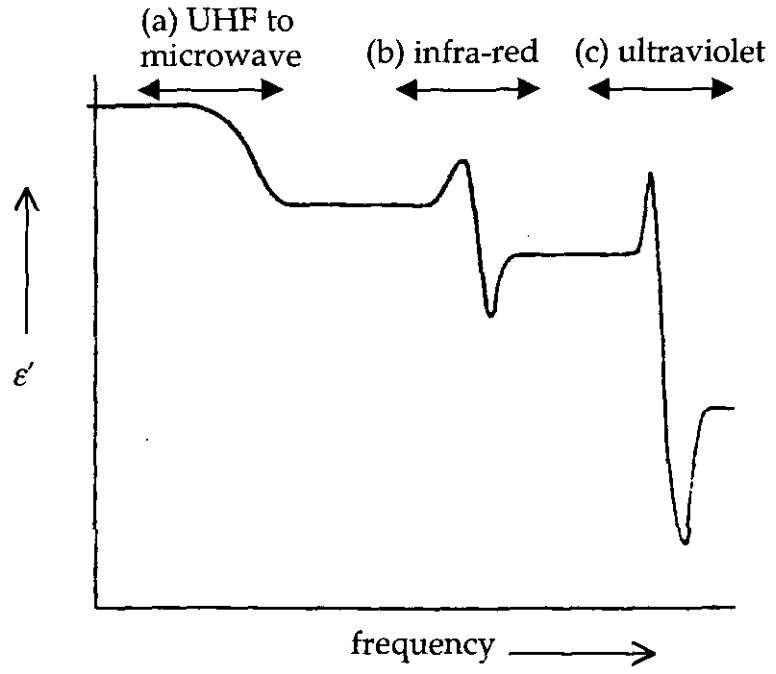

Figure 2.7 The variation of ε' with frequency for a simple dielectric.

There are two different types of mechanism which can give rise to this kind of behaviour: *resonance absorption* and *dipole relaxation*. At high frequencies, (microwave and beyond), the processes that take place are undamped resonances (Figure 2.7 (b) and (c)); real materials have several such resonances due to ionic and electronic polarisation. At lower frequencies all dispersions are heavily damped and relaxation effects are observed (Figure 2.7 (a)).

Any dipole can be described in terms of a positive and negative charge bound together by elastic restoring forces. This system will have a natural (angular) frequency of oscillation ω_o. If the frequency of the alternating field $\omega > \omega_o$, then the dipole will not be able to follow the field. This will result in an under-damped resonance. A pure resonance can be simulated by an electrical analogue which has no resistive terms, just a coil, or inductor, in series with a capacitor as shown in Figure

2.8(a). The variation of ε' and ε'' with frequency for a resonance absorption is shown in Figure 2.8(b).

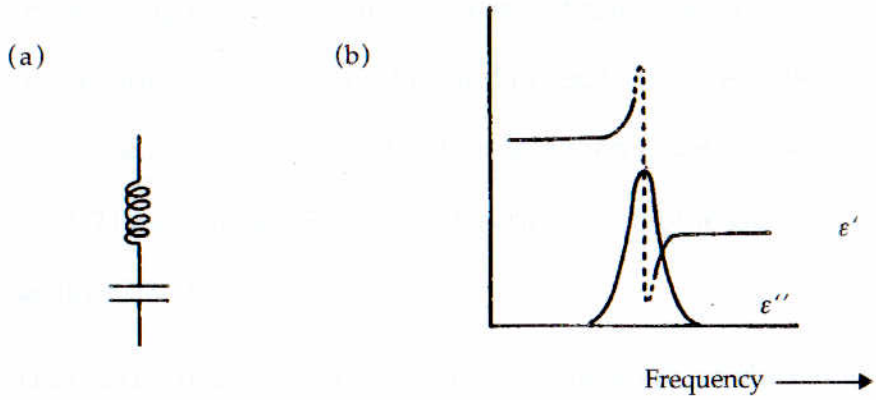

Figure 2.8 Resonance absorption. (a) The electrical analogue of a pure resonance dispersion; (b) the variation of ε' and ε'' with frequency.

At frequencies below those of microwaves (i.e. $< 10^9$ Hz), dielectric dispersions are called relaxations. A dipole will be displaced parallel to the field direction and eventually, by interaction with its surroundings, will relax back to its original position as illustrated in Figure 2.9.

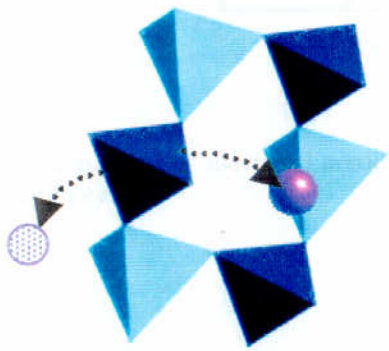

Figure 2.9 Dipole relaxation in an alternating electric field.

The rate of energy transfer to the surroundings can be assumed to be an exponential process with a characteristic time constant τ, the relaxation time, which is determined by the strength of the interaction between the dipole and the system to which it is transferring energy. (It should be noted that this relaxation time has no direct connection with the natural period of oscillation described previously.) If the period of oscillation of the applied field is less than τ, the dipole will not be able to follow the field. These relaxations can be described using the Debye equations (described in section 2.2.2).

There is no inductive contribution to relaxation, as shown in Figure 2.10 (a). The variation of ε' and ε'' with frequency for a relaxation absorption is shown in Figure 2.10(b).

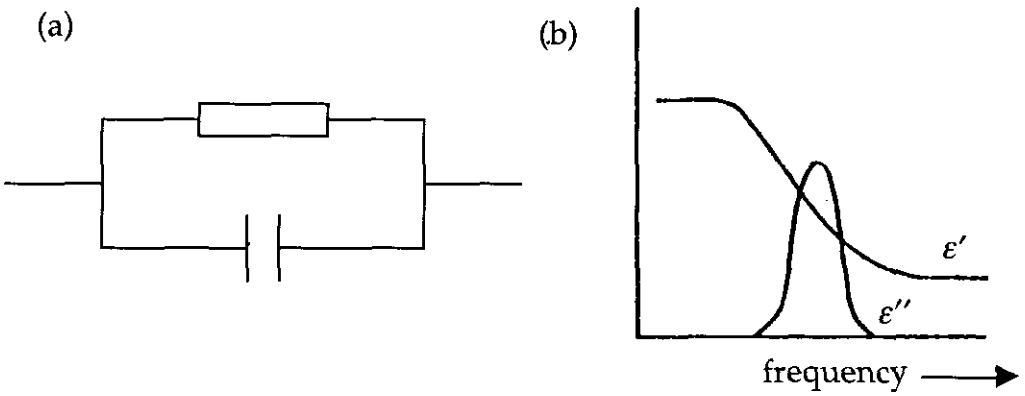

Figure 2.10 Relaxation absorption. (a) The electrical analogue of a relaxation dispersion; (b) the variation of ε' and ε'' with frequency.

2.2.2 The Debye equations

Dielectric relaxation involves an oscillating electric field as the stimulus, with a polarisation as the response. Using the simple electrical analogue of an RC parallel circuit (as described in section 2.1.2) as the basis for a mathematical description of relaxation, the Debye equations are a useful approximation for describing most relaxations. The polarisation, P, has been shown to be given by the equation:

$$P = (\varepsilon' - 1)\varepsilon_0 E \tag{2.14}$$

The dielectric relaxation of the system is the response to the time-dependent change in polarisation caused by the oscillating electric field. If at time $t = 0$ a static electric field, E, is applied to the sample, there will be an instantaneous polarisation, P_1, which will not vary; there will also be a time-dependent polarisation $P(t)$ which will gradually increase from 0 at $t = 0$ to a saturation value $P_2(\infty)$, the magnitude of which will depend on the applied field. The polarisation at time t, $P(t)$ is therefore given by:

$$P(t) = P_1 + P_2(t) \tag{2.27}$$

The effect of a static electric field can be considered to be the same as an oscillating field of infinite frequency, therefore, when $t = 0$, $\omega \rightarrow \infty$ and $\varepsilon' \rightarrow \varepsilon_\infty$ (the permittivity at infinite frequency).

Thus:

$$P(0) = P_1 + 0 \ = (\varepsilon_\infty - 1)\ \varepsilon_0 E \tag{2.28}$$

Similarly, as $t \rightarrow \infty$, $\omega \rightarrow 0$, (i.e. an alternating field of zero frequency) and $\varepsilon' \rightarrow \varepsilon_s$ (the permittivity for a static field), hence:

$$P(\infty) = P_1 + P_2(\infty) = \varepsilon_0(\varepsilon_s - 1)\ E \tag{2.29}$$

From equations 2.28 and 2.29:

$$P_2(\infty) = \varepsilon_0(\varepsilon_s - \varepsilon_\infty)\ E \tag{2.30}$$

The fundamental assumption of Debye Theory is that the dielectric relaxation follows an exponential function and that under a constant electric field, the sample polarisation increases with time at an exponential rate:

$$P_2(t) = P_2(\infty)[1 - \exp(-t/\tau)] \tag{2.31}$$

where τ, the time constant or relaxation time, defines the slowness of the induced polarisation increase. Equation 2.31 is illustrated graphically in Figure 2.11.

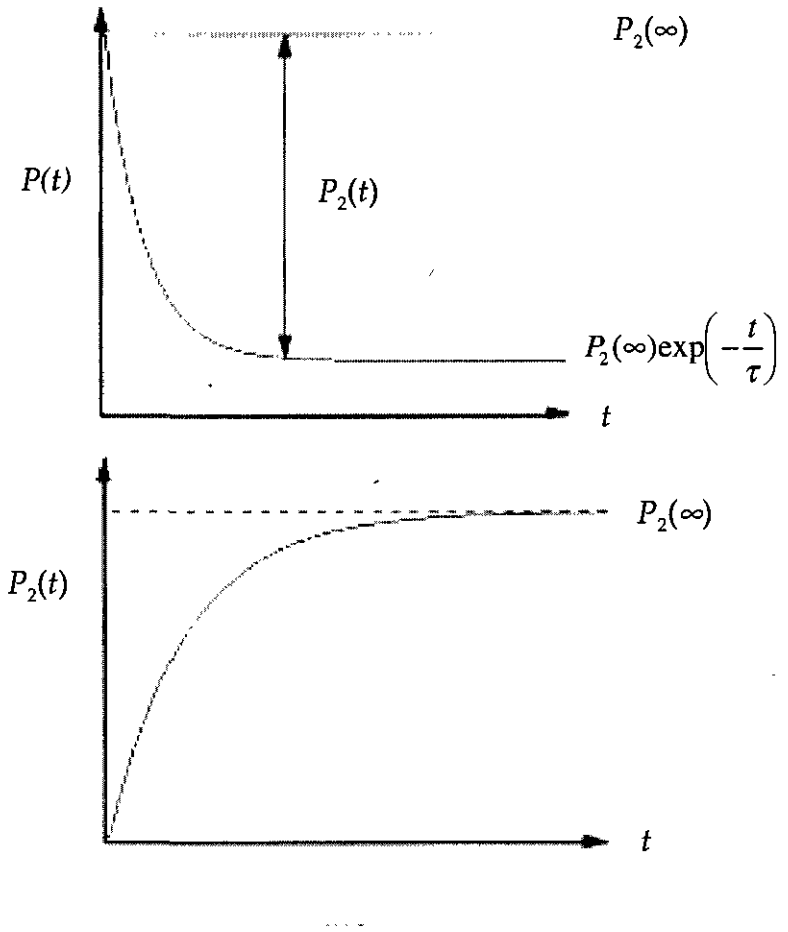

Figure 2.11 Graphical representation of equation 2.31, the main assumption of Debye theory.

Differentiating equation 2.31:

$$\begin{aligned}\frac{dP_2(t)}{dt} &= 0 - \frac{d}{dt}\left\{P_2(\infty)\exp\left(-t/\tau\right)\right\} \\ &= \frac{1}{\tau}P_2(\infty)\left[\exp\left(-t/\tau\right)\right] \\ &= \frac{1}{\tau}\left[P_2(\infty) - P_2(t)\right]\end{aligned} \tag{2.32}$$

If the dielectric is now considered to be in an oscillating time-dependent field, $E(t)$, where:

$$E(t) = E_o\exp(j\omega\tau) \tag{2.33}$$

then $P_2(\infty)$ will now have a time dependence since the electric field is no longer static. Therefore $P_2(\infty)$ is now the saturation value of the time-dependent part of $P(t)$, i.e. $P_2(t)$, if $E(t)$ were applied instantaneously. So, combining equations 2.30 and 2.33:

$$\begin{aligned}P_2(\infty) &= \varepsilon_o\left(\varepsilon_s - \varepsilon_\infty\right)E \\ &= \varepsilon_o\left(\varepsilon_s - \varepsilon_\infty\right)E_o\exp(j\omega\tau)\end{aligned} \tag{2.34}$$

therefore, from equation 2.32:

$$\frac{dP_2(t)}{dt} = \frac{1}{\tau}\left[\varepsilon_o\left(\varepsilon_s - \varepsilon_\infty\right)E_o\exp(j\omega t) - P_2(t)\right] \tag{2.35}$$

This rearranges to give:

$$\tau\frac{dP_2(t)}{dt} + P_2(t) = \varepsilon_o\left(\varepsilon_s - \varepsilon_\infty\right)E(t) \tag{2.36}$$

so that,

$$\tau\frac{dP_2(t)}{dt} + P_2(t) = KE(t) \tag{2.37}$$

where K is a constant. The solution of this differential equation is:

$$P(t) = \frac{\varepsilon_0\left(\varepsilon_s - \varepsilon_\infty\right)E(t)}{1 + j\omega\tau} + C\exp\left(-t/\tau\right) \tag{2.38}$$

where C is a constant. The exponential term decays very quickly with time and can therefore be neglected. From the definition of polarisation (equation 2.14):

$$P(t) = (\varepsilon^* - 1)\varepsilon_o E(t) \tag{2.39}$$

Using complex notation for the permittivity to describe a real dielectric:

$$P(t) = (\varepsilon^* - 1)\varepsilon_o E(t) = P_1 + P_2(t)$$
$$P(t) = \varepsilon_o(\varepsilon_\infty - 1)E(t) + \frac{\varepsilon_o(\varepsilon_s - \varepsilon_\infty)E(t)}{1 + j\omega\tau} \tag{2.40}$$

It follows that:

$$\varepsilon^* = \varepsilon_\infty + \frac{\varepsilon_s - \varepsilon_\infty}{1 + j\omega\tau} = \varepsilon' - j\varepsilon'' \tag{2.41}$$

Equating the real and imaginary parts:

$$\varepsilon' = \varepsilon_\infty + \mathrm{Re}\left\{\frac{\varepsilon_s - \varepsilon_\infty}{1 + j\omega\tau}\right\} \tag{2.42}$$

$$\varepsilon'' = \mathrm{Im}\left\{\frac{\varepsilon_s - \varepsilon_\infty}{1 + j\omega\tau}\right\} \tag{2.43}$$

It follows that:

$$\frac{\varepsilon_s - \varepsilon_\infty}{1 + j\omega\tau} = \frac{(\varepsilon_s - \varepsilon_\infty)(1 - j\omega\tau)}{(1 + j\omega\tau)(1 - j\omega\tau)} = \frac{(\varepsilon_s - \varepsilon_\infty)(1 - j\omega\tau)}{1 + \omega^2\tau^2} \tag{2.44}$$

The Debye equations are thus obtained:

$$\varepsilon' = \varepsilon_\infty + \frac{\varepsilon_s - \varepsilon_\infty}{1 + \omega^2\tau^2} \tag{2.45}$$

$$\varepsilon'' = \frac{(\varepsilon_s - \varepsilon_\infty)\omega\tau}{1 + \omega^2\tau^2} \tag{2.46}$$

and since $$\tan\delta = \frac{\varepsilon''}{\varepsilon'} \tag{2.26}$$

it follows that:

$$\tan\delta = \frac{(\varepsilon_s - \varepsilon_\infty)\omega\tau}{\varepsilon_s + \varepsilon_\infty\omega^2\tau^2} \tag{2.47}$$

The form of a Debye relaxation is shown in Figure 2.12.

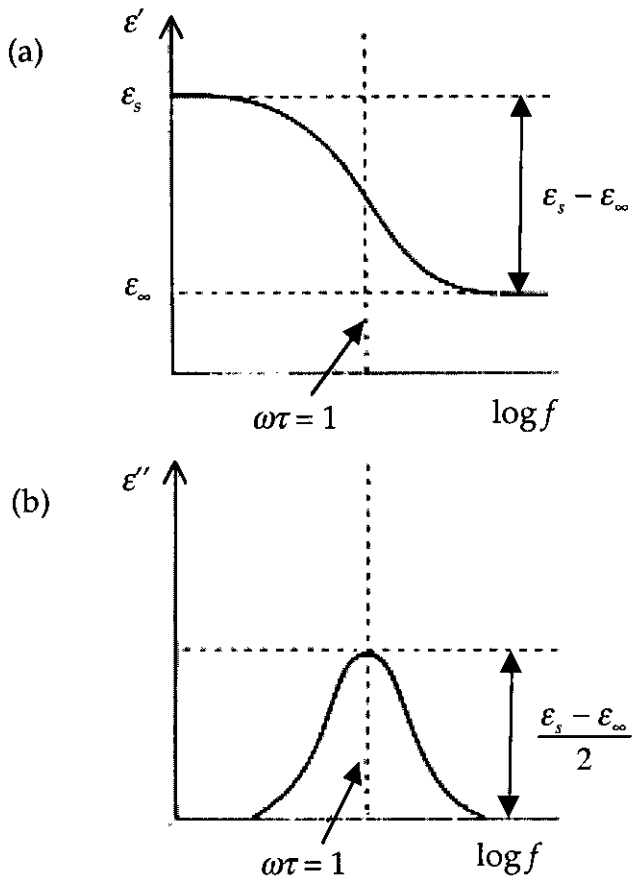

Figure 2.12 The variation of (a) ε'; (b) ε'' with frequency for a Debye relaxation.

Both the dielectric loss, tan δ, and the imaginary part of the dielectric function, ε'', show Lorentzian peaks centred around $\omega\tau = 1$ (for ε'') and $\omega\tau = \sqrt{\varepsilon_s/\varepsilon_\infty}$ (for tan δ). (This can be shown by differentiating the Debye equation for tan δ with respect to $\omega\tau$.) The peak heights are proportional to $(\varepsilon_s\text{-}\varepsilon_\infty)$, which relates to the total number of dipoles in the system. For tan δ the peak height is given by:

$$\frac{\varepsilon_s - \varepsilon_\infty}{2\sqrt{\varepsilon_s \varepsilon_\infty}} \tag{2.48}$$

Experimental peaks in ε'' and tan δ are often wider than the Debye model predicts. Therefore a distribution constant, β, is often introduced, substituting $j\omega\tau$ in equation 2.36 by $(j\omega\tau)^{1-\beta}$. This broadens the distribution and τ is now defined as the mean value of a distribution of time constants.

2.2.3 Temperature dependence of tan δ and ε''

The movement of the position of the maximum in tan δ or ε'' with temperature often shows an Arrhenius-type temperature dependence, so that an activation energy for the relaxation process can be measured:

$$\tau = \tau_0 \exp\left(\frac{-E_a}{k_B T}\right) \tag{2.49}$$

where τ depends on the activation energy, E_a, the temperature, T, and the Boltzmann constant, k_B.

2.2.4 The Maxwell-Wagner effect

Although the Debye equations may be derived for a variety of situations, the loss peaks do not necessarily follow an Arrhenius relation. One such example is relaxation due to multi-layer dielectrics, e.g. inter-grain polarisations, in which the loss peak is superimposed on a background curve and the analysis consists of considering the circuit shown in Figure 2.13(a) in terms of the simpler circuit of Figure 2.13(b). This is known as the Maxwell-Wagner effect. The value of τ is approximately constant and the peaks do not generally shift with temperature .

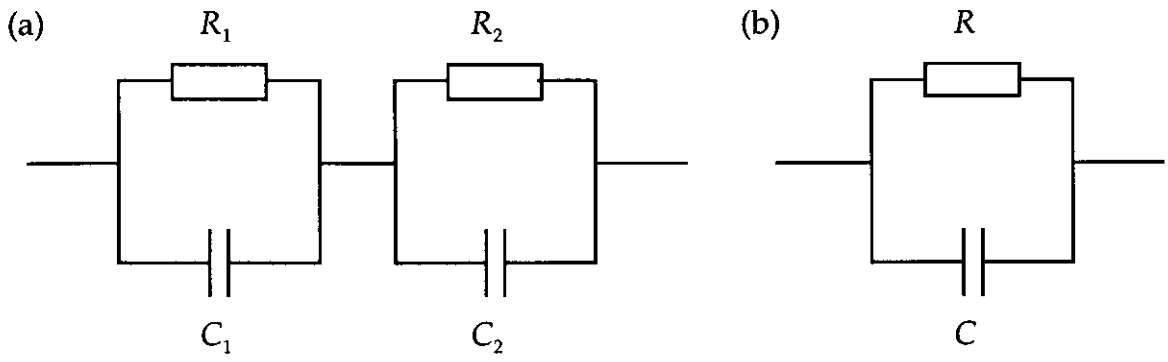

Figure 2.13 (a) Maxwell-Wagner two layer model; (b) the measured quantities.

2.2.5 The Cole-Cole plot

Dielectric measurements can also be presented in the form of complex plane diagrams known as Cole-Cole plots, in which the imaginary part of the dielectric function, ε'', is plotted as a function of the real part of the dielectric function, ε'. For a dielectric with a single relaxation time, τ, the resulting Cole-Cole plot is a semi-circle as shown in Figure 2.14.

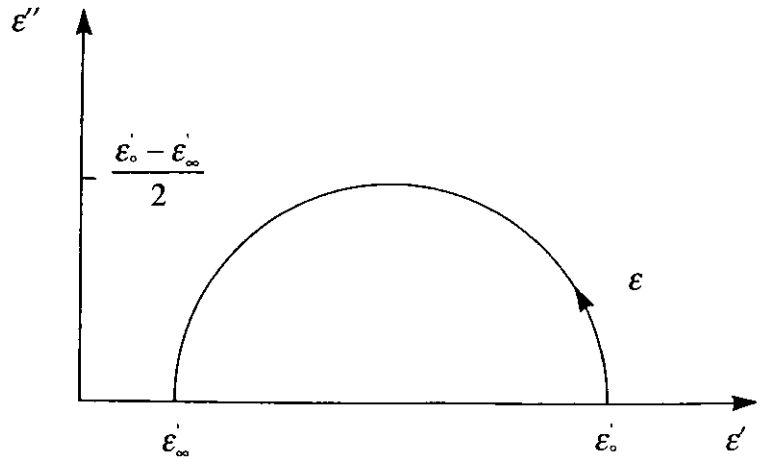

Figure 2.14 Cole-Cole complex plane plot for a dielectric.

It can be shown from the Debye equations:

$$\varepsilon' = \varepsilon_\infty + \frac{\varepsilon_s - \varepsilon_\infty}{1+\omega^2\tau^2} \quad \text{where: } \varepsilon_\infty \le \varepsilon' \le \varepsilon_s \tag{2.45}$$

$$\varepsilon'' = \frac{(\varepsilon_s - \varepsilon_\infty)\omega\tau}{1+\omega^2\tau^2} \text{ where: } 0 \le \varepsilon' \le \tfrac{1}{2}(\varepsilon_s - \varepsilon_\infty) \tag{2.46}$$

and that the equation between the real and imaginary parts describes a circle:

$$\left\{\varepsilon'(\omega) - \tfrac{1}{2}(\varepsilon_s - \varepsilon_\infty)\right\}^2 + \left\{\varepsilon''(\omega)\right\}^2 = \tfrac{1}{4}(\varepsilon_s - \varepsilon_\infty)^2 \tag{2.50}$$

The values of ε'_0 and ε'_∞ may be obtained by extrapolating the data to cut the ε' axis.

The peaks in the dielectric loss, ε'', are not always symmetric Debye peaks but are often broadened asymmetrically. Similarly, in practice, Cole-Cole plots are often not exactly semi-circular, but are distorted to varying degrees. This is due to the superposition of more than one relaxation process, each occurring at a different frequency.

2.2.6 The Clausius-Mosotti Equation

The electric field, E_{loc},which acts on a dipole is not the same as the applied external field, E (see section 2.1.3). This local field, E_{loc}, is usually higher than E due to the added effects of all the other dipoles in the crystal. As already described, it is possible to derive the Lorentz equation which relates the local electric field to the external field:

$$E_{loc} = E\left(\frac{\varepsilon' + 2}{3}\right) \tag{2.11}$$

This equation assumes mutually-interacting, infinitely-small dipoles in a cubic crystal structure, but it can be used to show how the polarisabilities of the ions in a unit cell relate to the dielectric permittivity of the crystal. It allows general comments to be made about the variation of capacitance with temperature for real materials.

It was shown in section 2.1.3 that:

$$P = \varepsilon_0 E(\varepsilon' - 1) \tag{2.14}$$

If the total number of dipoles per unit volume is N and m is the dipole moment of the dipole, then the polarisation, P, is given by:

$$P = Nm \tag{2.51}$$

Since $m = \alpha_D E_{loc}$, (section 2.1.3) where α_D is the polarisability of a given dipole and E_{loc} is the local field acting,

$$P = N\alpha_D E_{loc} = \varepsilon_0 E(\varepsilon' - 1) \tag{2.52}$$

Therefore,

$$\frac{E_{loc}}{E} = \frac{\varepsilon_0(\varepsilon' - 1)}{N\alpha_D} \tag{2.53}$$

Now from the Lorentz equation, (2.11),

$$\frac{E_{loc}}{E} = \left(\frac{\varepsilon' + 2}{3}\right) = \frac{\varepsilon_0(\varepsilon' - 1)}{N\alpha_D} \tag{2.54}$$

This gives the *Clausius-Mosotti* equation:

$$\frac{(\varepsilon' - 1)}{(\varepsilon' + 2)} = \frac{N_f \alpha_D}{3\varepsilon_0} \tag{2.55}$$

If N_f is the number of formula units per unit volume and V_f is the volume per formula unit, then the Clausius-Mosotti equation can also be expressed as:

$$\frac{(\varepsilon' - 1)}{(\varepsilon' + 2)} = \frac{\alpha}{3V_f\varepsilon_0} \tag{2.56}$$

giving:

$$\alpha = 3\varepsilon_0 V_f\left(\frac{\varepsilon' - 1}{\varepsilon' + 2}\right) \tag{2.57}$$

where α is the total polarisability per unit volume.

The Clausius-Mosotti equation only applies rigorously to substances having very small induced dipoles, ideally those where only electronic polarisation is significant. In these cases, i.e. in non-absorbing regions, the permittivity varies little with frequency and $\varepsilon \rightarrow \varepsilon_\infty$ and $\varepsilon' = n^2$, where n is the refractive index. If the volume per formula unit, V_f (m^3) is expressed as:

$$V_f = \frac{M}{N_A \rho} \tag{2.58}$$

where M is the relative formula mass, N_A is the Avogadro constant (6.023×10^{23} mol^{-1}) and ρ is the density (gm^{-3}), then the Clausius Mosotti equation can be rewritten as:

$$\alpha_D = 3\varepsilon_0 V_f \left(\frac{n^2 - 1}{n^2 + 2}\right) = 3\varepsilon_0 \frac{M}{N_A \rho}\left(\frac{n^2 - 1}{n^2 + 2}\right) \tag{2.59}$$

This equation, is known as the Lorentz-Lorenz equation. Since the optical refractive indices of silicate minerals are well known, it can be used to calculate the electronic polarisabilities of silicates.

2.3 Experimental measurement of dielectric properties

2.3.1 Sample preparation

The crystals used for dielectric measurements were selected on the basis of their overall quality: freedom from internal cracks is of paramount importance, as small cracks or grain boundaries may allow bulk conduction, concealing other processes occurring at the same frequencies. Other considerations include large size and well developed crystal faces, if possible, so that crystal orientation can be determined. Typically, specimens, which were either single crystals or polycrystalline, were 0.4 - 0.8 mm thick with a minimum diameter of 2 – 3 mm. Crystals were cut into thin

discs and polished to a smooth finish using 0.3 μm aluminium oxide. The area of each crystal was measured accurately by scanning the crystals using a flatbed scanner at high resolution (~2400 dpi). The area of the crystal was then calculated from the scanned image using the NIH Image computer program. The thickness of the disc was measured using a micrometer screw gauge.

2.3.2 Dielectric measurements

The crystals were placed between two platinum electrodes (diameter 3 mm) connected via shielded, coaxial cable to a Hewlett Packard HP4192A Impedance Analyser. The electrode assembly was mounted in a vertical tube furnace as shown in Figure 2.16. A pyrophyllite block resting on the electrode 'sandwich' was used to maintain good electrical contact and the large thermal mass of the assembly was designed to reduce temperature gradients inside the tube.

Capacitance, C, and conductance, G, were measured as a function of the frequency of the applied electric field at each temperature. The Impedance Analyser provided logarithmic frequency sweeps from 10 Hz to 13 MHz, recording mean values (averaged over 1 s) of C and G for each frequency. The data obtained were analysed using Igor Pro (WaveMetrics).

Test measurements

Test measurements were performed on crystals of analcime and leucite. Activation energies calculated from the dielectric measurements compared well with previously published values: 0.59 ± 0.06 eV for dehydrated analcime, c.f . 0.59 eV (Palmer, 1997) and 0.73 ± 0.13 eV for leucite, c.f. 0.77 eV (Palmer and Salje, 1990).

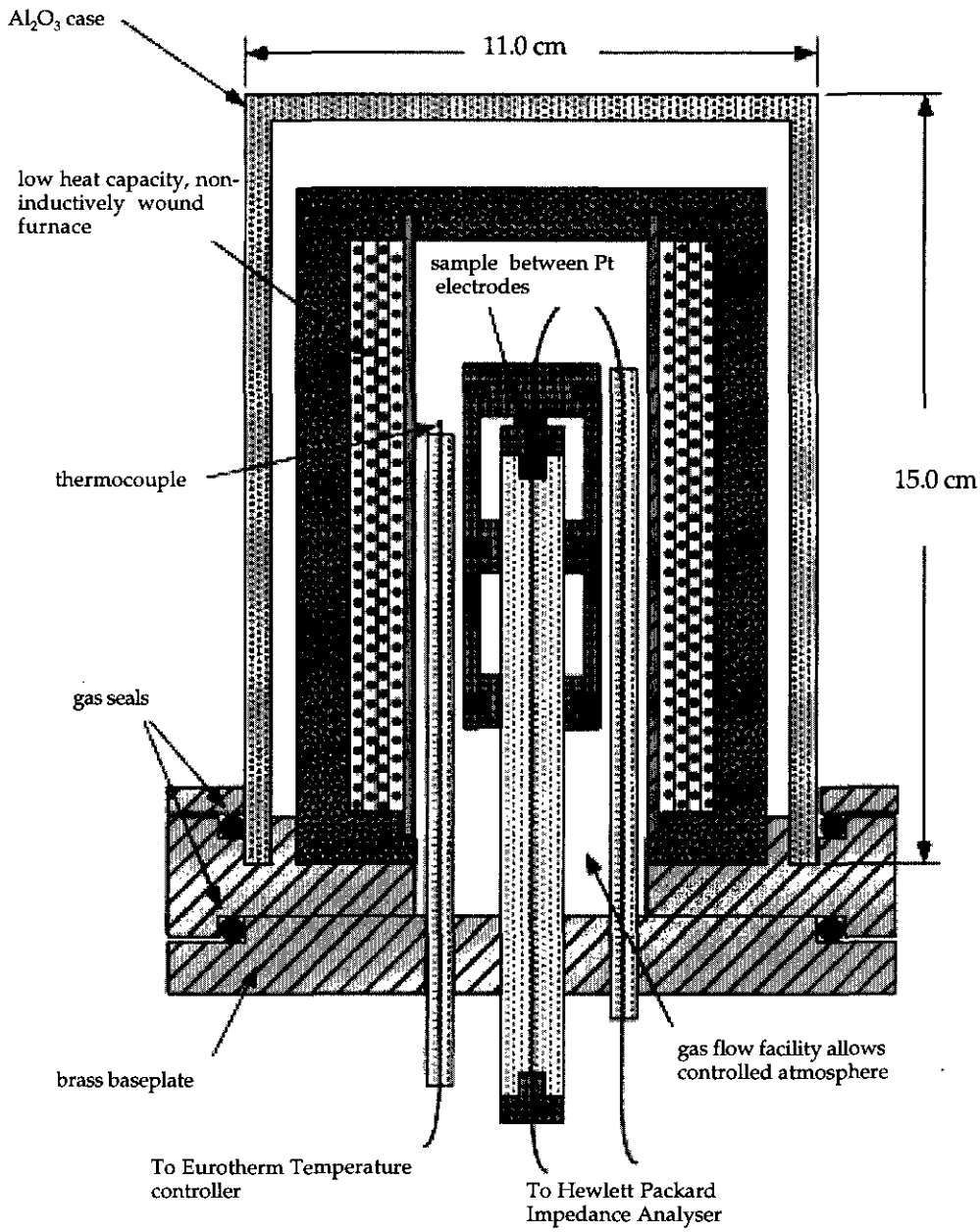

Figure 2.16 The furnace and sample holder used for dielectric measurements.

2.3.3 Temperature calibration and background correction

Temperature calibration

In order to calibrate the observed temperature scale of the furnace, a single crystal of sodium niobate, kindly supplied by Dr. Mike Glazer, University of Oxford, was used. Sodium niobate, $NaNbO_3$, undergoes a number of known phase transitions (Darlington and Knight, 1999) in the temperature range which was used for subsequent dielectric measurements. Measurements of *C* and *G* were made on a crystal of sodium niobate in the temperature range 300 K - 930 K. The evidence for four of the phase transitions can be seen in a plot of capacitance versus temperature (Figure 2.17).

The measured temperatures were then compared with the temperatures of the known phase changes of sodium niobate (Table 2.1), enabling a calibration to be made over the temperature range to be used in subsequent experiments. From the results of these measurements, the furnace was estimated to be accurate to within ± 5 K.

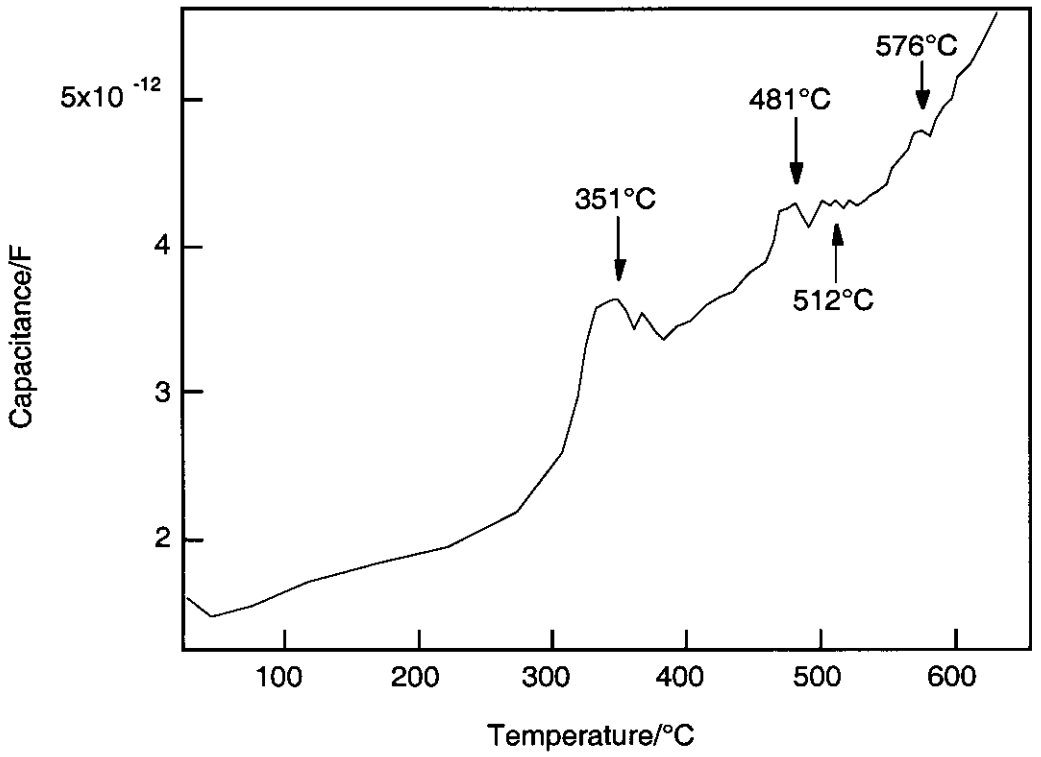

Figure 2.17 Plot of capacitance versus temperature for sodium niobate measured at 10 kHz.

Table 2.1 The phases of sodium niobate (Darlington and Knight, 1999)

Temperature/°C	Phase Transition
-80	rhombohedral → monoclinic
370	monoclinic → orthorhombic/I
480	orthorhombic I → orthorhombic II
520	orthorhombic II → orthorhombic III
575	orthorhombic III → tetragonal
640	tetragonal → cubic

Background correction

The background contributions to the measured capacitance and conductance due to instrumental effects (in the connecting cables, analyser etc.) were assumed to be temperature independent. Measurements of C and G for a crystal in the furnace at room temperature and in a test shunt directly connected to the analyser (no leads), together with measurements on the empty test shunt over the whole frequency range, were used to calculate the background capacitance and conductance as described below, e.g. the "true" capacitance, C_{true}, of the crystal is given by:

$$C_{(true)} = C_{(crystal\ in\ shunt)} - C_{(empty\ shunt)} \tag{2.60}$$

and the absolute value of the background capacitance, C_{back}, is given by:

$$\begin{aligned} C_{(back)} &= C_{(crystal\ in\ furnace\ at\ room\ temperature)} - C_{(true)} \\ &= C_{(crystal\ in\ furnace\ at\ room\ temperature)} - C_{(crystal\ in\ shunt)} + C_{(empty\ shunt)} \end{aligned} \tag{2.61}$$

The background conductance, G_{back}, was also calculated in this way. These background contributions to C and G were subtracted from all high temperature furnace measurements.

Chapter 3

Computer Simulation Methods

Contents

3.1 Introduction

Computer simulation studies have opened a new door into the study of the properties of minerals at an atomic level. They have already made widespread contributions to the study of a variety of materials, including catalysts (Catlow et al., 1990; Islam et al., 1994), high temperature superconductors (Islam et al., 1997; Winch and Islam, 1995) and ionic conductors (Islam et al., 1996; Stefanovich et al., 1994). These techniques allow control of macroscopic variables such as composition, temperature and pressure, while allowing the manipulation of microscopic variations in the structure, e.g. by modelling the introduction of features such as defects into the structure. This then allows the examination of the resultant macroscopic and microscopic effects on the properties and the crystal structure of the mineral, often providing an insight into the solution to problems which are difficult to obtain experimentally.

The basis of computer simulation techniques is to first represent a structure by an interatomic potential model which accurately reproduces the crystal structure of the system under investigation. When this has been achieved, calculations can then be performed on the structure to investigate the effects of defects, dopant substitution and ion migration.

This chapter describes the atomistic simulation techniques that have been used in the study of ion migration mechanisms in the minerals investigated in this thesis. More substantial reviews of these methods are given elsewhere (Catlow and Price, 1990; Catlow, 1987; Catlow, 1994; Islam, 2000).

3.2 Perfect lattice simulations

The basis of any computer simulation technique is the specification of a potential model, i.e. a description in mathematical terms of the energy of the system as a function of particle coordinates. The simulations are formulated within the Born model representation, in which an ionic crystal is regarded as comprising discrete ions. It includes a long-range Coulombic interaction between each pair of ions, *i* and *j*, together with a short-range term to model overlap repulsions and van der Waals forces. The reliability of the results of the simulations depends on the extent to which such models represent the system under study.

The most important perfect-lattice property in these calculations is the lattice energy, (U_L), which is defined as the energy required to bring together gaseous ions from an infinite separation to their equilibrium positions within the crystal. The calculation of the energetics of a three-dimensional system theoretically involves the evaluation of interactions between all species within the unit cell and their periodic replications to infinity. As some finite cut-off has to be placed on the computation of the interactions, the components of the lattice energy are decomposed into two classes: long-range and short-range potentials. A general expression for the lattice energy can be written as:

$$(U_L) = \sum_{ij} \frac{q_i q_j}{r_{ij}} + \sum_{ij} \Phi_{ij}(r_{ij}) + \sum_{ijk} \Phi_{ijk}(r_{ijk}) + ... \qquad (3.1)$$

where the summations refer to all pairs of ions *ij* and, for materials which deviate from ionic bonding, all trios of ions *ijk* in the crystal. The first term on the right-hand side of equation 3.1 is the sum of the Coulomb interactions between pairs of ions *i* and *j* separated by a distance r_{ij}. The summation of this term may present problems due to slow convergence, but this is improved by using a technique developed by

Ewald (1921) in which the summation is transformed into reciprocal space. In the Ewald summation, each point charge is viewed as being surrounded by a Gaussian charge distribution of equal magnitude and opposite sign (Heyes, 1981). This charge distribution screens the interaction between neighbouring point charges, effectively limiting them to short range. Consequently, the sum over all charges and their images in real space converges rapidly. To counteract this induced Gaussian distribution, a second Gaussian charge distribution, of the same sign and magnitude as the original distribution, is added for each point charge. This time the sum is performed concurrently in reciprocal space. Provided the real space electrostatic cut-off matches the short range reciprocal space cut-off, and it is kept at less than the shortest unit cell vector, the technique gives sufficiently accurate results for moderate to large systems.

The remaining terms on the right-hand side of equation 3.1 refer to short range interactions, which include the repulsive forces due to the overlap of ion charge clouds, the attractive terms due to dispersive interactions and to covalence in semi-ionic systems. The terms of the type $\Phi_{ij}(r_{ij})$ are the two-body, central force contributions to the short-range energy which vary with the distances between pairs of ions and have no angular dependency. These are the principal components of the short range energy in ionic systems. The additional "three-body" terms of the type $\Phi_{ijk}(r_{ijk})$ provide some degree of directionality and are functions of the coordinates of three atoms, taking the form of an angle-dependent, bond-bending function. They are known to have significant effects on the vibrational properties of ionic materials, but their contribution to the lattice energy is small. The greater the deviation from ionic bonding, the more important these terms become; they have been applied successfully to zeolites and silicates (Catlow, 1987; Jackson and Catlow, 1988). In

principle, terms involving larger numbers of ions could be included, but in practice it is rare to take the summations beyond the three-body terms.

3.2.1 Interatomic potentials

Interatomic interactions are described by ionic two-body potentials of the form:

$$V_{ij}(r_{ij}) = \left[-Z_i Z_j e^2/r\right] + \left[A_{ij}\exp(-r/\rho_{ij}) - C/r_{ij}^6\right] \tag{3.2}$$

where the first term represents the long-range Coulombic or electrostatic interaction between each pair of ions *i* and *j* in the structure. The second term is an analytical function of the Buckingham form which consists of a repulsive exponential and an attractive dispersion term between pairs of species, describing electron charge cloud overlap repulsions and van der Waals forces, respectively.

For aluminosilicates, it is also necessary to include an extra term in the potential to take account of the directionality of the bonding of oxygen with silicon or aluminium. This term, which is defined for each O-Si-O or O-Al-O bond, takes the form

$$V_{3\text{-body}} = (1/2)k(\theta - \theta_0)^2 \tag{3.3}$$

where k is the bond force constant and θ_0 is the equilibrium bond angle.

It should be stressed that employing such a potential model does not necessarily imply that the electron distribution corresponds to a fully ionic system. The validity of the model is assessed primarily by its ability to reproduce observed crystal properties. It is found that models based on formal charges work well, even for compounds such as silicates and zeolites in which there is a significant degree of covalency (Catlow, 1992b).

3.2.2 Ionic polarisability

It is essential to include ionic polarisability in the potential model since the calculation of physical properties, such as dielectric constant and optical phonon modes, are dependent on its accurate description. In addition, it is important that the response of the lattice to charged defects (which extensively polarise their surroundings) is modelled effectively.

The simplest model which has been used to describe the polarisation that arises from the distortion of electron charge clouds at the ions by the internal electric fields is the Point Polarisable Ion (PPI) model. In its basic form, a polarisability, α, is assigned to each ion, with the dipole moment, μ, in a field of magnitude, E, being given by:

$$\mu = \alpha E \tag{3.4}$$

However, since the coupling between polarisation and short range repulsion is neglected, this model performs unsatisfactorily in the calculation of dielectric properties and defect energies.

A more satisfactory model is the Shell Model , originally developed by Dick and Overhauser (1958). In this model, the ions are assumed to comprise the rigid core of the nucleus plus the tightly bound inner electrons and a loosely bound outer layer, or shell, of the remaining electrons. It is then assumed that the shell and core are held together by a harmonic interaction (i.e. the energy is proportional to the square of the distance between the centres) and the polarisation of the ion is directly proportional to the local electric field. If the charge on the massive core is X, the charge on the massless shell is Y and they are connected by a harmonic spring with force constant k (Figure 3.1a), then a dipole moment is created when an electric field is applied, since the shell is displaced relative to the core (Figure 3.1b).

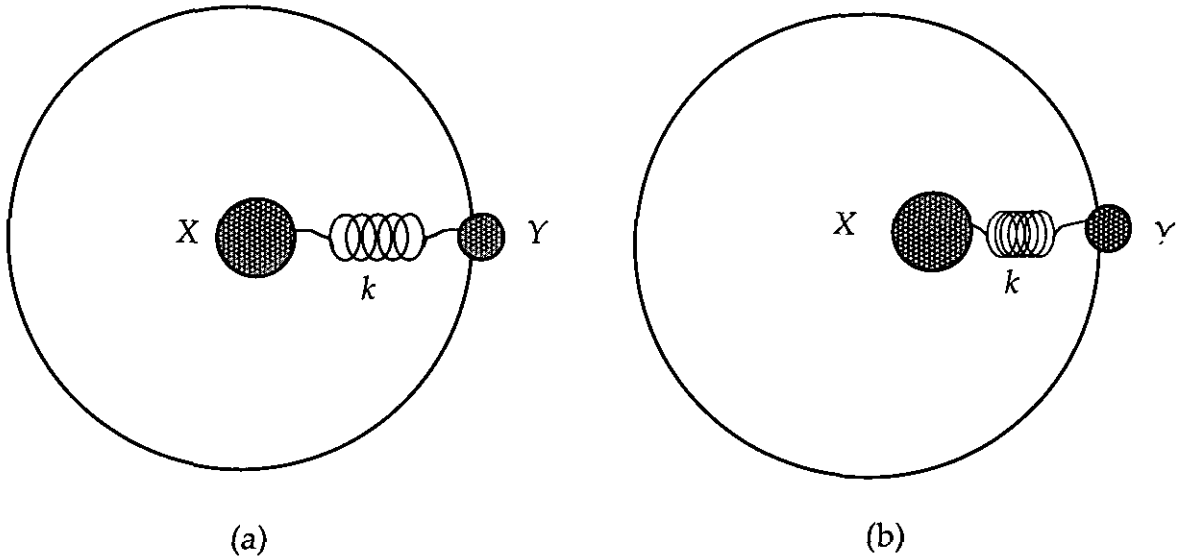

Figure 3.1 Schematic representations of the shell model: (a) no field (unpolarised); (b) applied field (polarised).

The polarisability of the free ion (α') is related to the shell charge and the spring constant by:

$$\alpha' = \frac{Y^2}{k} \tag{3.5}$$

The shell model therefore overcomes the problem of the PPI model, as coupling between the short-range forces and the polarisation is achieved by allowing the short-range potentials to interact exclusively with the shell species.

3.2.3 Energy minimisation

It is only possible to achieve valuable structural and defect properties by employing energy minimisation procedures. These involve adjusting structural parameters, (i.e. lattice parameters and atomic coordinates), until a minimum-energy configuration is attained. Efficient energy minimisation is an essential prerequisite for any subsequent evaluation of physical properties.

The energy of a crystal is a multidimensional function of the atomic coordinates and this variance with the atomic coordinates results in a complex energy surface or *hypersurface*. The minimum points on this potential energy surface, that refer to the stable arrangement of the atoms, are of most concern; any deviation from these local energy minima would result in a structure of higher energy and less stability. It is important to note that an energy minimum may be just a local minimum and it is not necessarily the global energy minimum. The most widely used methods used to identify the global energy minimum are those based on gradient techniques. These involve the use of calculated first derivatives of the energy function with respect to the structural parameters that are being varied. The parameters are then adjusted iteratively until the minimum energy configuration is achieved. Convergence may be greatly accelerated by making use of second, in addition to first, derivatives and the most widely used of these methods is the Newton-Raphson procedure. The GULP program (Gale, 1997) uses a symmetry-adapted energy minimisation technique in which symmetry information can be used to identify the minimum set of variables needed for the minimisation procedure. This increases the rate of calculation of the energy, together with its first and second derivatives during optimisation.

3.2.4 Mean Field Approach

Problems are often encountered in the simulation of complex mineral structures because of the fact that they are often partly disordered or involve "partial occupancies" of sites. These problems can be partly overcome by generating a supercell so that several permutations of structure may be examined. However, the number of possibilities is normally too large to examine each one individually to locate the most stable configuration and this process may alter the symmetry of the crystal.

An alternative approach to handling partial occupancies is to use a mean field approach which allows fractional occupancies to be specified for crystallographic sites. The effect of this is that each site experiences a potential which is the mean of all possible configurations on the disordered positions. This assumes that all possible configurations are equally likely, irrespective of their stability. This assumption may apply to materials where there is little energetic difference between configurations or to ones which were formed under kinetic rather than thermodynamic control and have not had a chance to achieve a Boltzmann distribution. It must therefore be decided for any given material whether it is appropriate to use this approach.

In practical terms the implication of using mean field theory is that all interactions just become scaled by the site occupancies of both atoms. Mean field theory has been implemented in the GULP code (Gale, 1997) such that site occupancy can be specified in addition to the atomic coordinates. The methodology also ensures that the total occupancy of a site does not exceed unity and where two different ions share a site with partial occupancy, they are constrained to move as a single ion during optimisation.

3.3 Modelling of defects and ion migration

The introduction of a defect into a crystal system introduces an extensive perturbation of the surrounding lattice. In the case of ionic crystals, the relaxation field is long-range, as the nature of this perturbation is mainly Coulombic in origin. Realistic defect simulations must therefore include an accurate treatment of lattice relaxation and this can be done by adopting the "two region strategy", which is based on Mott-Littleton methodology (Mott and Littleton, 1938; Lidiard, 1989; Catlow, 1989). Defect energies are calculated by minimising the potential energy

function, Φ, of the defective lattice, with respect to displacements of the ions that surround the defect. The defect energy can then be calculated from the difference in Φ for perfect and defective lattices. This strategy involves partitioning the crystal lattice surrounding the defect into two regions as shown in Figure 3.2.

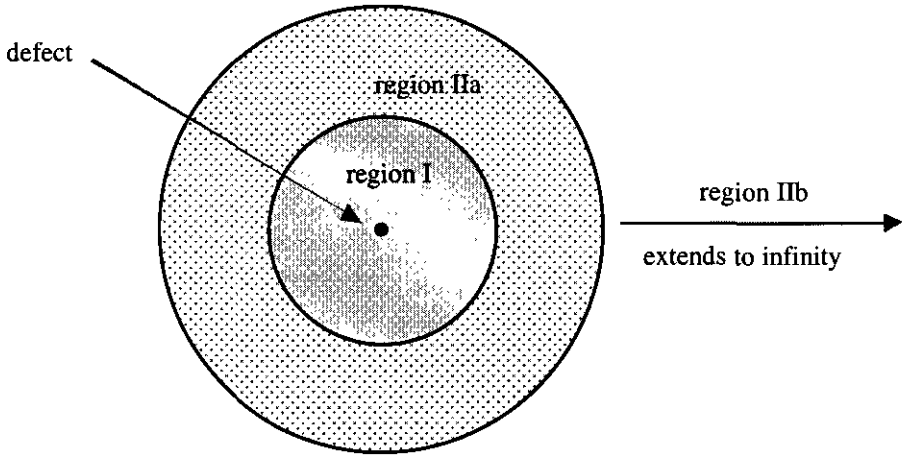

Figure 3.2 Schematic representation of the Mott-Littleton "two region strategy".

The inner region (region I), immediately surrounding the defect, contains typically around 200 ions. All the ions in this region are relaxed explicitly using Newton-Raphson minimisation procedures and all the coordinates, (core and shell if used), are adjusted until the minimum energy configuration is attained. This is essential for region I as the forces exerted by the defect on the surrounding lattice are strong. In contrast, in the more distant regions of the crystal, i.e. in region II, which extends to infinity, the forces are relatively weak and may be treated using pseudo-continuum methods such as the Mott-Littleton approximation (Mott and Littleton, 1938). This assumes that the response of region II is essentially a dielectric response to the effective charge of the defect.

Continuum dielectric theory gives the polarisation, P, of the crystal, per unit cell, at a distance r from the defect as:

$$P = \frac{V}{4\pi}\left(1 - \frac{1}{\varepsilon_0}\right)\frac{qr}{r^3} \tag{3.6}$$

where V is the unit cell volume, q is the effective charge of the defect and ε_0 is the static dielectric constant of the continuum. The polarisation can be divided into atomistic components according to the nature of the interatomic potential model that is being used. For shell model potentials the division is into core and shell displacements. After dividing the crystal into two regions, the total defect energy, E_D, can be evaluated from the expression:

$$E_D = E_I(x) + E_{IIa}(x,y) + E_{IIb}(y) \tag{3.7}$$

where E_I is a function of the ion coordinates, x, and dipole moments of the ions in region I. $E_{IIa}(x,y)$ arises from interaction between regions I and II; it is necessary to include an interface region (IIa) between regions I and II which allows for smoother convergence during minimisation. The displacements of the ions within region IIa are treated using the Mott-Littleton approximation and are calculated as the sum of those due to all the charged defects in region I. $E_{IIb}(y)$ is dependent only on the displacements (y) of ions in region IIb and these are calculated assuming that the crystal responds only to the net charges on the defect. It has been shown (Catlow, 1989) that, provided the size of region I is sufficiently large, the calculations are not sensitive to further expansion of this region and are essentially exact, within the approximations arising from the interatomic potential model and from the static description of the lattice.

The investigation of diffusion mechanisms and defect phenomena on a microscopic scale underpins the understanding of macroscopic transport behaviour. However, it

is often difficult to extract sufficient information from the majority of diffusion or conductivity experiments to identify the atomistic mechanisms controlling ionic mobility. In the static lattice approach employed in this investigation, it is assumed that ion migration is effected by discrete jumps (or hops) of atoms by interstitial mechanisms. Given this hopping description, an adaptation of absolute rate theory (Vineyard, 1957) gives the following for the jump frequency, ν:

$$\nu = \nu_{\circ}\exp\left(-E_{a} / kT\right) \tag{3.8}$$

where the activation energy, E_a, is derived from simulating the potential energy surface for the migrating ion. This allows the identification of the maximum (or saddlepoint) in the energy profile for the most favoured pathway. Such an approach has successfully been applied in studies of defect transport in many polar solids (Catlow, 1987; Catlow et al., 1997).

Chapter 4

Nepheline

Contents

4.1 Introduction

Nepheline is a stuffed derivative of tridymite containing sodium and potassium ions located in channels within the structure of an aluminosilicate framework. The intrinsic flexibility of the Al-O-Si linkages of the framework allows the structure to relax into different conformations to accommodate Na^+ and K^+ cations between successive sheets of silica tetrahedra in [001] structural channels.

The interactions between the mobile cationic species and the framework have been explored by investigating the dynamic behaviour of sodium and potassium ions in single crystals of nepheline using high temperature dielectric spectroscopy. This technique, which is sensitive to short-range diffusive motion (cf. diffusion studies of bulk samples, which may average over a range of diffusion mechanisms), is well suited to this type of investigation as it allows multiple phenomena to be probed over a range of frequencies at a given temperature and only the mobile charged species respond to the relatively low frequency (<10 MHz) electric fields. By probing the microscopic behaviour of the loosely-bound channel ions in nepheline it has been possible to measure activation energies of specific ion mobility processes.

In addition, atomistic simulation techniques have been used to investigate the energetics and mechanism of cation migration in nepheline, and thereby interpret the dielectric data in structural terms. Although similar computer simulation studies have been used to establish diffusion pathways in inorganic solids (Catlow, 1992a; De Souza et al., 1999; Fisher et al., 1997; Islam, 2000), the use of these techniques in the assignment of the ion movements observed using dielectric spectroscopy is a novel approach to this type of study.

4.2 Scientific background

4.2.1 Composition and phase relations in the nepheline-kalsilite system

Nepheline is a feldspathoid mineral which occurs as a primary phase in many plutonic and volcanic rocks of varying compositions. It is most likely to be found in silica-poor alkaline igneous rocks in syenites (nepheline syenite), pegmatites and in schists and gneisses (Deer et al., 1992). It commonly forms as prismatic hexagonal crystals which are frequently twinned.

Nepheline, $Na_3KAl_4Si_4O_{16}$, is a stable intermediate phase of the nepheline-kalsilite series, $NaAlSiO_4$ - $KAlSiO_4$. Kalsilite, $KAlSiO_4$, is the potassium end member and at high temperatures there is extensive solid solution between sodium and potassium end members. Natural nephelines also show extensive solid solution towards SiO_2 (Figure 4.1).

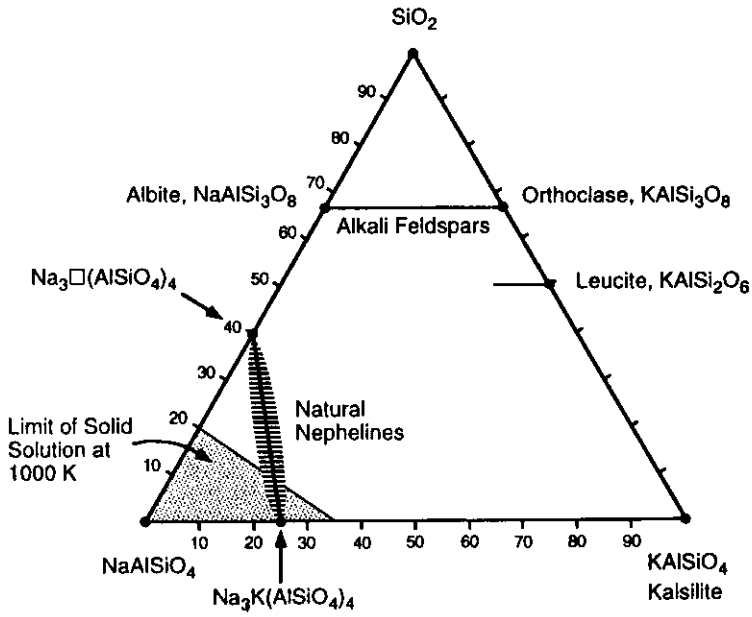

Figure 4.1 Ternary diagram showing composition of phases in the nepheline-kalsilite-SiO_2 system.

The symmetry and lattice parameters of some of the phases in the $NaAlSiO_4$ - $KAlSiO_4$ system are given in Table 4.1.

Table 4.1 The symmetry and room temperature lattice parameters of some of the phases in the $NaAlSiO_4$ - $KAlSiO_4$ system (Foreman and Peacor, 1970; Perotta and Smith, 1965; Withers and Thompson, 1993)

Phase	Spacegroup	Lattice parameters/Å	
		a	*c*
nepheline, $Na_3KAl_4Si_4O_{16}$	$P6_3$	10.02	8.40
carnegieite, $NaAlSiO_4$	$F\bar{4}3m$	7.81	
kalsilite, $KAlSiO_4$	$P6_3$	5.16	8.69

Na-nepheline, $NaAlSiO_4$, is stable up to 1248°C after which it inverts to the high temperature polymorph carnegieite. Carnegieite can be obtained at room temperature by quenching. At 680°C high carnegieite (cubic, $F\bar{4}3m$) undergoes a displacive transition to low carnegieite ($Pb2_1a$) which exists as a metastable modification of $NaAlSiO_4$. Below 1100°C, there is a solvus (miscibility gap) between kalsilite, $KAlSiO_4$, and nepheline, $Na_3KAl_4Si_4O_{16}$ (Tuttle and Smith, 1958). Under equilibrium conditions, intergrowths of nepheline and kalsilite form on cooling, the rate of exsolution being strongly dependent on composition and temperature (Yund et al., 1972). (Although the nucleation rate would be expected to be higher at low temperatures it is opposed by a lower rate of growth due to slower volume diffusion.) Later work on the nepheline-kalsilite solvi at a range of pressures (Ferry and Blencoe, 1978), is in good agreement with that of Tuttle and Smith (1958). However, at high temperatures, there are small discrepancies which are probably due to the rapid exsolution rates of nepheline and kalsilite from the solid solution, (followed by reaction and re-equilibration at lower temperatures if the quenching rate is too slow).

Although the ideal composition of nepheline is $Na_3KAl_4Si_4O_{16}$, this depends on the origin and composition of the host rock. Some natural nephelines contain small

amounts of calcium and the Na/K and Al/Si ratios may vary, therefore many nephelines contain more than 4 Si per unit formula (Deer et al., 1992).

4.2.2 Stuffed derivatives of tridymite

Tridymite is a polymorph of silica and consists of corner linked SiO_4 tetrahedra forming a three-dimensional network of open six-membered rings as shown in Figure 4.2 (Kihara, 1978). The symmetry of the structure is $P6_3/mmc$ which is the topological symmetry for all other related phases within this framework family.

Nepheline and kalsilite are stuffed derivatives of tridymite in which Na^+ or K^+ ions occupy the channels between the rings of tetrahedra.

In kalsilite half of the silicon is replaced by aluminium and charge balance is maintained by K^+ ions. The main features of the structure are:

- Collapse of the six-fold tetrahedral rings in a ditrigonal pattern about a centrally-located K^+ ion as shown in Figure 4.3 (Perotta and Smith, 1965).
- A displacive phase transition from the low temperature $P6_3$ phase to $P6_3mc$ occurs at 1138 K, with the possibility of Al/Si disordering at high temperatures (Andou and Kawahara, 1982; Kawahara et al., 1987).

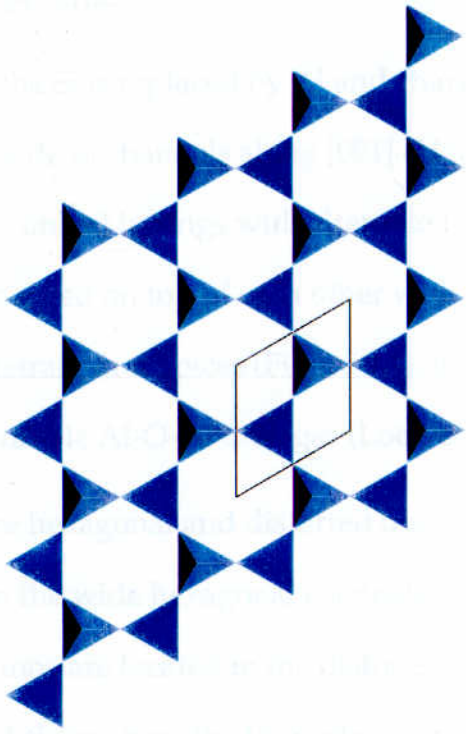

Figure 4.2 The tridymite structure (Kihara, 1978), as viewed along [001]: layers of tetrahedra are linked with alternate tetrahedra pointing up and down, to form hexagonal rings. The layers are stacked, joined by the tetrahedral apices.

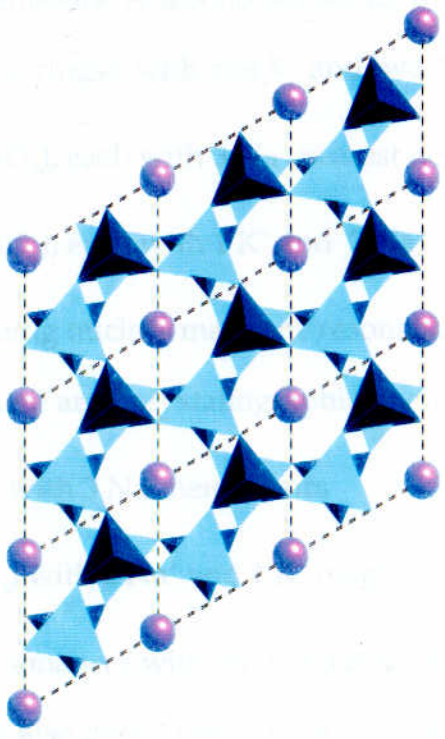

Figure 4.3 The structure of kalsilite (Perotta and Smith, 1965) as viewed along [001]: K^+ ions in ditrigonal rings of tetrahedra.

4.2.3 Structure of nepheline

In nepheline, half of the Si is replaced by Al and charge balance is maintained by Na^+ and K^+ ions which reside in channels along [001] (Hahn and Buerger, 1954). The Si and Al tetrahedra are linked in rings with alternate tetrahedra pointing up and down. The layers are then stacked on top of each other with the [SiO_4] tetrahedral apices joined to the [AlO_4] tetrahedral apices (Figure 4.4). In this arrangement there are no energetically unfavourable Al-O-Al linkages (Loewenstein, 1954).

In nepheline there are hexagonal and distorted oval channels in the ratio of 1:3. The K^+ ions are located in the wide hexagonal channels, 9-fold coordinated by oxygen, and the smaller Na^+ ions are located in the distorted oval channels, 8-fold coordinated by oxygen. Figure 4.4 shows how the four tetrahedral (T) sites can be grouped into two classes. One set resides on *special equivalent positions*, along the [001] triads, with three Na^+ nearest neighbours. A second set lies on the *general equivalent positions* (forming the hexagonal rings), with one K^+ and two Na^+ nearest neighbours:

- T_1 (AlO_4) and T_2 (SiO_4), each with 3 Na^+ nearest neighbours
- T_3 (SiO_4) and T_4 (AlO_4), each with 1 K^+ and 2 Na^+ nearest neighbours

^{29}Si magic-angle-spinning nuclear magnetic resonance (MAS NMR) (Hovis et al., 1992) confirms that there are 2 crystallographically unique tetrahedral sites:

- one site (T_1 and T_2) with 3 Na^+ neighbours
- the other (T_3 and T_4) with 2 Na^+ and 1 K^+ neighbour

These produce two resonances with an integrated ratio of 1:3 in the ^{29}Si MAS NMR spectrum. ^{27}Al spectra also give 2 peaks with an area ratio of 1:3, again confirming the structure described above. There are no resonances to the higher-frequency side of

these (Hovis et al., 1992), showing that there are no Al-O-Al linkages, in line with the aluminium avoidance rule (Loewenstein, 1954).

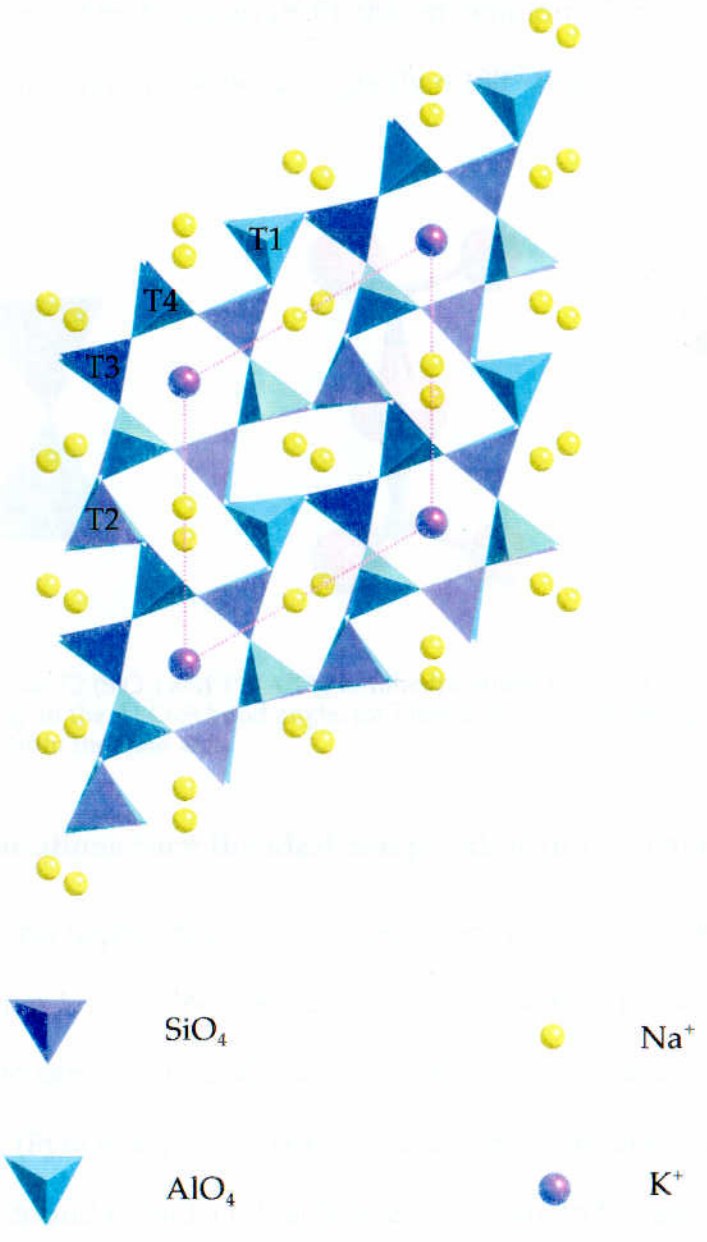

Figure 4.4 The basic structure of nepheline as viewed along [001] showing the unit cell, the alternating Si (T_2 and T_3) and Al (T_1 and T_4) tetrahedra, the hexagonal rings containing the K^+ ions and the distorted oval rings containing the Na^+ ions (Hahn and Buerger, 1954).

The AlO_4 (T1) and SiO_4 (T2) tetrahedra in adjacent layers are connected by an Al–O–Si bond with a bond angle of 133.5° because the apical oxygen on the triad axis is off-centred and almost certainly dynamically disordered. Its position can be approximated by a three-site model, first suggested by Hahn and Buerger (1954) and later confirmed by Dollase (1970), the off-centering of the apical oxygen giving a more energetically favourable bond angle than 180° (Figure 4.5).

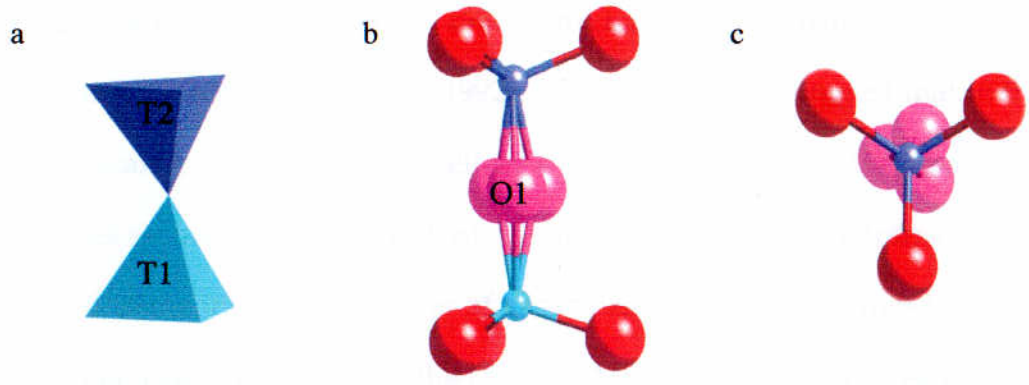

Figure 4.5 (a) T2 (SiO_4) and T1 (AlO_4) tetrahedra linked by O1 oxygen; (b) Detail showing the effect of off-centering on the Al-O-Si bond angle; (c) View down [001] showing the ~0.3Å displacement of the O1 oxygen from the triad axis.

4.2.4 Variations from the ideal composition and structure

Most natural nephelines exhibit a deficiency of alkali ions because the ratio of Si/Al is greater than 1. Provided there are no Al-O-Al bonds present in the structure, the Si/Al ratio can be calculated from the relative areas of the peaks in a ^{29}Si MAS NMR spectrum (Fyfe et al., 1983). For a natural nepheline from Bancroft, Ontario the Si/Al ratio was found to be 1.11 (Stebbins et al., 1986). In this study four well defined resonances in the ^{29}Si NMR spectrum were found: 2 sites with 4 Al neighbours, 1 site with 3 Al neighbours and possibly another site with no Al neighbours. The excess of

Si results in vacancies (□) on the hexagonal sites normally occupied by K^+ ions to maintain charge balance as shown by:

$$K^+Al^{3+} \leftrightarrow \square Si^{4+}$$

Therefore, although the "ideal" composition of nepheline is $Na_3KAl_4Si_4O_{16}$, the composition of a natural nepheline is more likely to be $Na_3K_{1-x}\square_xAl_{4-x}Si_{4+x}O_{16}$ $(0 \leq x \leq 1/3)$, hereafter referred to as the "non-ideal" composition.

The Na^+ sites in the distorted oval rings are always occupied to stabilise the framework (Hahn and Buerger, 1954). This has been confirmed by X-ray powder diffraction studies (Hovis et al., 1992), where the results suggest that in the more silicic vacancy-rich natural nephelines the K^+ ions may enter the smaller distorted oval sites at lower molar K content. It is also possible that the framework may respond to the increased number of vacancies in these nephelines by forming more hexagonal rings. The fact that the $\square Si^{4+} \leftrightarrow Na^+Al^{3+}$ substitution results in an increase in volume (Hovis et al., 1992) agrees with the preference of vacancies for the larger alkali sites in nepheline.

In Na-nephelines, the Na^+ ions also occupy the larger hexagonal sites. However, because sodium has a smaller ionic radius than potassium, Na^+ does not occupy the central site on the 3-fold axis, but three off-axis positions with equal occupation of 1/3. The Na^+ ion in the wide channel therefore takes a one-sided coordination with smaller Na-O bond distance (Hippler and Böhm, 1989). ^{23}Na MAS NMR studies of nephelines have shown that where the ratio of $Na^+/K^+ + \square$ is greater than 3:1, there are 2 peaks, showing that the Na^+ ions are occupying 2 different sites - the excess Na^+ being in the larger hexagonal K^+ sites as well as the smaller oval sites (Hovis et al.,

1992). There may also be chemical variation, e.g. calcium is a constituent of many natural nephelines (Deer et al., 1992):

$$\square Ca^{2+} \leftrightarrow 2(Na^{+}, K^{+})$$

If Ca^{2+} ions are present they are more likely to occupy the smaller Na^{+} sites because of their similar ionic radius.

4.2.5 Site ordering

Al/Si order-disorder

Early reports suggested varying degrees of Al/Si order-disorder. When there is a deficiency of potassium and sodium and the Si/Al ratio is greater than 1, this may introduce some degree of Al/Si disorder (Dollase and Peacor, 1971; Hahn and Buerger, 1954). Measurements of birefringence at room temperature suggested that the degree of order depended on the origin of the nepheline, i.e. its cooling history (Sahama, 1962). The Al/Si order was found to decrease from 80% for a gneissic nepheline from Bancroft, Ontario, to just 40% for a volcanic nepheline from Monte Somma, Vesuvius (Dollase and Peacor, 1971). Dollase and Peacor concluded that there was a decrease in the degree of Al/Si ordering with increasing cooling rate, so that volcanic nephelines are the least well ordered. They also suggested that both the T1 and T2 sites, and the T3 and T4 sites, show similar degrees of disorder, but the T1 and T2 sites (which tend to be more Si-rich) less so than the T3 and T4 sites. This may be linked with the fact that the T1 and T2 tetrahedra are surrounded by Na^{+} ions only, whereas the T3 and T4 tetrahedra are surrounded by Na^{+} ions, K^{+} ions, vacancies and possibly Ca^{2+} ions. Also, the T1 and T2 tetrahedra are bonded to O(1), the oxygen atom which is positionally disordered off the 3-fold axis (Hahn and Buerger, 1954). Much of this was supported in a later refinement of the crystal structure, invoking a

domain model for the ordering pattern, correlated to O(1) disorder, tetrahedral site occupancy and K-site occupancy (Simmons and Peacor, 1972).

^{29}Si and ^{27}Al MAS NMR (Hovis et al., 1992) showed that there is normally little or no disorder of Al and Si among the tetrahedral sites. However, ^{29}Si MAS NMR (Hovis et al., 1992) shows that a slight excess of Si will give rise to increased intensity on the lower frequency side of the Si peaks which can be attributed to the presence of a Si with three Al and one Si nearest neighbours. There is no such observation in ^{27}Al MAS NMR spectra, therefore it appears that the Al avoidance rule is preserved. Although these findings contradict the earlier reports, it should be remembered that NMR is sensitive to the local structure of Si sites and this could be different from the average structure observed by XRD; e.g. a crystal could be made up of domains with a high degree of short-range order but with little or no long-range order, (Stebbins et al., 1986).

Na/K order

There is no evidence for Na/K disordering from high temperature X-ray structure refinements (Foreman and Peacor, 1970). Any degree of disorder would involve migration of K^+ ions into the smaller oval sites: occupation of the highly-distorted oval Na site by the large K^+ ion would cause substantial framework strain and would be energetically unfavourable.

K-vacancy order

The excess of Si substituting for Al normally found in nepheline, coupled with Ca substitution for Na, is the principal cause of the vacancies at the larger K site. The number of vacancies necessary to maintain charge balance is normally of the order of one third of the available K-sites in natural nephelines. McConnell (1962) showed that

at low temperatures, there appears to be ordering of the K^+ ions and vacancies, but there is some evidence from studies of the intensity of satellite reflections in nepheline that above 100°C disordering of K^+ ions and vacancies occurs, resulting in a superstructure with cell parameters $a' = a\sqrt{3}$ relative to the substructure of the cell, (McConnell, 1981). The additional intensity maxima imply a statistical antisymmetrical distribution with a unit cell of three times the volume of the average cell, i.e. consistent with an ordered defect structure involving one third of the K sites, (McConnell, 1962).

4.2.6 Structural behaviour on heating

Nepheline is an optically uniaxial material and any order/disorder transition should be detectable by studying the birefringence. Evidence obtained from birefringence measurements show that there are no discontinuities in the optical properties of nepheline with change in temperature (Sahama, 1962). X-ray diffraction studies of nepheline (de Dombal, 1992; Foreman and Peacor, 1970), have shown no evidence for a structural transition in the temperature range 280 K to 1180 K; only a progressive widening of the small oval channels is observed with the large hexagonal channels remaining almost unchanged. Nepheline has moderately large thermal-expansion coefficients of about 0.2Å and 0.1Å per 1000 K for the *a* and *c* unit cell parameters respectively, (Foreman and Peacor, 1970). The thermal expansion may be due to both anisotropic thermal vibration and as a result of rotation of the tetrahedra about the bridging oxygens. Evidence for the latter may be seen in the way that the orientation of the tetrahedra change as a function of temperature: the values of the T-O-T angles increase by an average of 5.4° over 900 K, the bridging oxygens taking up a more symmetric position with increasing temperature as a result of thermal vibration (Foreman and Peacor, 1970; Taylor, 1972).

4.2.7 Conductivity

Framework silicates such as nepheline are potentially good candidates for fast ion diffusion since they possess a rigid framework and a system of channels throughout the framework. Impedance measurements carried out on synthetic sodium nephelines have shown that there is a strong anisotropy of the specific conductivity in nepheline and ion transport can occur most easily in the wide hexagonal channels parallel to the *c*-axis (Roth and Böhm, 1986). It has been shown that there is a general decrease in conductivity with increasing ionic radius in similar framework silicates (Gregorkiewitz, 1986). Gregorkiewitz explained this in terms of the size relation between the diffusing species and the windows in the channel system, where window size was defined by both the free diameter and the conformational distortions of the silicate six-rings. Measurements of activation energies for diffusion of potassium ions in kalsilite, which has a framework with tridymite topology (Perotta and Smith, 1965), and in kaliophilite, which has its own topology (Abbot, 1984), have shown that diffusion is inhibited along smaller, distorted channels similar to the Na-sites in nepheline (Gregorkiewitz, 1986).

Vacancies are only formed in the wide hexagonal channels in nepheline, and it is possible that rapid ion transport along these channels could take place by a multiple-jump mechanism. An additional factor contributing to this possible accelerated diffusion is that the rigidity of the framework around these wide channels (induced by the remaining part of the structure) minimises momentum interchange with the diffusing particles, regardless of their size in relation to the channel (Gregorkiewitz, 1986). However other diffusion mechanisms in the nepheline structure are also possible. Multinuclear MAS NMR studies on both natural and synthetic sodium nephelines have indicated that the vacancies on the alkali metal sites play an

important role in the crystal chemical behaviour of these minerals (Hovis et al., 1992). In addition, ^{23}Na MAS NMR investigations in a high-Na nepheline at temperatures up to 773 K have determined Na-site exchange rates which are consistent with ionic conductivity data (Stebbins et al., 1989). Recent impedance measurements (Jiménez and Gregorkiewitz, 1999) on a sodium-rich nepeheline have been interpreted in terms of a Na^+ ion migration process in the *ab* plane at high temperatures.

4.2.8 Incommensurate phase

Structures formed in intermediate phases represent an attempt by the system to minimise its total energy by a reorganisation of the framework and by ordering the atomic positions. To establish an ordering scheme compatible with any changes in composition, as well as keeping the strain energy to a minimum, involves the formation of an incommensurate structure: a modulated structure with a well defined periodicity. The periodicity, however, is not an integral multiple of the translational periodicity of the underlying lattice.

Above 180°C nepheline exists as a defect structure with hexagonal symmetry $P6_3$. At lower temperatures this structure is no longer stable, principally because the Na^+ ions in the oval channels are not well coordinated with the oxygen atoms on all sides and there is a tendency for an off-centering of the O(1) apical oxygen atoms on the triad axis. It has been suggested (McConnell, 1981) that the large hexagonal channels in the structure allow considerable K^+ migration at these low temperatures, and that there is a tendency for the K^+ ions and the vacancies to order. The incommensurate structure of nepheline below 180°C shows anomalous diffraction effects comprising additional intensity maxima paired about the points ±(1/3, 1/3, 0) in the hexagonal cell at approximately ±0.20 along c^* (McConnell, 1962), (Figure 4.6).

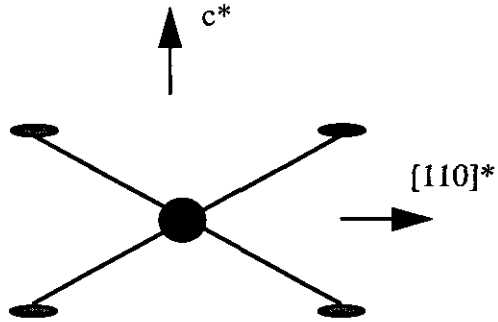

Figure 4.6 Distribution of diffuse diffracted intensity around each Bragg maximum in the c*:[110]* reciprocal lattice secion of nepheline (McConnell, 1962).

The presence of these maxima indicates that the structure of nepheline as described by Buerger (Hahn and Buerger, 1954), must be regarded as an average over the true structure involved. The additional maxima imply an arrangement in which the unit cell is much larger than the conventional unit cell of nepheline with $a' = a\sqrt{3}$, and $c' = 5c$, where a and c are the standard cell dimensions of the Buerger unit cell.

McConnell (1981) suggested that the incommensurate phase of nepheline arose as a result of an interaction of K^+-□ ordering along [001] and O1 displacement modes. However, more recent studies (Hayward et al., 2000) using Rigid Unit Mode (RUM) analysis (Dove et al., 1993a; Dove et al., 1993b; Hammonds et al., 1996) have shown that for nephelines with K^+-□ order, the vacancy ordering scheme must fit the possible modulations of the framework. This proposal provides an explanation as to why the modulation wavelength does not display a strong dependence on the fraction of vacant K^+ sites as it does in the McConnell model. Therefore, although K^+–□ order may enhance the stability of the incommensurate phase, the underlying reason for the incommensurate structure is primarily due to properties of the framework.

4.3 Experimental

4.3.1 Sample characterisation

Nephelines from two different origins were available for investigation in this study: volcanic nepheline from Monte Somma, Vesuvius, and plutonic nepheline from Bancroft Ontario, (Figure 4.7).

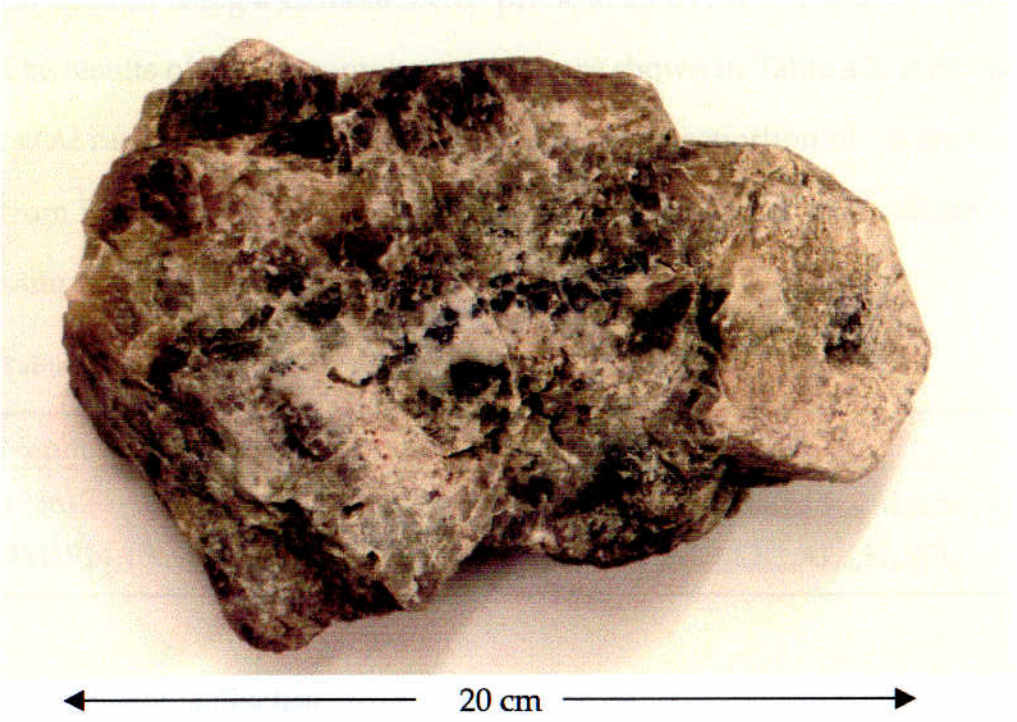

Figure 4.7 Bancroft nepheline, BM1914,1569, from The Natural History Museum.

The volcanic nepheline consisted of colourless crystals embedded in cavities in a rock groundmass. However, these crystals were extremely small and found to vary in composition. The Bancroft nepheline, shown in Figure 4.7, was found to be of uniform composition and was available in sufficient quantities for full characterisation and subsequent dielectric spectroscopy experiments. For this reason, the Bancroft specimen was used for a substantive part of this investigation. The samples used for the dielectric spectroscopy were crystalline and free from cracks.

Although the crystals appeared to be single in hand specimen, examination with an optical microscope showed them to consist of a small number of grains, of different orientations, fused together.

Electron microprobe analysis

Sample compositions were determined using electron microprobe analysis. This was carried out using a Cameca SX100 probe at 20 kV, 20 nA and a 10 μm spot diameter. The results of the microprobe analyses are shown in Table 4.2. It can be seen that the Si/Al ratios are similar, but there is a greater proportion of vacancies in the sample from Bancroft (BM1914, 1569) and there is a small amount of calcium in the volcanic sample (193617).

Table 4.2 Origin and composition of nephelines

Nepheline	Origin	Composition
193617	Monte Somma	$Na_{0.75}K_{0.12}Ca_{0.04}\square_{0.05}Al_{0.94}Si_{1.06}O_4$
BM1914,1569	Bancroft	$Na_{0.76}K_{0.18}\square_{0.06}Al_{0.94}Si_{1.06}O_4$

X-ray powder diffraction

Room temperature data for the Bancroft nepheline, BM1914,1569, were obtained at The Open University using a Siemens D5000 in reflection mode using Cu$K\alpha$ radiation. Scans were made over a 5-80° 2θ range at 0.1 °/min. Lattice parameters were determined by refining the corrected data using UnitCell (Holland and Redfern, 1997), a computer program which uses regression diagnostics combined with nonlinear least-squares to refine cell parameters from powder diffraction data. These data are shown in Table 4.3.

The room temperature XRD pattern for the Bancroft nepheline is shown in Figure 4.8 and is almost identical to the calculated diffraction pattern, thus confirming the identity of the sample.

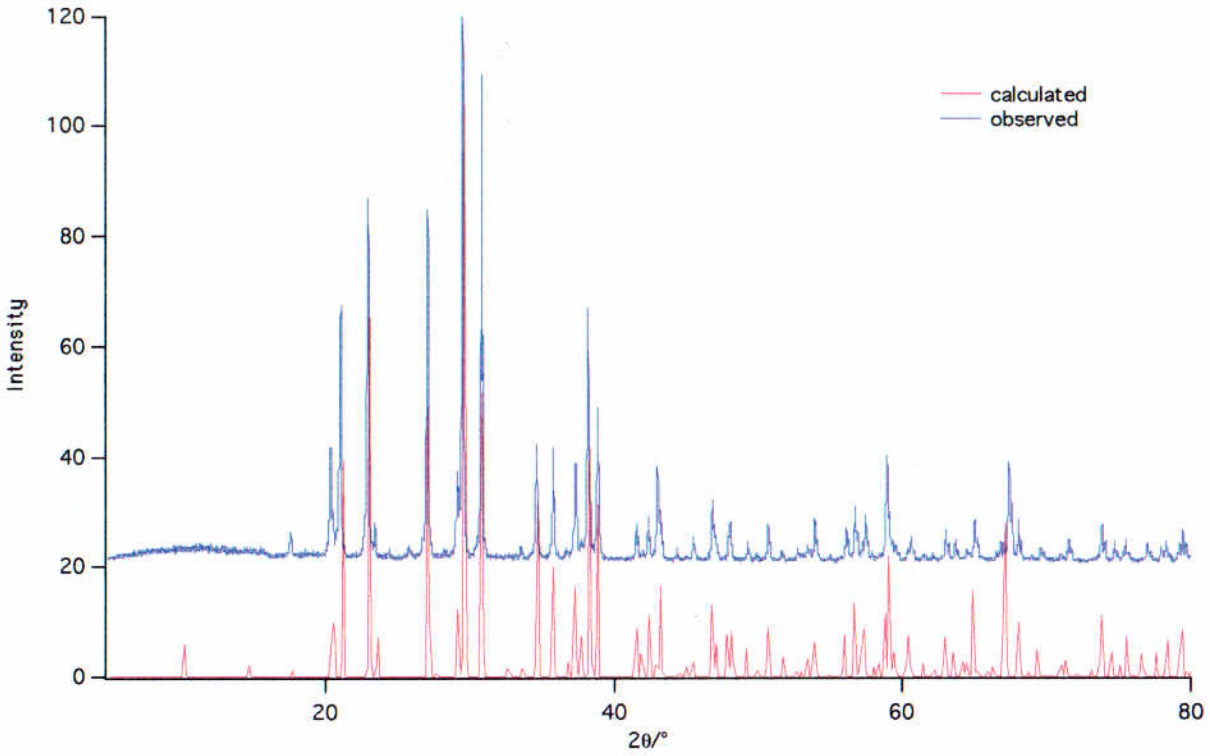

Figure 4.8 Observed (BM1914,1569) and calculated (CrystalDiffract, 1995-2000) diffraction profiles for nepheline.

The lattice parameters were also determined as a function of temperature for the Monte Somma volcanic nepheline, 193617, from room temperature to 1100 K. This work was carried out in the Mineralogy Department at the Natural History Museum using an Enraf-Nonius X-ray diffractometer with a position-sensitive detector. The room temperature lattice parameters are shown in Table 4.3.

Table 4.3 Room temperature lattice parameters for volcanic and plutonic nephelines

Parameter	193617	BM1914,1569
a	9.9886±0.0006	10.0086±0.0030
c	8.3766±0.0010	8.3908±0.0039

The high temperature data are shown in Figure 4.9 and it can be seen that there are no obvious departures from linearity. The expansion of the *a* axis was found to be roughly three times that of the *c* axis; Foreman and Peacor (1970) found the expansion of the *a* axis to be approximately twice that of the *c* axis for a plutonic nepheline. The absolute values differed significantly as can be seen in Table 4.4.

Table 4.4 Thermal expansion of volcanic and plutonic (Foreman and Peacor, 1970) nephelines

Lattice parameter	Thermal expansion/ $ÅK^{-1}$	
	Volcanic (193617)	Plutonic
a	1.202×10^{-4}	2.30×10^{-4}
c	3.820×10^{-5}	1.06×10^{-4}

The difference in thermal expansion between these data and those of Foreman and Peacor may be explained by the different origin of the nephelines. Foreman and Peacor used a plutonic nepheline from Bancroft, Ontario, whereas the data presented here are for a volcanic nepheline from Monte Somma, Vesuvius.

Evidence linking optical birefringence with thermal expansion data suggests that the degree of ordering may also account for differences in thermal expansion (Sahama, 1962). Sahama found a correlation between the changes in optical birefringence at different temperatures and the thermal expansion of plutonic (ordered) and volcanic (disordered) nephelines.

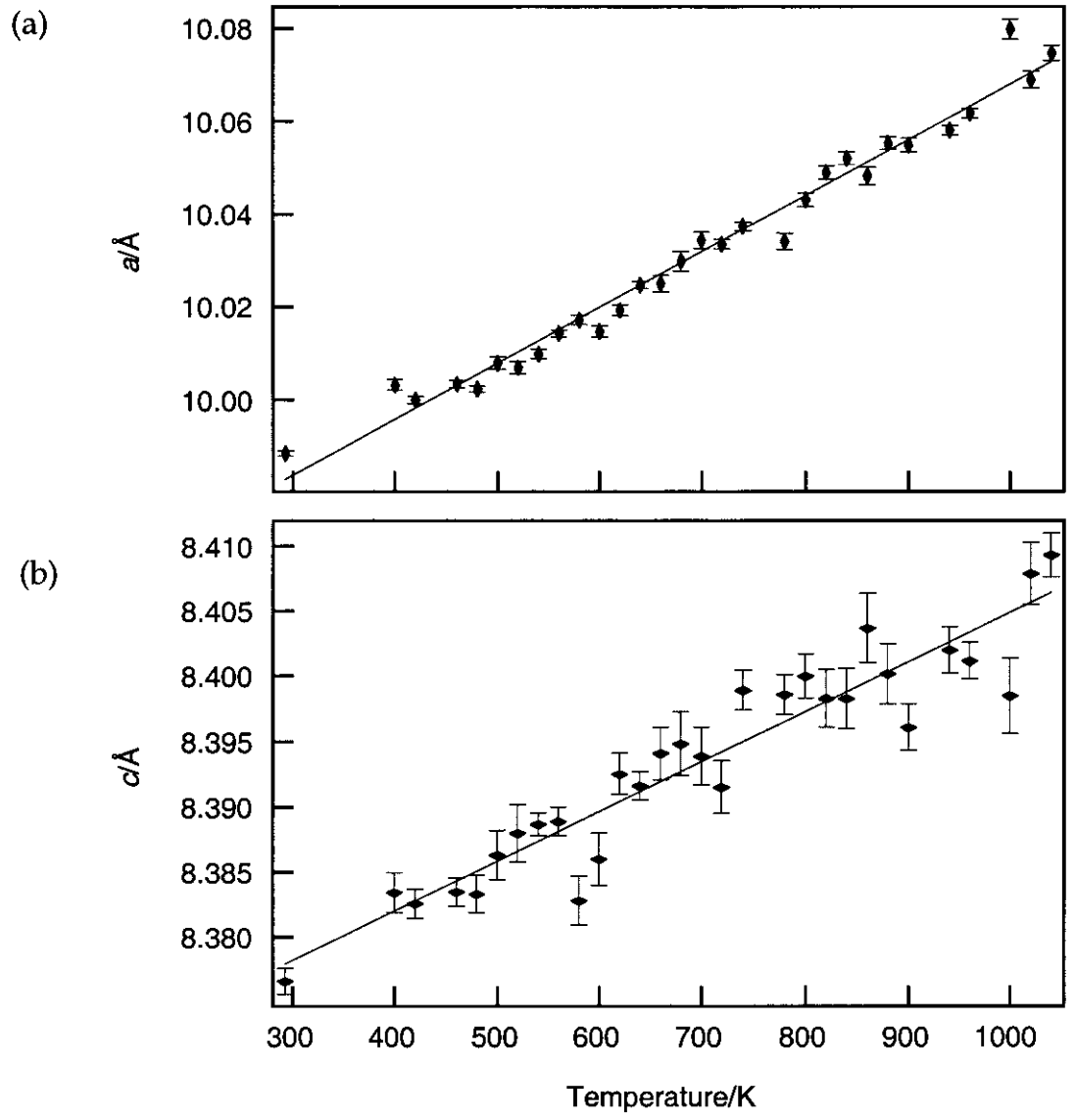

Figure 4.9 Lattice parameters of volcanic nepheline 193617 as a function of temperature: (a) unit cell parameter *a*; (b) unit cell parameter *c*. The error bars correspond to the standard deviation, σ, of the points.

Transmission Electron Microscopy

Transmission Electron Microscopy, (TEM), carried out at the Open University using a Jeol 2000fx transmission electron microscope, confirmed that samples were crystalline, homogeneous, and free from inclusions and grain boundaries. The energy

dispersive spectrometer (EDS) on the TEM also provided an initial means of determining the composition of samples.

4.3.2 Dielectric measurements

Dielectric measurements were made on crystals of Bancroft nepheline, BM1914,1569, using the methods described in Chapter 2.

Isothermal measurements

Isothermal measurements of capacitance and conductance were made on previously unheated crystals at 423 K over a period of approximately 3 hours in order to detect any signs of K^+-□ disorder. This temperature was chosen with reference to previous studies of the incommensurate phase of nepheline (de Dombal, 1992; McConnell, 1981). Any changes in dielectric constant, conductivity and dielectric loss could be indicative of a disordering process occurring.

Temperature dependent measurements

Capacitance and conductance measurements were made at room temperature and then at regular intervals up to approximately 1100 K. From these measurements the dielectric constant, conductivity and dielectric loss were calculated at each frequency.

4.4 Atomistic Computer Modelling

The interatomic potentials and shell model parameters used (listed in Table 4.5) were all taken from previous simulation studies (Freeman and Catlow, 1990; Jackson and Catlow, 1988) where reliability in modelling silicates and aluminosilicates (zeolites) has been demonstrated widely (Catlow, 1992b).

The starting point for the present calculations was the simulation of the hexagonal crystal structure. The unit cell dimensions and atomic coordinates, taken from a high temperature structure refinement of a Bancroft nepheline at 1181 K (Foreman and Peacor, 1970), were equilibrated under constant pressure conditions. (This structure was chosen for the calculations because the dielectric spectroscopy experiments were carried out on a Bancroft nepheline at temperatures up to 1100 K.) The calculated values for the lattice parameters and selected bond-distances and their comparison with experimental values are listed in Table 4.6. This shows good agreement (< 0.3%) between experimental and simulated structures for this complex system, thus supporting the validity of the potentials used for the subsequent calculations.

Table 4.5 Interatomic potentials used for modelling the nepheline structure

(i) Two-body Buckingham

Interaction[a]	A/eV	ρ/Å	C/eV Å^{-6}
K^+ ..... O^{2-}	902.8	0.3698	0.0
Na^+ ..... O^{2-}	1226.84	0.3065	0.0
Si^{4+} ..... O^{2-}	1283.907	0.32052	10.66158
Al^{3+} ..... O^{2-}	1460.3	0.29912	0.0
O^{2-} ..... O^{2-}	22764.3	0.1490	27.879

(ii) Shell model[b]

Species	Y/e	k/eV Å^{-2}
O^{2-}	-2.86902	74.92

(iii) Three-body

Interaction	Force constant / eV rad^{-1}
O - Si - O	2.0972
O - Al - O	2.0972

[a] Potential cutoff = 10 Å
[b] Y and k refer to the shell charge and harmonic force constant respectively

Table 4.6 Calculated and experimental structural parameters for the nepheline structure

(i) Unit cell parameters

Parameter	Experimental	Calculated	Difference/%
a	10.21±0.02 Å	10.2219 Å	0.12
b	10.21±0.02 Å	10.2221 Å	0.12
c	8.49±0.02 Å	8.5142 Å	0.28
α	90.00°	90.00°	0.00
β	90.00°	90.00°	0.00
γ	120.00°	120.01°	0.01

(ii) Selected bond distances

Bond distance	Experimental/Å	Calculated/Å
K - O6	2.972	3.097
K - O5	3.640	3.692
Na - O1	3.066	3.024
Na - O4	2.673	2.682

4.5 Results and discussion

4.5.1 Dielectric spectroscopy

Isothermal measurements

No significant (<0.5%) changes were detected in the frequency profiles of ε', σ and tan δ after heating samples for up to 3 hours at 423 K, (Figure 4.10). It has been suggested by de Dombal (1992) and McConnell (1981) that above 373 K disordering of K^+ ions and vacancies can occur. Thus at 423 K such changes might be expected to be reflected in changes in the fundamental dielectric properties. However, there is no indication (e.g. changes in dielectric constant, conductivity or dielectric loss) of any such time-dependent disordering occurring in the present work.

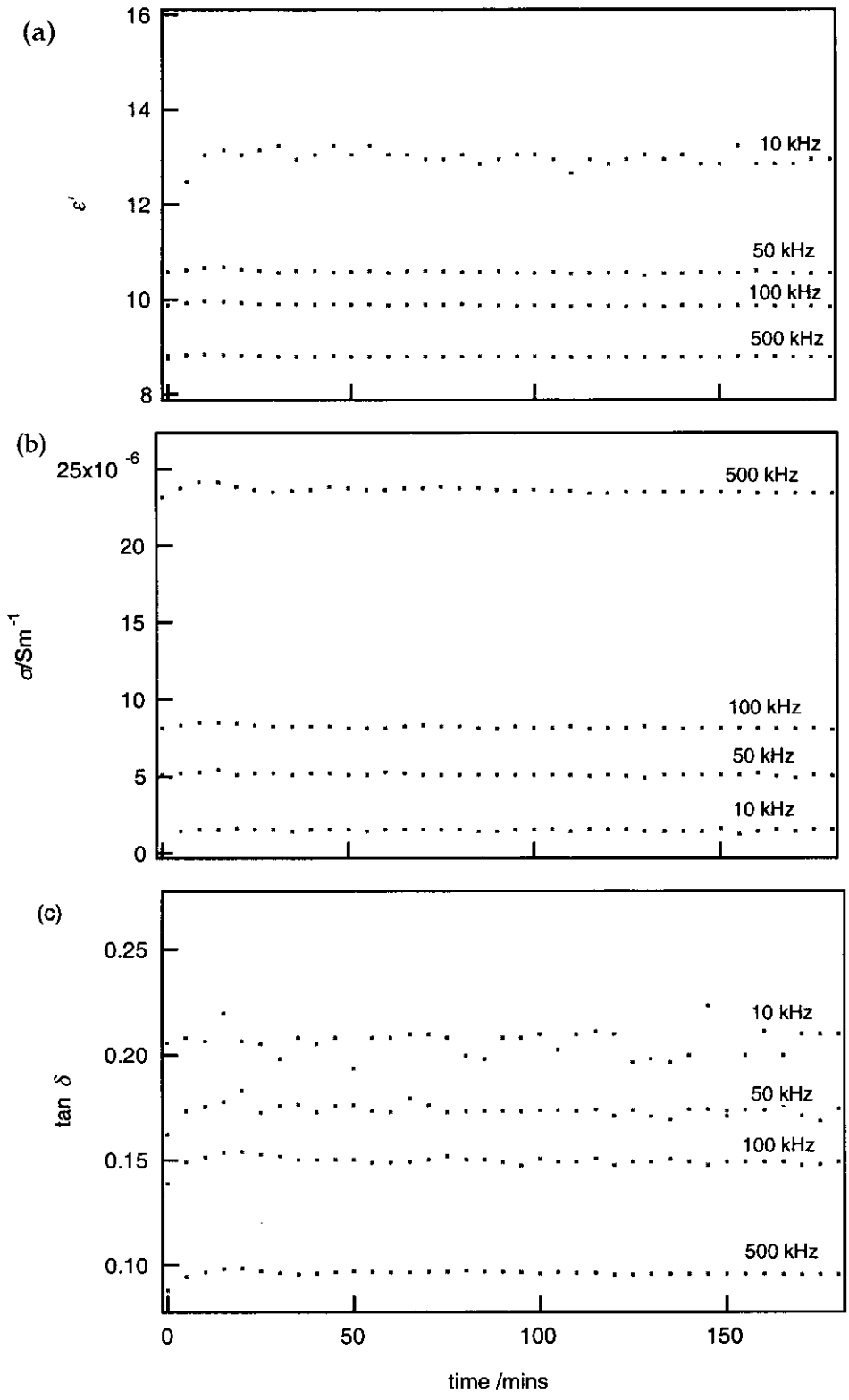

Figure 4.10 (a) ε'; (b) σ; (c) tan δ as a function of frequency and time.

Temperature-dependent measurements

Figure 4.11 shows the behaviour of ε' and σ with temperature and frequency. The dielectric constant has a value close to 8 for all frequencies at room temperature, rising slightly at low frequencies up to 800 K, after which there is a dramatic increase (the greatest changes being at low frequencies). Similar behaviour is found for the conductivity, except that the low frequency (i.e. approaching d.c.) conductivity remains low at all temperatures, whereas the high frequency conductivity increases dramatically above 800 K.

The temperature dependence of ε' and tan δ as a function of frequency between 860 K and 1095 K is shown in Figures 4.12 (a) and (b), respectively. It should be noted that there was no significant dielectric loss peak below 860 K. It can be seen that at the point where ε' undergoes its maximum rate of change with frequency, tan δ is at a maximum.

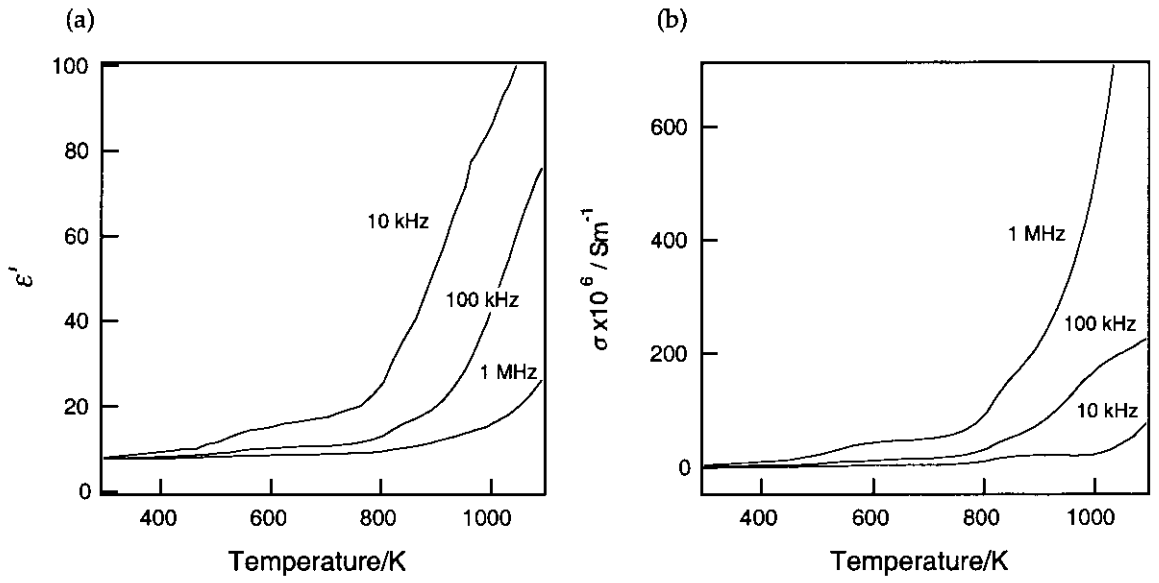

Figure 4.11 Temperature dependence of (a) ε'; (b) σ at selected frequencies.

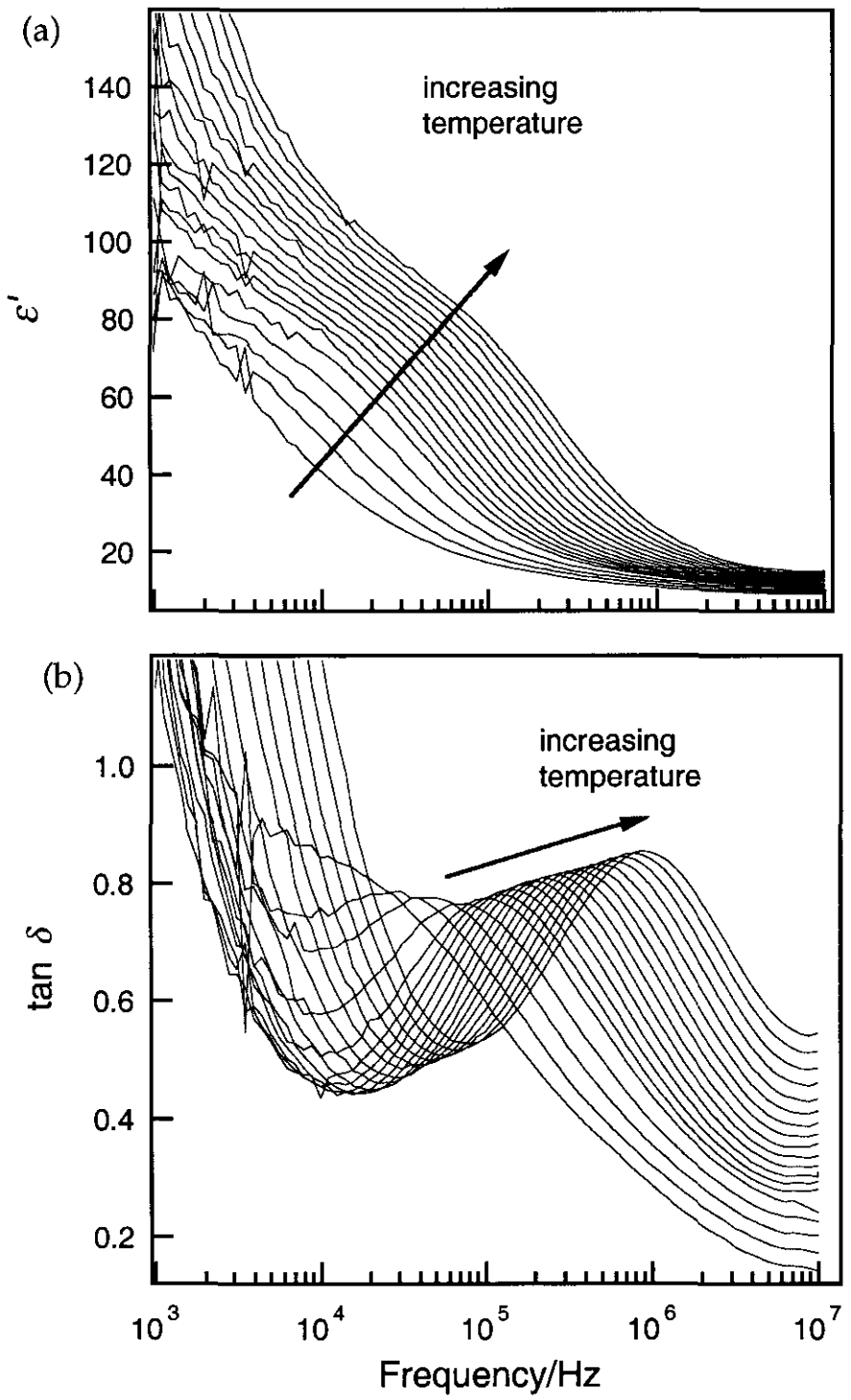

Figure 4.12 Temperature and frequency dependence of (a) ε'; (b) tan δ between 860 K and 1095 K.

The dielectric loss spectrum, shown as a surface plot in Figure 4.13, shows a pronounced low frequency signal (below 5 kHz) at high temperatures, indicative of large scale motions, e.g. bulk diffusion/ionic conduction (Barrer and Saxon-Napier, 1962; Ohgushi and Kazuhide, 1998) and a Debye-type relaxation peak at high frequencies which can be accounted for by the limited motions of an ion within a channel (Debye, 1929; Ohgushi and Kazuhide, 1998; Palmer and Salje, 1990). These peaks are seen to be rather more broadened than would be expected. One possible explanation for this would be the superposition of several relaxation times. However, as analysis by Cole-Cole plots (Cole and Cole, 1941) revealed only a single relaxation, the peak broadening is therefore more likely to be due to damping of the dielectric relaxation.

The temperature dependence of the frequency of the maximum absorption follows an Arrhenius relationship as shown in Figure 4.14. The activation energy is calculated to be 1.38 ± 0.02 eV (133.0 ± 1.9 $kJmol^{-1}$).

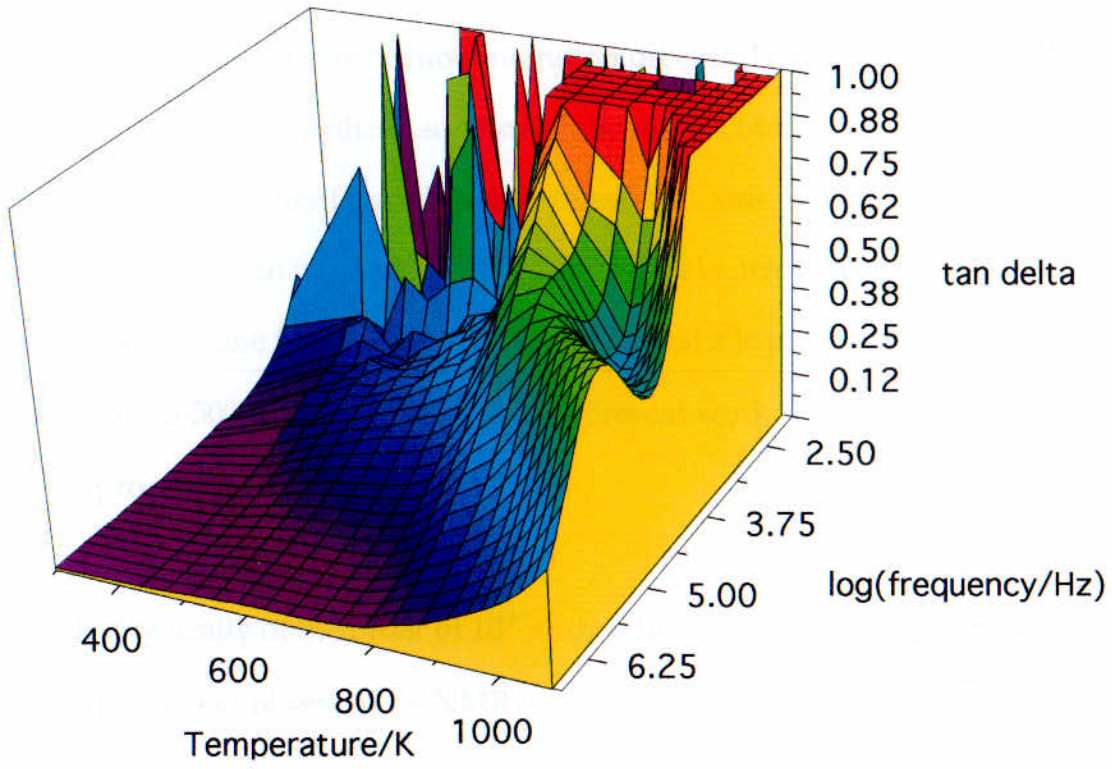

Figure 4.13 Surface plot showing the dielectric loss as a function of frequency and temperature.

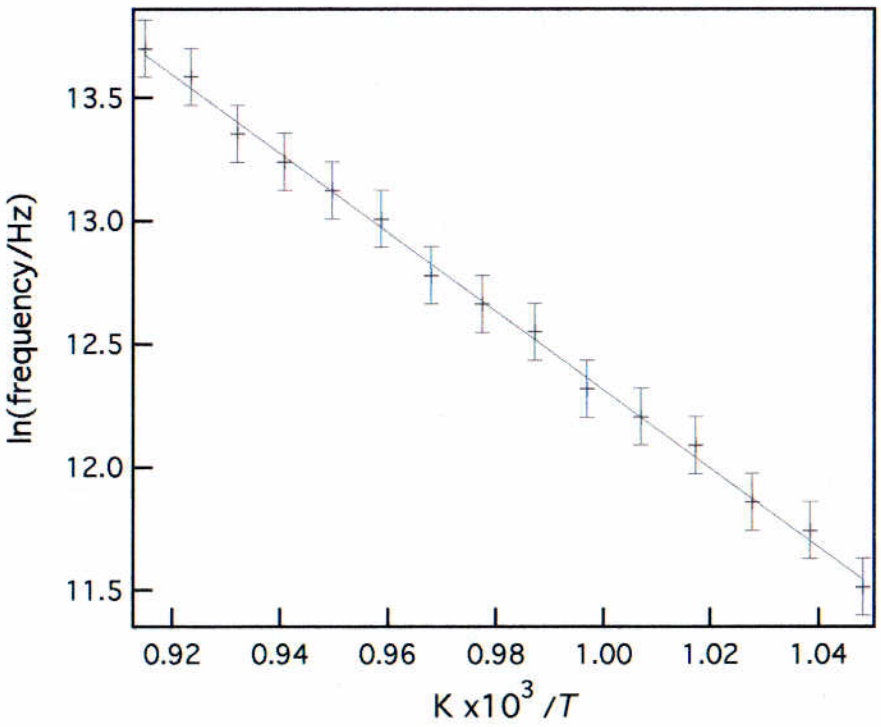

Figure 4.14 Arrhenius plot showing the temperature dependence of the maxima in the dielectric loss. The error bars represent the uncertainty in determining the peak position at each temperature.

It is not possible, on the basis of the dielectric measurements alone, to attribute this activation energy to a specific cation migration process. However, ^{23}Na MAS NMR lineshape studies for a synthetic sodium nepheline (Stebbins et al., 1989) have provided strong evidence for exchange between Na^+ ions in oval and hexagonal sites at high temperature. In particular, at 773 K, motional narrowing gives rise to a single ^{23}Na line and the time (τ) required for a fundamental site jump was estimated to be of the order of 300-500 μs. Assuming, as in the present work, a single, thermally activated process so that,

$$\tau = \tau_o \exp(E/RT)$$

and with τ_o typically of the order of 10^{-13} s, then the activation energy for the exchange process as observed by NMR is in the region 1.4-1.5 eV.

Overall, therefore, the NMR and dielectric measurements seem to be sensitive to the same Na^+ ion migration processes. Such a conclusion is also supported by the recent impedance measurements of Jiménez and Gregorkiewitz (1999). In their work an activation energy of 1.32 eV was measured in a synthetic Na-rich nepheline and attributed to the migration of Na^+ ions in the *ab* plane. To investigate the ion migration process in nepheline further, atomistic simulation was used.

4.5.2 Ion migration mechanisms and energetics

Na^+ migration in the (001) plane

A possible Na^+ ion migration pathway, taking into account symmetry considerations, would be to follow a trajectory in the (001) plane from an equilibrium position in the oval channel, through an interconnecting side channel, to a vacant K^+ site in the adjacent hexagonal channel (Fig. 4.15).

Figure 4.15 A view of part of the nepheline structure, in schematic form, showing a path through an interconnecting side channel between an occupied Na^+ site in the oval channel and a vacant K^+ site in the hexagonal channel.

In order to determine the approximate route taken by a migrating Na^+ ion as it passes through the distorted six-fold tetrahedral ring, several hundred lattice energy calculations were made across the whole of the (001) plane of translation. The results of these calculations revealed a curved pathway, shown as a contour plot in Figure 4.16. The migration energy of the Na^+ ion was determined by calculating the defect energy at different points along this pathway, allowing full relaxation of the lattice at each position. In order to confirm that a true saddlepoint had been found, defect calculations were also carried out in a direction perpendicular to the migration pathway in the (001) plane around the position of maximum energy. These revealed no significant deviations from the results of the initial calculations. In this way the saddlepoint configuration was identified.

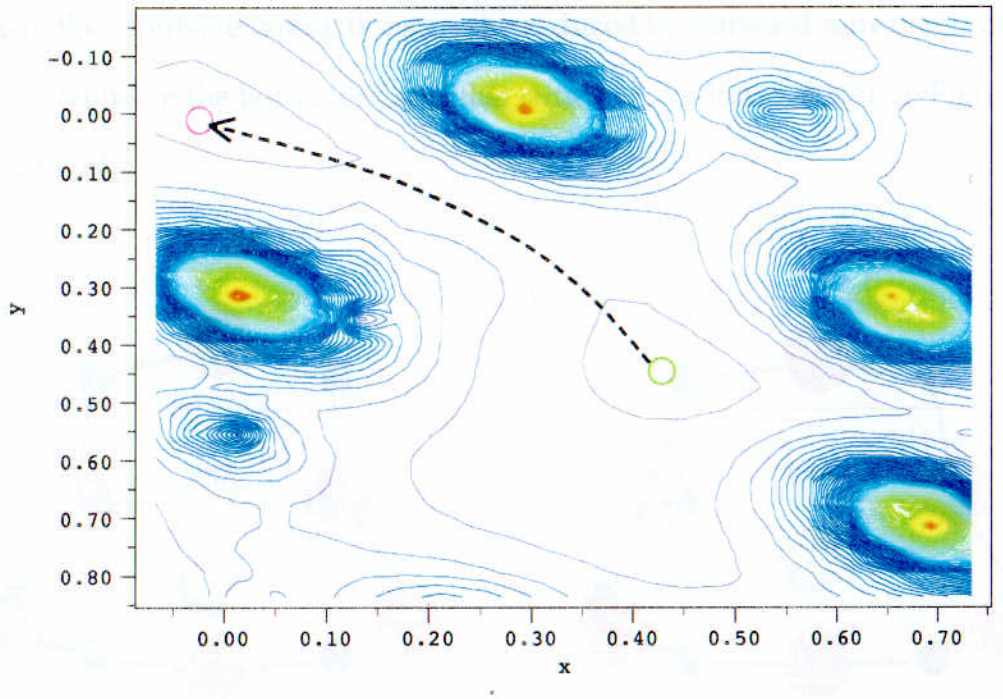

Figure 4.16 Contour plot showing the variation in the lattice energy in the (001) plane between an occupied Na site (green circle) and a vacant K site (pink circle). The approximate migration pathway between the occupied and vacant site is indicated.

Figure 4.17(a) shows the curved path taken by the migrating ion between the two sites along the (001) plane. In the saddlepoint configuration the migrating cation must pass through the constricted side-channel shown in Figure 4.17(b).

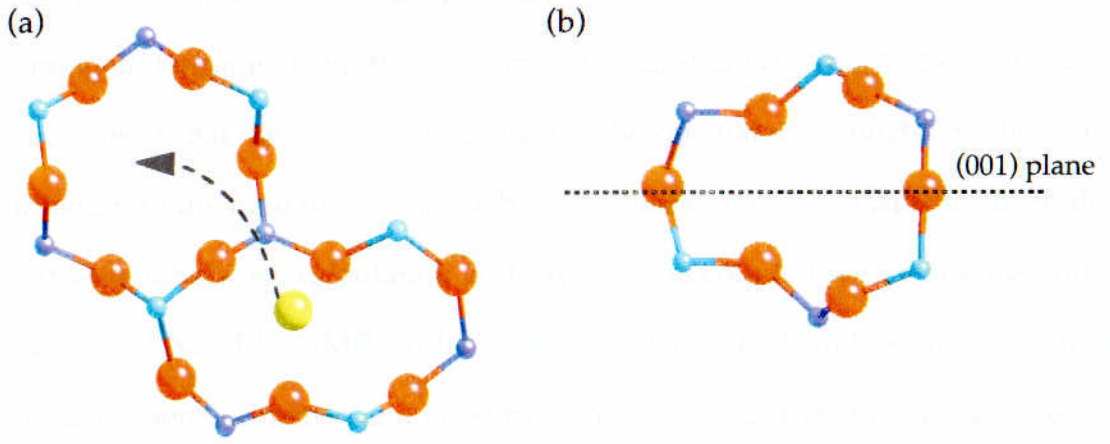

Figure 4.17 (a) The migration pathway of Na^+ ion between oval and hexagonal channel (view down [001]); (b) The distorted six-fold ring between oval and hexagonal channels (view down [320]).

Clearly the repulsive interactions can be reduced by outward movement of the oxygen atoms in the bottleneck and this lattice relaxation is shown in Figures 4.18 (a) and 4.18 (b).

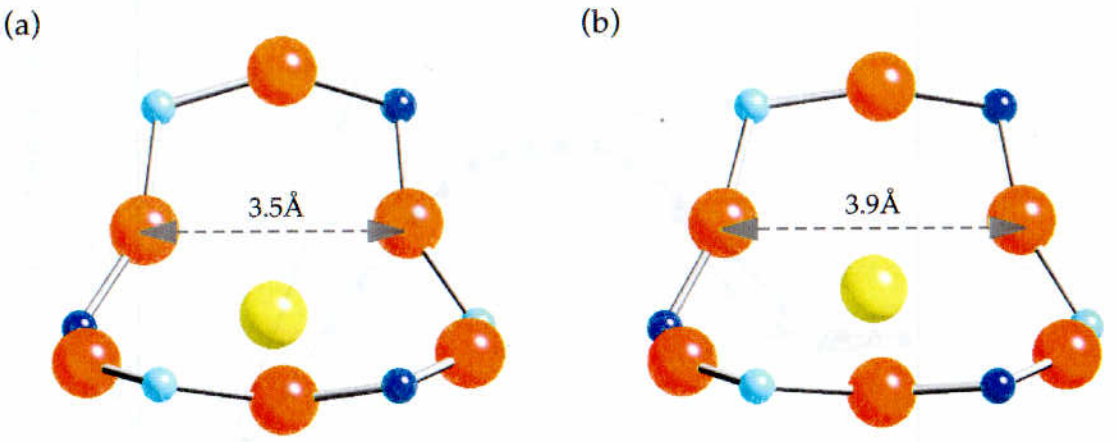

Figure 4.18 (a) The interconnecting side channel between Na^+ and K^+ sites in nepheline (view down [320]); (b) Relaxation of the structure of this side channel with the Na^+ ion at the saddlepoint.

Figure 4.19 shows the calculated energy profiles for the migration of the Na^+ ion as described above and for a direct linear path. The energy barrier to the migrating Na^+ ion along the curved path is calculated to be 1.38 eV, resulting in a significantly lower energy barrier to cation migration than a direct linear path which is calculated to be 2.49 eV. Although this value of 1.38 eV is in very good agreement with the activation energy determined from the dielectric measurements (1.38 ± 0.02 eV), it must be recognised that there are uncertainties in the calculated value due to the assumptions inherent in the modelling approach. Nonetheless, it is reasonable to conclude that the agreement between calculation and experiment, coupled with evidence from previous ^{23}Na MAS NMR studies (Stebbins et al., 1989), and recent impedance measurements (Jiménez and Gregorkiewitz, 1999) confirm the migration of Na^+ ions in nepheline at high temperatures.

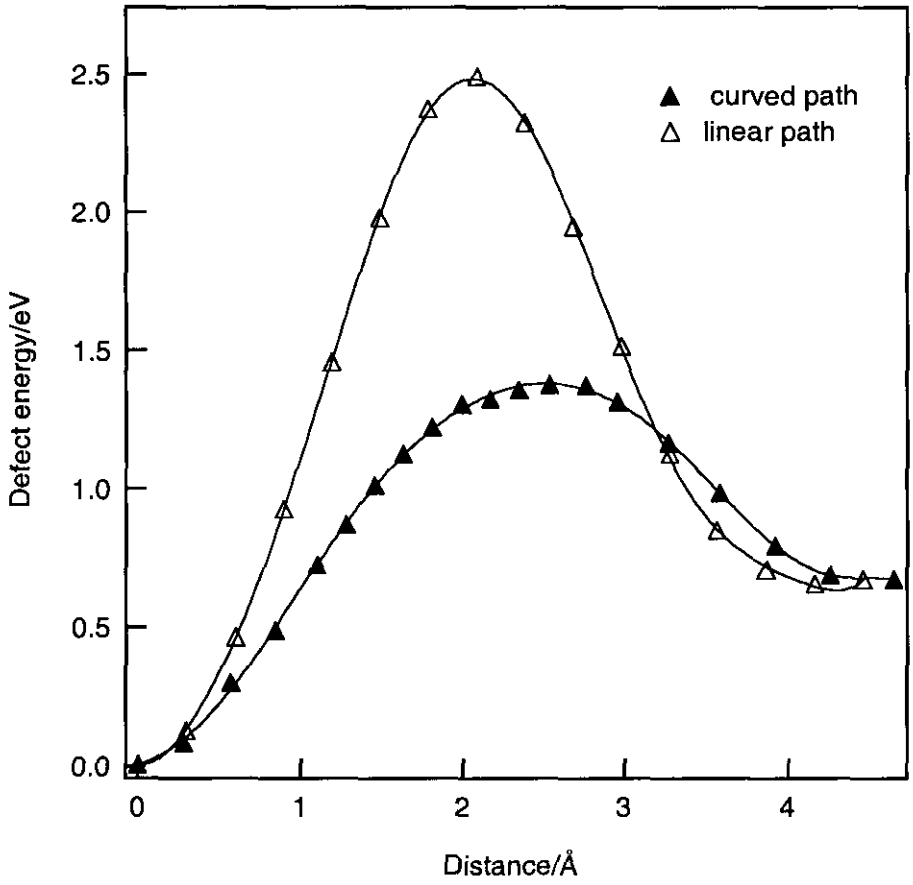

Figure 4.19 The calculated energy profiles for a Na^+ ion migrating between its equilibrium position in the oval channel and an adjacent vacant K^+ site in the hexagonal channel along curved and linear pathways. The points indicate the calculated defect energies at points along the migration path.

Other possible migration pathways for Na^+ and K^+ ions in nepheline

Other possible cationic migration mechanisms were also examined using the same simulation approach. The results of these calculations are summarised in Table 4.7 which also includes an estimate of the width of the bottleneck relevant to the migration process. None of these additional calculations yielded an activation energy which correlated with the observed dielectric response. The calculated energy profiles for these migration pathways are shown in Figure 4.20.

Table 4.7 Calculated activation energies for ion migration mechanisms in nepheline

Migration mechanism	[a]Channel width /Å	[b]Ion	E_a /eV
Na^+ ion moving along (001) through side channel	4.1	Na^+	1.38
Na^+ ion moving along hexagonal channel in [001] direction	5.3	Na^+	0.28
Na^+ ion moving along oval channel between two Na-sites	3.8	Na^+	1.84
K^+ ion moving along (001) through side channel	4.1	K^+	2.50

[a] Channel widths measured using the CrystalMaker program
[b] The ionic radii of Na^+ and K^+ are 1.16 Å and 1.52 Å, respectively, in six coordination (Shannon and Prewitt, 1976)

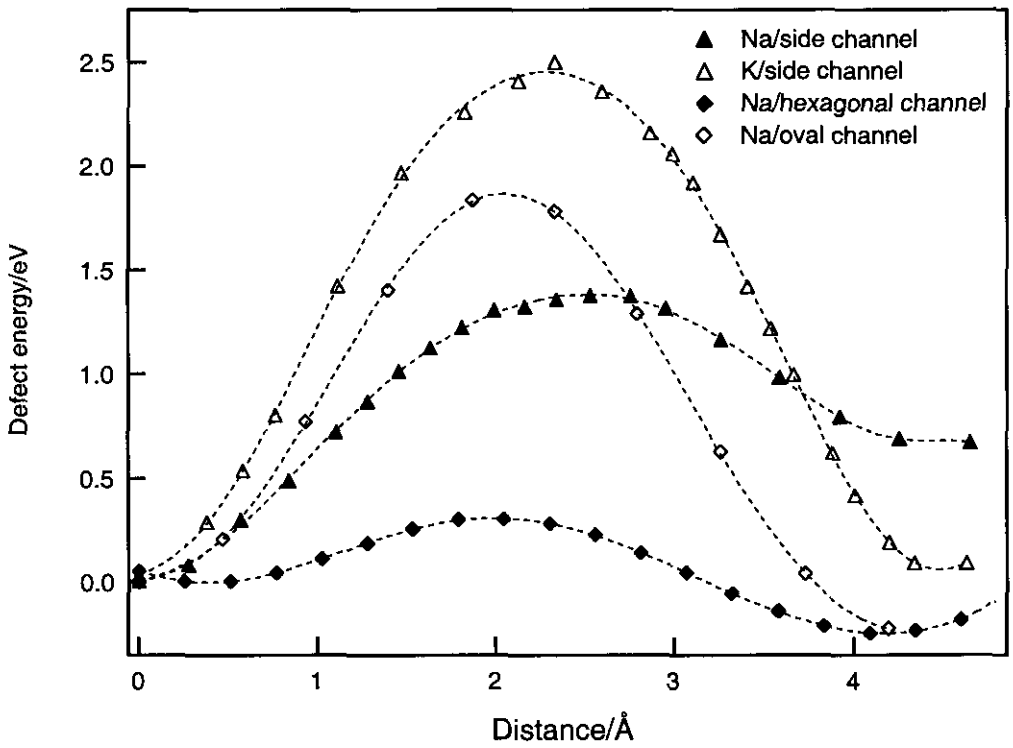

Figure 4.20 Calculated energy profiles for migration pathways of Na^+ and K^+ ions in the nepheline structure.

Initial calculations for a Na^+ ion moving along the hexagonal channel in the [001] direction gave a low activation energy (0.28 eV), as might be expected for a small ion

moving within a large channel. Subsequent calculations, in which the positions of the K-vacancies were changed relative to the migrating Na^+ ion, resulted in only a small change (< 0.02 eV) in the activation energy. This would suggest that the migration energy of the small Na^+ ion along the large hexagonal channel is unaffected by the occupation of adjacent sites.

These calculations also showed that the Na^+ ion was positioned centrally in the hexagonal channel in a completely ordered structure as shown in Figure 4.21(a), provided the adjacent oval channel is fully occupied. Previous work on sodium nepheline (Hippler and Bohm, 1989) has indicated that sodium ions in the hexagonal channel do not occupy the central site on the 3-fold axis but three off-axis positions with equal occupancy of 1/3 with a shift off the central positions of 0.35Å. Modelling a disordered structure has shown that the Na^+ ion takes a one-sided coordination in the hexagonal channel as shown in Figure 4.21(b) with a shift off the central position of approximately 0.2 Å. A similar one-sided coordination was found to occur in an ordered structure if any of the adjacent oval sites were vacant.

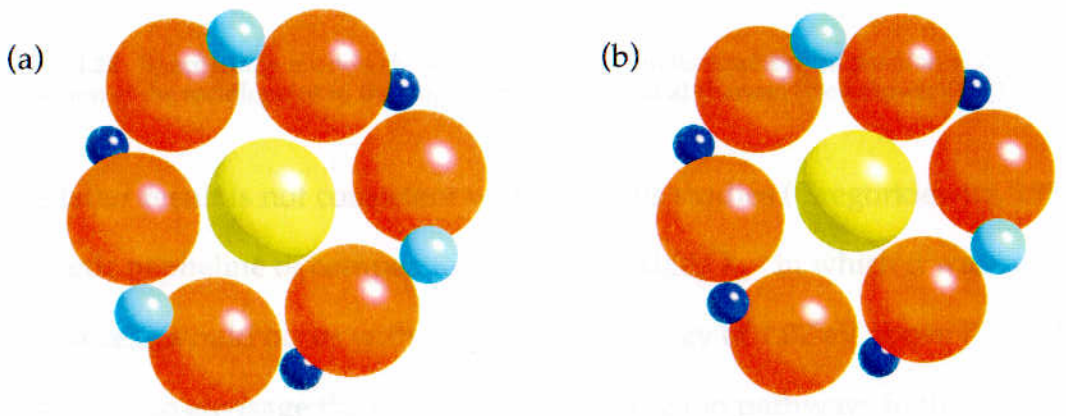

Figure 4.21 Space filling models (viewed down [001]) showing (a) the centrally positioned Na^+ ion in a fully ordered structure; (b) the one-sided coordination of the Na^+ ion in a disordered structure.

As expected, a high activation energy (1.84 eV) was calculated for a Na^+ ion moving along the oval channel between two Na-sites. Figures 4.22(a) and (b) show a Na^+ ion in its equilibrium position and the lattice relaxation when the Na^+ ion is at the saddlepoint in the migration between two Na-sites along the oval channel. Although the channel width increases from 3.56 Å, with the Na^+ ion in the equilibrium position, to 4.26 Å, with the Na^+ ion at the saddlepoint, it can be seen that this is a highly constricted pathway and unlikely to offer a favourable migration route.

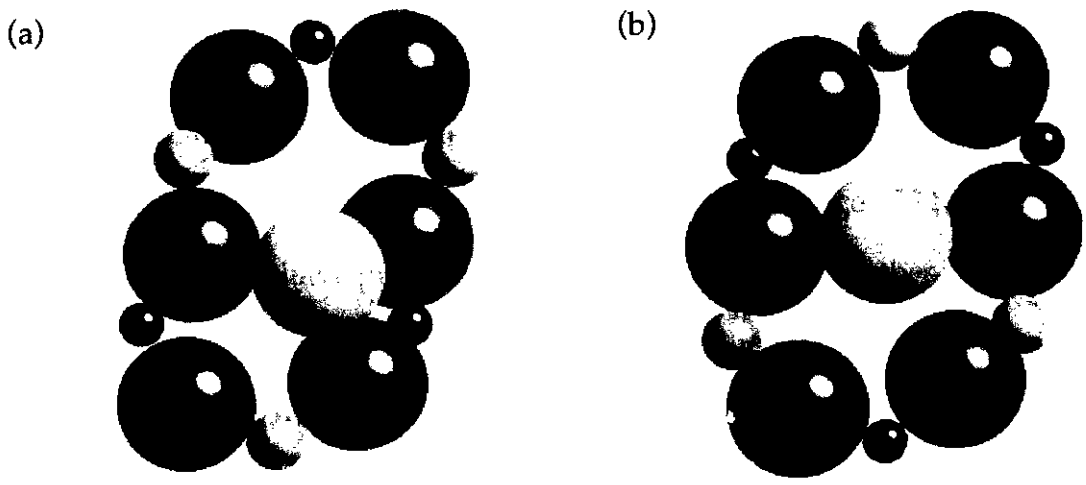

Figure 4.22 Space filling models showing (a) a Na^+ ion in its equilibrium position and (b) the lattice relaxation at the saddlepoint in the migration along the oval channel (view down [001]).

This latter result is not consistent with previous studies (Gregorkiewitz, 1986) on a synthetic nepheline of composition $Na_{3.36}K_{0.64}Al_4Si_4O_{16}$ in which it was suggested that this process would occur with an activation energy of 1.02 eV above 773 K. It is reasonable to envisage the creation of new diffusion pathways in the smaller oval channels at higher temperatures, but the increase in the size of the oval rings in the high-temperature structure is very small (<4%) (Foreman and Peacor, 1970). The

simulation results clearly indicate that such a narrow channel would offer an unfavourable energy barrier to Na^+ ion migration.

The simulation of a K^+ ion moving in the (001) plane into a Na^+ site via a side channel gave an activation energy of 2.50 eV, considerably greater than that found for Na^+ ions moving along the same pathway. The higher calculated activation energy is not unexpected for a larger ion moving through the same bottleneck, but as the oval channel is fully occupied, this process is unlikely to occur.

Longer range ion transport

Finally, it is possible that rapid ion transport could take place along the wide hexagonal channels by a multiple jump mechanism (Wittingham, 1975). Previous structural studies on nepheline at temperatures in the range 373 K - 423 K (McConnell, 1981) have proposed that cation ordering along these channels occurs with an activation energy of 0.80 eV (77 $kJmol^{-1}$). The feasibility of K^+ ion movement along the large channels parallel to [001] was therefore also examined. A range of activation energies (1.15-1.60 eV), that depended on the ordering of K^+ ions and vacancies, was calculated. These calculations were carried out on a *3c* supercell which has six K sites along [001] in the unit cell. The results of these calculations are summarised in Table 4.8 and Figure 4.23.

Table 4.8 Calculated activation energies for the migration of K^+ ions along the hexagonal channel in nepheline

Order	K - □ order in [001]	Defect energy at saddlepoint/eV
(1)	K K* □ K K □	1.43
(2)	K K* □ □ K K	1.15
(3)	K* □ K □ K K	1.30
(4)	K □ K* □ K K	1.60

K* is the K^+ ion which is migrating along the hexagonal channel in each calculation; □ denotes a vacancy; □ is the vacancy to which the interstitial K^+ ion is migrating.

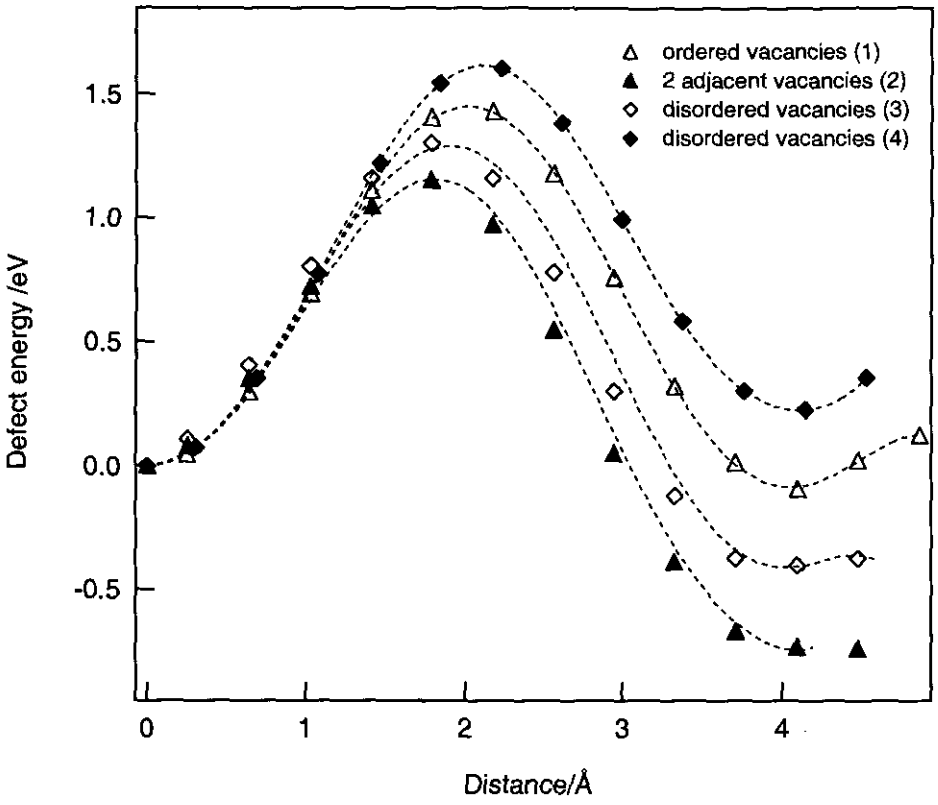

Figure 4.23 Calculated energy profiles for the migration of a K^+ ion along [001] in the nepheline structure.

These findings are consistent with studies carried out over the temperature range 300 K to 1000 K on sodium nephelines (Roth and Böhm, 1986). Roth and Böhm found that the activation energies, dielectric constant and specific conductivities depended strongly on the concentration of charge carriers in the wide hexagonal channel. Their results suggested that for high carrier densities a cooperative migration mechanism might be predominant, whereas for low concentrations diffusion by conventional "discrete hopping" occurs. The type of defect calculation carried out in the present work is more applicable to distinct Debye-type ion-hopping processes rather than a correlated movement of ions along a channel. Molecular dynamics (MD) simulations would therefore be useful to probe such effects and is a subject of future investigation.

4.6 Conclusions

The combination of dielectric spectroscopy with computer simulations has enabled a mechanism for ion migration in nepheline to be established. As a result of the very good agreement obtained between the experimentally determined activation energy, using dielectric spectroscopy, and the calculated defect energy, the following conclusions can be made:

- Migration of Na^+ ions in nepheline occurs in the *ab* plane between its equilibrium position and a K-vacancy by an activated hopping mechanism.
- The lowest energy migration pathway between the two sites is via a curved trajectory rather than a linear route.
- The calculations have demonstrated the importance of lattice relaxation effects at the migration saddlepoint.
- The calculated defect energies are dependent on the size of the migrating ion and the effective channel width.

This study of nepheline has demonstrated how computer modelling techniques may be used to complement data obtained using dielectric spectroscopy, and thereby elucidate the mechanisms for experimentally observed processes. The method offers the opportunity to investigate diffusion-related processes in different frameworks with different ionic content. Extension of this approach should subsequently enable the development of crystal chemical systematics, thus allowing the prediction of diffusion pathways and energetics in other framework silicates from a correlation of ionic size and charge with framework geometry.

Chapter 5

Yoshiokaite

Contents

5.1 Introduction

Yoshiokaite, $CaAl_2SiO_6$, is a Ca-stuffed derivative of tridymite which occurs naturally on the moon. Small amounts of the mineral were found in a rare lunar regolith breccia collected by astronauts from the Apollo 14 mission.

The structural similarities between yoshiokaite and nepheline have enabled a comparison of their high temperature behaviour to be made. Although the channel structure of the yoshiokaite framework closely resembles that of nepheline, an investigation into Ca^{2+} ion mobility should provide an opportunity to investigate the influence of ionic charge on mobility processes and the effect of cation/framework interactions on ion migration energetics.

In this investigation, ionic mobility in yoshiokaite has been studied using a combination of dielectric spectroscopy and atomistic simulations. Dielectric spectroscopy was used to investigate the mobility of calcium ions from room temperature to 1100 K. In addition to this, atomistic simulation techniques were used to investigate the energetics and mechanism of Ca^{2+} migration within the yoshiokaite structure, and thereby interpret the dielectric data in structural terms. The results of these investigations, together with the results of a high-resolution neutron powder diffraction study (Palmer et al., 2001), have enabled a detailed study of the high temperature behaviour of yoshiokaite to be made, focussing on the mobility of Ca^{2+} ions within the structural channels.

5.2 Scientific background

5.2.1 Occurrence and composition

Yoshiokaite occurs as shocked crystal fragments and in devitrified glasses along with minerals such as anorthite, corundum and gehlenite (Vaniman et al., 1988). Several single crystals found in the lunar regolith breccia (Vaniman et al., 1989) have a stoichiometry near $Ca_3Al_6Si_2O_{16}$, and the full range of compositions overlaps that of a metastable phase made by devitrification of synthetic CaO-Al_2O_3-SiO_2 glasses, at temperatures of about 950–1200 °C (Yoshioka, 1970). Yoshioka's metastable solid solution between $CaAl_2Si_2O_8$ and $CaAl_2O_4$ had properties consistent with the mineral found in the lunar regolith breccia, and because he carried out the basic research on the synthetic phase, the mineral was named after him. The compositions of the phase from the lunar sample can be described as $Ca_{8-0.5x}\square_{0.5x}Al_{16-x}Si_xO_{32}$ ($2.8<x<6.0$), where $\square$ represents a vacancy.

5.2.2 Synthesis of yoshiokaite

Crystals of a hexagonal polymorph of $CaAl_2SiO_6$ were first prepared from a stoichiometric, dry melt of the same composition by Kirkpatrick (1973). The melt was produced by melting together the required amounts of $CaCO_3$, Al_2O_3 and SiO_2 in a platinum crucible in a $MoSi_2$ resistance furnace at 1600 °C. It was then quenched to room temperature, ground up and the fusion/quenching process repeated twice more. The glass product was then crystallised between 950 °C and 1050 °C. It was thought that nucleation within the glass occurred on undissolved Al_2O_3. Crystallisation was complete in approximately 14 hours. Earlier workers (de Neufville and Schairer, 1966) had previously investigated the system $CaMgSi_2O_6$-

$CaAl_2SiO_6$ and found that below 1350 °C the composition $CaAl_2SiO_6$ consisted of the assemblage gehlenite + anorthite + spinel + alumina. None of these phases, except undissolved corundum, was found by Kirkpatrick.

5.2.3 Structure of yoshiokaite

The X-ray diffraction pattern and the cell dimensions of the lunar material as determined by Vaniman and Bish (1990) closely match those of the synthetic phase synthesised by Yoshioka (1970). The phase close to $CaAl_2SiO_6$ synthesised by Kirkpatrick (1973), as described above, was shown to be a type of stuffed tridymite with some structural features similar to those found in nepheline. The cell dimensions of the synthetic phases prepared by Yoshioka and Kirkpatrick are compared with those of the lunar phase in Table 5.1.

Table 5.1 Lattice parameters for synthetic and natural yoshiokaite

Lattice parameter	Synthetic[a]	Lunar[b]	Synthetic[c]
a/Å	9.923(5)	9.9961	9.943
c/Å	8.226(6)	8.2195	8.228

[a]Yoshioka (1970); [b]Vaniman and Bish (1989); [c]Kirkpatrick and Steele (1973).

The X-ray diffraction patterns, cell parameters and optical properties all suggest that both the lunar and the synthetic materials have similar structures, which are based on the tridymite framework. Although Kirkpatrick (1973) showed the symmetry to be consistent with spacegroup $P3c1$ and $P\bar{3}c1$, a later refinement (Steele and Pluth, 1990) suggested violations of the c glide. Although the relation to the tridymite structure was obvious, the nepheline structure is not compatible with $P\bar{3}c1$ symmetry in the neighbourhood of the threefold axis because of the c glides. Refinement was therefore done in $P\bar{3}$, which is not inconsistent with the nepheline structure.

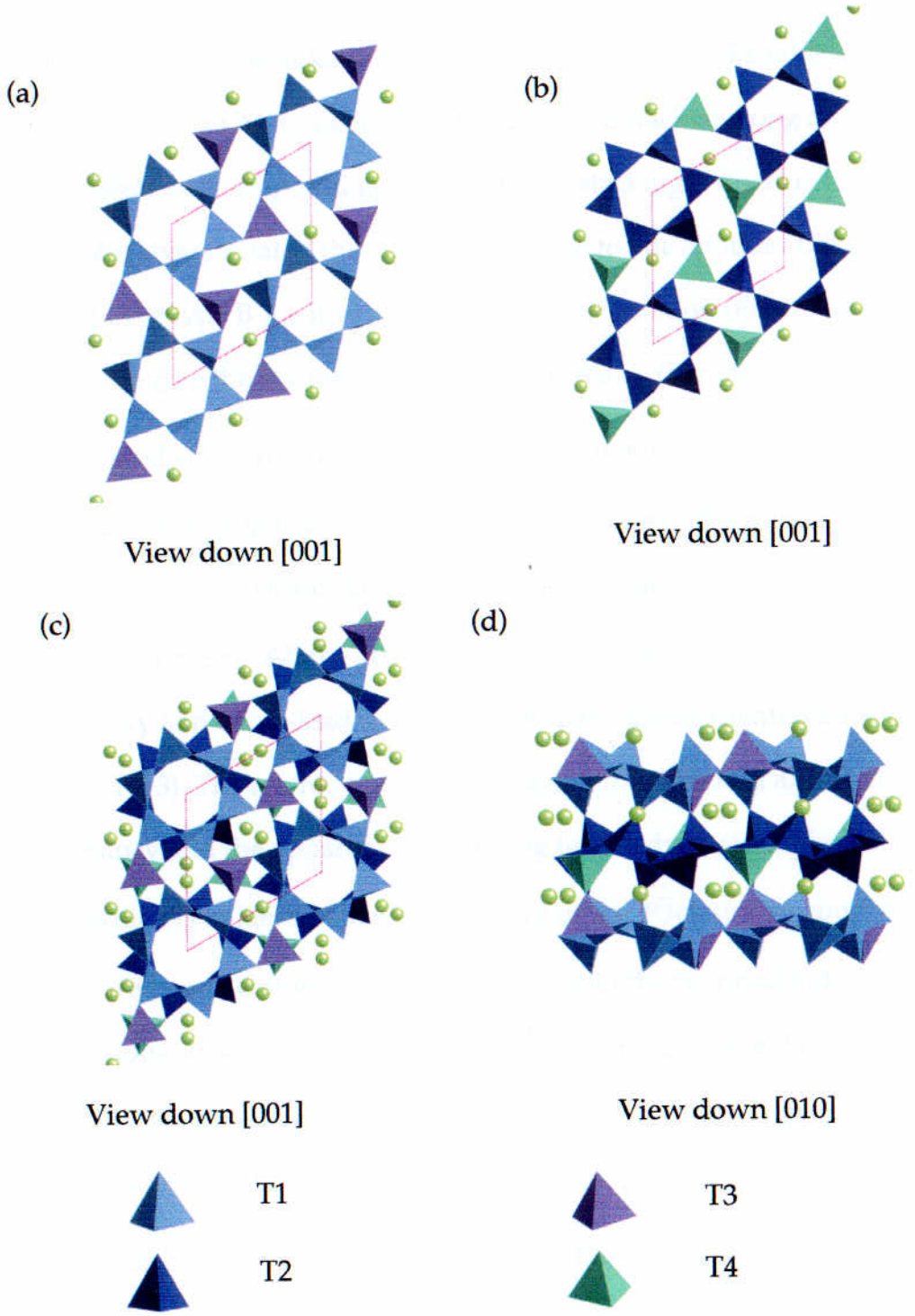

Figure 5.1 The yoshiokaite structure: (a) layer type A; (b) layer type B′; (c) and (d) ……AB′A…… stacking sequence.

The basis of the yoshiokaite structure, shown in Figure 5.1 (a) is a single nepheline layer (layer type A). In nepheline the layers are stacked along *c* so that they are almost completely superimposed giving rise to the stacking sequence ...ABAB... , with the alternate layers rotated through 180° relative to one another. In yoshiokaite a second layer (layer type B'), with an opposite sense of rotation (Figure 5.1 (b)), is stacked along *c* to give the stacking sequence ...AB'AB'... (Figures 5.1 (c) and (d)).

The refined structure from Steele and Pluth (1990) takes into account possible micro-twinning, with apparent $P\bar{3}c1$ symmetry. To satisfy this refinement, the tetrahedra sharing apical O4 atoms have to be given an occupancy of 0.5 and an apparent face-sharing geometry. All the atoms except those located on the threefold axis obey $P\bar{3}c1$ symmetry and hence lead to the original space-group identification (Kirkpatrick and Steele, 1973). The atomic configuration along the threefold axis, including the half occupancy and the apparent face-sharing tetrahedra, was explained by a [110] twin axis, which is in fact a symmetry element of the $P\bar{3}c1$ space group. The structure therefore has a symmetry so close to $P\bar{3}c1$ that the twinned individuals form a continuous structure only differing by the tetrahedral orientations on the threefold axis. The violations of the *c* glide of $P\bar{3}c1$ result from the departure from $P\bar{3}c1$ for only those Si and O atoms located on the threefold axis.

A neutron diffraction study carried out on the same sample of yoshiokaite has provided data for the high temperature structure (Palmer et al., 2001). These refinements were based on the room temperature structure determined by Steele and Pluth (1990). Refinements in space group $P\bar{3}c1$ gave better fits than those in $P\bar{3}$, confirming the significance of the fine-scale twinning observed by Kirkpatrick and Steele (1973). It was found that the thermal parameter of Ca changed little with

temperature, suggesting no anomalous Ca behaviour between room temperature and 1123 K. In addition to this, the Ca occupancy of the hexagonal site was found to be extremely small (X_{Ca} = 0.06-0.08).

5.2.4 Phase transitions

X-ray diffraction studies (Steele and Pluth, 1990) carried out on a sample of the yoshiokaite prepared by Kirkpatrick (1973) from 300 K to 1170 K revealed discontinuities in intensity indicating phase changes at 823 ± 10 K and 978 ± 10 K. The diffraction patterns in the three temperature regions were found to be similar, suggesting no major structural changes. However, the change at 823 K was accompanied by a splitting of the 100 diffraction and a weakening of the 002 diffraction, suggesting a possible lowering of symmetry to the orthorhombic $CaAl_2O_4$ structure. The change at 978 K was marked by distinct changes in the intensity of nearly all diffractions, by the 100 diffraction reverting to a singlet and by the reappearance of the 002 diffraction. The room temperature pattern after heating showed a sharpening of most diffractions and subtle intensity changes relative to the starting material, suggesting that some tetrahedral ordering may have occurred during the three days of heating.

In the recent high resolution neutron powder diffraction study by Palmer et al. (2001), it was found that the crystal structure of yoshiokaite appears to remain largely unaltered with increasing temperature, and there was no evidence of any phase transitions occurring.

5.3 Experimental

5.3.1 Sample characterisation

The material used in this study was a polycrystalline sample supplied by Professor R. J. Kirkpatrick and was synthesised by him as described in section 5.2.2. It should be noted that this is the same material as used by Steele and Pluth (1990) in their structural investigation of yoshiokaite.

Electron microprobe analysis

The composition of the sample was determined using electron microprobe analysis. This was carried out using a Cameca SX100 probe at 20 kV, 20 nA and a 10 μm spot diameter. The composition of the sample was calculated to be $Ca_{1.03}Al_{1.98}Si_{0.99}O_6$. This is very similar to that determined by Kirkpatrick (1973): $Ca_{1.01}Al_{1.95}Si_{1.03}O_6$. The slight excess of (Si + Ca) over Al probably results from aluminium deficiency of the melt.

5.3.2 Thermal expansion

The temperature dependence of the hexagonal lattice parameters *a* and *c*, as determined in the neutron powder diffraction study (Palmer et al., 2001) is shown in Figures 5.2 (a) and (b), respectively. Both *a* and *c* show a slight curvature at low temperatures, and linear behaviour above 500 K. The thermal expansion of the *c*-axis is greater than the *a*–axis but there are no discontinuities in either case. These results show no evidence for any phase transition occurring over the temperature range studied.

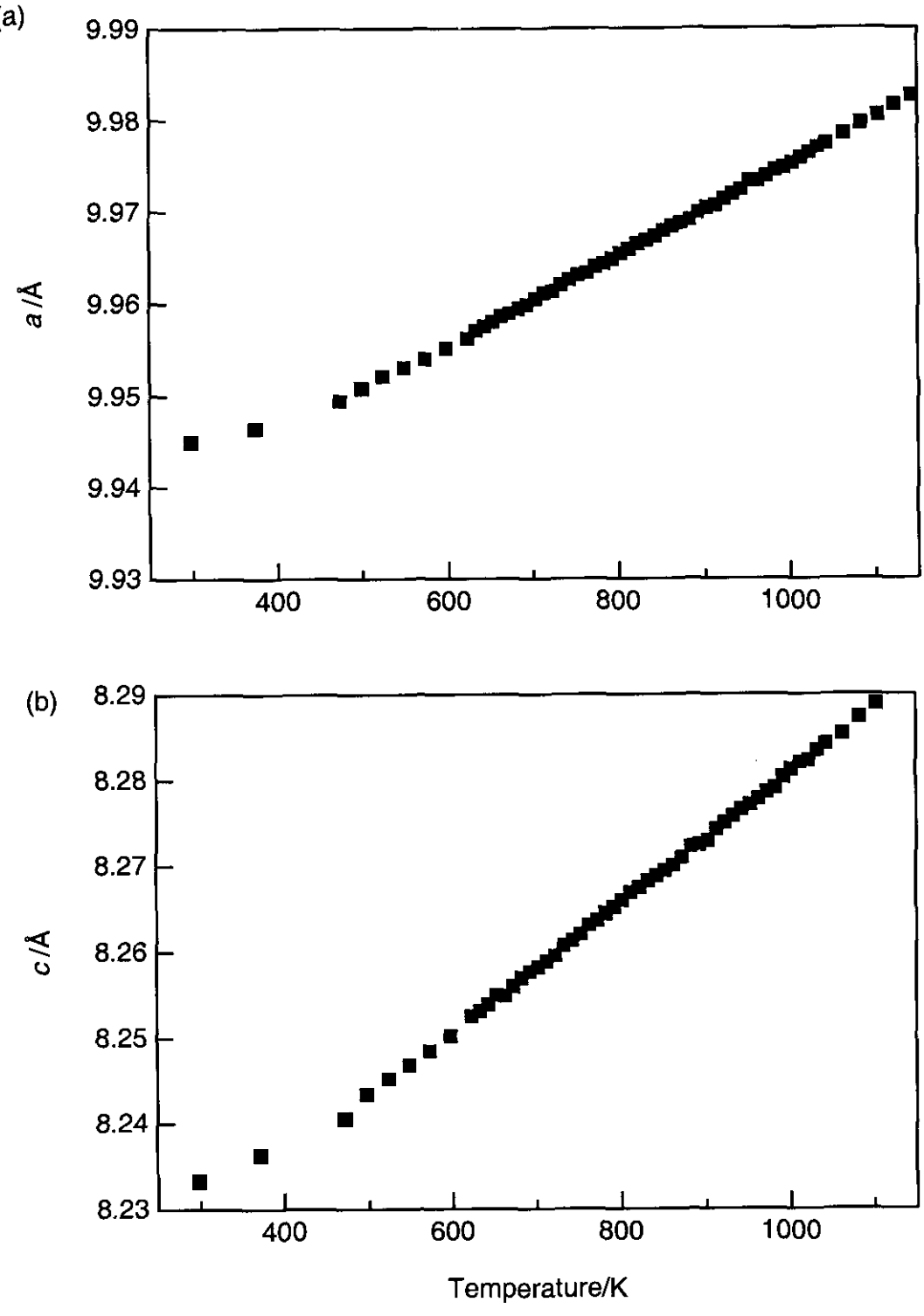

Figure 5.2 Temperature dependence of lattice parameters (a) *a* ; (b) *c* for yoshiokaite. Error bars are smaller than the plotted points.

5.3.3 Dielectric measurements

Dielectric measurements were made on thin slices of the polycrystalline material using the methods described in Chapter 2. Measurements of capacitance and conductance were made at room temperature and at regular intervals up to 1100 K. From these measurements the dielectric constant, conductivity and dielectric loss were calculated at each frequency.

5.4 Atomistic computer modelling

The interatomic potentials and shell model parameters used are listed in Table 5.2. They were taken from previous simulation studies (Bush et al., 1994; Freeman and Catlow, 1990) and were found to be the most appropriate for the present study.

The starting point for the calculations was the simulation of the yoshiokaite structure. The unit cell dimensions and atomic coordinates used for the calculations were taken from the Steele and Pluth refinement (1990), but with each Ca site given an occupancy of 0.89 in order to maintain the charge balance. This is lower than the 0.92 occupancy assigned to the Ca sites by Steele and Pluth, but was necessary in order to perform the calculations on what could be described as the 'true' yoshiokaite structure, (i.e. without consideration of the micro-twinning and inclusion of the apparent face-sharing tetrahedra as described in section 5.2.3). The calculated values for the lattice parameters and selected bond distances and their comparison with experimental values (Kirkpatrick and Steele, 1973) are listed in Table 5.3. Examination of the differences shows a very good agreement between experimental and simulated structures. This provides a reliable starting point for the defect calculations.

Table 5.2 Interatomic potentials used for modelling the yoshiokaite sructure

(i) Two-body Buckingham

Interaction[a]	A/eV	ρ/Å	C/eV Å^{-6}
Ca^{2+} ...O^{2-}	2272.741	0.2986	0.0000
Si^{4+} ...O^{2-}	1283.907	0.32052	10.66158
Al^{3+} ...O^{2-}	1460.3	0.29912	0.0
O^{2-} ...O^{2-}	22764.3	0.1490	27.879

(ii) Shell model[b]

Species	Y/e	K/eV Å^{-2}
O^{2-}	-2.86902	74.92
Ca^{2+}	1.2810	34.05

(iii) Three-body

Interaction	Force constant/eV rad^{-1}
O – Si – O	2.0972
O – Al – O	2.0972

[a] Potential cut off = 10 Å.
[b] Y and k refer to the shell charge and harmonic force constant, respectively.

Table 5.3 Calculated and experimental structural parameters for the yoshiokaite structure

(i) Unit cell parameters

Parameter	Experimental	Calculated	Difference/%
a	9.927000 Å	9.925579 Å	0.01
b	9.927000 Å	9.919105 Å	-0.08
c	8.220000 Å	8.216382 Å	-0.04
α	90.0000°	89.991075°	-0.01
β	90.0000°	90.009201°	0.01
γ	120.0000°	120.019917°	0.02

Table 5.3 (continued)

(ii) Selected bond distances

Bond distance	Experimental/Å	Calculated/Å
O1 – T1	1.699	1.703
O3 – T1	1.724	1.729
Ca – O1	2.417	2.335
Ca – O3	2.482	2.608

Although there is good agreement of the lattice parameters in the experimental and calculated structures, the agreement of the coordination distances of the calcium ions with the framework are not so good (~ 5% difference). This may be a result of the partial occupancy assigned to each Ca-site within the structure.

5.5 Results and discussion

5.5.1 Dielectric spectroscopy

Figure 5.3 shows how tan δ changes with temperature and Figures 5.4 (a) and (b) show the behaviour of ε' and σ, respectively, with temperature for a selected range of frequencies. The dielectric constant has a value of ~9 for all frequencies at room temperature, rising slightly up to 800 K, after which there is an increase which is most prominent at low frequencies. The low frequency conductivity remains low at all temperatures, whereas the high frequency conductivity increases markedly above 800 K. There are observed increases in tan δ around 673 K, 833 K and 993 K, and in σ at approximately 673 K at all frequencies above 250 kHz. The temperatures of the increased dielectric loss closely correspond to the reported phase transition

temperatures of 823 K and 978 K (Steele and Pluth, 1990), but there was no reported phase transition at 673 K. There therefore remains a degree of uncertainty regarding the possibility of one or more phase transitions occurring within this temperature range, as the high temperature neutron diffraction study (Palmer et al., 2001) showed no evidence for a phase transition occurring.

The temperature dependence of ε' and tan δ as a function of frequency between 893 K and 1033 K is shown in Figures 5.5 (a) and (b) respectively. There was no significant dielectric loss peak below 893 K. The dielectric loss spectrum, shown as a surface plot in Figure 5.6, shows only a Debye-type relaxation peak at high temperature and high frequencies. There is no significant low frequency absorption, which would be indicative of large scale motions of ions (Barrer and Saxon-Napier, 1962; Ohgushi and Kazuhide, 1998). This would suggest that the yoshiokaite structure does not allow any kind of correlated movement of ions along channels, as was the case in nepheline. The temperature dependence of the frequency of the maximum absorption follows an Arrhenius relationship as shown in Figure 5.7. The activation energy is calculated to be 1.34 ± 0.02 eV (128.9 ± 1.7 $kJmol^{-1}$).

Although it is not possible to attribute this activation energy to any specific Ca^{2+} migration process on the basis of these dielectric measurements alone, the range of possible cation migration mechanisms is limited due to the constraints of the yoshiokaite framework geometry. This will be discussed in section 5.5.2. Atomistic simulation was therefore used to investigate a number of feasible mechanisms.

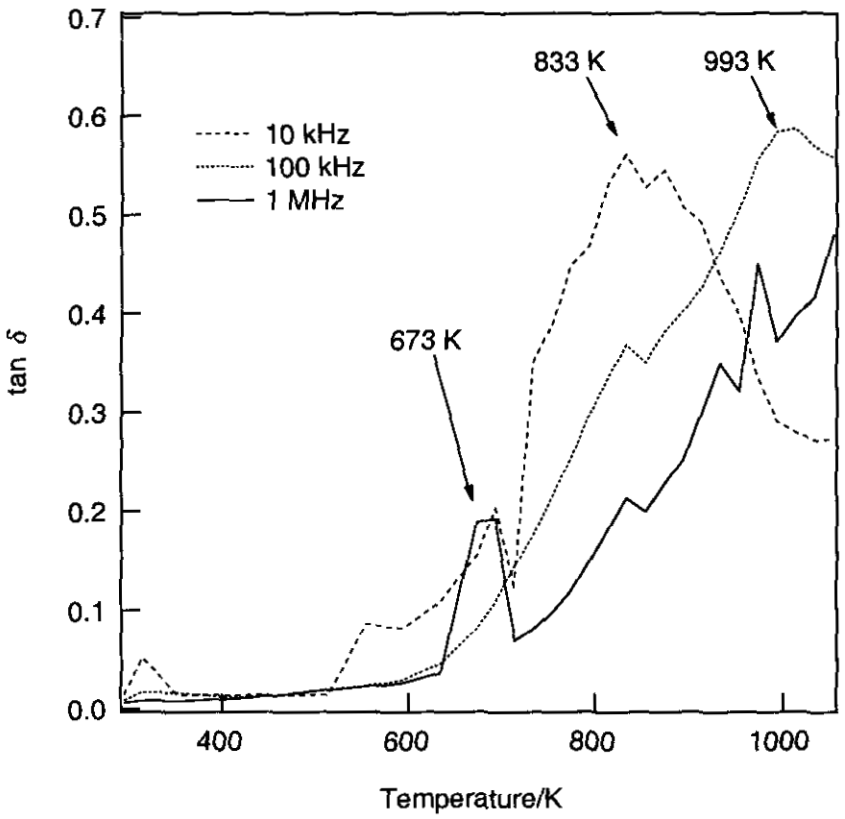

Figure 5.3 Temperature dependence of tan δ at selected frequencies.

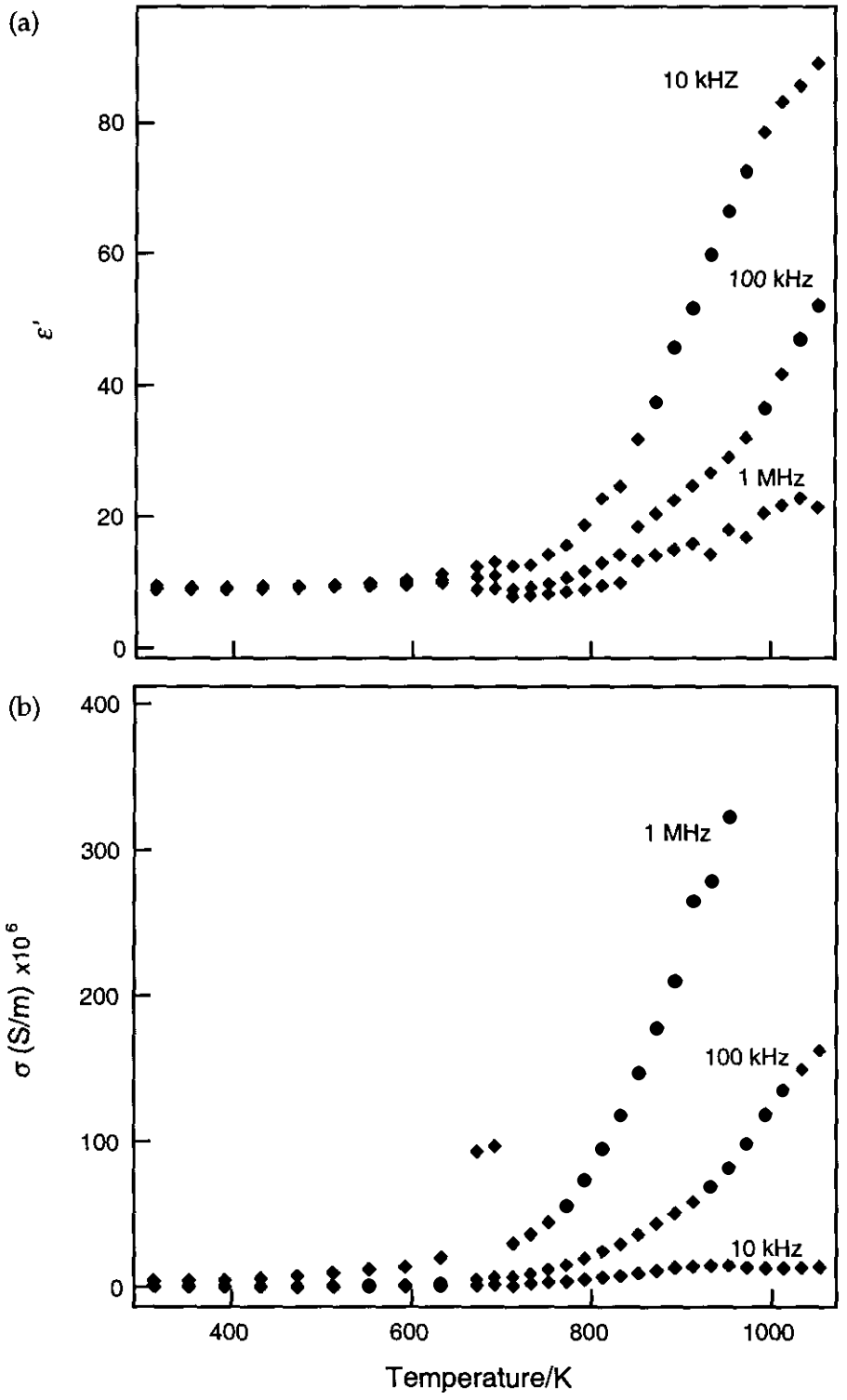

Figure 5.4 Temperature dependence of (a) ε'; (b) σ at selected frequencies.

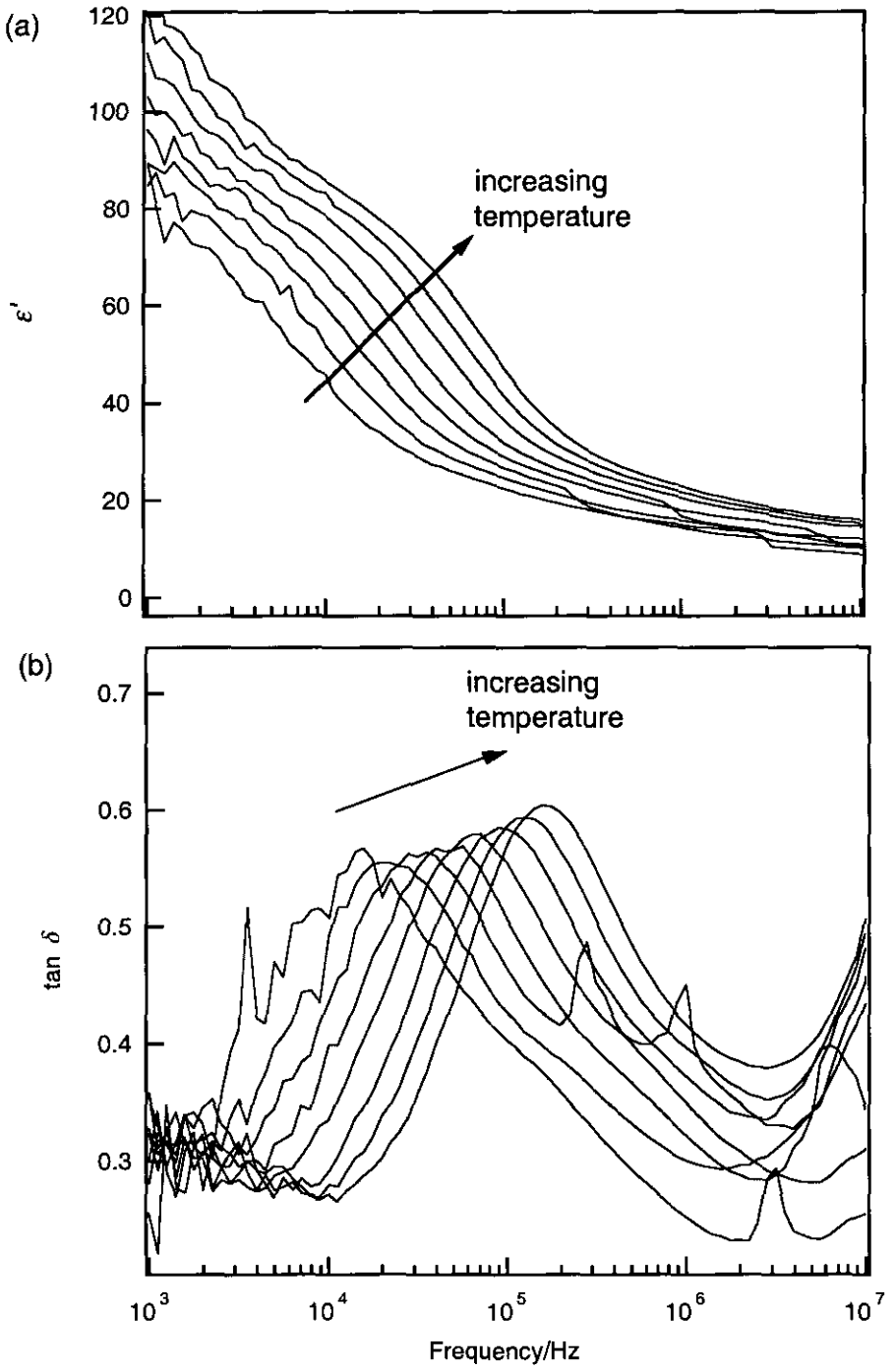

Figure 5.5 Temperature and frequency dependence of (a) ε'; (b) tan δ between 893 K and 1033 K.

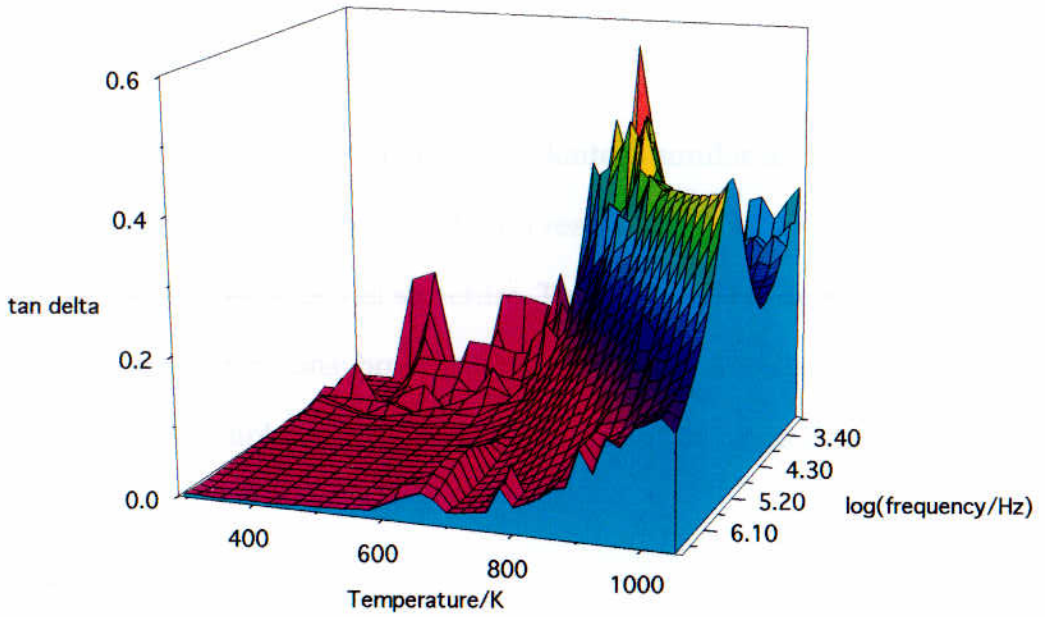

Figure 5.6 Surface plot showing the dielectric loss as a function of frequency and temperature.

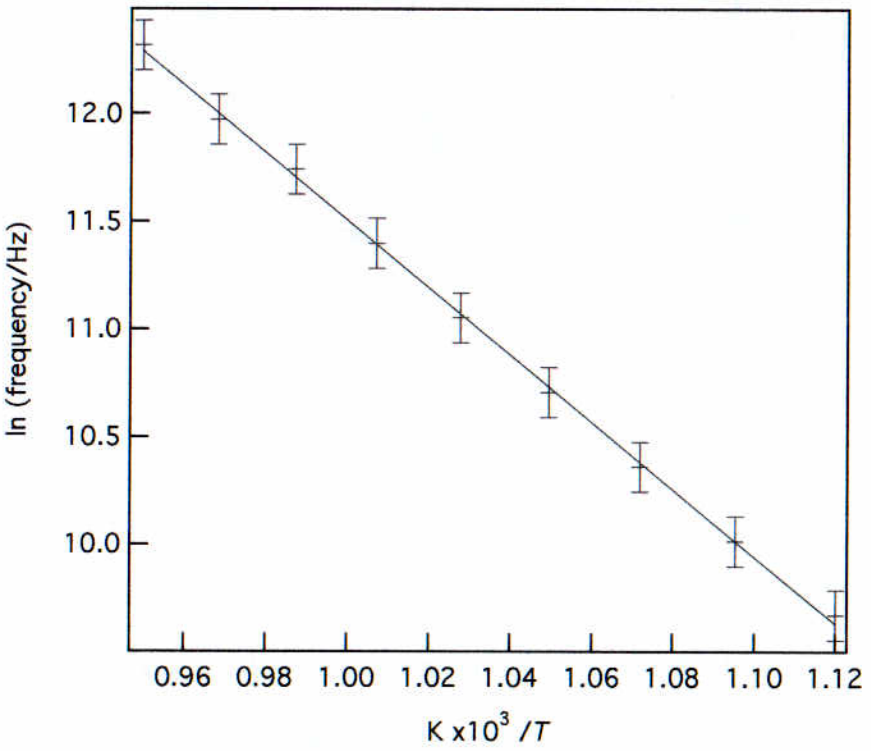

Figure 5.7 Arrhenius plot showing the temperature dependence of the maxima in the dielectric loss. The gradient of the line indicates an activation energy of 1.34 ± 0.02 eV. The error bars represent the uncertainty in determining the peak position at each temperature.

5.5.2 Ion migration mechanisms and energetics

A migration pathway for Ca^{2+} in yoshiokaite

Although the framework structure of yoshiokaite is similar to that of nepheline, the 90° rotation of alternate layers of tetrahedra results in a framework geometry with a significantly constrained channel structure. The oval and hexagonal channels are of similar shape and dimensions; however, the side channel linking the two is highly constricted in the yoshiokaite structure compared to the nepheline structure as shown in Figure 5.8.

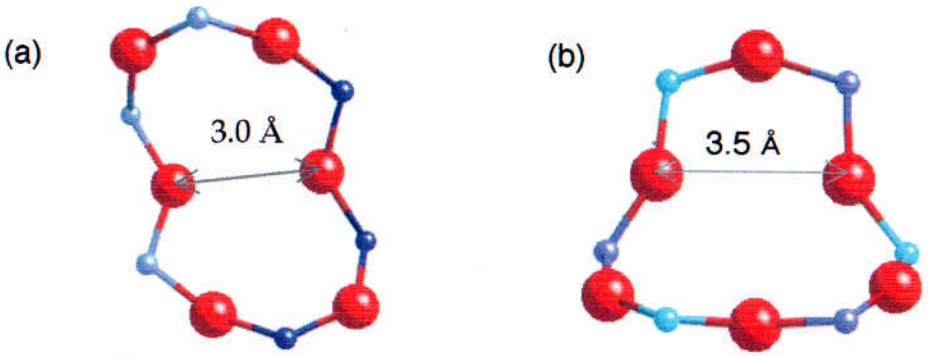

Figure 5.8 Interconnecting side channel between the oval and hexagonal channel in (a) yoshiokaite; (b) nepheline.

The corresponding side channel in the nepheline structure allowed a migration pathway for a Na^+ ion moving along a trajectory in the (001) plane (Chapter 4, section 4.5.2). Migration along such a pathway in yoshiokaite is likely to be energetically unfavourable, given the dimensions of the distorted 6-fold side channel and taking into account the double charge on the Ca^{2+} ion.

The only possible migration pathway for a Ca^{2+} ion to move within the yoshiokaite structure would appear to be directly along the [001] hexagonal channel. The hexagonal sites in yoshiokaite are reported to be vacant (Steele and Pluth, 1990), but there may be a small amount of calcium present in these channels (Palmer et al., 2001). In order to test this assumption, defect calculations were carried out on the migration of an interstitial Ca^{2+} ion along the hexagonal channel. Figure 5.9 (a) shows the position of the interstitial Ca^{2+} ion in the hexagonal channel and Figure 5.9 (b) shows the Ca^{2+} ion in the minimum energy positions at the start and finish of the migration pathway, on either side of the highly distorted bottleneck. The positions of the Ca^{2+} ion shown in Figure 5.9 (b) correspond to the minima in the energy profile shown in Figure 5.10. The energy barrier for this migration process was calculated to be 1.18 eV. This result is very close to the activation energy measured using dielectric spectroscopy (1.34 ± 0.02 eV).

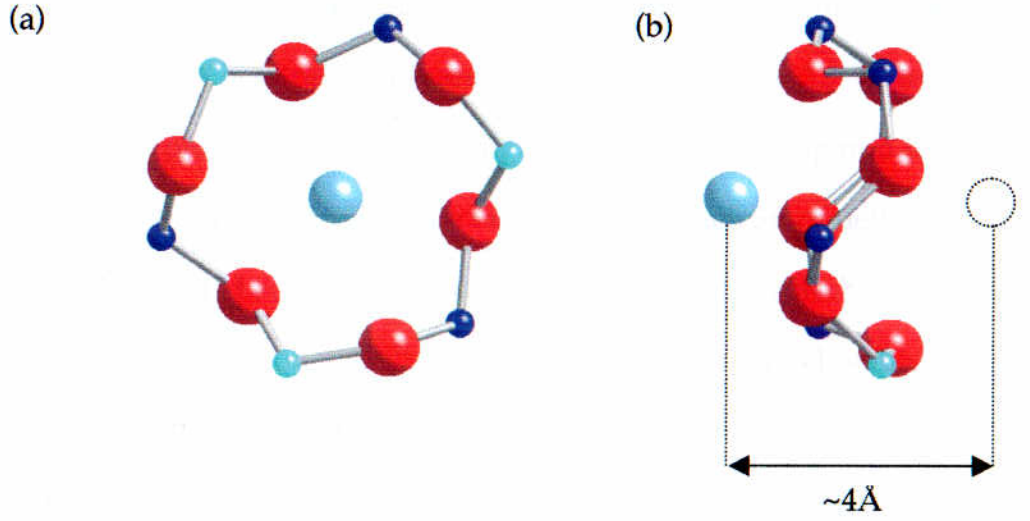

Figure 5.9 (a) View down [001] showing the Ca^{2+} ion in the hexagonal channel; (b) View down [100] showing the highly distorted bottleneck and the positions of the migrating Ca^{2+} ion at the energy minima in the migration pathway.

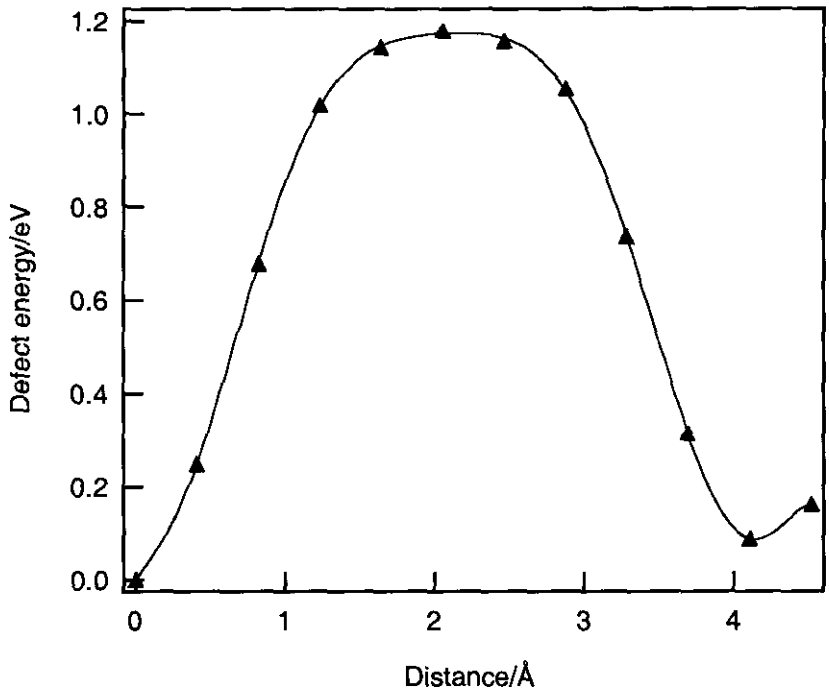

Figure 5.10 The calculated energy profile for an interstitial Ca^{2+} ion migrating along [001] in the hexagonal channel. The points indicate the calculated defect energies along the migration path.

Alternative Ca^{2+} migration pathways

Defect calculations were also carried out on alternative migration pathways in the (001) plane. These pathways are illustrated in Figure 5.11. Figure 5.12 shows the energy profiles of these cation migration processes compared to the energy profile for the migration of Ca^{2+} along the hexagonal channel. Since neither of these alternative pathways yield activation energies which correlate with the observed dielectric response, migration of Ca^{2+} along the hexagonal channel would appear to be the only possible migration pathway within the yoshiokaite structure. Although the distinct Debye peak observed in the dielectric loss spectrum (Figure 5.6) can be attributed to this ion migration mechanism, the magnitude of the peak would suggest a Ca occupancy greater than that assigned to the hexagonal channel by Palmer at al. (2001) in their high resolution neutron powder diffraction study.

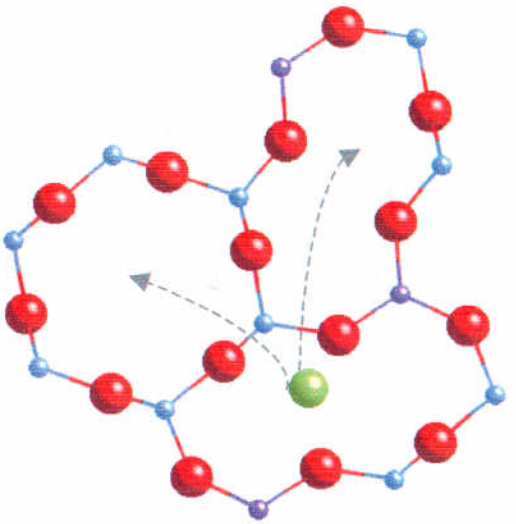

Figure 5.11 Alternative migration pathways for the Ca^{2+} ion in the (001) plane in yoshiokaite (viewed down [001]).

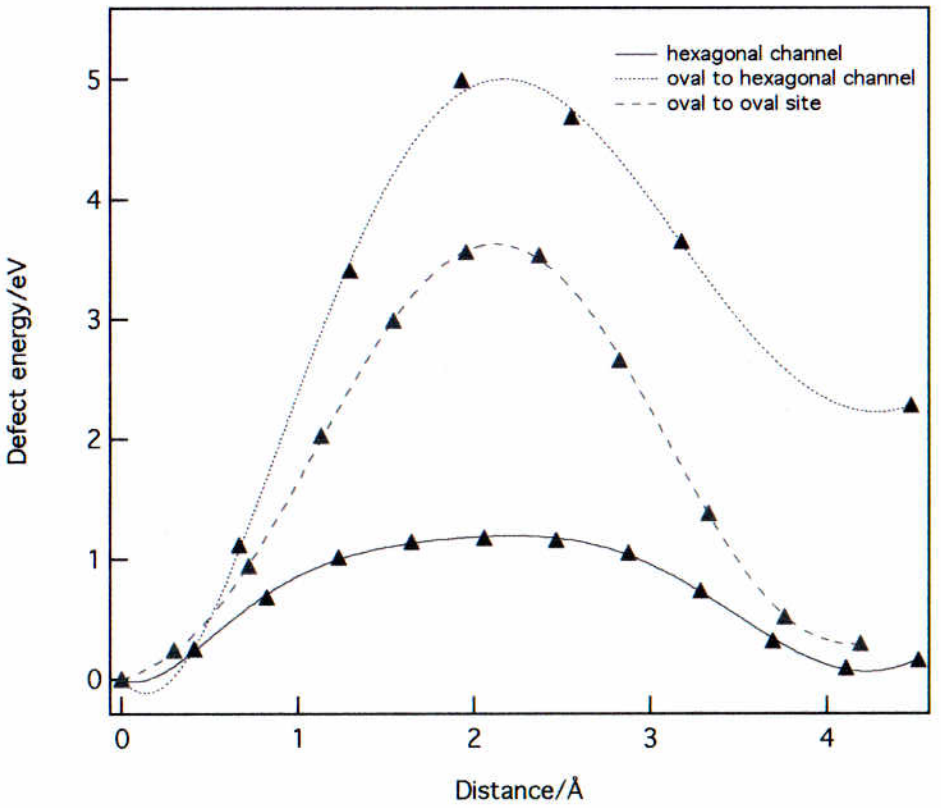

Figure 5.12 The calculated energy profiles for migration of a Ca^{2+} ion within the yoshiokaite structure.

The Ca^{2+} ions seem to be effectively 'trapped' in the oval sites by the distorted tetrahedral framework. It is possible that this framework distortion, and consequent lack of mobility of the Ca^{2+} ions, can be accounted for by the strong Ca-framework interaction. This strong interaction may also explain the observed low thermal expansion: although the framework is strong, it is not rigid as there are no forces holding it open (Taylor, 1972). It has been shown in previous studies of the sodalite group of minerals (Taylor, 1968) that inter-framework cations appear to have some effect on both room temperature and high temperature cell parameters.

Considering the microporous nature of the yoshiokaite framework, with its mainly unoccupied hexagonal channels, the apparent stability of the structure at high temperatures (Palmer et al., 2001) is unexpected. However, it would appear that the hexagonal channels may be held open by the largely immobilised Ca^{2+} ions in the smaller neighbouring oval sites. On close examination of the Ca^{2+} site environment, it is likely that the divalent nature of the inter-framework ions could be constraining the open structure, even at high temperatures. If this were the case, then ion diffusion from the oval sites would be prevented. Conversely, Ca^{2+} ion migration within the hexagonal channel is theoretically possible; this is supported by the reasonably good agreement between the experimentally determined activation energy and calculated energy barrier to ion migration for this process.

The findings presented here have demonstrated that a microporous material, such as yoshiokaite, could potentially provide a means of immobilising other divalent ions of similar size within the 'crumpled' structure. This partial collapse of a framework around the small divalent Ca^{2+} ion is also observed in anorthite and will be discussed in Chapter 7.

Chapter 6

β-eucryptite

Contents

6.1 Introduction

β-eucryptite, $LiAlSiO_4$, is a lithium-stuffed derivative of β-quartz of considerable technological importance. It has very low thermal expansion (Lichtenstein et al., 1998; Schulz, 1974) and can therefore be used in low thermal expansion ceramics. It also shows significant lithium mobility (Alpen et al., 1977; Nagel and Böhm, 1982), leading to superionic conductivity at high temperatures and it therefore has a potential use as a solid electrolyte in lithium based solid-state batteries (Julien and Stoynov, 2000). The importance of lithium mobility also extends to geological phases, as lithium and its isotopes are routinely used as diagnostic tracers of continental weathering, alteration of the oceanic crust (Chan et al., 1992) and fluid flow in geological systems (James et al., 1999).

Most of the literature to date has concentrated on the long range mobility of the lithium ions within the clearly defined channel structure of β-eucryptite (Böhm, 1975; Follstaedt and Richards, 1976; Guth and Heger, 1979). However, although other ion migration mechanisms have been postulated (Brinkman et al., 1981), the complexity of the structure makes it very difficult to interpret experimental data in terms of specific Li-mobility mechanisms. This investigation combines the results of dielectric spectroscopy and atomistic simulations in order to provide greater insight into mechanisms of lithium ion migration within the β-eucryptite structure. In addition, there is some evidence from transmission electron microscopy studies (Xu et al., 1999a) that β-eucryptite undergoes a phase transition via an incommensurate structure at high temperatures. It was envisaged that the dielectric spectroscopy would reveal further insights on this transformation.

6.2 Scientific background

6.2.1 The structure of β-quartz

As the structure of β-eucryptite is derived from β-quartz, it is appropriate to first consider the structure of β-quartz and examine the structural requirements necessary for the accommodation of interstitial cations. The β-quartz structure (spacegroup $P6_422$) comprises parallel 3- and 6-fold helices of SiO_4 tetrahedra, forming an interlinked framework with distorted 6- and 8-fold tetrahedral rings. The channel structure is defined by double helices along [001]. Distorted tetrahedral cavities are created between the two helices, sharing edges with one SiO_4 tetrahedron from each helix (Figure 6.1). The distance from the centre of the interstice to the centres of the surrounding oxygen atoms is ~2 Å; therefore, assuming the crystal radius of O to be 1.35 Å (Shannon, 1976), and an undistorted framework, this site is only just big enough to accommodate a Li^+ ion (crystal radius 0.90 Å). Also, as the distance between adjacent tetrahedral cavities is only 1.82 Å ($c/3$), they cannot be occupied simultaneously. The midpoint between two tetrahedral cavities is at the centre of a highly distorted octahedron, with two small O-O distances (~1.7 Å). The restricted nature of the framework cavities means that only significant Li substitution has been observed (Palmer, 1994), charge balance being achieved by replacing a proportion of the silicon with aluminium.

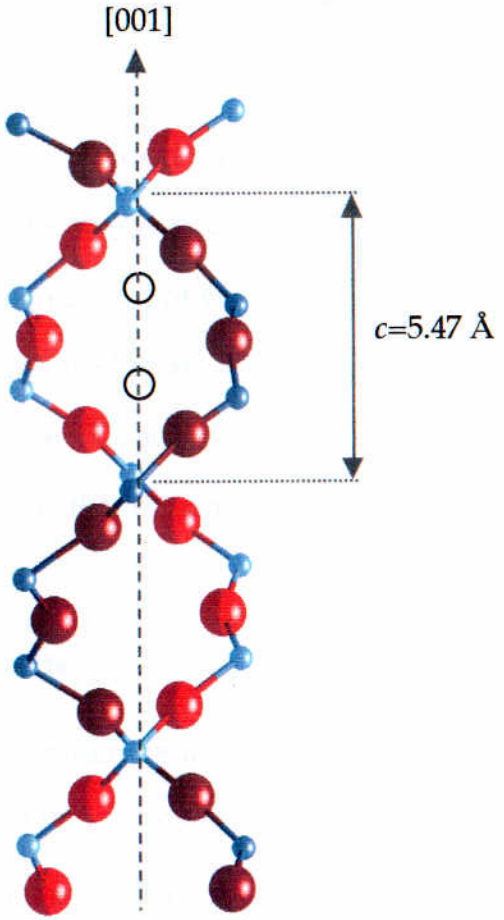

Figure 6.1 The double helix structure of β-quartz viewed down [100]. The distorted tetrahedral interstices (shown as open circles) occur between the helices at the same heights as the Si atoms and spaced at $c/3$ along [001].

6.2.2 Lithium-stuffed derivatives of β-quartz

The substitution of aluminium and lithium for silicon in the quartz structure produces a range of aluminosilicates, $Li_{1-x}Al_{1-x}Si_{1+x}O_4$ ($0 \leq x \leq 1$), which crystallise in either the α- or β-quartz structure. These compounds are of interest for their unique physical properties and for the insight they provide into general crystal chemical systematics (Palmer, 1994). The end member, β-eucryptite ($LiAlSiO_4$), has one dimensional superionic conductivity above ~ 500°C (Alpen et al., 1977; Nagel and Böhm, 1982). Intermediate compositions, which have near-zero thermal

expansion, are common components of high-temperature glass-ceramic products (Beall, 1994).

The $LiAlSiO_4$-SiO_2 system offers an ideal range of structures for systematically investigating the effects that the charge-coupled substitution $Li^+ + Al^{3+} \rightarrow Si^{4+}$ exerts on the structure, thermodynamics and physical properties. Many minerals in nature experience impurity-induced phase transitions in which dopants mimic the effects of changing temperature. The substitution of Li and Al for Si in quartz should therefore clarify the role that dopants play in the α-β phase transition in quartz (Xu et al., 2000).

6.2.3 Synthesis of β-eucryptite

β-eucryptite is prepared by high-temperature sintering using stoichiometric amounts of Li_2CO_3, Al_2O_3 and SiO_2 at 1373 K for 15 hours. The resulting products are then ground and annealed at 1573 K for 24 hours (Xu et al., 1999b). This method is only suitable for preparation of compositions between $LiAlSiO_4$ and $Li_{0.8}Al_{0.8}Si_{1.2}O_4$ as they are stable phases between 1273 K and 1673 K. Compositions of $Li_{1-x}Al_{1-x}Si_{1+x}O_4$ for values of $x > 0.2$ yield a stuffed keatite and an α-cristobalite phase using this method. Phases of these compositions have to be synthesised by either high pressure, high temperature processing or glass annealing (Xu et al., 1999b).

6.2.4 Structure of β-eucryptite

The structure of β-eucryptite was first investigated by Winkler (1948) who showed it to be based on that of β-quartz with space group $P6_422$. He found that tetrahedral Al and Si atoms alternate within the layers normal to *c*, thereby causing a doubling of the *c*-axis relative to that of β-quartz. The aluminium avoidance rule

(Loewenstein, 1954) is satisfied because each Si is surrounded by four Al tetrahedra and vice-versa. Winkler also suggested that the Li^+ ions are coplanar with the Al atoms and are tetrahedrally coordinated by oxygen. Buerger (1948) observed that the *a*-axis is doubled relative to that of the quartz structure and he later classed β–eucryptite as a stuffed derivative of β-quartz (Buerger, 1954). More recent structure refinements (Guth and Heger, 1979; Pillars and Peacor, 1973; Tscherry et al., 1972a; Tscherry et al., 1972b) confirm that at low temperatures the unit cell is doubled along x, y and z relative to the β-quartz structure, and that the Al and Si tetrahedra are ordered on alternate layers parallel to z.

The Li^+ ions are also ordered (Tscherry et al., 1972b), but not as Winkler had suggested. There are four 6-fold channels in the unit cell, each containing Li^+ ions. In only one channel do they reside within layers of Al atoms (Li1); the remaining three symmetrically equivalent channels contain Li2 and Li3 sites and reside within layers of SiO_4 tetrahedra (Figure 6.2). Along each channel axis there is an alternation of occupied and vacant Li tetrahedral sites with adjacent (Al,Si)- and Li-tetrahedra sharing edges (Figure 6.3). These occupied and vacant Li tetrahedral sites are reversed in adjacent channels parallel to *a* or *b*. This gives rise to the possibility of anti-phase domains (APDs), related by an $a/2$ translation vector (Muller and Schulz, 1976). These *a*-APDs (to distinguish then from APDs arising from Al/Si ordering), have been imaged by Xu et al. (1999a) using dark field TEM. They showed that the *a*-antiphase domain boundaries (*a*-APBs) show a strong preferred orientation along the *c*-axis and are generated by the loss of one of the channels down [001]. The domain widths can vary from 10 to 250 nm.

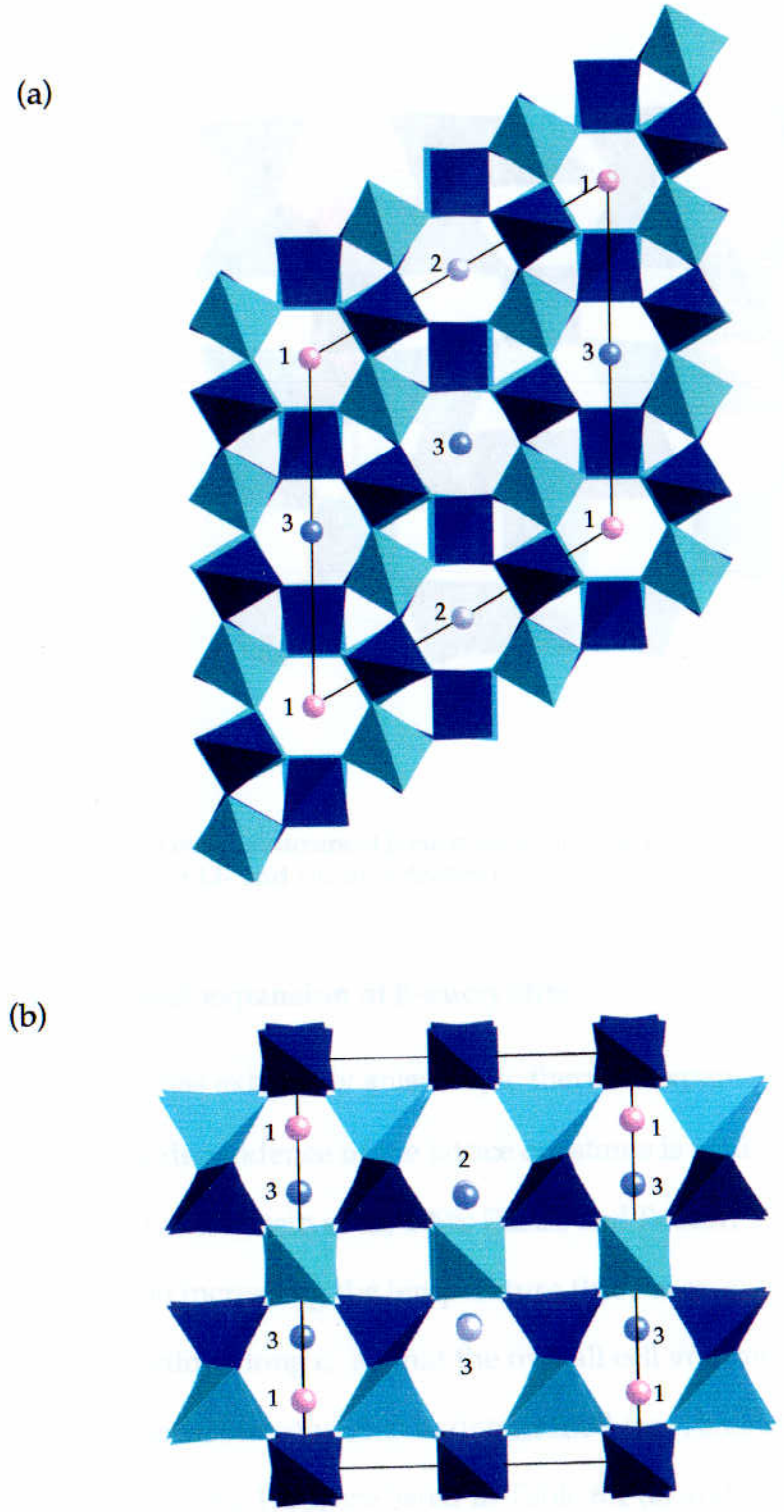

Figure 6.2 Projections of the low temperature structure of β-eucryptite showing the three distinct Li sites (1-3); (a) view down [001]; (b) view down [100]. Structural data from Pillars and Peacor (1973).

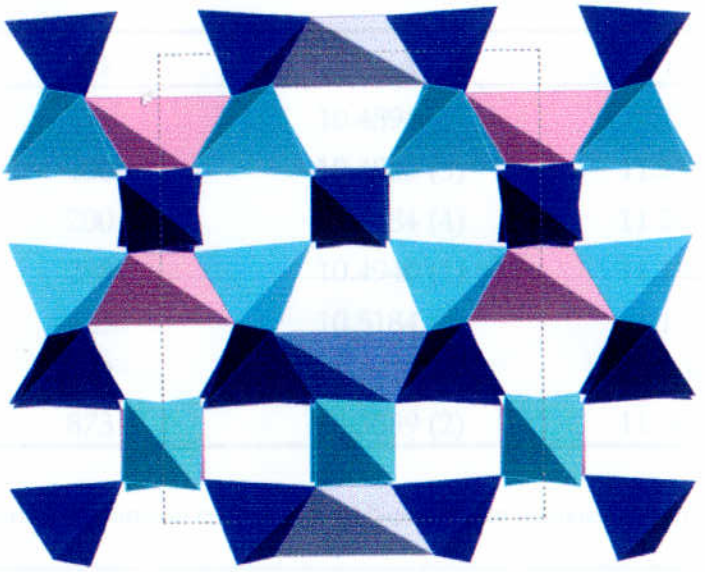

Figure 6.3 Part of the structure of β-eucryptite (view down [010]) showing the adjacent edge sharing distorted Li- and (Al,Si)-tetrahedra.

6.2.5 Thermal expansion of β-eucryptite

β-eucryptite has extremely anisotropic thermal-expansion coefficients. The temperature dependence of the lattice constants is well documented (Gillery and Bush, 1959; Lichtenstein et al., 1998; Pillars and Peacor, 1973; Schulz, 1974; Xu et al., 1999c) and on increasing the temperature there is an expansion in the (001) plane, but a contraction along *c*, so that the overall cell volume thermal expansion is negative. The lattice constants as determined from a neutron diffraction study (Lichtenstein et al., 1998) are listed in Table 6.1 (a) and the calculated thermal expansion coefficients are listed in Table 6.1 (b).

Table 6.1 (a) Lattice constants of β-eucryptite obtained from neutron diffraction data (Lichtenstein et al., 1998).

T/K	*a*/Å	*c*/Å
20	10.4894 (3)	11.2227 (4)
100	10.4883 (3)	11.2167 (4)
200	10.4884 (4)	11.2032 (5)
298	10.4940 (1)	11.1921 (1)
523	10.5184 (3)	11.1544 (4)
748	10.5417 (4)	11.1081 (4)
873	10.5539 (2)	11.0821 (2)

Table 6.1 (b) Thermal expansion coefficients of β-eucryptite measured from 20 K to 873 K.

Parameter	Thermal expansion coefficient/ Å/1000 K
a	0.076
c	-0.165

Glass ceramics that comprise β-eucryptite and other isostructural compounds in the LAS (Li_2O-Al_2O_3-SiO_2) system can therefore achieve very low bulk thermal expansion with the consequent benefits of exceptional thermal stability and thermal shock resistance. LAS glass-ceramic products have been used not only as domestic cookware, but within high-precision machines such as jet engines (Beall, 1994).

Several models have been used to explain the anisotropic thermal behaviour of β–eucryptite (Gillery and Bush, 1959; Palmer, 1994; Schulz, 1974) . The rationalisation put forward by Palmer is explained below. He reasoned that high temperatures would induce expansion within the (001) plane in order to reduce the repulsion between channel Li^+ ions and framework Al/Si cations. However, since adjacent (Al,Si)- and Li-tetrahedra share edges, it was reasoned that the shared O-O

edges must shorten along *c* to maintain constant cation-oxygen bond distances (Figure 6.4).

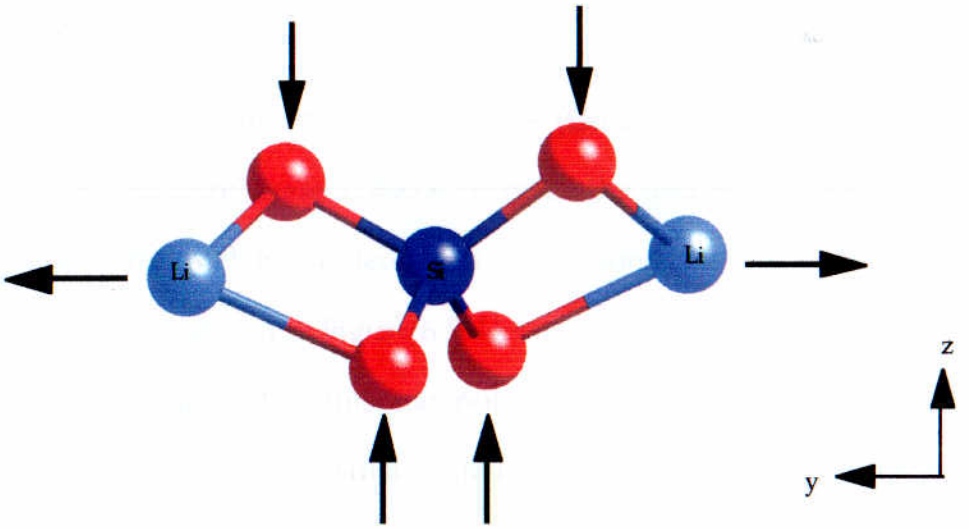

Figure 6.4 Part of the β-eucryptite structure in schematic form (view down [100]) showing how expansion in the (001) plane reduces the repulsive force between Li and Al/Si, and contraction along [001] maintains the metal-oxygen bond distances.

6.2.6 Phase transitions in β-eucryptite

The high-temperature phase transition of β-eucryptite is well documented (Guth and Heger, 1979; Pillars and Peacor, 1973; Schulz and Tscherry, 1972b; Tscherry and Laves, 1970). High temperature X-ray and neutron diffraction experiments showed that *a*-superlattice reflections became weaker and more diffuse with increasing temperature and disappear at some temperature between 673 K and 755 K. The large range of reported critical temperatures (T_c) is due to different synthesis conditions of the samples and to variations in the resolution of the analytical techniques used. The *a*-reflections are generally very weak and hence difficult to detect; in contrast, the *c* reflections remain sharp at all temperatures. This decrease in intensity of the *a*-reflections suggests a progressive disordering of the Li

distribution with temperature. The room temperature ordering of the Li^+ ions is destroyed at temperatures above 673 K and probably replaced by a statistical distribution of the Li^+ ions over all sites, resulting in a smaller (*a*/2) unit cell (Pillars and Peacor, 1973; Schulz and Tscherry, 1972a).

Single crystal neutron diffraction experiments (Guth and Heger, 1979) carried out on the high temperature phase at 800 K revealed the unit cell to be equivalent to that of β-quartz, but with a doubled *c* axis, the Li^+ ions being disordered over two sites, Li1 and Li2, as shown in Figure 6.5. However, there is evidence from high temperature TEM studies that this may not be the case, and at high temperatures the Li^+ ions may be dynamically distributed over all possible sites within the channels (Xu et al., 1999a).

6.2.7 Incommensurate phase of β-eucryptite

Neutron scattering (Press et al., 1980) and X-ray diffraction studies (Böhm, 1983) have revealed an incommensurate structure that bridges the boundary between the low-temperature, ordered phase and the high-temperature, disordered phase, occurring over a temperature range of 60 K (703-763 K). Although it is generally agreed that the transition which occurs in β-eucryptite is due to Li^+ positional disordering, the exact nature of the phase transition and the characteristics of the incommensurate phase remain unclear. Schulz and Tscherry (1972a; 1972b) argue that structural elements in the low temperature phase are α-quartz-like, such that the Al/Si framework undergoes a displacive transition accompanying the change in Li order-disorder at ~673 K. It has also been suggested that the transition in β-eucryptite involves a distortion of the Al/Si framework (Böhm, 1983; Press et al., 1980) by analogy with the incommensurate phase that occurs over a temperature range of 1.3 K between α- and β-quartz (Heaney and Veblen, 1991).

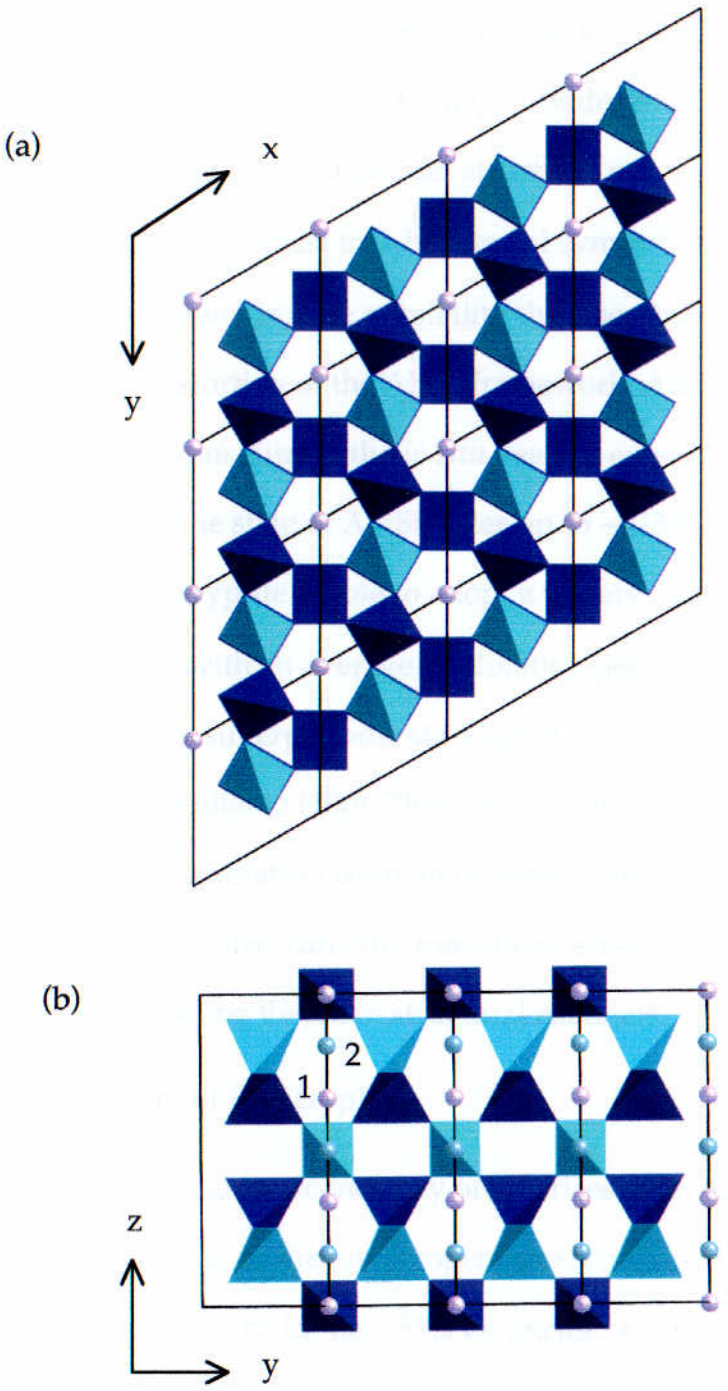

Figure 6.5 Projections of the high temperature structure of β-eucryptite showing the Li ions disordered over two sites Li1 and Li2; (a) view down [001] ; (b) view down [100]. Structural data from Guth and Heger (1979).

Direct observation by *in situ* transmission electron microscopy (TEM) at the transition was used by Xu et al. (1999a) in order to provide some critical insights into the reaction mechanism. They found no evidence from their TEM study for the merohedral twinning that accompanies structural collapse at the β- to α-quartz transition. This would suggest true hexagonal symmetry for the β-eucryptite framework, thus eliminating the possibility that the phase transition could arise from a displacive distortion of the Al/Si framework. Additionally, the constant presence of *c*-reflections during the *in situ* heating experiments indicated that there were no changes in the state of Al/Si order up to ~923 K. It was therefore concluded that β-eucryptite is able to adopt a variety of modulated structures parallel to the *a*-axis with an average modulation period of 6.5 *a*. These modulated structures arise from superperiodic stacking of two structural units with different Li configurations parallel to (100). They can be transformed by heating or prolonged electron irradiation from an ordered structure, via an incommensurate phase, to a disordered structure, the transitions arising from positional order-disorder of Li^+ ions along the main structural channels.

6.2.8 Conductivity of β-eucryptite

In solid electrolytes high ionic mobility often arises from the availability of several unoccupied lattice sites. In the low temperature structure of β-eucryptite within each channel there are 50% Li^+ and 50% vacancies. Above T_c, at around 673 K, the Li^+ ions become disordered over the vacant sites, the *a* superlattice reflections become weak and diffuse and the intensity distribution suggests strong one dimensional correlation between Li^+ ions in the structural channels. Studies have shown that at temperatures above T_c there is very high Li^+ ion conductivity parallel

to [001] in β–eucryptite but virtually none in the (001) plane (Alpen et al., 1977). β-eucryptite can thus be considered to be a one-dimensional superionic conductor.

The Li diffusion is thermally activated and is thought to be a cooperative, "single file" process between occupied and vacant sites (Li1 and Li2) parallel to [001]. Alpen (1977) measured the activation energy for this process from the temperature dependence of the ionic conductivity as 0.74 eV. This is in good agreement with NMR relaxation measurements made by Follstaedt and Richards (1976) who measured an activation energy of 0.79 eV above T_c and presented a model interpreting their results in terms of highly correlated one-dimensional Li^+ motion. Böhm (1975) determined activation energies of 0.62 eV and 0.83 eV from dielectric measurements made on β-eucryptite between room temperature and 673 K. These measurements were made on the low-temperature, ordered structure and the activation energies were determined from the dielectric loss tangent. Conductivity studies have also been carried out by Nagel and Böhm (1982) on four single crystals of composition $Li_{1-x}\square_{1+x}Al_{1-x}Si_{1+x}O_4$ with $x = 0$ (β-eucryptite) to $x = 0.22$. The results of this study suggested that the activation energy for the ionic motion, (determined to be 0.79 ± 0.02 eV), is independent of the crystallographic direction and of the chemical composition. In addition to this they observed that, depending on the synthesis conditions, some samples were found to have a modulated structure along the *a*-axis. However, although the structural state of the crystal, (i.e. whether it was modulated along the *a*-axis or not), did not affect the activation energy, the conductivity of a crystal with a modulated structure was found to be considerably less anisotropic ($\sigma_c/\sigma_a \approx 10$) than that of one which did not have a modulated structure ($\sigma_c/\sigma_a \approx 10^2 - 10^3$). The conductivity parallel to the *c* axis was

approximately the same for the two structural states, but it was much higher perpendicular to the *c* axis in the modulated structure.

6.3 Experimental

A single crystal of β-eucryptite, which had been synthesised by H. Böhm, was provided by Peter Heaney and Hongwu Xu. The sample, which had been previously characterised by Xu et al (1999a), was cut into two thin sections, one with its faces perpendicular to [001] and the other with its faces parallel to [001].

6.3.1 Sample characterisation

Electron microprobe analysis

The composition of the sample was determined using electron microprobe analysis. This was carried out using a Cameca SX100 probe at 20 kV, 20nA and a 10μm spot diameter. It is not possible to analyse for the lithium content using microprobe analysis, so the lithium content was calculated from the aluminium, silicon and oxygen ratios. The approximate composition of the crystal was calculated to be: $Li_{0.81}Al_{0.96}Si_{1.07}O_4$. Therefore, although the sample was not a stoichiometric end member, the structure of the framework would not be significantly different (Xu et al., 2000), but with approximately 20% of the lithium sites vacant.

6.3.2 Dielectric measurements

Dielectric spectroscopy experiments were performed on the Böhm sample from room temperature to 1100 K. Measurements were made on single crystals in two different orientations:

(i) crystal faces perpendicular to [001], i.e. electric field parallel to [001];

(ii) crystal faces parallel to [001], i.e. electric field perpendicular to [001].

Capacitance and conductance measurements were made on both crystals at room temperature and then at regular intervals up to approximately 1100 K. From these measurements the dielectric constant, conductivity, and the dielectric loss were calculated at each frequency.

6.4 Atomistic computer modelling

The interatomic potentials and shell model parameters, which are listed in Table 6.2, were taken from previous simulation studies (Freeman and Catlow, 1990; Jackson and Catlow, 1988).

Before carrying out defect and migration calculations, in order to test the validity of the potentials used for the calculations, the unit cell dimensions and atomic coordinates, taken from a structure refinement of a phase of composition $Li_{0.8}Al_{0.8}Si_{1.2}O_4$ (Xu et al., 2000), were equilibrated under constant pressure conditions. The calculated values for the lattice parameters and selected bond-distances and their comparison with experimental values are listed in Table 6.3. The calculated lattice parameters vary by an average of 1.4 % from the experimentally determined values, but the agreement is reasonably good for such a complex system.

Table 6.2 Interatomic potentials used for modelling the β-eucryptite structure

(i) Two-body Buckingham

Interaction[a]	A/eV	ρ/Å	C/eV Å^{-6}
Li^+ ..... O^{2-}	292.3	0.3472	0.0
Si^{4+} ..... O^{2-}	1283.907	0.32052	10.66158
Al^{3+} ..... O^{2-}	1460.3	0.29912	0.0
O^{2-} ..... O^{2-}	22764.3	0.1490	27.879

(ii) Shell model[b]

Species	Y/e	k/eV Å^{-2}
O^{2-}	-2.86902	74.92
Li^+	1.0	99999

(iii) Three-body

Interaction	Force constant / eV rad^{-1}
O - Si - O	2.0972
O - Al - O	2.0972

[a] Potential cut-off = 10 Å
[b] Y and k refer to the shell charge and harmonic force constant respectively

Table 6.3 Calculated and experimental structural parameters for the β-eucryptite structure

(i) Unit cell parameters

Parameter	Experimental	Calculated	Difference/%
a	10.4949(2) Å	10.5881 Å	0.89
b	10.4949(2) Å	10.6787 Å	1.75
c	10.9650(3) Å	10.7928 Å	-1.57
α	90.00°	90.00°	0.00
β	90.00°	90.00°	0.00
γ	120.00°	119.98°	0.01

Table 6.3 (continued)

(ii) Selected bond distances

Bond distance	Experimental/Å	Calculated/Å
Li3 - O2	2.065	2.066
Li3 - O3	3.393	3.408
Li3 - O4	1.979	2.038
Al2 - O3	1.781	1.701

6.5 Results and discussion

6.5.1 Dielectric spectroscopy

Figure 6.6 shows the behaviour of ε' and σ with temperature and frequency for the two crystals in different orientations. With the electric field parallel to [001], ε' was approximately twice that of ε' with the electric field perpendicular to [001] for all frequencies at room temperature (Table 6.4).

Table 6.4 Room temperature values of ε' for β-eucryptite with the electric field parallel to [001] and perpendicular to [001] at selected frequencies.

Electric field orientation	ε'			
	1 kHz	10 kHz	100 kHz	1 MHz
Parallel to [001]	33.6	26.7	23.1	19.9
Perpendicular to [001]	13.2	11.9	11.2	10.8

Above ~700 K there is a dramatic increase in ε' (the greatest changes being at low frequencies). The differences in conductivity for the two orientations of the crystal are much more pronounced. At room temperature the conductivity parallel to the *c*

axis is between 4 and 8 times higher than the conductivity in the perpendicular direction, depending on the frequency (Table 6.5).

Table 6.5 Room temperature values of σ for β-eucryptite with the electric field parallel to [001] and perpendicular to [001] at selected frequencies

Electric field orientation	σ/Sm^{-1}			
	1 kHz	10 kHz	100 kHz	1 MHz
Parallel to [001]	4.29×10^{-7}	1.76×10^{-6}	1.31×10^{-5}	1.14×10^{-4}
Perpendicular to [001]	8.53×10^{-8}	3.84×10^{-7}	2.08×10^{-6}	1.56×10^{-5}

Above ~750 K there is a significant increase in the conductivity at high frequencies, while the low frequency (i.e. approaching d.c.) conductivity remains relatively low at all temperatures. The temperature dependence of ε' and tan δ as a function of frequency, for both orientations at high temperatures, is shown in Figures 6.7 and 6.8.

The dielectric loss spectra are shown as surface plots in Figures 6.9 (a) and (b). With the crystal in both orientations there is a small peak in the dielectric loss at around 400 K, and a much more pronounced loss above 800 K (peaks I*c* and I*ab*). However, there is an additional loss peak (II*ab*) between 550 K and 700 K with the *c*-axis perpendicular to the field. The detail of the temperature dependence of tan δ as a function of frequency within this temperature range is shown in Figure 6.10.

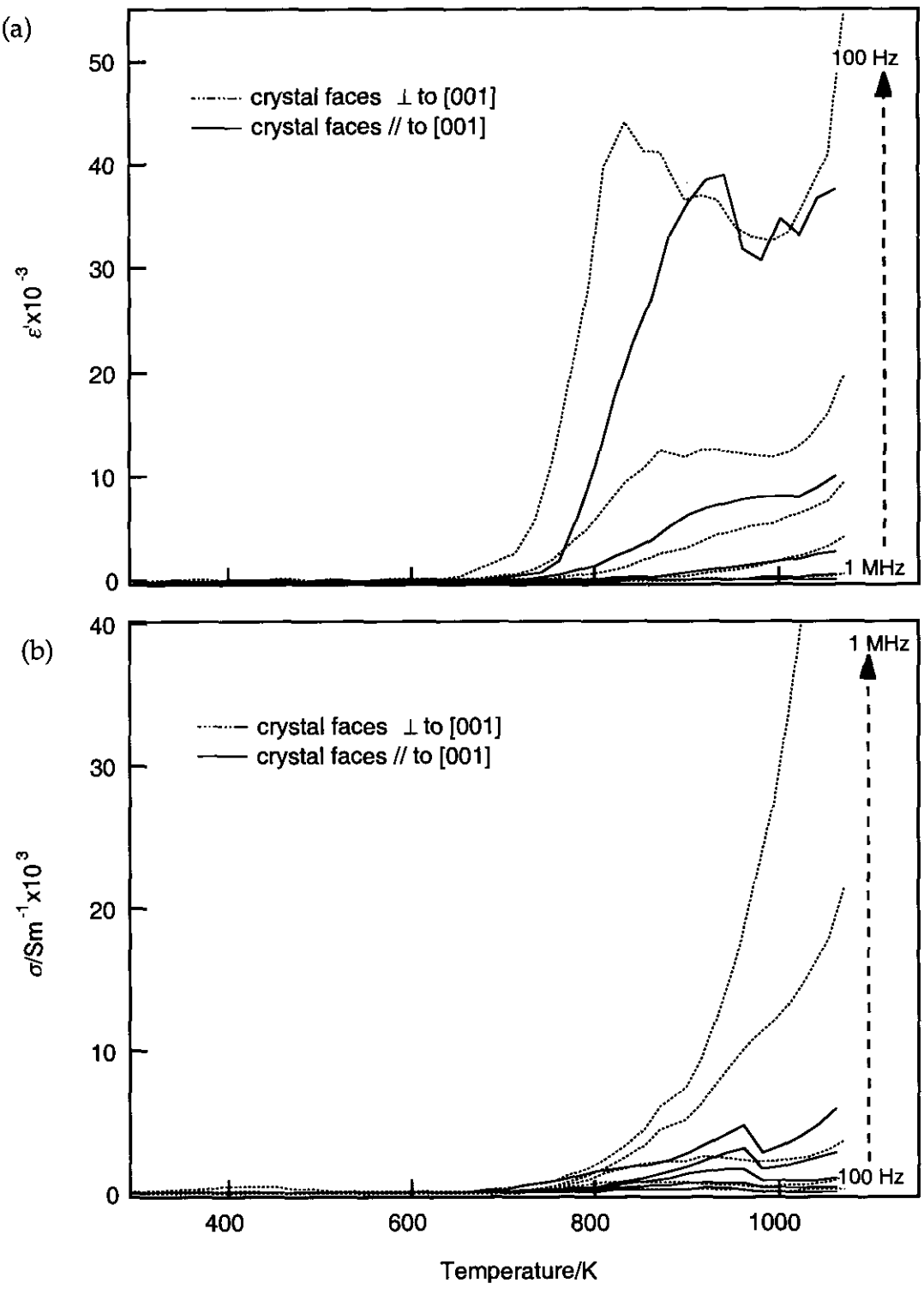

Figure 6.6 Temperature dependence of (a) dielectric constant; (b) conductivity at selected frequencies.

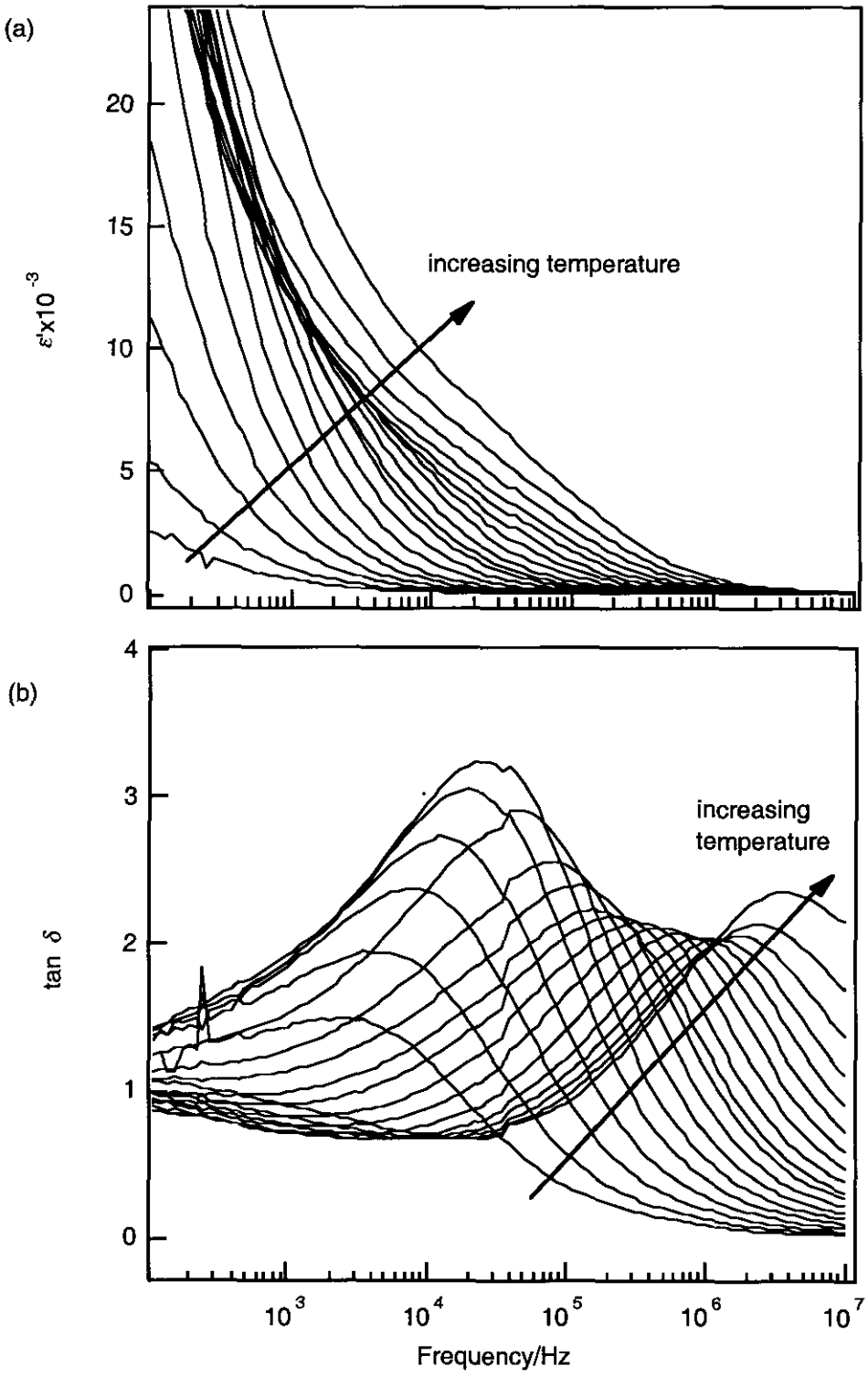

Figure 6.7 Temperature and frequency dependence of (a) dielectric constant; (b) dielectric loss between 783 K and 1043 K with the electric field parallel to the *c*-axis.

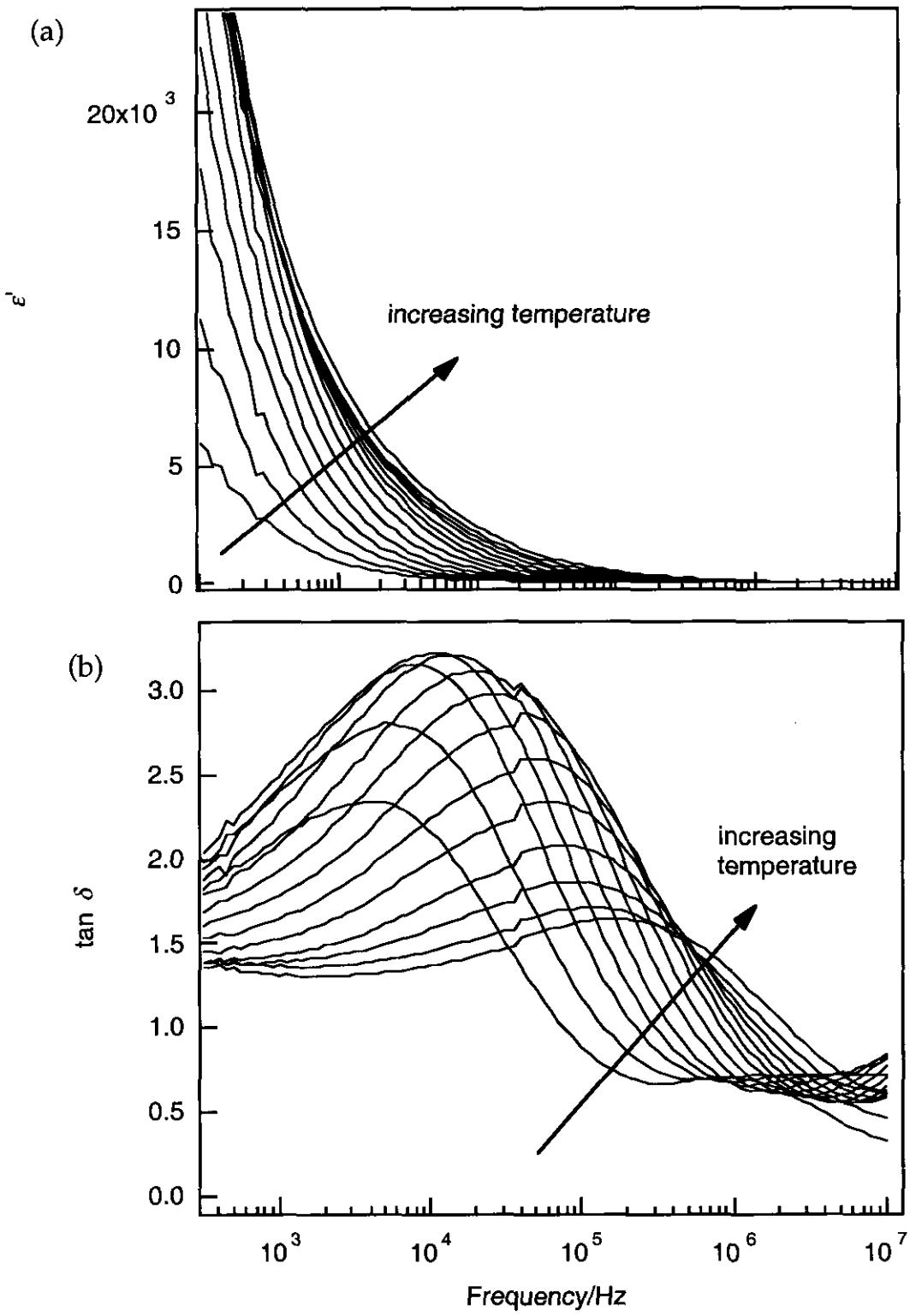

Figure 6.8 Temperature and frequency dependence of (a) dielectric constant; (b) dielectric loss between 783 K and 1043 K with the electric field perpendicular to the *c*-axis.

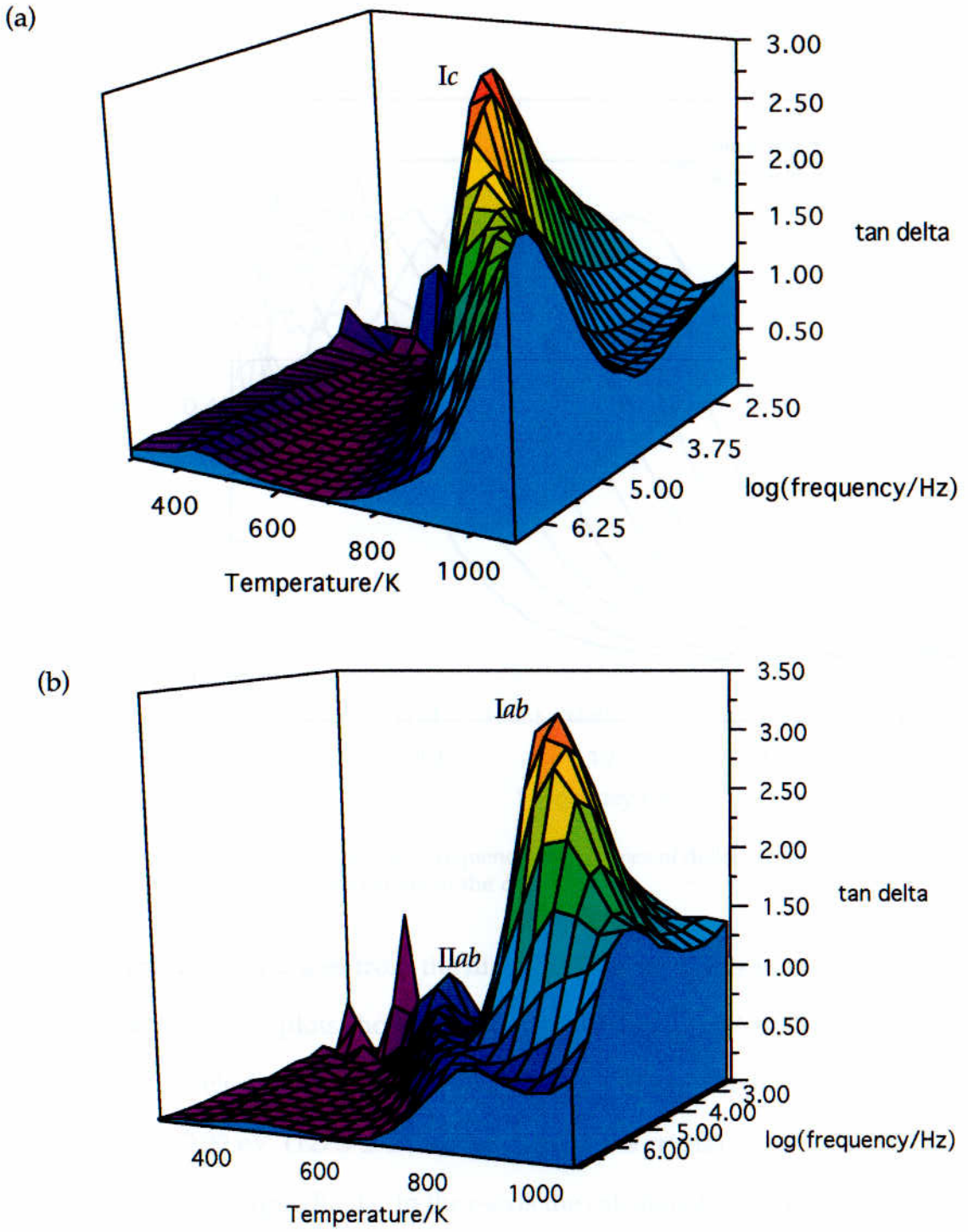

Figure 6.9 Surface plots showing the dielectric loss, tan δ, as a function of frequency and temperature for (a) the electric field parallel to the *c*-axis; (b) the electric field perpendicular to the *c*-axis.

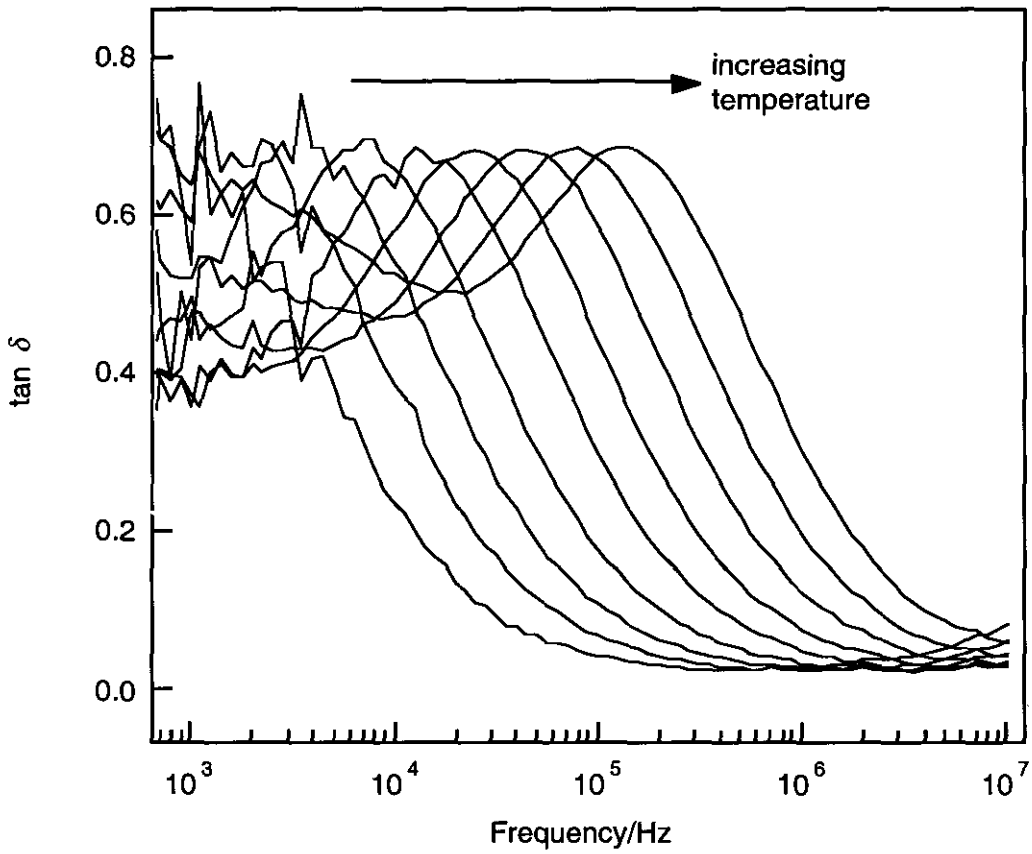

Figure 6.10 Temperature and frequency dependence of dielectric loss between 540 K and 700 K with the electric field perpendicular to the *c*-axis.

Activation energies from the high temperature measurements were calculated from the Arrhenius plots shown in Figures 6.11 and 6.12. With the crystal orientated such that the electric field was parallel to the *c*-axis the calculated activation energy was 1.33 ± 0.02 eV (127.9 ± 1.5 kJ mol^{-1}); with the crystal orientated such that the electric field was perpendicular to the *c*-axis the calculated activation energy was 1.06 ± 0.02 eV (102.6 ± 2.3 kJ mol^{-1}). These activation energies were calculated from the dielectric loss peaks I*c* and I*ab*, respectively, shown in Figure 6.9.

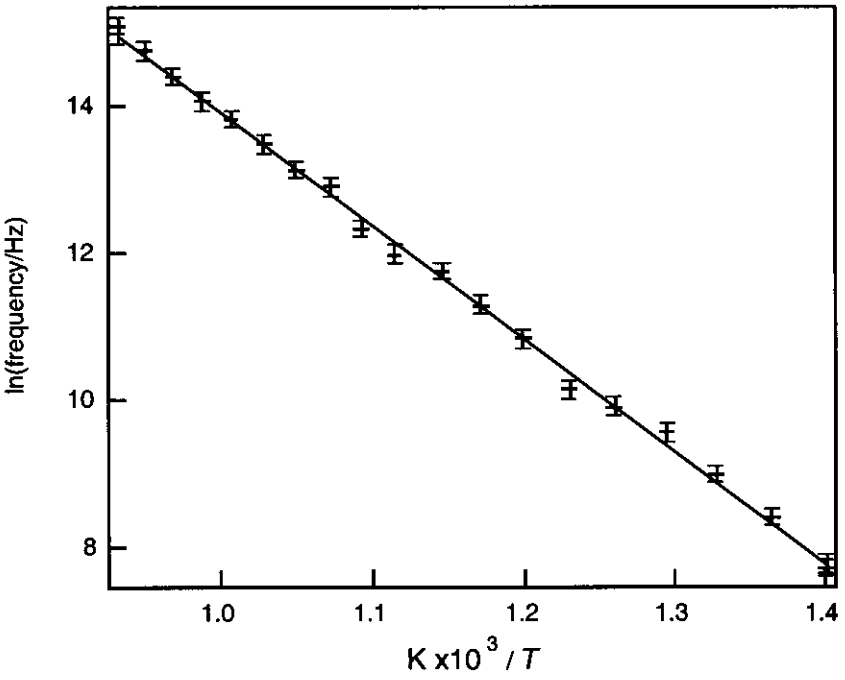

Figure 6.11 Arrhenius plot showing the temperature dependence of the maxima in the dielectric loss from 715-1073 K with the electric field parallel to the *c*-axis. The gradient of the line indicates an activation energy of 1.33 ± 0.02 eV. The error bars represent the uncertainty in determining the peak position at each temperature.

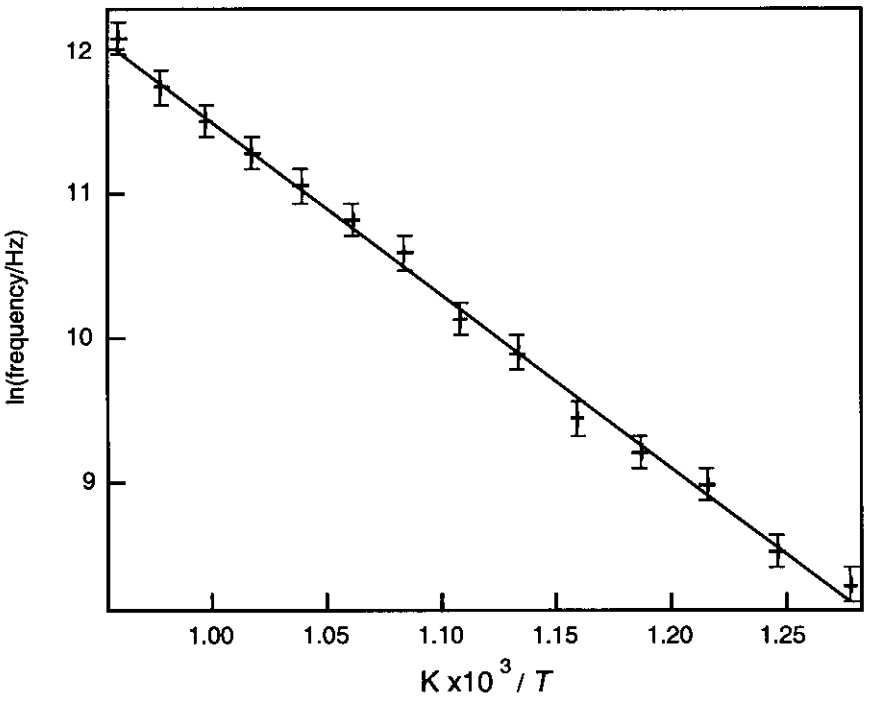

Figure 6.12 Arrhenius plot showing the temperature dependence of the maxima in the dielectric loss from 783 -1043 K with the electric field parallel to the *c*-axis. The gradient of the line indicates an activation energy of 1.06 ± 0.02 eV. The error bars represent the uncertainty in determining the peak position at each temperature.

The activation energy calculated from the temperature dependence of the frequency of the maximum absorption up to 700 K with the crystal orientated such that the field was perpendicular to the *c*–axis, i.e. peak *IIab* in Figure 6.9(b), was 1.08 ± 0.01 eV (103.8 ± 1.0 kJ mol^{-1}). The Arrhenius plot for this low temperature absorption is shown in Figure 6.13.

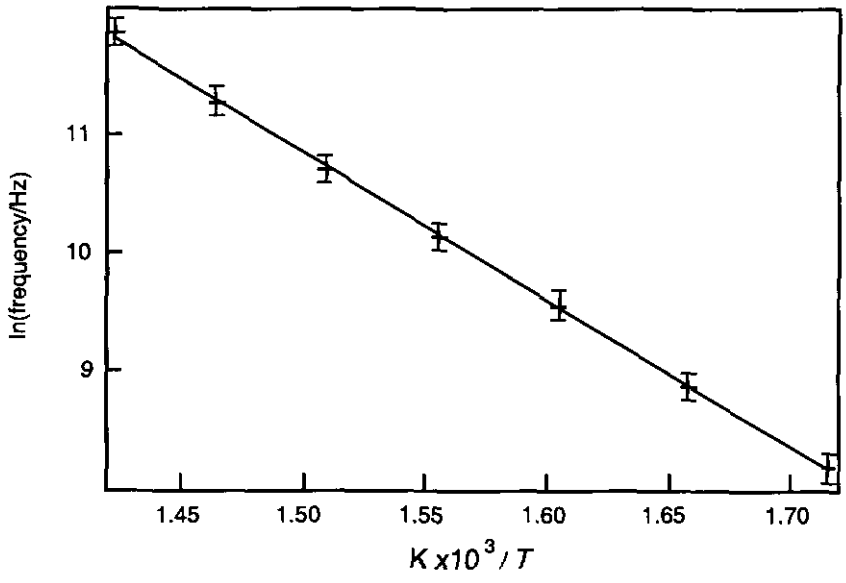

Figure 6.13 Arrhenius plot showing the temperature dependence of the maxima in the dielectric loss from 540-700 K with the electric field perpendicular to the *c*-axis. The gradient of the line indicates an activation energy of 1.08 ± 0.01 eV. The error bars represent the uncertainty in determining the peak position at each temperature.

A second set of measurements, made between 775 K and 1065 K, on the crystal aligned with its *c*–axis perpendicular to the electric field, gave an activation energy of 1.35 ± 0.04 eV (130.6 ± 3.9 $kJmol^{-1}$). This is very close to the value obtained when the orientation of the crystal was such that the *c*-axis was parallel to the field.

It can be seen in Figure 6.9(b) that the relative amplitudes of the low-temperature and high-temperature loss peaks are significantly different. In addition to this, the high temperature dielectric loss does not show a consistent (Debye type) behaviour, as the amplitude itself shows a marked temperature dependence, increasing to a

maximum at around a frequency of 10 kHz. This effect shows a degree of criticality with the possible implication of a phase transition occurring over this temperature range.

The height of a Debye peak is directly related to the number of oscillators involved in the relaxation process. These results would therefore suggest that between 700 K and 800 K a significantly greater number of oscillators are contributing to the observed relaxation process. It has been reported that between 700 K and 760 K the Li^+ ions start hopping from occupied to unoccupied sites within the channels along [001] (Schulz, 1974; Schulz and Tscherry, 1972b). There is also evidence that the Li^+ ions are able to migrate throughout the (Al, Si)O_4 lattice framework (Alpen et al., 1977), therefore the probability of site-hopping at these elevated temperatures would be expected to increase. Only a very weak low temperature relaxation is observed when the crystal is oriented such that the *c*-axis is parallel to the field. It is possible therefore that the observed low temperature response is at a minimum in this orientation.

6.5.2 Phase transition in β-eucryptite

As already mentioned, there are anomalies in the dielectric spectra of β–eucryptite, as in addition to its expected high conductivity and a pronounced dielectric loss peak at high temperatures, there is an unexpected increase in the amplitude of the dielectric loss at high temperatures. Above ~650 K there is an increase in the amplitude of the tan δ peak to a maximum occurring at 813 K. This is followed by a sharp decrease in the amplitude until 950 K, after which there is no further change. Figure 6.14 shows how the dielectric loss, measured at a frequency of 10 kHz, changes with temperature for both orientations. It has been suggested by Xu et al. (1999a) that an incommensurate phase with a modulation of 6.5 *a* exists within the

temperature range for the observed changes in tan δ. They were unable to identify the exact transition temperature in their *in situ* heating experiments, other than the fact that it occurs somewhere between 710 K and 923 K. They came to the conclusion that the reversible transition behaviour observed was due to positional disordering of Li along the main structural channels. As the measured dielectric loss is proportional to the total dipole moment of a system, if the transition behaviour is due to positional disordering of Li^+ ions, the observed changes in tan δ could be related to these movements of Li^+ ions within the main structural channels.

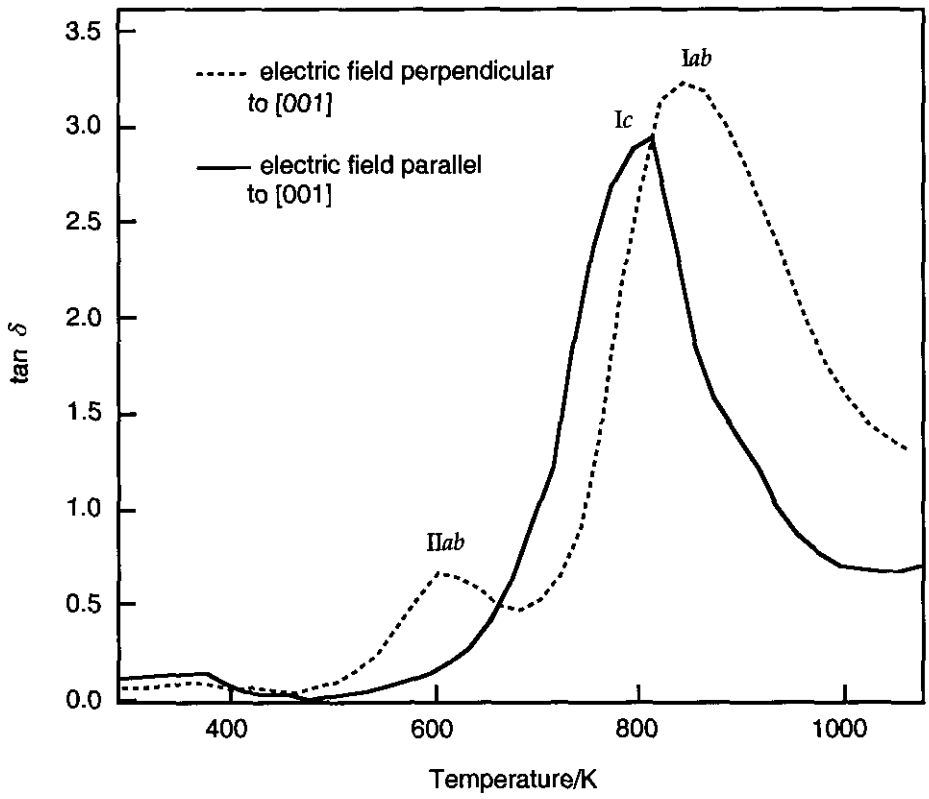

Figure 6.14 Temperature dependence of dielectric loss measured at a frequency of 10 kHz. The peaks Ic, I*ab* and II*ab* correspond to the absorption peaks shown in Figure 6.9.

Earlier conductivity studies of β-eucryptite (Nagel and Böhm, 1982) described a similar modulated phase which exhibited considerably higher conductivity perpendicular to the *c*-axis. These data are in agreement with the results presented

in section 6.5.1 (Figure 6.6) where the conductivity perpendicular to the *c*-axis started to increase at around 700 K and then decreased after 963 K. The activation energy (0.79 eV), as determined by Nagel and Böhm from the electrolyte resistance, was lower than the values determined in this study. However, their measurements, which were carried out on a range of compositions ($Li_{1-x}\square_{1+x}Al_{1-x}Si_{1+x}O_4$ with $0 \leq x \leq 0.22$), suggested that the activation energy for the ionic motion was independent of the crystal orientation, the chemical composition and the structural state of the crystal. They concluded that they were observing a cooperative type of Li-motion rather than a discrete ion-hopping mechanism. It is therefore not appropriate to make a direct comparison of their measurements of activation energy with those determined in this study from the loss peaks in the dielectric spectrum.

6.5.3 Ion migration mechanisms and energetics

(i) Migration of Li along [001]

Movement of lithium ions within the β-eucryptite structure might be expected to occur primarily along [001] within the hexagonal channels. There is evidence from conductivity measurements which suggests that migration of Li^+ ions between occupied and vacant sites within these channels occurs with an activation energy of 0.74 eV (Alpen et al., 1977). This is supported by measurements of relaxation times using NMR which give an activation energy of 0.79 eV (Follstaedt and Richards, 1976). In a neutron diffraction study, Lichtenstein et al. (1998) investigated the energy barriers for diffusion of Li in the *c* direction. They concluded that the energy barrier for correlated Li motion (~0.3 eV per Li^+ ion) is much less than the energy required for uncorrelated hopping (~0.8 eV). This is in quite good agreement with the findings from a single crystal ^7Li and ^6Li NMR study on the

dimensionality effects of Li diffusion in β-eucryptite (Brinkman et al., 1981). This study revealed two diffusion processes: one-dimensional diffusion along the channels parallel to [001], with an activation energy of 0.1 eV (this being the dominant process up to 400 K) and hopping of Li^+ ions between different channels with an activation energy of 0.6 eV (the dominant process from 400 K up to 760 K).

It must be emphasised that the type of defect calculations used in this study are not suitable for modelling a correlated movement of ions. Migration of Li^+ along the [001] channels in β-eucryptite is highly likely, and, if the channel is fully occupied, it would involve such a correlated movement of ions. Molecular dynamics simulations would be useful to probe such a mechanism and this could be a subject of future investigation. However, if there are vacancies in the channel, then a discrete ion hopping mechanism is possible and defect calculations can be used to model such ion migration mechanisms.

A single vacancy was created in one of the [001] structural channels of the β–eucryptite structure and a neighbouring Li^+ ion moved along the channel as shown in Figure 6.15(a). Figure 6.15(b) shows the relative positions of the Li^+ ions, the vacancy and the surrounding O, Si and Al atoms in the channel. The migration energy of the Li^+ ion was determined by calculating the defect energy at different points along the [001] channel, allowing full relaxation of the lattice at each position. The calculated energy profile for this migration pathway is shown in Figure 6.16. The maximum energy barrier for this process is calculated to be 0.15 eV.

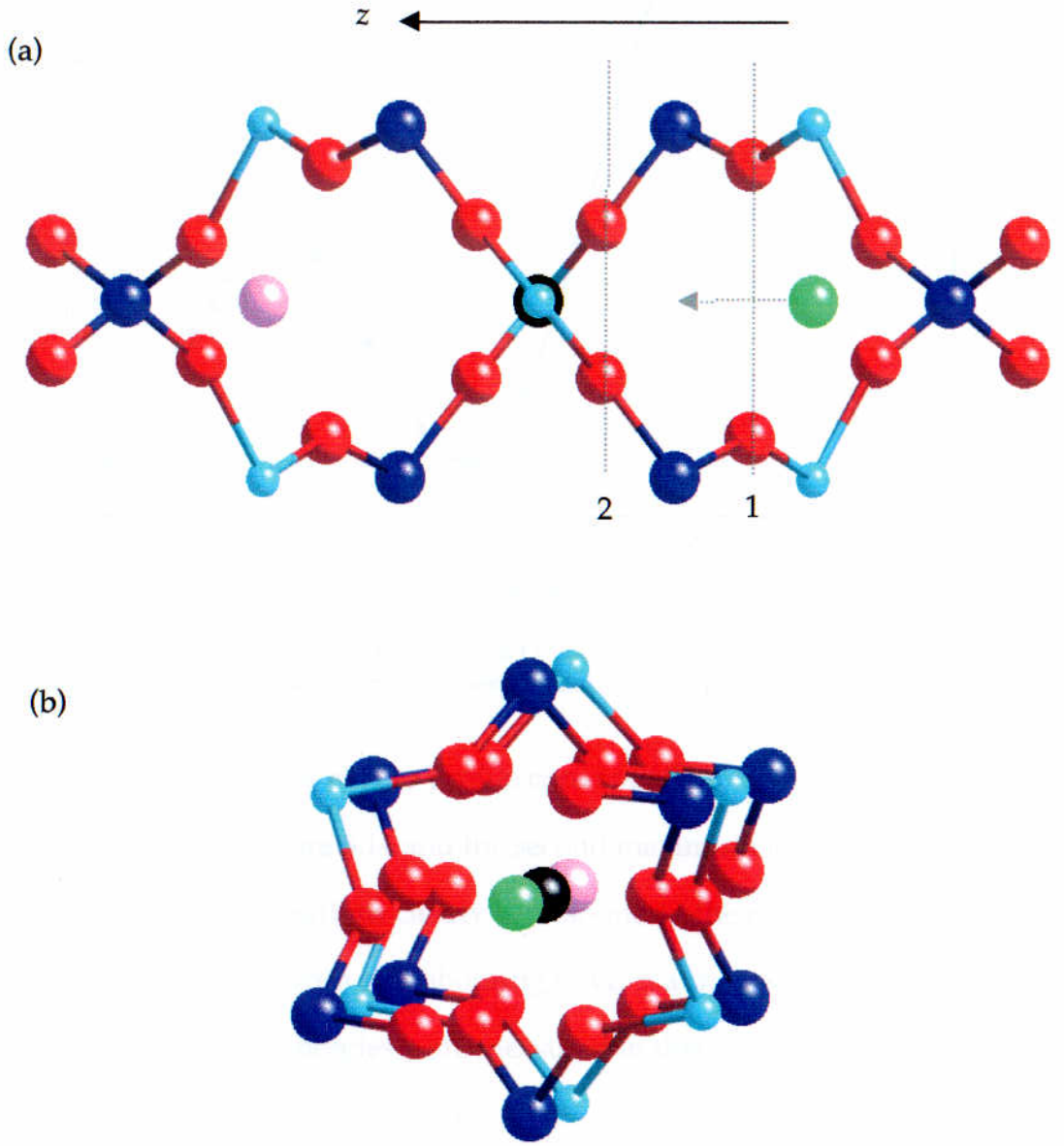

Figure 6.15 (a) Part of the β-eucryptite structure (viewed down [100]) showing the [001] structural channel. The path of the migrating Li^+ ion (green) towards the vacancy (black) is indicated; (b) The same structural channel, (viewed down ~[001]), showing the migrating Li^+ ion (green) and the vacancy (black).

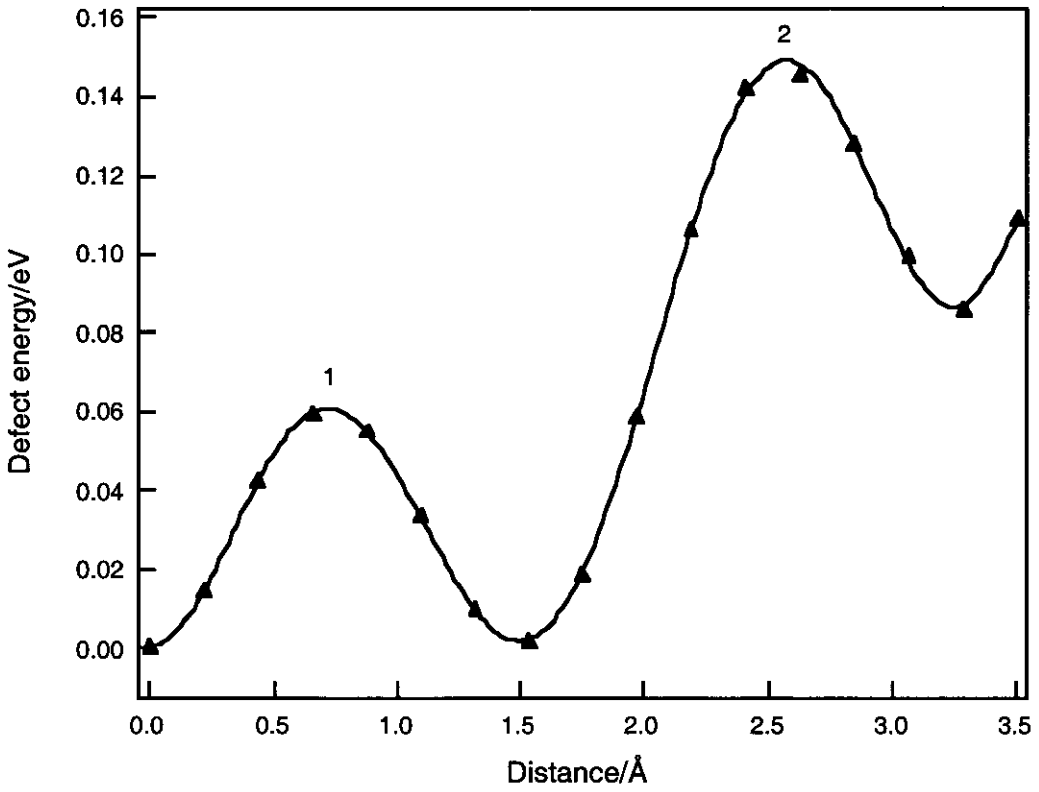

Figure 6.16 The calculated energy profile for a Li^+ ion migrating down [001] towards a vacant site. The points indicate the calculated defect energies along the migration pathway.

The first maximum in this energy profile corresponds to the position of the Li^+ ion as it passes line 1 on Figure 6.14 and the second maximum is where it passes line 2 on Figure 6.14. These positions clearly correspond to the regions where the electrostatic interaction with neighbouring oxygen atoms will be greatest.

Two distinct activation energies were measured in this investigation using dielectric spectroscopy: an activation energy of ~1.1 eV measured at both low (< 700 K) and high (> 783 K) temperatures with the crystal oriented such that the electric field was perpendicular to [001], and an activation energy of 1.33 eV measured at high temperatures (> 715 K) with the crystal oriented such that the electric field was parallel to [001]. It is reasonable to assume, on the basis of the previous studies described above (Alpen et al., 1977; Follstaedt and Richards, 1976; Lichtenstein et al., 1998), where an activation energy of ~ 0.8 eV was measured, and on the

calculations carried out here, that the processes being observed in the dielectric spectra are not due to the migration of Li^+ ions along the hexagonal channel.

(ii) Migration of Li in the (100) plane

In view of the evidence that at high temperatures the Li^+ ions may be disordered over all possible sites within the [001] channels (Pillars and Peacor, 1973; Xu et al., 1999a), it is possible to envisage a migration pathway between adjacent channels. Such a pathway, which might offer a higher energy barrier than that calculated for Li^+ ion migration along [001], would be a trajectory in the (100) plane from an occupied site in one channel to a vacant site in an adjacent channel as shown in Figure 6.17.

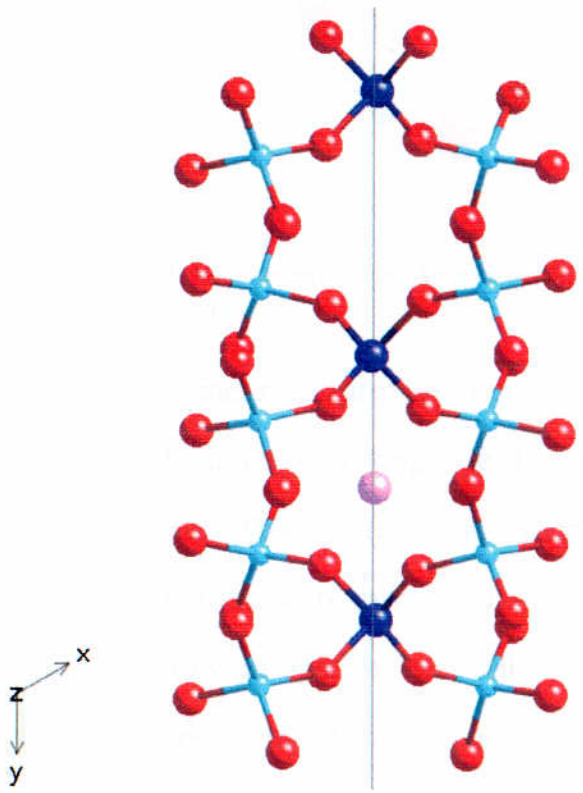

Figure 6.17 Part of the β-eucryptite structure (viewed down [001]) showing an Li^+ ion in the hexagonal channel and a vacant site in an adjacent channel.

Figure 6.18 shows the interconnecting side channel between the occupied and vacant sites. It can be seen that a linear route from the occupied Li^+ site to the vacancy in the adjacent channel is unlikely to offer the lowest energy barrier to migration, in view of the proximity of the oxygens at the saddlepoint of such a trajectory. It was therefore necessary to carry out detailed simulations to determine the most likely pathway for this proposed Li^+ ion migration.

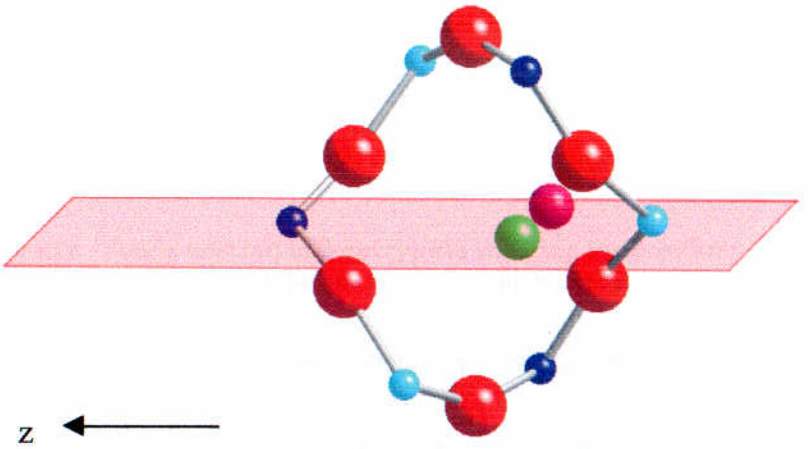

Figure 6.18 View of the interconnecting side channel between occupied (green) and vacant (pink) Li sites in the (100) plane.

In order to determine the approximate route taken by a migrating Li^+ ion as it passes through the interconnecting side channel, lattice energy calculations were carried out across the (100) plane in the region between the occupied and vacant sites. These calculations were carried out on several different structures in which there were three Li vacancies per unit cell. As there are 12 Li sites per unit cell (Figure 6.19), the positions of the vacancies could be varied. The results of the lattice energy calculations were then used to determine a migration pathway for each structure from a contour plot.

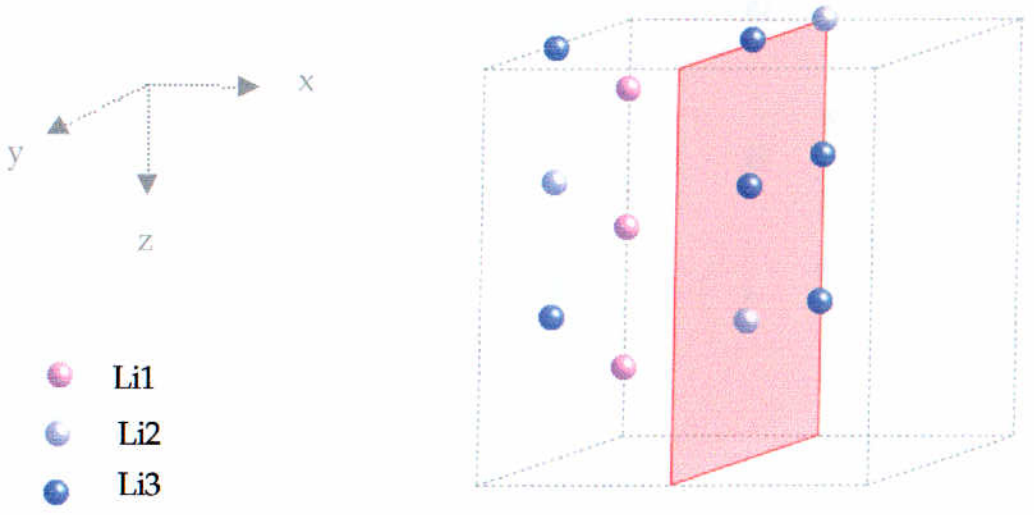

Figure 6.19 Single unit cell of β-eucryptite showing the positions of all the Li^+ ions when all sites are occupied, and the (100) lattice plane in which the lattice energy calculations were carried out.

The results of some of the calculations carried out are described below.

Migration of Li in the (100) plane to an unoccupied channel

Three adjacent Li vacancies were created in one of the [001] channels. As there are four [001] channels per unit cell, and 12 Li sites, this channel was then effectively unoccupied by Li^+ ions (Figure 6.20). The results of the lattice energy calculations are shown on the contour plot in Figure 6.21. The migration energy of the Li^+ ion was determined by calculating the defect energy at different points along this pathway, allowing full relaxation of the lattice at each position. In addition to this, defect calculations were carried out in a direction perpendicular to the (100) plane around the position of maximum energy, thus confirming that a true saddlepoint had been found.

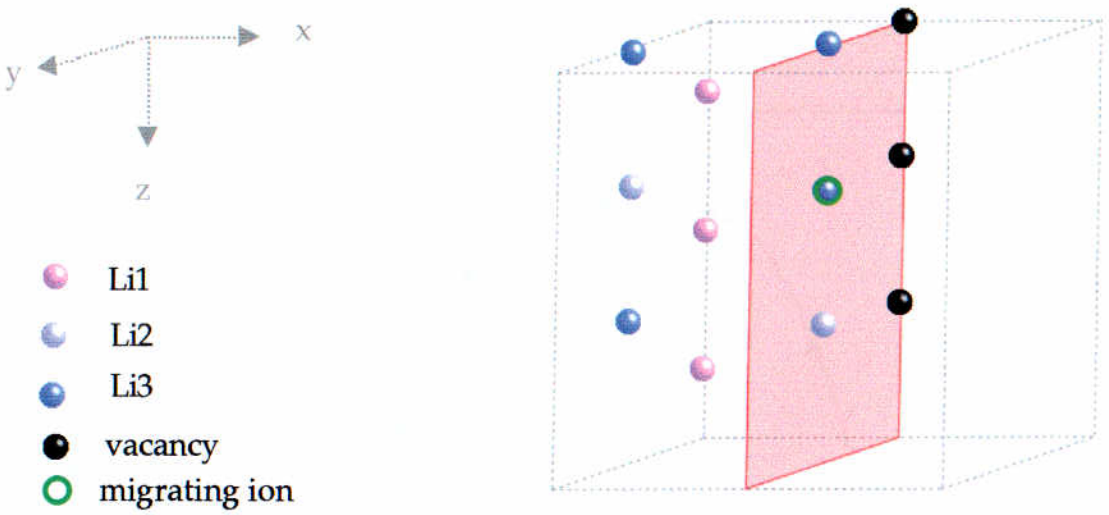

Figure 6.20 Single unit cell of β-eucryptite showing the positions of the Li^+ ions. The three vacancies and the migrating ion in the (100) lattice plane are also shown.

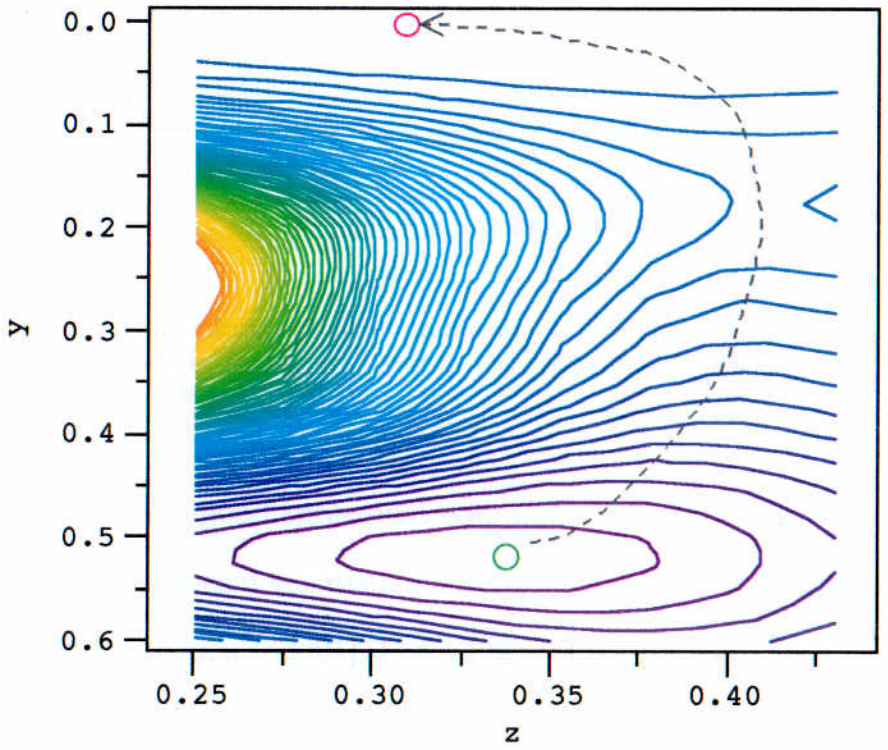

Figure 6.21 Contour plot showing the variation in the lattice energy in the (100) plane. The approximate migration pathway between an occupied Li site (green circle) and a vacant Li site (pink circle) is indicated.

The calculated energy profile for the migration of a Li^+ ion as described above is shown in Figure 6.22. The energy barrier is calculated to be 1.00 eV.

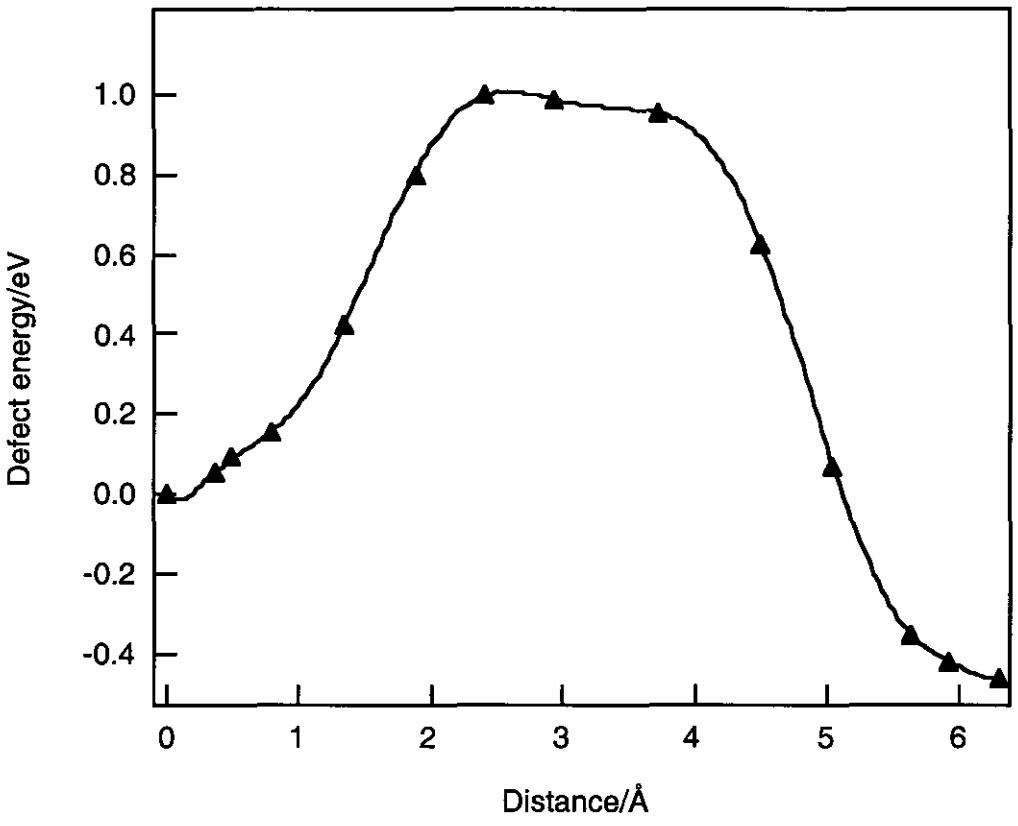

Figure 6.22 The calculated energy profile for a Li^+ ion migrating between its equilibrium position and a vacant site in an adjacent channel. The points indicate the calculated defect energies at points along the migration path.

This value is in good agreement with the activation energy determined from the dielectric measurements made on the crystal when it was aligned with the electric field perpendicular to [001] (1.06 – 1.08 eV).

Migration of Li in the (100) plane to a partially occupied channel

Two Li vacancies were created in one of the [001] channels and a third vacancy in an adjacent channel (Figure 6.23). Lattice energy calculations were carried out in the (100) plane, as before, and the results were used to determine the migration

pathway of the Li^+ ion to the vacant site. The result of this migration process would be to leave the [001] channel of the migrating ion unoccupied. The migration energy of the Li^+ ion was determined by calculating the defect energy at different points along this pathway, allowing full relaxation of the lattice at each position.

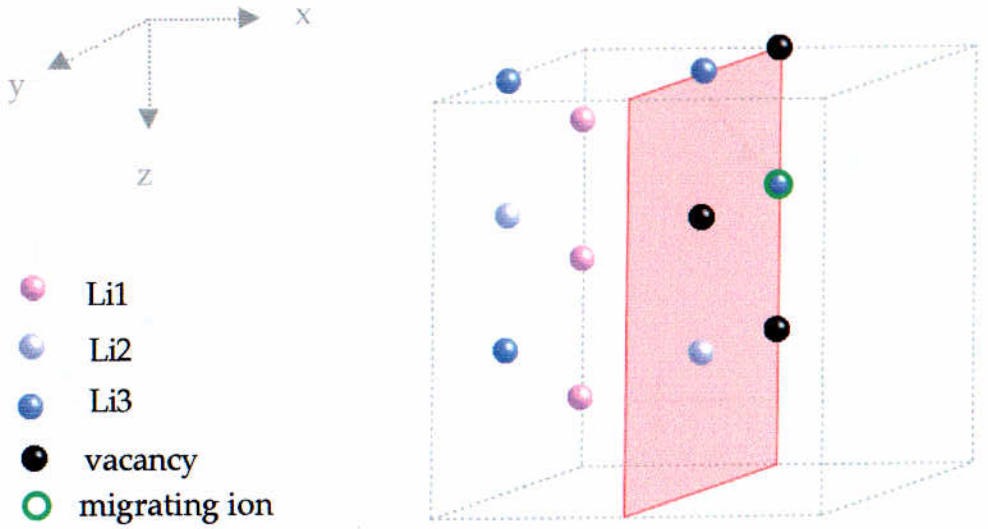

Figure 6.23 Single unit cell of β-eucryptite showing the positions of the Li^+ ions. The three vacancies and the migrating ion in the (100) lattice plane are also shown.

The calculated energy profile for the migration of a Li^+ ion as described above is shown in Figure 6.24. The energy barrier is calculated to be 1.44 eV. This value is much closer to the activation energy determined from the high temperature dielectric measurements made on the crystal aligned such that the field was parallel to [001] (1.33 eV) and on the second set of high temperature measurements made with the crystal in the other orientation (1.35 eV). However, as the activation energy for the migration process appears to depend on the ordering of vacancies within the structure, further calculations were carried out.

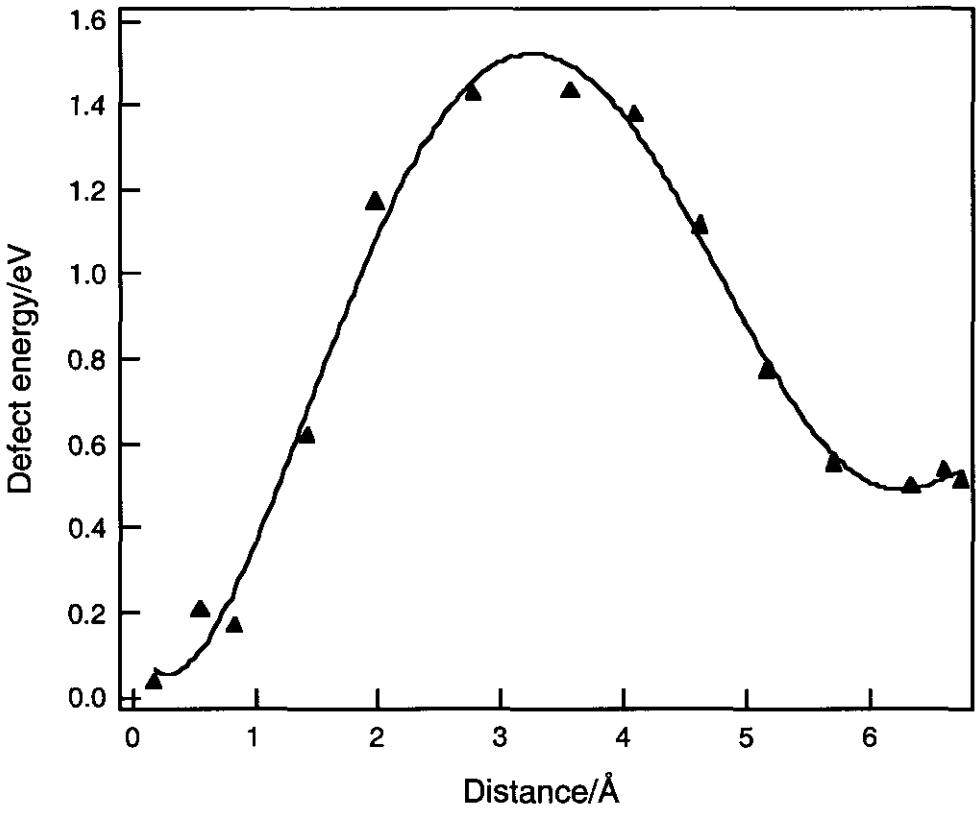

Figure 6.24 The calculated energy profile for a Li^+ ion migrating between its equilibrium position and a vacant site in an adjacent channel. The points indicate the calculated defect energies at points along the migration path.

Migration of Li in the (100) plane in a structure with a single vacancy

Calculations were then carried out on a structure with the same composition as before, but with a single Li vacancy. Instead of having three distinct Li vacancies, one vacancy was created in the position to which the ion was migrating, and all of the other Li^+ ions in the unit cell, apart from the migrating ion, were given a partial occupancy of 0.8 (Figure 6.25). This retained the stoichiometry but effectively disordered the remaining Li^+ ions over the remaining occupied Li sites and, unlike the previous two sets of calculations, it did not involve either starting with, or resulting in, an unoccupied [001] channel.

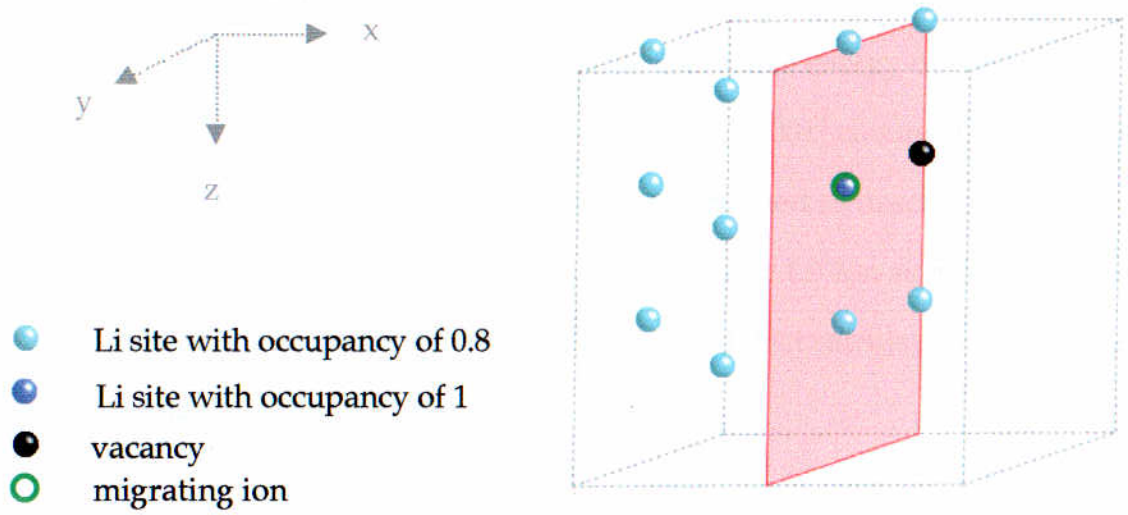

Figure 6.25 Single unit cell of β-eucryptite showing the positions of the Li^+ ions with an average occupancy of 0.8. The single vacancy and the migrating ion in the (100) lattice plane are also shown.

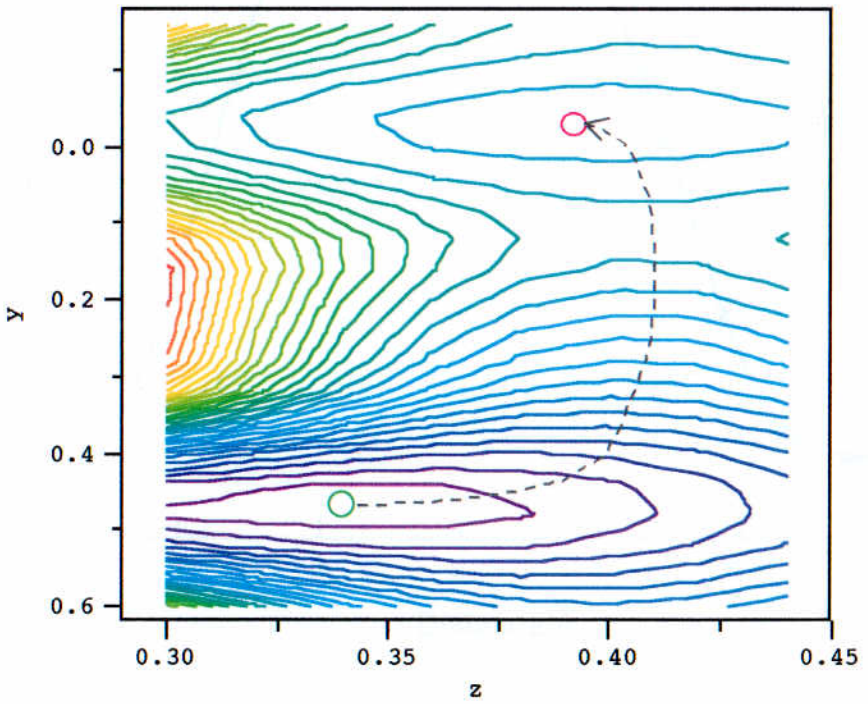

Figure 6.26 Contour plot showing the variation in the lattice energy in the (100) plane in a structure with 1 vacancy per unit cell. The approximate migration pathway between an occupied Li site (green circle) and a vacant Li site (pink circle) is indicated.

As before, lattice energy calculations were carried out across the (100) plane in the region between the occupied and vacant sites in order to determine the migration pathway . It can be seen from Figure 6.26 that the lattice energy distribution is somewhat different when there is no longer a vacant [001] channel (cf. Figure 6.21). The migration energy of the Li^+ ion was then determined as described previously and the calculated energy profile for the migration of a Li^+ ion as described above is shown in Figure 6.27. As with the preceding set of defect calculations, the energy barrier is calculated to be 1.44eV.

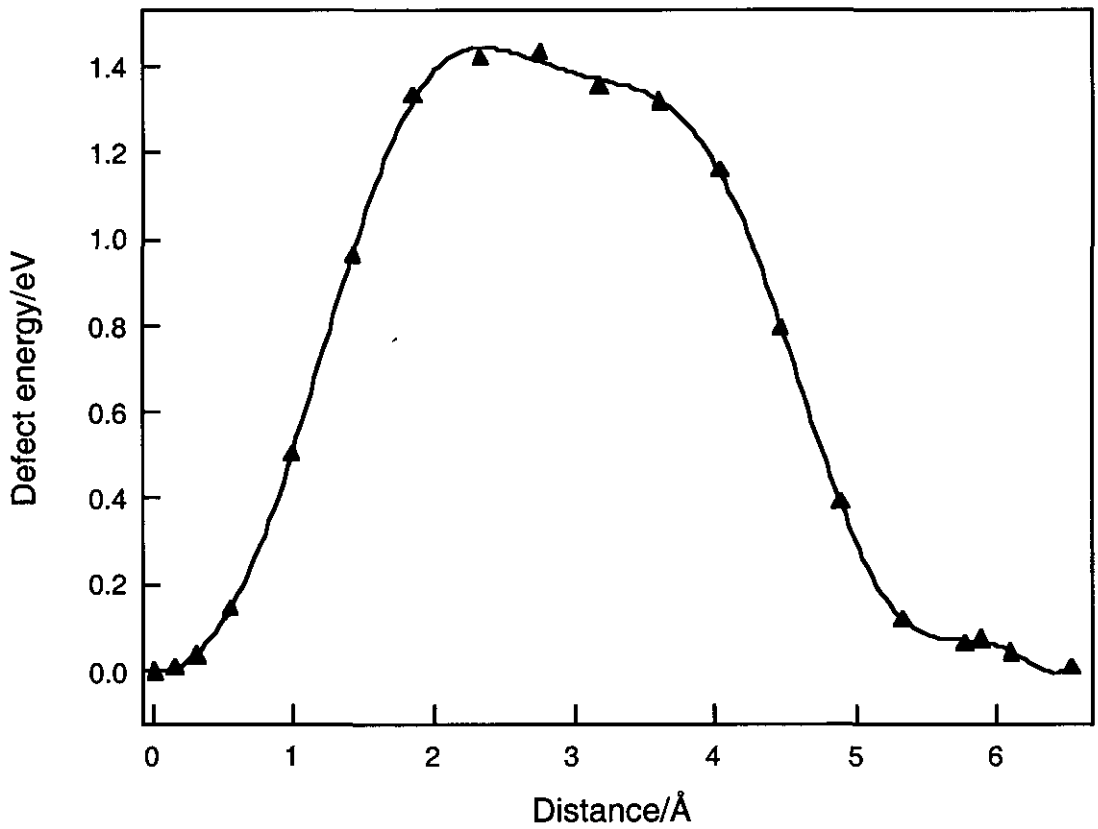

Figure 6.27 The calculated energy profile for a Li^+ ion migrating between its equilibrium position and a vacant site in an adjacent channel. The points indicate the calculated defect energies at points along the migration path.

(iii) Migration of Li in the (010) plane

Similar calculations were performed on migration processes between two adjacent [001] channels along a trajectory in the (010) plane between the vacant and occupied sites as shown in Figure 6.28. The methods used were the same as those described for migration in the (001) plane and these were carried out on structures with the same stoichiometry.

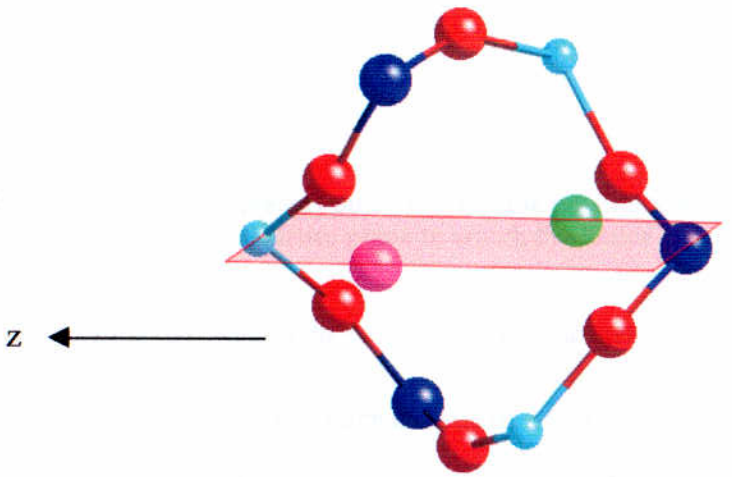

Figure 6.28 View of the interconnecting side channel between occupied (green) and vacant (pink) Li sites in the (010) plane.

The positions of the 12 Li sites in the unit cell and the (010) plane along which the migration pathways were investigated are shown in Figure 6.29.

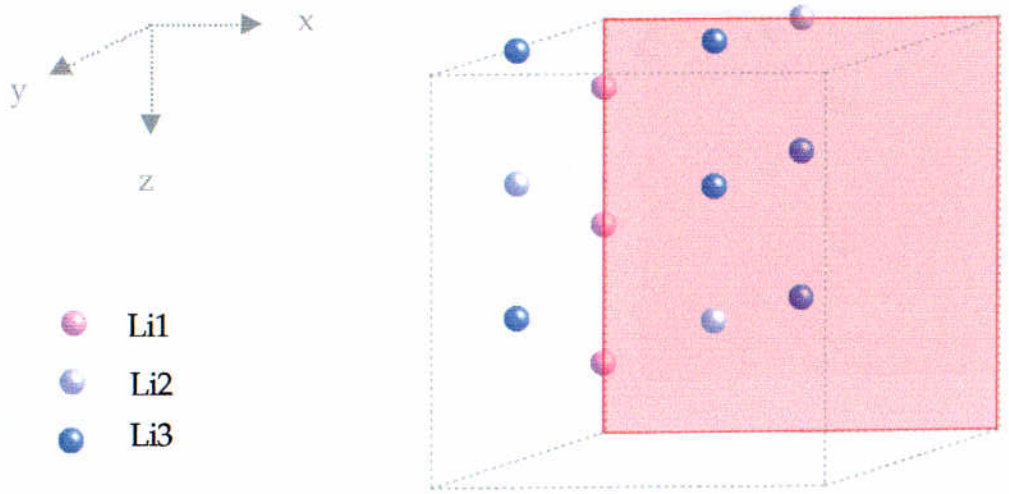

Figure 6.29 Single unit cell of β-eucryptite showing the positions of all the Li^+ ions when all Li sites are occupied, and the (010) lattice plane in which the lattice energy calculations were carried out.

Migration of Li in the (010) plane to an unoccupied channel

Lattice energy calculations were carried out in a structure containing three Li vacancies in one of the [001] channels (Figure 6.30). This effectively means that this channel was unoccupied. The results of these calculations are shown in Figure 6.31, and the migration energy of the Li^+ ion from the adjacent [001] channel was determined by calculating the defect energy at different points along this pathway, allowing full relaxation of the lattice at each position. As had been found for migration in the (100) plane, the optimum route for the Li^+ ion is a curved pathway between the two sites. The calculated energy profile for this migration is shown in Figure 6.32. The energy barrier is calculated to be 1.14 eV, which is in good agreement with the activation energy determined from the dielectric measurements made on the crystal when it was aligned with the field perpendicular to [001] (~ 1.1 eV).

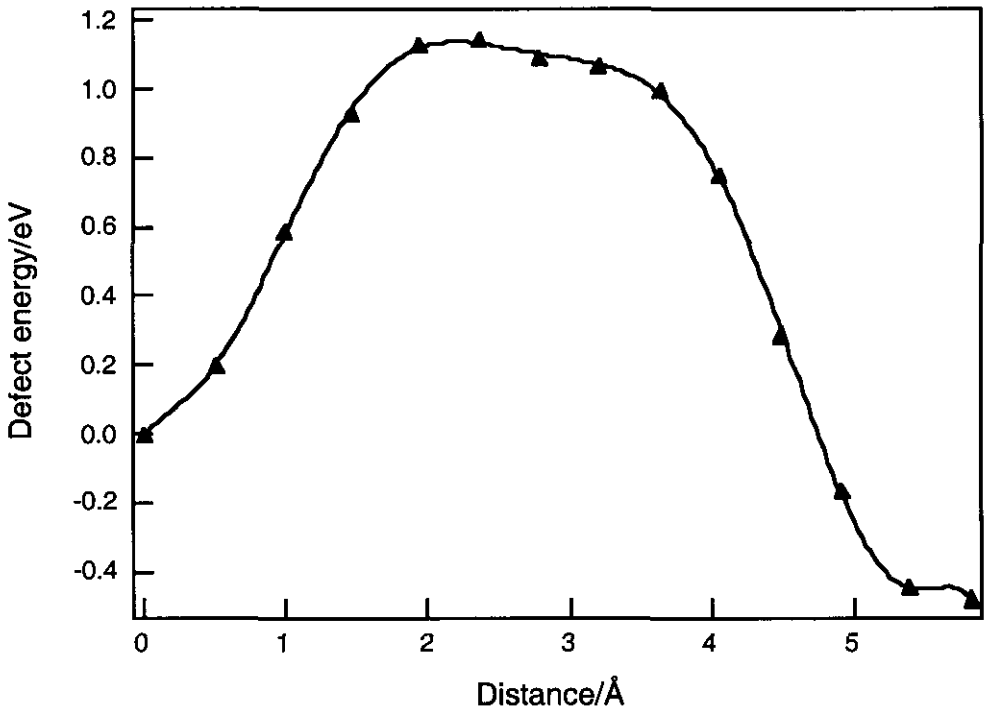

Figure 6.32 The calculated energy profile for a Li^+ ion migrating across (010) between its equilibrium position and a vacant site in an adjacent unoccupied channel. The points indicate the calculated defect energies at points along the migration path.

Migration of Li in the (010) plane in a structure with a single vacancy

Calculations were then carried out on a structure with the same composition as before, but with a single Li vacancy. Instead of having three distinct Li vacancies, one vacancy was created in the position to which the ion was migrating, and all of the other Li^+ ions in the unit cell, apart from the migrating ion, were given a partial occupancy of 0.8 (Figure 6.33).

Lattice energy calculations were carried out across the (010) plane in the region between the occupied and vacant sites in order to determine the migration pathway (Figure 6.34), and the migration energy determined as described previously. The calculated energy profile for the migration process is shown in Figure 6.35 and the energy barrier is calculated to be 1.49 eV.

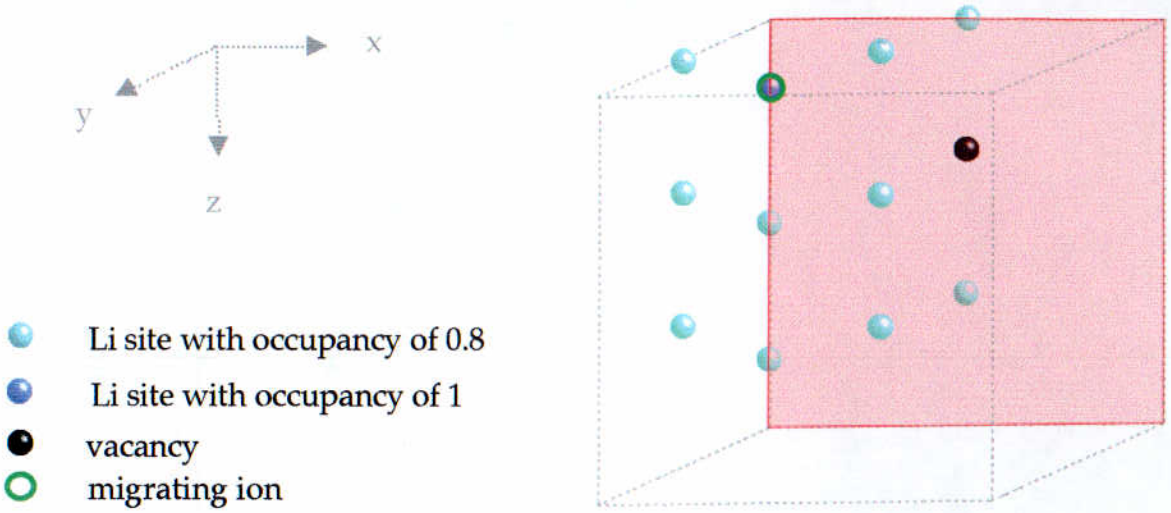

Figure 6.33 Single unit cell of β-eucryptite showing the positions of the Li^+ ions with an average occupancy of 0.8. The single vacancy and the migrating ion in the (010) lattice plane are also shown.

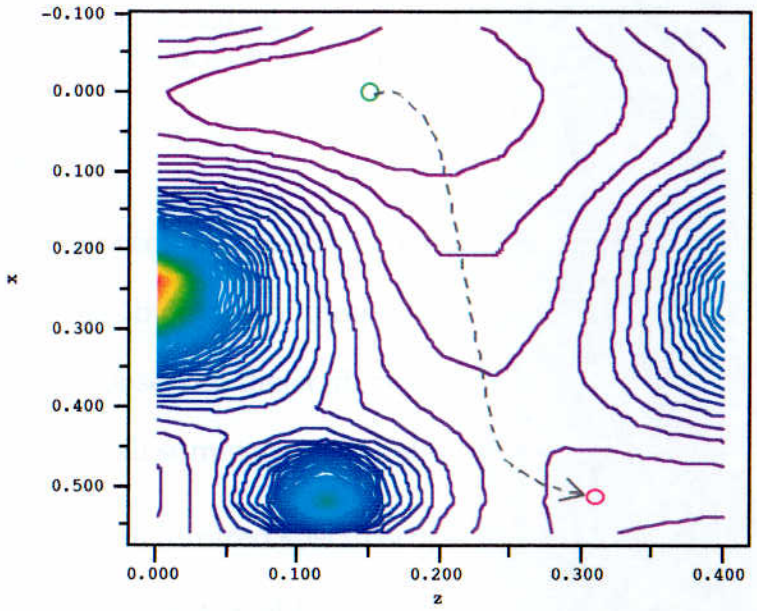

Figure 6.34 Contour plot showing the variation in the lattice energy in the (010) plane in a structure with 1 vacancy per unit cell. The approximate migration pathway between an occupied Li site (green circle) and a vacant Li site (pink circle) is indicated.

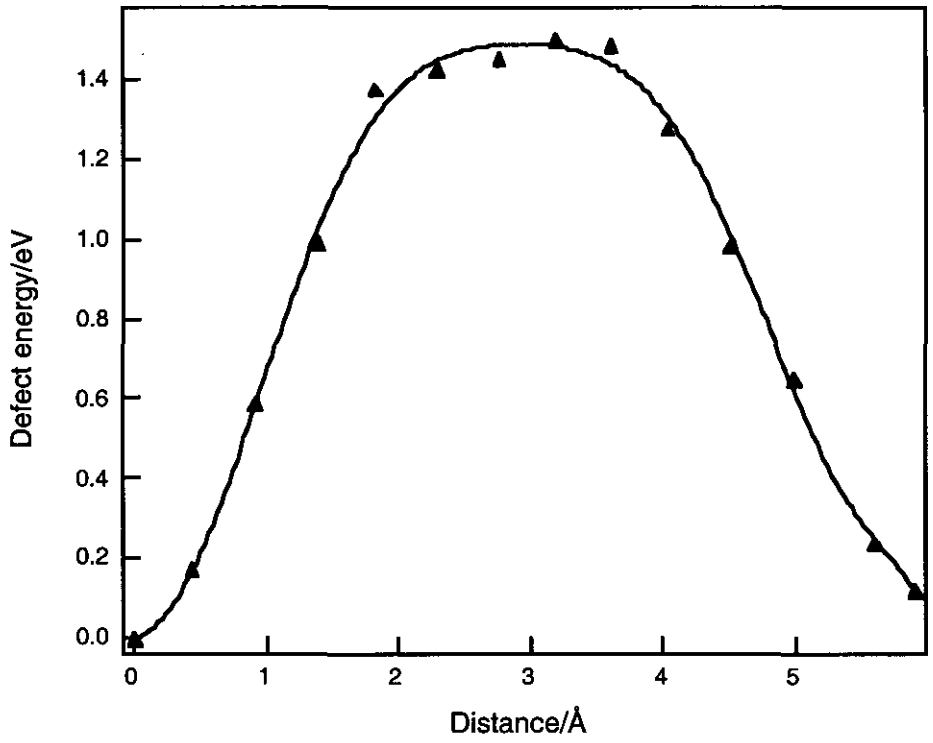

Figure 6.35 The calculated energy profile for a Li^+ ion migrating across (010) between its equilibrium position and a vacant site in an adjacent channel. The points indicate the calculated defect energies at points along the migration path.

6.5.4 Summary

Other possible migration mechanisms were also examined using the same simulation approach, but none of these yielded activation energies which correlated with the observed dielectric response. The results of the calculations described above are all summarised in Table 6.4.

There is evidence from infrared spectroscopic experiments (M. Zhang, personal communication) that the lowest temperature for the movement of Li^+ ions in β-eucryptite is ~500 K. Subtle changes in framework geometry accompanying this initial disordering, opening up new diffusion channels, could well account for the observed low-temperature dielectric loss.

Table 6.4 Calculated energy barriers to Li^+ migration in β-eucryptite

Migration mechanism	Defect energy/ eV
Li migration along partially occupied [001] structural channel	0.15
Migration in (100) plane between occupied and vacant sites in an adjacent unoccupied[001] channel	1.00
Migration in (100) plane between occupied and vacant sites in adjacent partially occupied[001] channel	1.44
Migration in (010) plane between occupied and vacant sites in adjacent unoccupied[001] channel	1.09
Migration in (010) plane between occupied and vacant sites in adjacent partially occupied[001] channel	1.49

It is possible that the observed relaxation with an activation energy of ~ 1.1 eV, is due to migration of Li^+ ions along a trajectory in either the (100) plane or the (010) plane between adjacent [001] channels. There is good agreement between the observed dielectric response and the results of calculations which were carried out on a unit cell in which the Li vacancy occurred in a channel which was completely unoccupied by Li^+ ions. This does not necessarily imply that this is a prerequisite for this low energy ion migration process to occur by this mechanism; it merely suggests that the presence of a significant number of adjacent vacancies in a channel may facilitate the process. There is some evidence that there could be unmixing of small quartz aggregates within the β-eucryptite matrix (Böhm, 1981) which would result in regions of unoccupied [001] channels. Figure 6.36 illustrates the calculated effect of a vacant channel on the local framework dimensions when the migrating Li^+ ion is at the saddlepoint. The more open structure adjacent to several unoccupied Li sites may well account for the lower activation energy measured using the defect calculations.

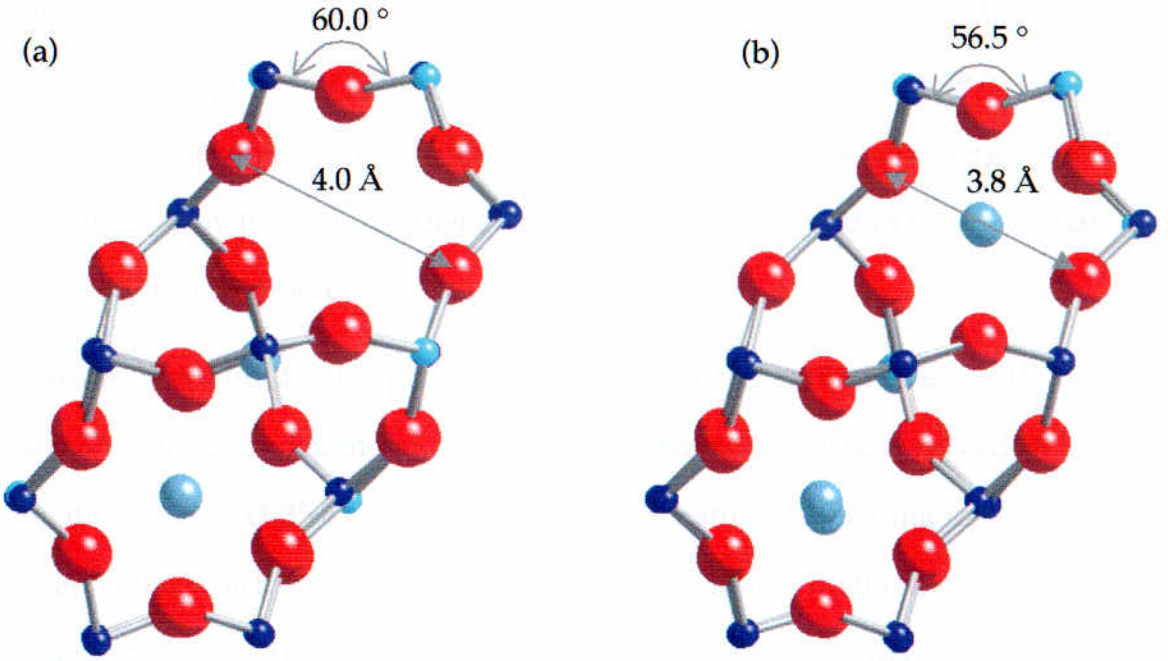

Figure 6.36 View down [001] of part of the β-eucryptite structure showing the calculated effect on the local framework dimensions of (a) a vacant channel; (b) a partially occupied channel, when the migrating Li^+ ion is at the saddlepoint.

The low energy relaxation was not observed in the dielectric measurements when the electric field was parallel to the [001] channels, and it is possible that the observed dielectric response for this migration pathway is at a minimum with the crystal in this orientation, i.e. with the (001) plane perpendicular to the electric field. When the crystal was aligned with the (001) plane perpendicular to the field there was a very small peak in tan δ at low temperatures (from 375 K), but the absorption was so weak it was not possible to measure an activation energy.

A high temperature relaxation process was observed with the crystal in both orientations. The changes in the amplitude of the dielectric loss peak around the temperature of the phase transition would suggest that a greater number of ions were involved in the relaxation process and it is highly likely that this is a result of

the disordering of Li^+ ions accompanying the transition (Pillars and Peacor, 1973; Schulz and Tscherry, 1972a). New migration pathways opening up as the temperature approaches T_c may account for the increasing amplitude of tan δ. On the basis of the computer modelling results, the higher activation energy could be accounted for by the fact that there are no longer regions within the [001] channels which are largely unoccupied.

However, this would not explain why two different activation energies (1.06 eV and 1.33 eV), which depended on the crystal orientation, were observed. A higher activation energy (1.35 eV), was obtained on repeating the heating measurements on the crystal which had initially given the lower value (with the electric field perpendicular to *c*); it is possible that thermally activated disordering of Li^+ within the channels occurred during the heating process, thereby removing regions of adjacent unoccupied Li sites. When the crystal was aligned with the electric field parallel to *c*, disordering of Li^+ ions along [001] may have occurred more readily as a direct effect of the field direction.

It should also be recognised that these calculations were carried out on a room temperature structure. In the high temperature structure (Guth and Heger, 1979) the Li^+ ions are disordered over two sites. Although it was possible to model this structure successfully, giving each Li site an occupancy of 0.5, attempts to perform defect calculations on this structure gave unrealistic results and were not pursued further. The activation energy determined from the high temperature dielectric measurements was determined above 800 K. As explained in section 6.2.5, although β-eucryptite has an extremely low bulk thermal expansion, it has anisotropic thermal expansion coefficients. The linear thermal expansion coefficients have been determined as: α_a = 0.076 Å/K and α_c = -0.165 Å/K

(Lichtenstein et al., 1998). The positive expansion in the (001) plane, and the subsequent widening of the interconnecting side channel between the occupied and vacant Li^+ sites, as shown in Figure 6.37, may contribute to the calculated value of the activation energy being higher than the experimental value.

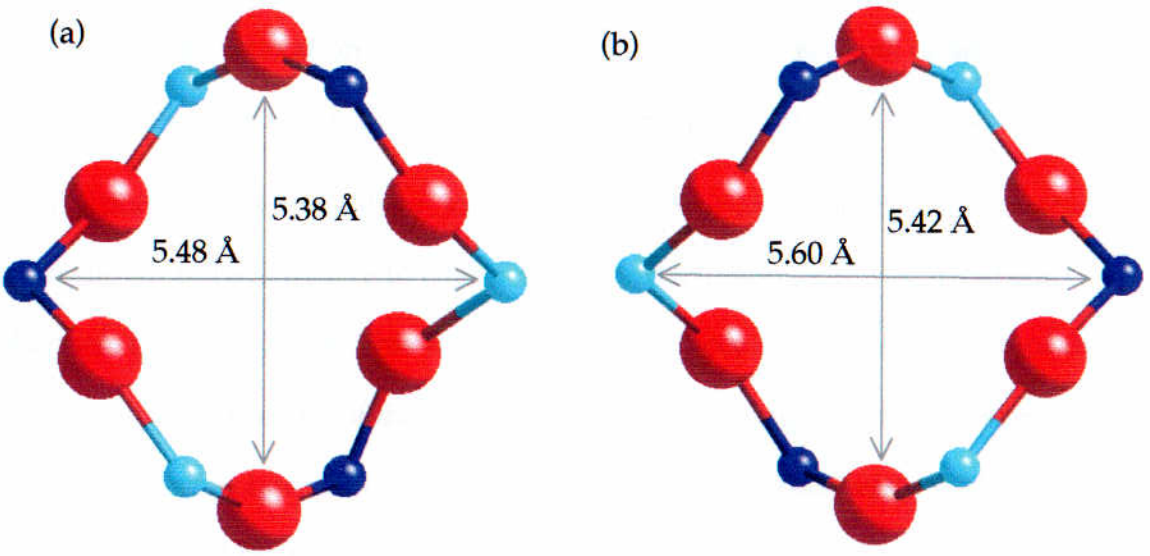

Figure 6.37 View down [010] of the interconnecting side channel between an occupied and a vacant Li site in (a) the room temperature structure; (b) the high temperature structure.

6.6 Conclusions

The combination of dielectric spectroscopy with computer modelling has provided a means of determining the mechanism and energetics of various Li migration pathways within the β-eucryptite structure. In summary:

- Migration of Li^+ occurs by two distinct mechanisms: a correlated movement of ions along the [001] structural channels and an activated hopping mechanism along trajectories in the (100) and (010) planes between these channels.
- The experimentally determined activation energies depend on both the orientation of the crystal with respect to the electric field and on the degree of Li disorder within the [001] channels.
- Framework relaxation effects due to the presence of regions of adjacent vacancies have a significant effect on the energetics of ion diffusion.

In addition to these insights on ion migration processes, dielectric spectroscopy has been shown to be sensitive to changes in Li order-disorder in the structural channels of β-eucryptite. This may allow a more accurate determination of the critical temperature (T_c) of the phase transition involving Li redistribution. The results presented here would suggest that this temperature was ~ 830 K (cf. the range suggested by Xu et al. (1999a) of somewhere between 710 K and 923 K.)

Short-range lithium mobility has been observed in this investigation, but in order to get a fuller picture of the longer-range ion transport which leads to β–eucryptite's superionic conductivity at high temperatures, it will be necessary to investigate the possible cooperative movement of ions along the structural channels. The type of defect calculations carried out here are more applicable to distinct Debye-type ion-hopping processes, rather than a correlated movement of ions along a channel; a molecular dynamics approach would therefore be useful to probe such behaviour and could be the subject of a future investigation.

Chapter 7

The Feldspars

Contents

7.1 Introduction

Feldspars are the most commonly occurring minerals in the Earth's crust and a wide range of compositions and structural states can be found in rocks with different cooling histories. The feldspars therefore provide an opportunity for studying the way a structure responds to a changing geological environment.

The feldspar minerals are aluminosilicates whose structures comprise an infinite corner-sharing framework of AlO_4 and SiO_4 tetrahedra. Charge balancing cations occupy large, irregular cavities in the tetrahedral framework. The general formula is MT_4O_8 with between 25% and 50% of the Si replaced by Al in the T sites, M is Ca^{2+} or Ba^{2+} for $MAl_2Si_2O_8$ *alkaline-earth feldspars*, and Na^+ or K^+ for the $MAlSi_3O_8$ *alkali feldspar* series of solid solutions and mixed crystals. A complete range of compositions is observed in the *plagioclase feldspar* series, $Na_yCa_{1-y}Al_{2-y}Si_{2+y}O_8$ $(0 \leq y \leq 1)$. The compositions of most natural feldspars lie in the $KAlSi_3O_8$-$NaAlSi_3O_8$- $CaAl_2Si_2O_8$ triangle (Figure 7.1) in which the shaded area represents the extent of high temperature solid solution.

This study investigates ion mobility processes in the three end members, sanidine (K-feldspar), albite (Na-feldspar) and anorthite (Ca-feldspar). Although there are many common structural features, there are also major differences in Al/Si ordering and more subtle differences involving framework distortions. The feldspars therefore provide a non-channel framework in which to test new models for Na, K and Ca mobility mechanisms using dielectric spectroscopy in combination with atomistic simulation techniques.

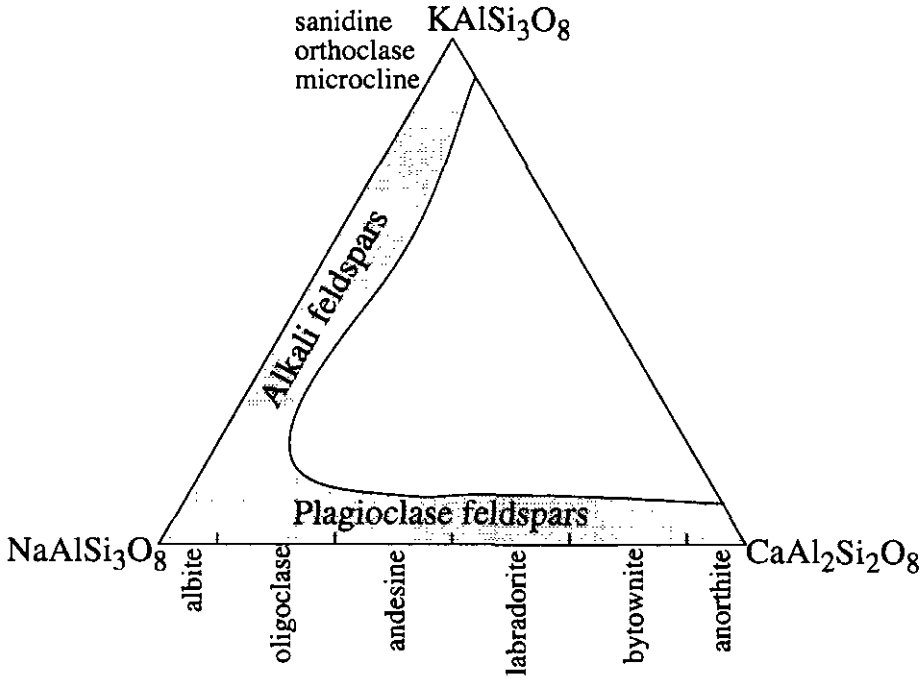

Figure 7.1 The extent of solid solution in alkali and plagioclase feldspars at high temperature. The plagioclase feldspars are subdivided according to composition as indicated (Putnis, 1995).

7.2 Scientific background

7.2.1 Structural features and behaviour

The essential features of the feldspar structure are described below by considering the structure of high albite, $NaAlSi_3O_8$ (Winter et al., 1979). This will be followed by more specific descriptions of the various modifications which occur in other feldspars.

In high albite, the Al and Si are disordered so that the average occupancy of each tetrahedron is 25% Al, 75% Si. The tetrahedral framework consists of rings of four tetrahedra, with alternate pairs of vertices pointing in opposite directions, joined in layers as shown in Figures 7.2(a) and 7.2(b). The rings are related by mirror planes parallel to (010) and diads parallel to the *b* axis. There are two sets of tetrahedra, T_1 and T_2, not related to one another by symmetry.

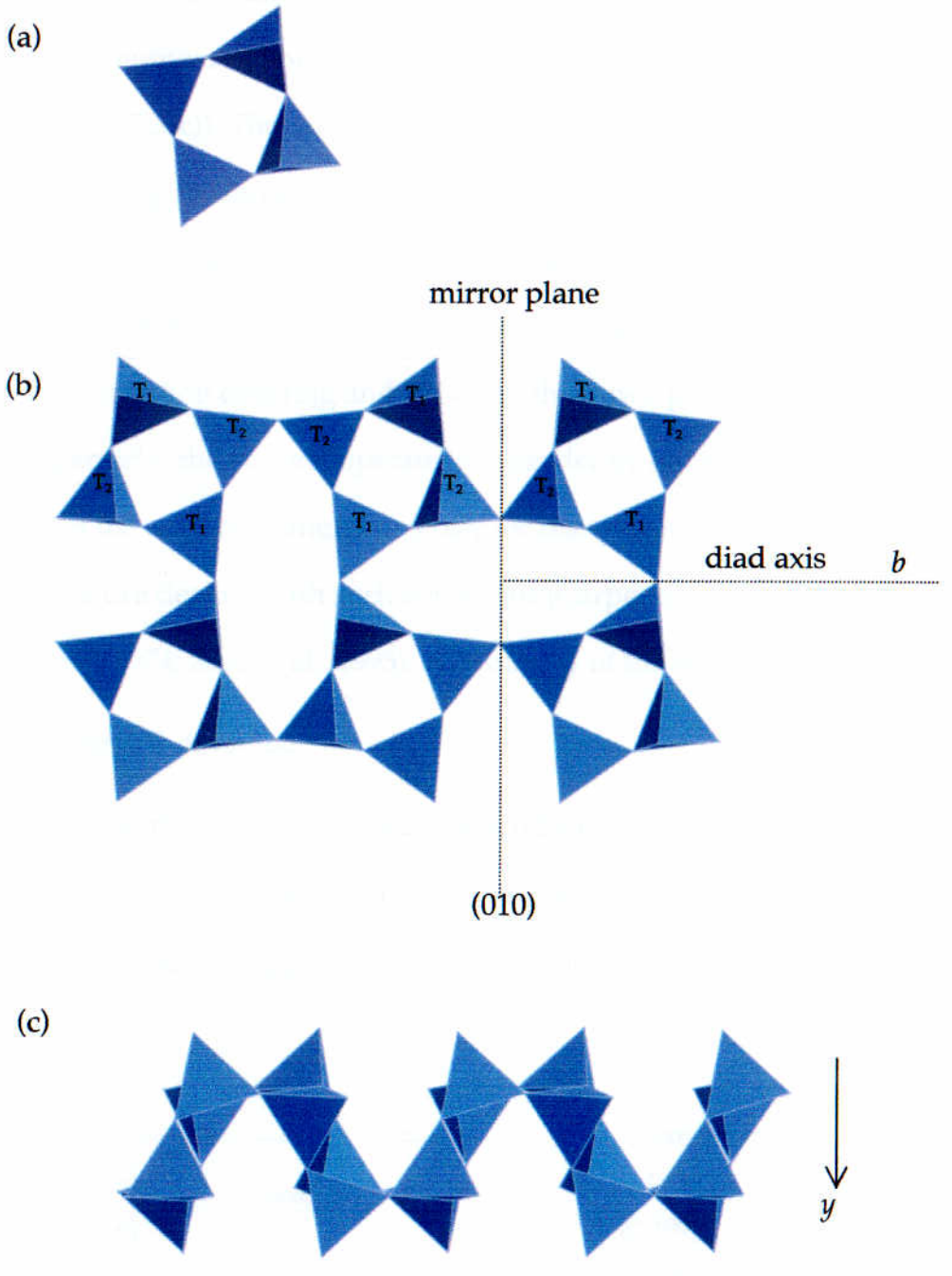

Figure 7.2 (a) The four membered ring of tetrahedra with a pair of tetrahedra pointing up and down; (b) The four-fold rings joined to form a single layer (viewed down [100]); (c) The linkage between the four-fold rings showing how they are linked by their apices forming a crankshaft-like chain.

Cations occupy the large oval-shaped cavities between the rings. The rings are joined to one another by the apices, forming crankshaft-like chains parallel to the x axis (Figure 7.2(c)). The cations lie in the mirror planes between the crankshafts, occupying the largest cavities in the framework. This gives a monoclinic structure, spacegroup $C2/m$, which is the parent structure from which the other feldspar structures are derived. The symmetry will be reduced by framework distortions and/or cation ordering and although these two processes can be considered separately, they do not operate independently of each other. These processes have been the subject of intensive study for many years and there is a vast body of literature dealing with such behaviour (Carpenter, 1988; Megaw, 1974; Sipling and Yund, 1974; Xiao et al., 1995). A summary of the main points is given below.

Framework distortion

Framework collapse may occur around small interstitial cations at low temperatures, reducing the symmetry to triclinic, spacegroup $C\bar{1}$. This is a spontaneous displacive transformation. Figure 7.3 shows how this symmetry change is controlled by cation size.

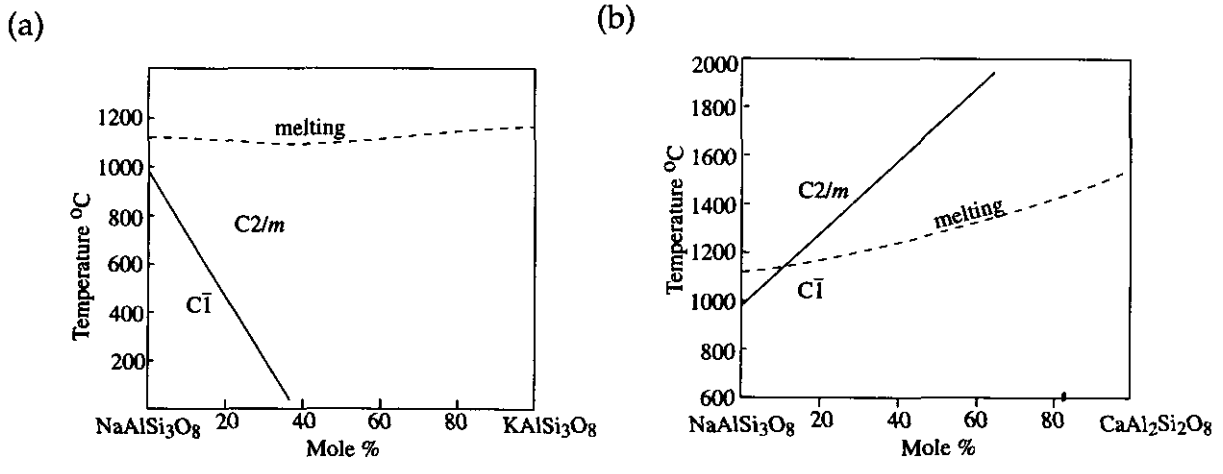

Figure 7.3 (a) The decrease in the temperature of the $C2/m \Rightarrow C\bar{1}$ distortion as more K^+ ions are present in the structure; (b) The increase in temperature of the $C2/m \Rightarrow C\bar{1}$ distortion as more Ca^{2+} ions are present in the structure (Putnis, 1995).

The temperature at which the structure collapses decreases as the composition moves from Na-feldspar towards K-feldspar and increases as the composition moves from Na-feldspar towards Ca-feldspar.

Al,Si ordering

There is a tendency for Al,Si ordering to occur at low temperatures, a slow process involving breaking of Al-O and Si-O bonds. As shown in Figure 7.2, the $C2/m$ structure has only two sets of tetrahedra, T1 and T2, present in equal numbers. Since T1 and T2 are not related by symmetry in $C2/m$, complete randomness of occupation is possible. However, if perfect order is to be achieved, the specification of more than two types of T sites is required and the symmetry must be lowered. Loss of the mirror plane and the diad axis lead to triclinic symmetry, spacegroup $C\bar{1}$.

Therefore, although the displacive mechanism in itself is instantaneous, the symmetry change is controlled by the very much slower process of Al,Si ordering or disordering. The structural distortion and the Al,Si ordering are coupled and the way these structures behave on heating and cooling very much depends on how the two processes interact.

Albite (Na-feldspar)

Albite, $NaAlSi_3O_8$, is monoclinic $C2/m$ above 980 °C (monalbite) but collapses around the small Na^+ ion to the triclinic structure at low temperatures. At high temperatures there is very little Al,Si order and it is called high albite, however as it is cooled below 700 °C, ordering begins and at low temperatures fully ordered low albite is formed. These structures are shown in Figures 7.4(a) and 7.4(b), respectively.

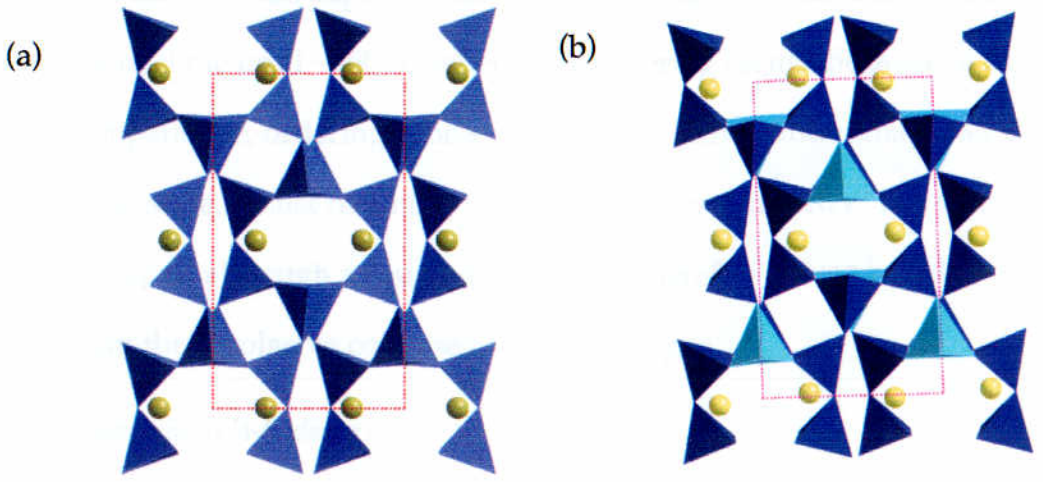

Figure 7.4 (a) The disordered structure of high albite (Winter et al., 1979); (b) the fully ordered structure of low albite (Harlow and Brown, 1980) viewed down [001].

Sanidine (K-feldspar)

Sanidine, $KAlSi_3O_8$, is the high temperature monoclinic $C2/m$ form of potassium feldspar. The structure of sanidine is shown in Figure 7.5 .

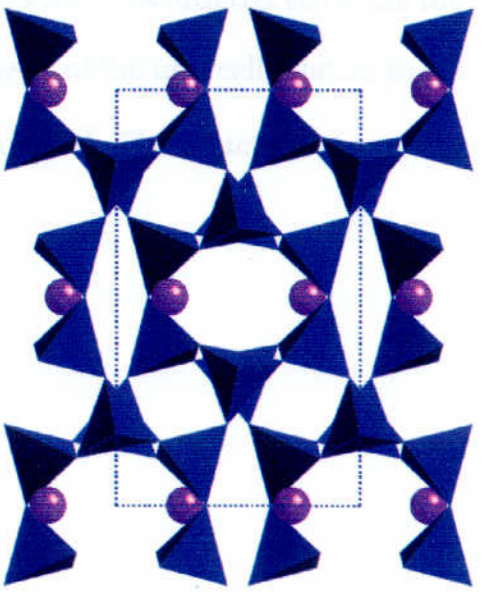

Figure 7.5 The structure of sanidine (viewed down[001]) (Deubener et al., 1991).

The large K^+ ion supresses the displacive transformation and the structure remains monoclinic until ~450 °C when Al,Si ordering begins. Because of the relatively low temperature, ordering proceeds extremely slowly and it may lead to ordering on a local scale, whilst retaining the original $C2/m$ symmetry. The symmetry change in K-feldspar, although a coupled process, is therefore driven by Al,Si ordering, rather than the displacive collapse as in Na-feldspar.

Anorthite (Ca-feldspar)

Anorthite, $CaAl_2Si_2O_8$ is one of the end members of the plagioclase feldspar series. (The other end member is albite, $NaAlSi_3O_8$.) In pure anorthite, the Ca^{2+} ion is unable to support the expanded monoclinic $C2/m$ structure at any temperature below the melting point. Since the Al:Si ratio is 1:1 any degree of disorder will result in the formation of Al-O-Al linkages and, as this is energetically unfavourable (Loewenstein, 1954), the tendency to order is greater than in the alkali feldspars (Angel et al., 1990). This ordered structure therefore results in a doubling of the c lattice parameter of the unit cell relative to that of albite. Ordered anorthite is triclinic with spacegroup $I\bar{1}$. The structure of anorthite is shown in Figure 7.6.

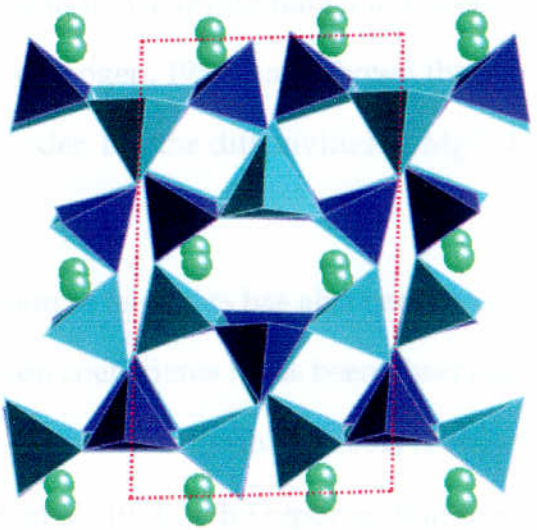

Figure 7.6 The structure of anorthite (viewed down [001]) (Wainwright and Starkey, 1970).

7.2.2 Diffusion in feldspars

Diffusion of alkali ions in alkali feldspars is of geological interest as it determines the rates of alkali ion exchange between alkali feldspars and their surroundings, and of exsolution. The process is also of interest because of its connection with the diffusion of trace elements, including argon, into or out of alkali feldspar crystals. Diffusion in feldspars has therefore been extensively studied and by far the most reliable and exhaustive data on diffusivity of cations in minerals are those obtained on feldspar minerals (Bailey, 1971; Giletti and Shanahan, 1997; Lin and Yund, 1972; Sippel, 1963; Yund, 1983).

There is evidence that diffusion of sodium is faster than that of potassium in a given feldspar (Dowty, 1980), but there is no strong evidence that diffusion of either ion is faster in potassium feldspar than in albite, even although the difference in porosity between K-feldspar and albite is proportionally much less than the difference in ionic

radii of K and Na. Diffusion of Mg^{2+} and Fe^{2+} in olivine seems to occur at the same rate as diffusion of alkalis in feldspar (Buening and Buseck, 1973), whereas studies carried out on quartz (Verhoogen, 1952) have shown that the diffusivities of Li^+, Na^+ and K^+ decrease in that order, but the diffusivities of Mg^{2+}, Fe^{2+}, Ca^{2+} and Al^{3+} are undetectably small.

The anisotropy of diffusion in feldspars has also been widely studied. From measurements of diffusion coefficients it has been observed that alkali diffusion in albite normal to (010) is slower than normal to (001) (Petrovic, 1972). Similar results were obtained by Giletti et al (1974), who reported that the diffusion coefficient for potassium in low albite normal to (010) is one tenth that normal to (001).

However, although there is an abundance of data describing the bulk diffusion of cations in feldspars and related minerals, there is a paucity of published data regarding the atomic mechanisms of these diffusion processes. Rates of diffusion on a macroscopic scale are inherently dependent on the controlling factors behind such processes, and these can only be established by investigating the mechanism and energetics of ion migration on an atomic scale.

7.3 Experimental

Samples of albite, K-feldspar and anorthite were kindly provided by Mike Henty (The Open University), Dr. Mark Welch (Natural History Museum) and Dr. Michael Carpenter (University of Cambridge), respectively. Single crystals were selected from each sample and were prepared for dielectric spectroscopy measurements, as described in Chapter 2.

7.3.1 Sample characterisation

Electron microprobe analysis

Sample compositions were determined using electron microprobe analysis. This was carried out using a Cameca SX100 microprobe, operating at 20 kV, 20nA and with a 10 μm spot diameter. All samples were found to be of uniform composition. The results of the microprobe analyses are shown in Table 7.1.

Table 7.1 Composition and origin of feldspars

Feldspar	Composition	Origin
Albite	$Na_{0.99}Al_{1.01}Si_{2.99}O_8$	Brazil
K-feldspar	$Na_{0.08}K_{0.92}Al_{1.02}Si_{2.98}O_8$	Unknown (BM1924, 1244 Natural History Museum,)
Anorthite	$Ca_{0.97}Na_{0.04}Al_{1.92}Si_{2.05}O_8$	Japan (3779 Cambridge mineral collection)

7.3.2 Dielectric spectroscopy

Dielectric measurements were made on polished crystals of albite, K-feldspar and anorthite at room temperature and at regular intervals up to 1100 K. From these measurements the dielectric constant, conductivity and the dielectric loss were calculated at each frequency.

7.4 Atomistic computer modelling

The interatomic potentials and shell model parameters used (listed in Table 7.2) were all taken from previous simulation studies (Bush et al., 1994; Freeman and Catlow, 1990; Jackson and Catlow, 1988).

Table 7.2 Interatomic potentials used for modelling the feldspar sructures

(i) Two-body Buckingham

Interaction[a]	A/eV	ρ/Å	C/eV Å^{-6}
Na^{+} ...O^{2-}	1226.84	0.3065	0.0000
K^{+} ...O^{2-}	902.8	0.36198	0.0000
Ca^{2+} ...O^{2-}	2272.741	0.2986	0.0000
Si^{4+} ...O^{2-}	1283.907	0.32052	10.66158
Al^{3+} ...O^{2-}	1460.3	0.29912	0.0
O^{2-} ...O^{2-}	22764.3	0.1490	27.879

(ii) Shell model[b]

Species	Y/e	K/eV Å^{-2}
O^{2-}	-2.86902	74.92
Ca^{2+}	1.2810	34.05

(iii) Three-body

Interaction	Force constant/eV rad^{-1}
O – Si – O	2.0972
O – Al – O	2.0972

[a] Potential cut off = 10 Å
[b] Y and k refer to the shell charge and harmonic force constant respectively

The starting point for the calculations was the simulation of the structure of each of the three feldspar crystal structures. The unit cell dimensions and atomic coordinates used for the calculations were taken from structure refinements of similar composition to those used in this investigation. These are summarised in Table 7.3.

Table 7.3 Composition of feldspars used for atomistic simulations

Feldspar	Composition
Albite	$NaAlSi_3O_8$ (Winter et al., 1979)
K-feldspar (sanidine)	$K_{0.9}Na_{0.1}AlSi_3O_8$ (Phillips and Ribbe, 1973)
Anorthite	$CaAl_2Si_2O_8$ (Wainwright and Starkey, 1970)

The unit cell dimensions and atomic coordinates were equilibrated under constant pressure. The calculated values for the lattice parameters and selected bond distances and their comparison with experimental values are listed in Table 7.4. Overall there is quite good agreement between the experimental and simulated structures, considering the complexity of these systems. However, the *a* lattice parameter in K-feldspar shows a larger difference between the experimental and calculated values than might be expected (4.39 %). This will inevitably affect the results of subsequent defect calculations and will be discussed more fully in section 7.5.2 .

Table 7.4 Calculated and experimental structural parameters for the feldspar structures

(a) Albite

(i) Unit cell parameters

Parameter	Experimental	Calculated	Difference/%
a	8.2970 Å	8.4573 Å	1.93
b	12.9940 Å	12.9664 Å	-0.21
c	7.1440 Å	7.1263 Å	-0.25
α	90.00°	90.6229°	0.69
β	116.01°	116.17°	0.13
γ	90.00°	90.12°	0.13

(ii) Selected bond distances

Bond distance	Experimental/Å	Calculated/Å
Na – O1	2.765	2.802
Na – O2	3.806	3.781
Na – O3	5.278	5.193
Na – O5	2.825	2.902

(b) K-feldspar

(i) Unit cell parameters

Parameter	Experimental	Calculated	Difference/%
a	8.539(4) Å	8.9142 Å	4.39
b	13.015(5) Å	12.9886 Å	-0.20
c	7.179(3) Å	7.1919 Å	0.18
α	90.00°	90.00°	0.00
β	115.99°	115.81°	-0.15
γ	90.00°	90.00°	0.00

Table 7.4 (cont.)

(ii) Selected bond distances

Bond distance	Experimental/Å	Calculated/Å
K – OA(2)	3.399	3.245
K – OB	3.012	3.226
K – OC	4.639	4.496
K – OD	2.938	3.033

(c) Anorthite

(i) Unit cell parameters

Parameter	Experimental	Calculated	Difference/%
a	8.173±0.001 Å	8.2101 Å	0.45
b	12.869±0.001 Å	12.8118 Å	-0.44
c	14.165±0.001 Å	14.0264 Å	-0.98
α	93.11°	92.66 °	-0.49
β	115.91°	115.85°	-0.06
γ	91.26°	91.07°	-0.21

(ii) Selected bond distances

Bond distance	Experimental/Å	Calculated/Å
Ca4 – OA2oi	3.717	3.724
Ca4 – OA1zi	2.454	2.442
Ca3 – OA2zi	4.186	4.027
Ca3 – Odooi	2.432	2.422

In order to carry out defect calculations, the potentials used in these simulated structures were used with the same structure refinements to prepare supercells and "non-ideal" structures, i.e. datasets containing vacancies at appropriate cation

positions. These supercells and non-ideal structures gave similar agreement to the initial calculations on the single unit cell "ideal" structures and they could therefore be used to model the migration of cations from their equilibrium positions into vacancies.

7.5 Results and discussion

7.5.1 Dielectric spectroscopy

(a) Albite

Figures 7.7 (a) and (b) show the behaviour of ε' and σ with temperature and frequency, respectively. The dielectric constant has a value close to 8 for all frequencies at room temperature, rising slightly at low frequencies up to 800 K, after which there is a dramatic increase (the greatest changes being at low frequencies). Similar behaviour is found for the conductivity, except that the low frequency conductivity remains low at all temperatures and the high frequency conductivity increases dramatically above 800 K.

The temperature dependence of ε' and tan δ as a function of frequency between 963 K and 1073 K is shown in Figures 7.8 (a) and (b), respectively. There was no significant dielectric loss peak below 963 K. The temperature dependence of the frequency of the maximum absorption follows an Arrhenius relation as shown in Figure 7.9, and the activation energy is calculated to be 1.33 ± 0.02 eV (128.3 ± 0.2 kJmol^{-1}).

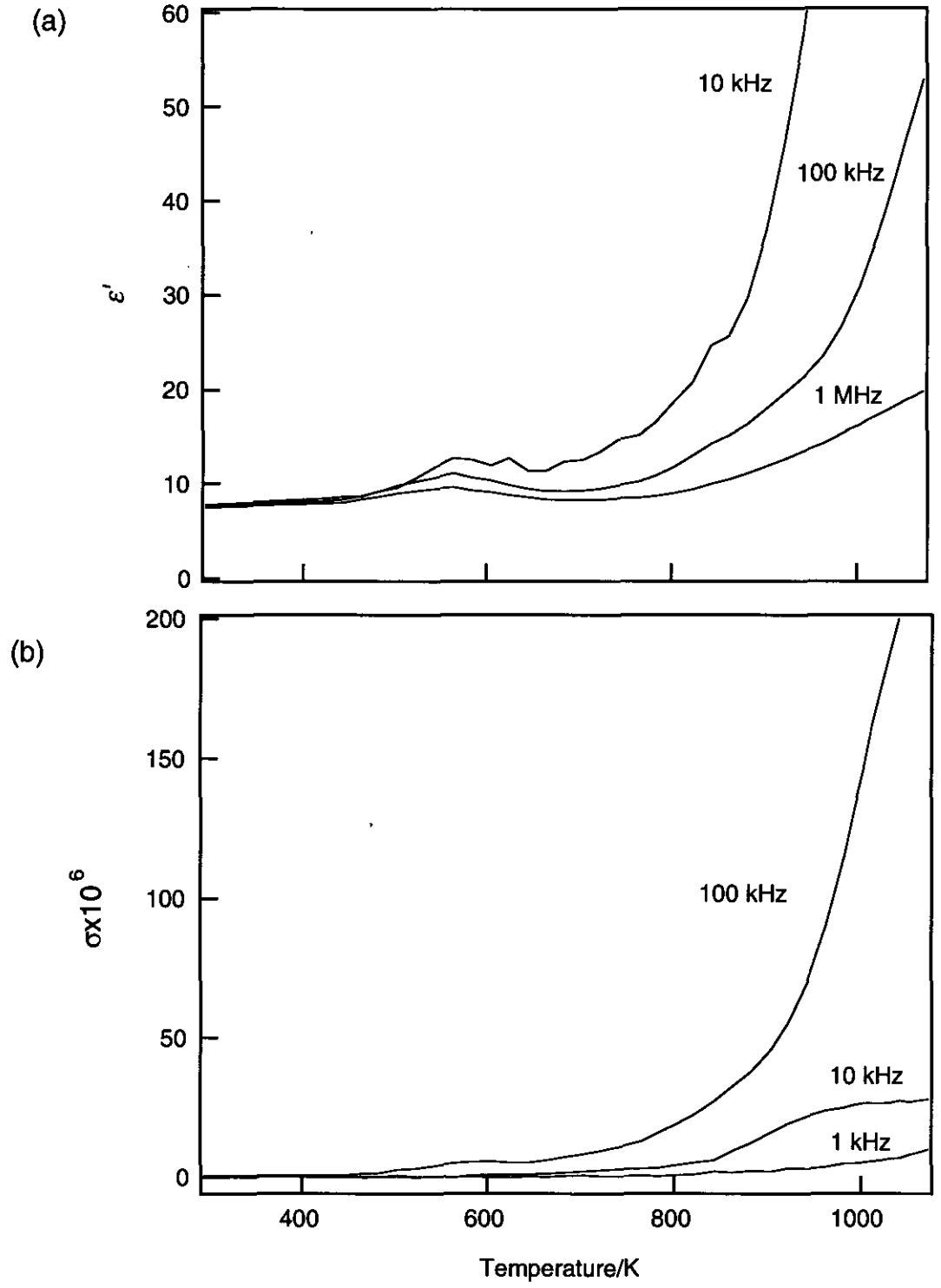

Figure 7.7 Temperature dependence of (a) ε'; (b) σ of albite at selected frequencies.

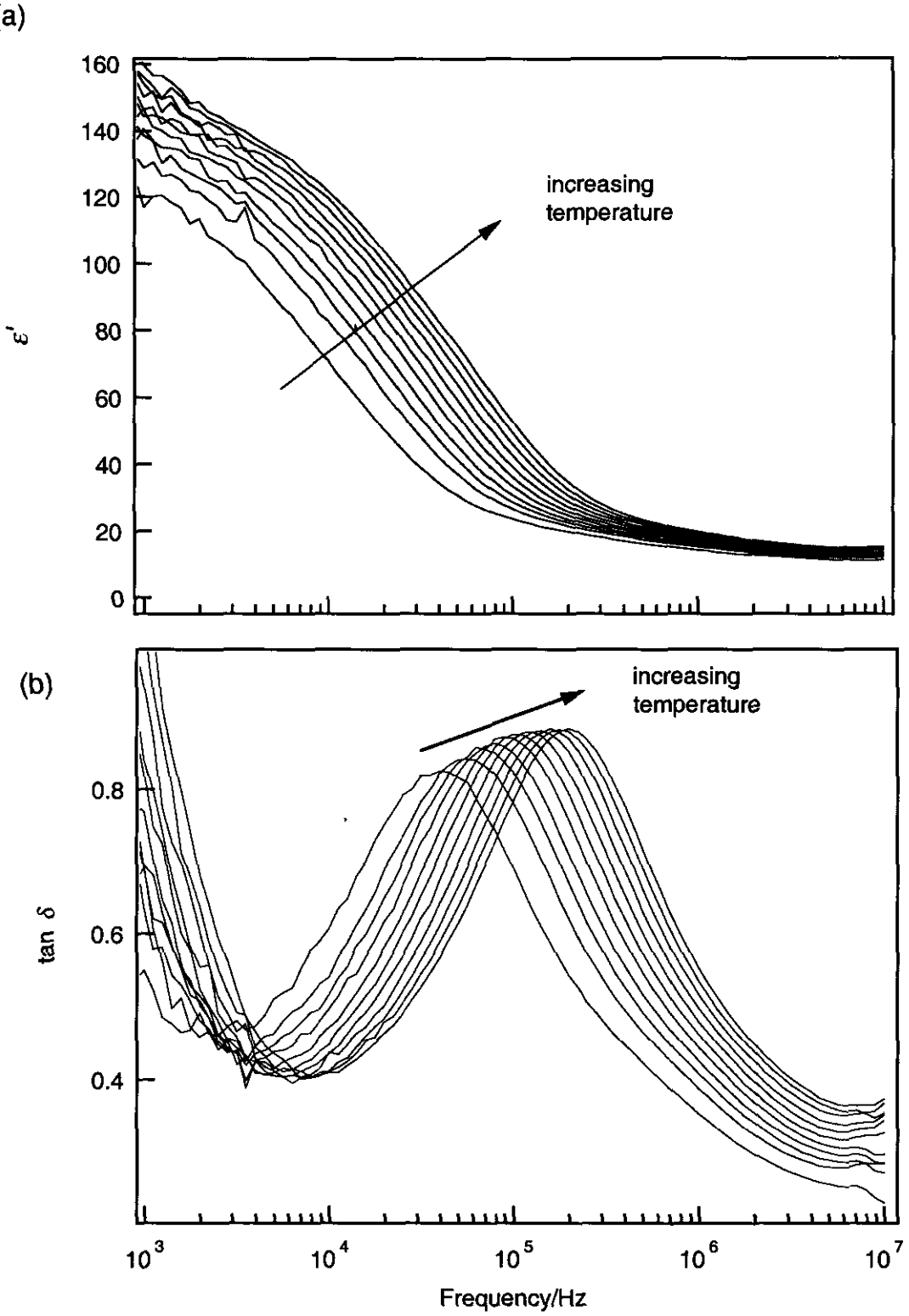

Figure 7.8 Temperature and frequency dependence of (a) ε'; (b) tan δ of albite between 963 K and 1073 K.

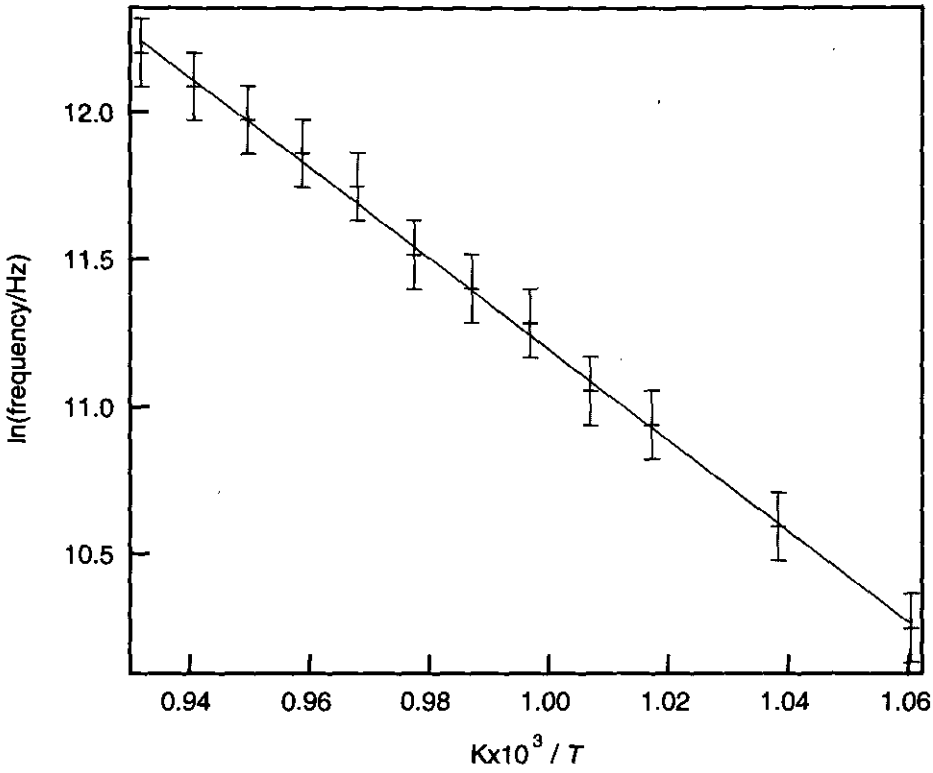

Figure 7.9 Arrhenius plot showing the temperature dependence of the maxima in the dielectric loss for albite. The gradient of the line indicates an activation energy of 1.33 ± 0.02 eV. The error bars represent the uncertainty in determining the peak positions.

(b) K-feldspar

Figures 7.10 (a) and (b) show the behaviour of ε' and σ with temperature and frequency, respectively. The temperature dependence of ε' and tan δ as a function of frequency between 902 K and 1083 K is shown in Figures 7.11 (a) and (b), respectively. The dielectric constant has a value close to 8 at room temperature, for all frequencies, and it can be seen that patterns of behaviour are very similar to those of albite. The temperature dependence of the frequency of the maximum absorption follows an Arrhenius relation as shown in Figure 7.12, and the activation energy is calculated to be 1.33 ± 0.03 eV (128.4 ± 3.0 kJmol^{-1}).

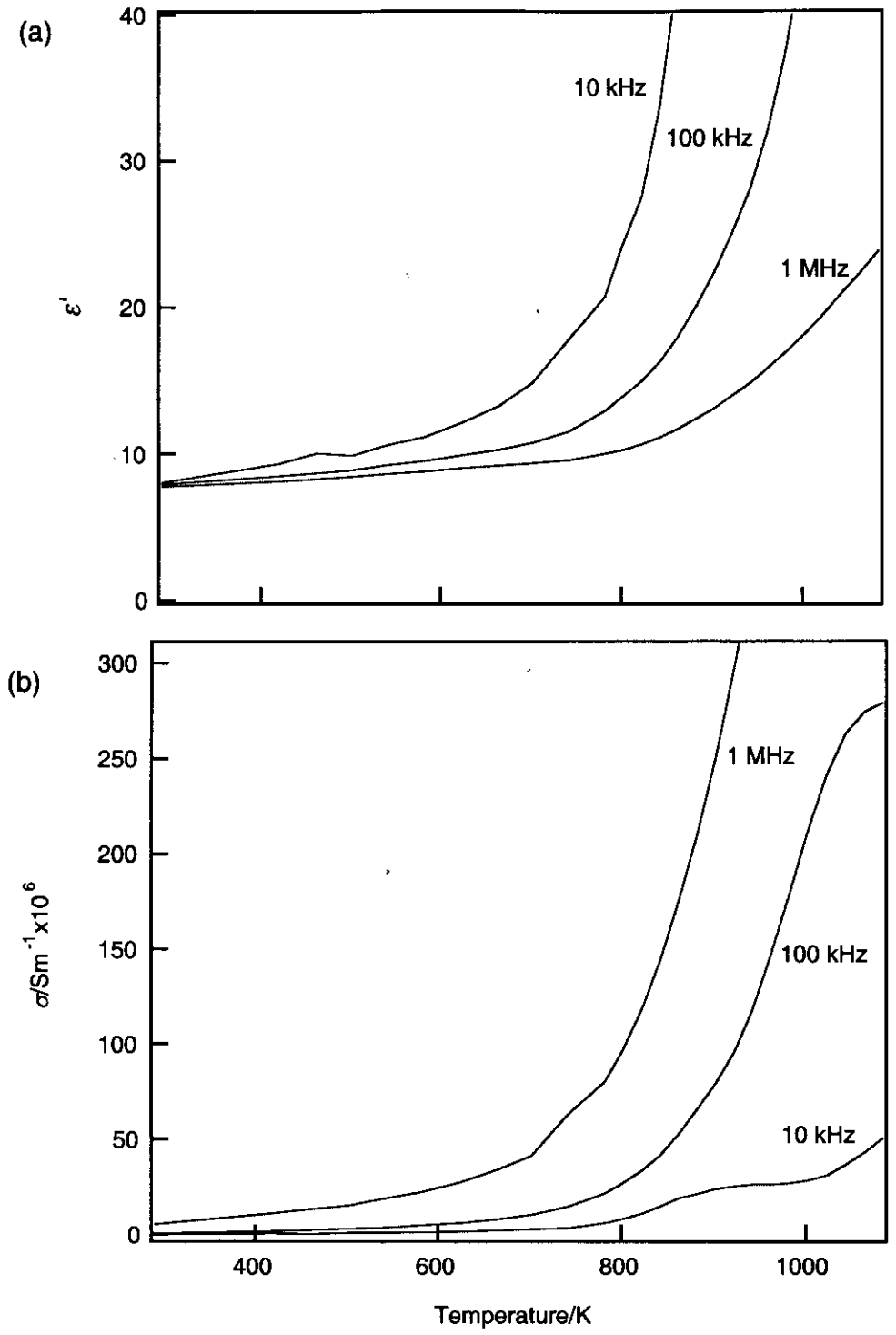

Figure 7.10 Temperature dependence of (a) ε'; (b) σ of K-feldspar at selected frequencies.

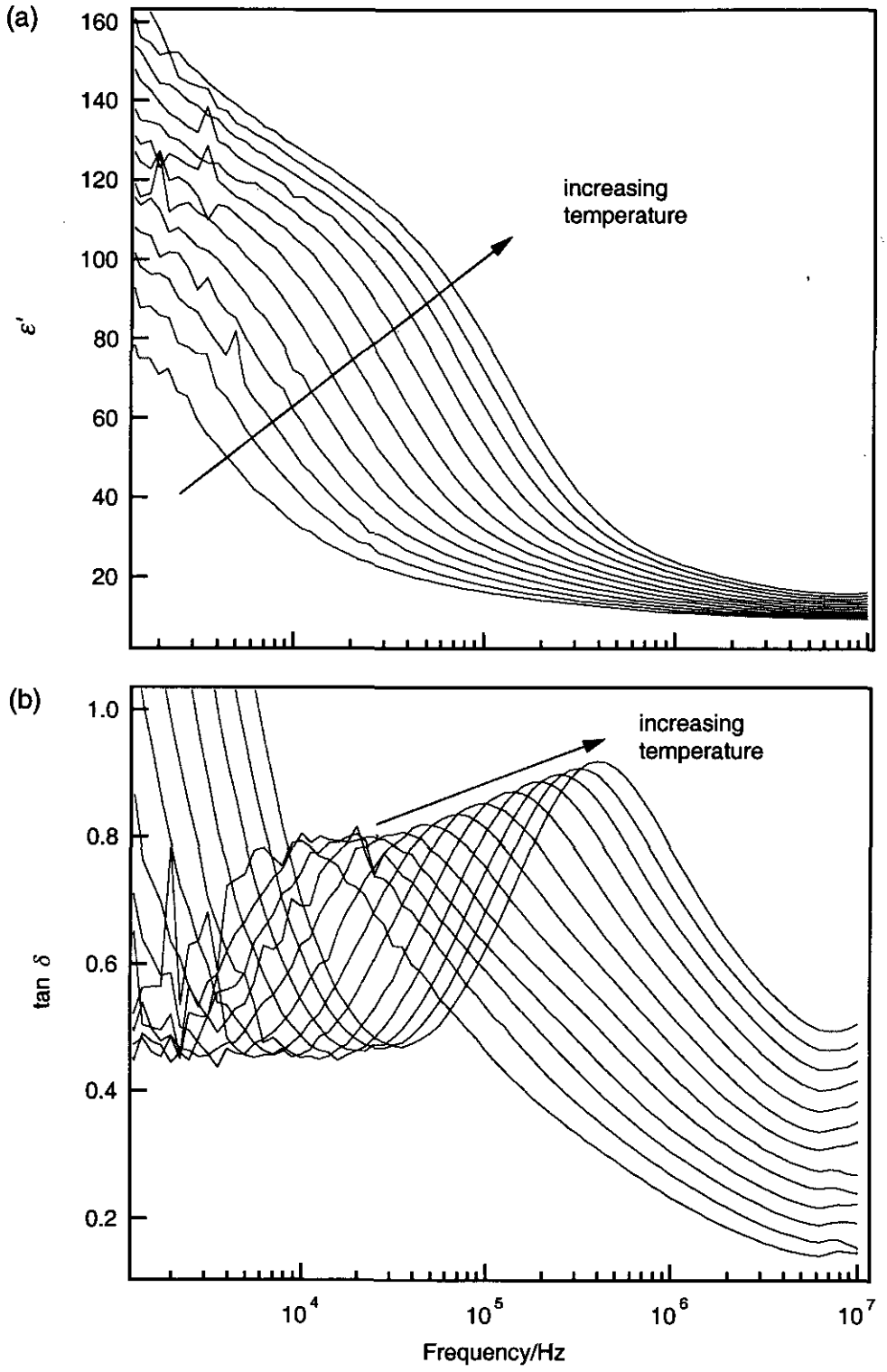

Figure 7.11 Temperature and frequency dependence of (a) ε'; (b) tan δ of K-feldspar between 902 K and 1083 K.

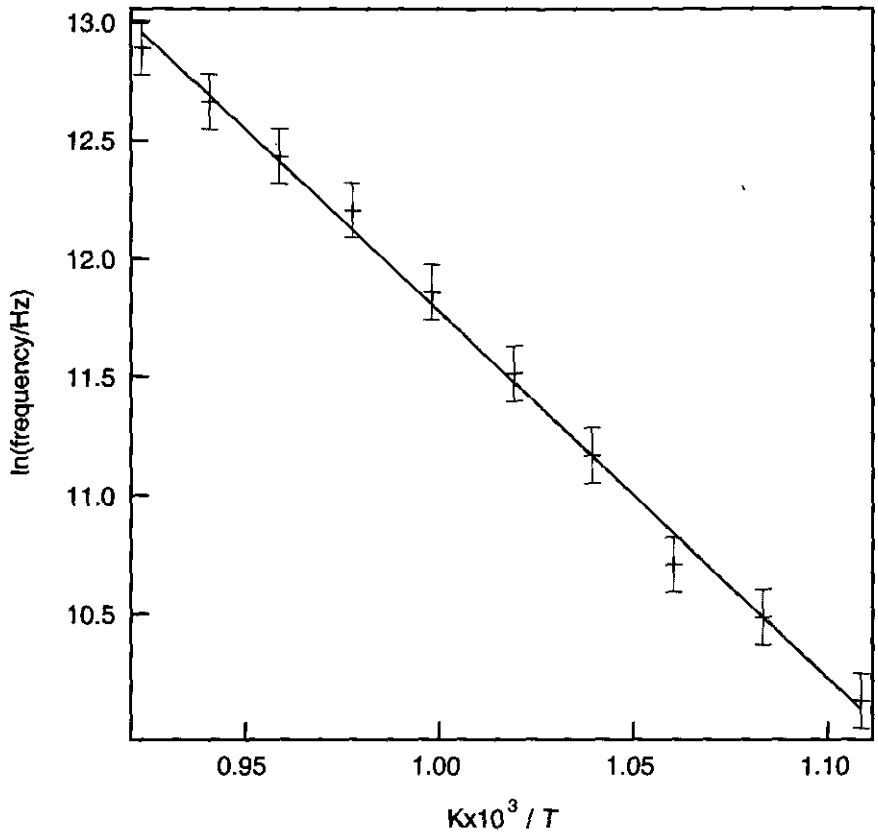

Figure 7.12 Arrhenius plot showing the temperature dependence of the maxima in the dielectric loss for K-feldspar. The gradient of the line indicates an activation energy of 1.33 ± 0.03 eV. The error bars represent the uncertainty in determining the peak positions.

(c) Anorthite

Figures 7.13 (a) and (b) show the behaviour of ε' and σ with temperature and frequency, respectively. The dielectric constant has a value close to 6 for all frequencies at room temperature. This is lower than that found for albite (~8) and K-feldspar (~8) but apart from this difference, the patterns of behaviour are very similar. The temperature dependence of ε' and tan δ as a function of frequency between 875 K and 1073 K is shown in Figures 7.14 (a) and (b) respectively. An Arrhenius plot showing the temperature dependence of the frequency of the maximum absorption is shown in Figure 7.15. The activation energy was calculated to be 1.32 ± 0.03 eV (127.27 ± 2.92 kJmol^{-1}).

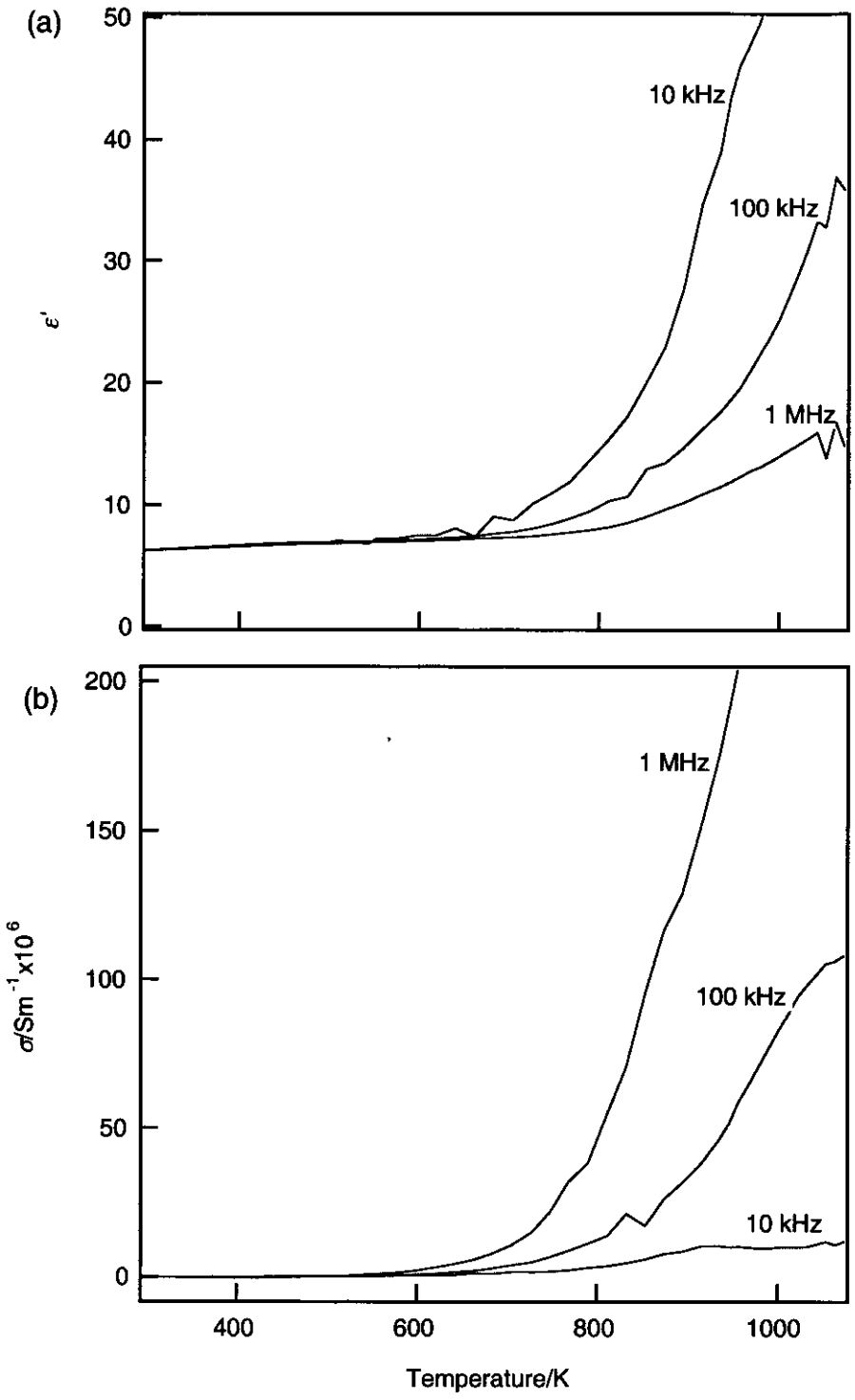

Figure 7.13 Temperature dependence of (a) ε'; (b) σ of anorthite at selected frequencies.

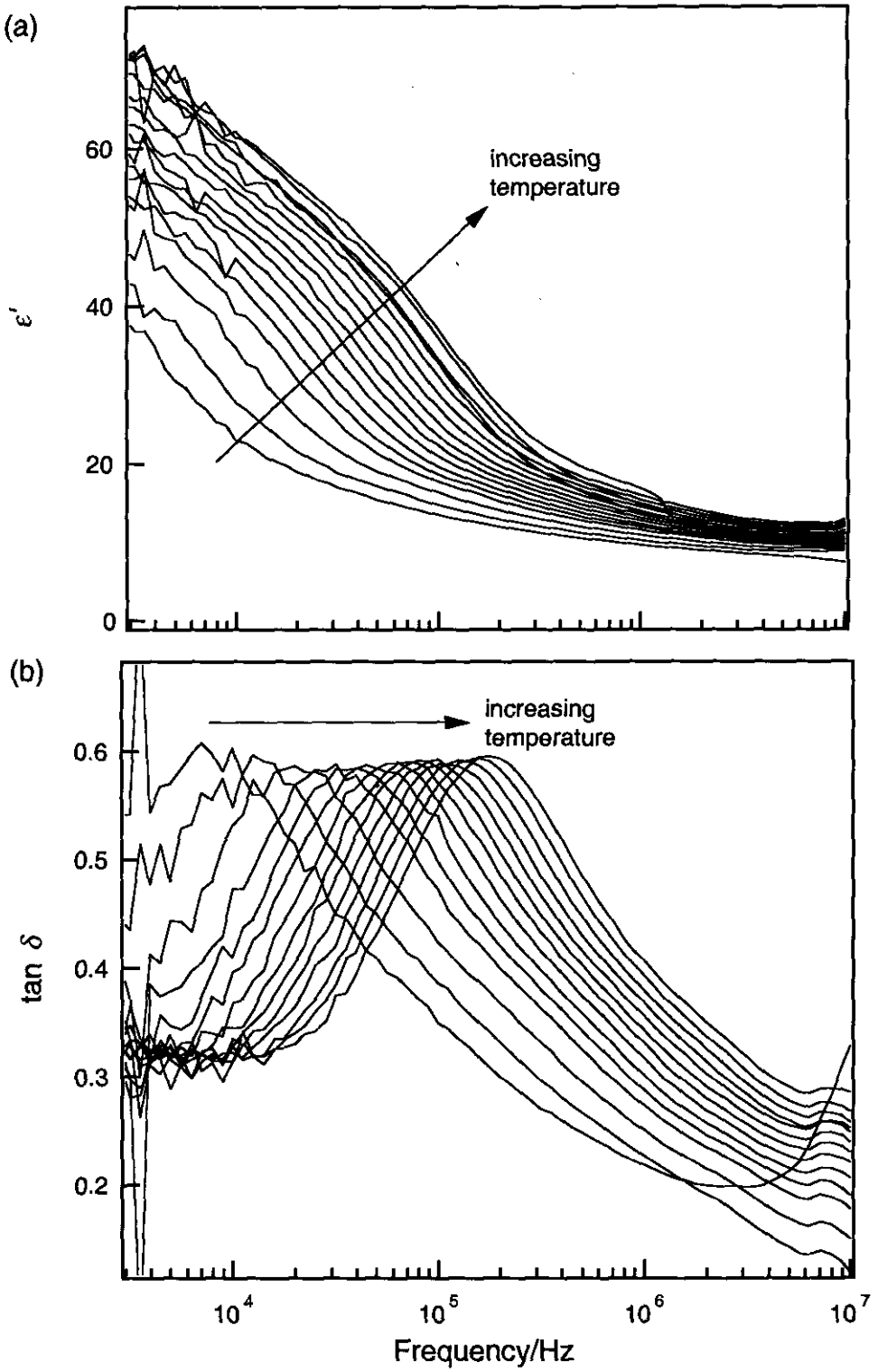

Figure 7.14 Temperature and frequency dependence of (a) ε'; (b) tan δ in anorthite between 936 K and 1073 K.

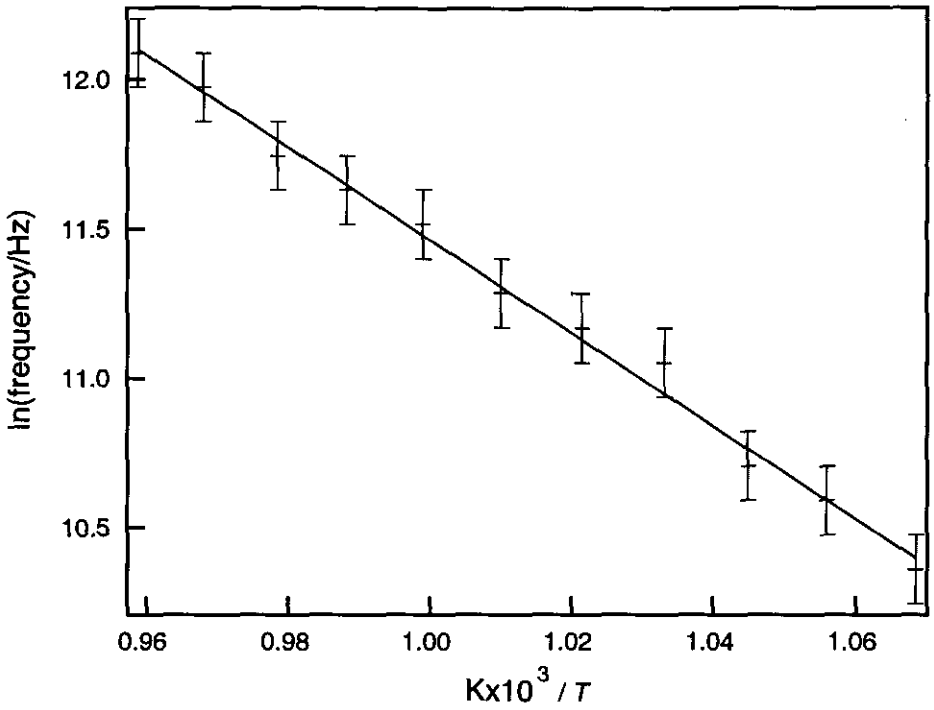

Figure 7.15 Arrhenius plot showing the temperature dependence of the maxima in the dielectric loss for anorthite. The gradient of the line indicates an activation energy of 1.32 ± 0.03 eV. The error bars represent the uncertainty in determining the peak positions.

It is not possible, on the basis of these dielectric measurements alone, to attribute the activation energies measured for the feldspars to specific cation migration processes. Although the framework geometry of these minerals is similar, the interstitial ions vary in size and charge, and the migration processes were therefore investigated further using atomistic simulation processes.

7.5.2 Ion migration processes and energetics

(a) Albite

A possible migration pathway for a Na^+ ion in albite would be to follow a trajectory in the (010) plane between an occupied and vacant Na site as shown in Figure 7.16. Initial calculations were done on a single unit cell in which a single Na vacancy had been created. In order to determine the approximate route taken by a migrating Na^+ ion between the two sites, lattice energy calculations were carried out across the (010)

plane of translation. The result of these calculations suggested that the optimum migration route would be a linear pathway as shown in Figure 7.17.

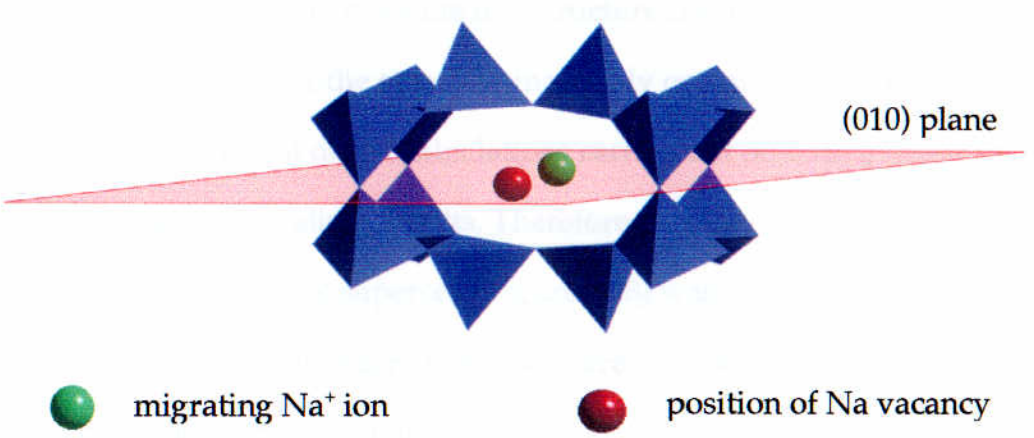

Figure 7.16 A view of part of the albite structure, showing the (010) plane and the positions of the migrating Na^+ ion and the vacant site.

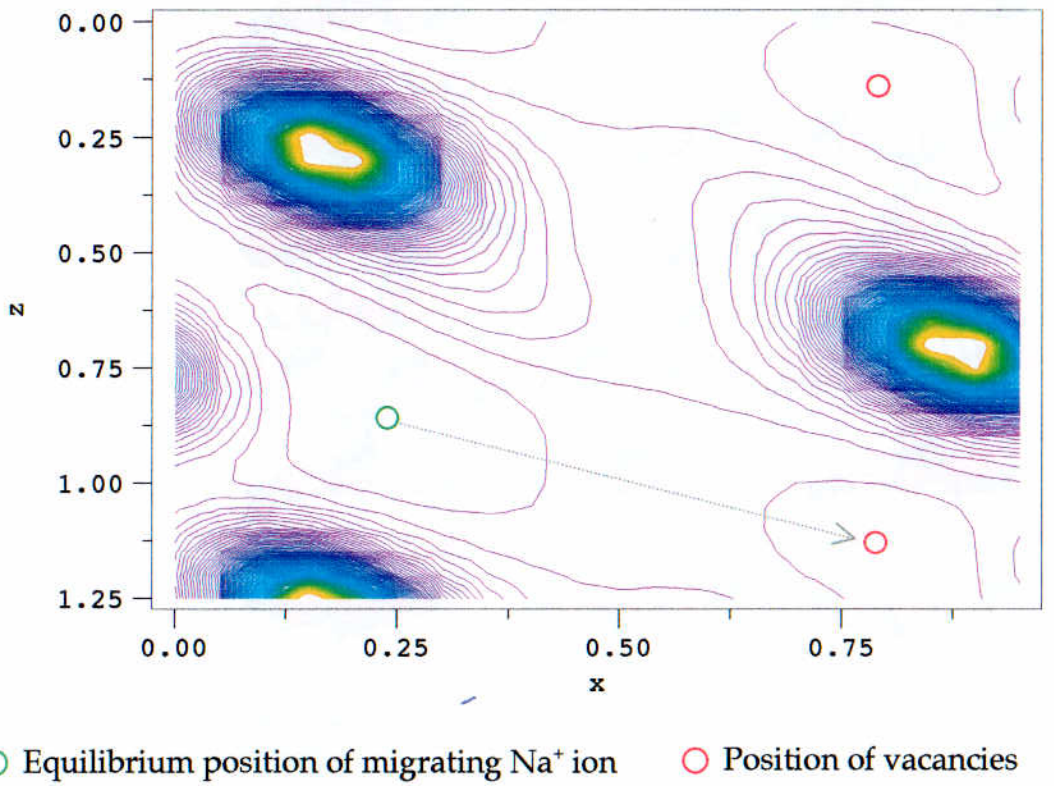

Figure 7.17 Contour plot showing the variation in lattice energy in the (010) plane in albite. The migration pathway of a migrating Na^+ ion and a vacant Na site is indicated.

The migration pathway shown above seems reasonable. However, one Na vacancy per unit cell represents 25% of the total sodium content of the albite, and, as can be seen from the contour plot, it results in a structure comprising a channel of adjacent vacant sites. Relaxation of the structure inevitably occurs around these vacancies (Kieffer, 1999) and initial defect calculations carried out on both a single unit cell, and a $3y$ supercell gave unrealistic results. Therefore, in order to create isolated vacancies within the structure, a $2a2c$ supercell (Figure 7.18) was used for the subsequent defect calculations along the migration pathway, thereby avoiding the problem of having adjacent vacancies in the (010) plane.

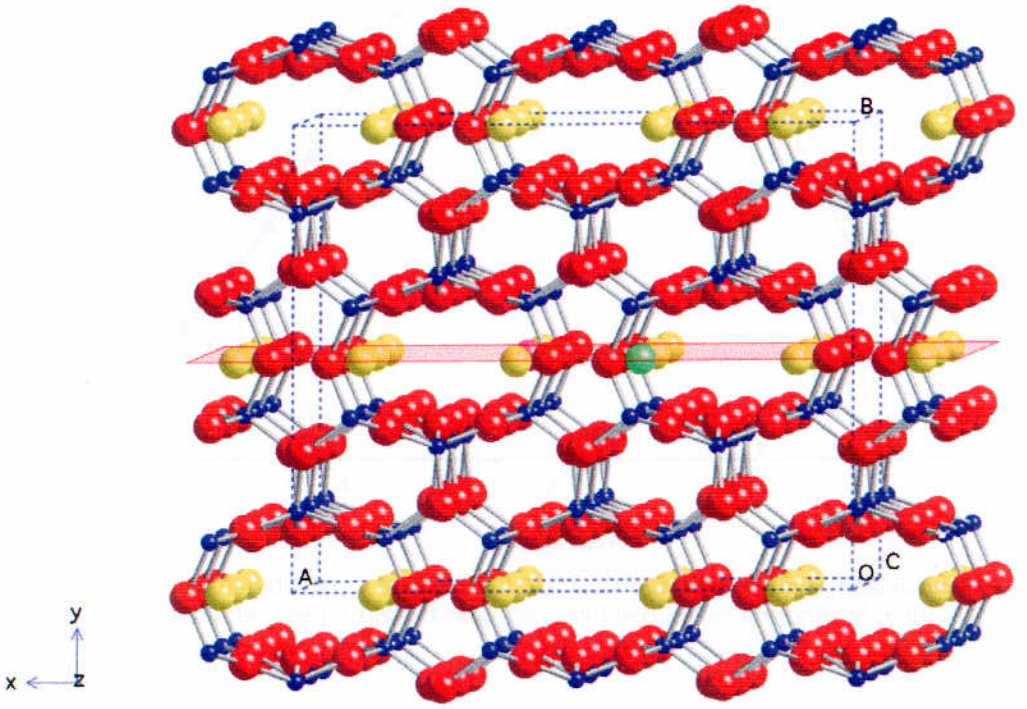

Figure 7.18 $2a2c$ albite supercell. The migrating ion (green) and the position of the Na vacancy (pink) are shown in the (010) plane.

The migration energy of the Na^+ ion was determined by calculating the defect energy at different points along the pathway, allowing full relaxation of the lattice at each point. In this way the saddlepoint configuration was identified and the energy barrier to migration was calculated. Figure 7.19 shows the calculated energy profile for the migration of the Na^+ ion as described above. The energy barrier is calculated to be 1.31 eV.

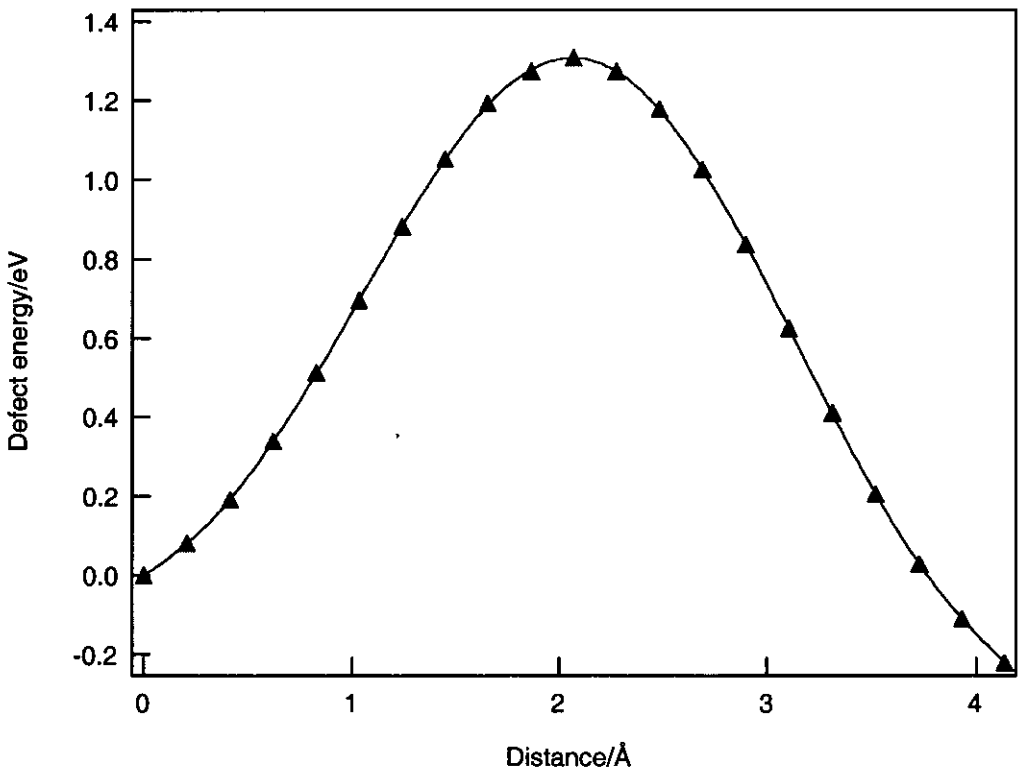

Figure 7.19 The calculated energy profile for a Na^+ ion migrating from its equilibrium position to an adjacent vacancy in albite. The points indicate the calculated defect energies at points along the linear migration pathway.

This value is in very good agreement with the activation energy determined from the dielectric measurements (1.33 ± 0.02 eV), and it would therefore be reasonable to assume that the process being observed in the dielectric spectroscopy is due to the migration of Na^+ ions along the trajectory described above.

(b) K-feldspar

The sanidine structure (Phillips and Ribbe, 1973) used for the assessment of the potential model for K-feldspar contained approximately 10% Na, 90% K in the cation sites (as did the sample BM1924,1244 which was used for the dielectric measurements). There are 4 cation sites per unit cell of $KAlSi_3O_8$ therefore, in order to simulate the migration of K^+ within the structure as accurately as possible, a $2a2c$ supercell was created in which there was one vacant cation site, one K^+ ion with full site occupancy and all other sites were given a K/Na occupancy such that the overall cation composition remained at 10% Na, 90% K. As with albite, the creation of the supercell avoided the problem of relaxation of the structure around a channel of adjacent vacancies.

The most likely migration pathway for a K^+ ion within the sanidine structure is along a trajectory, similar to that mapped out for albite, in the (010) plane. Such a pathway between an occupied and vacant site would offer the most energetically favourable route in terms of the proximity of the K^+ ion to the nearest neighbour oxygens at the saddlepoint position. The migration energy of the K^+ ion was therefore determined by calculating the defect energy at several points along this pathway. In this way the saddlepoint configuration was identified and the energy barrier to migration was calculated. The calculated energy profile is shown in Figure 7.20, and the energy barrier to migration is calculated to be 0.99 eV.

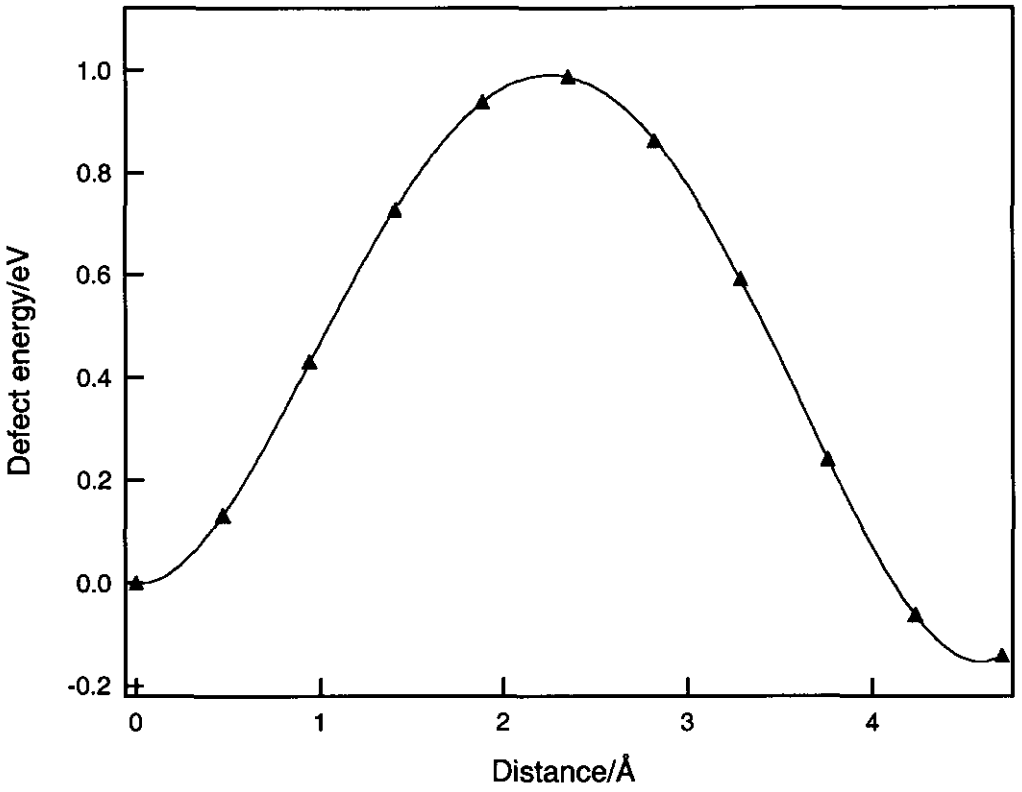

Figure 7.20 The calculated energy profile for a K^+ ion migrating from its equilibrium position to an adjacent vacancy in sanidine. The points indicate the calculated defect energies at points along the linear migration pathway.

Other similar migration pathways in the (010) plane were also investigated. These are shown, in addition to the pathway described above, in Figures 7.21 and 7.22. They yielded higher activation energies as a result of the narrower bottleneck width (measured between the nearest oxygens in the (010) plane at the saddlepoint). The results of these calculations are shown in Table 7.5 and the corresponding energy profiles are shown in Figure 7.23.

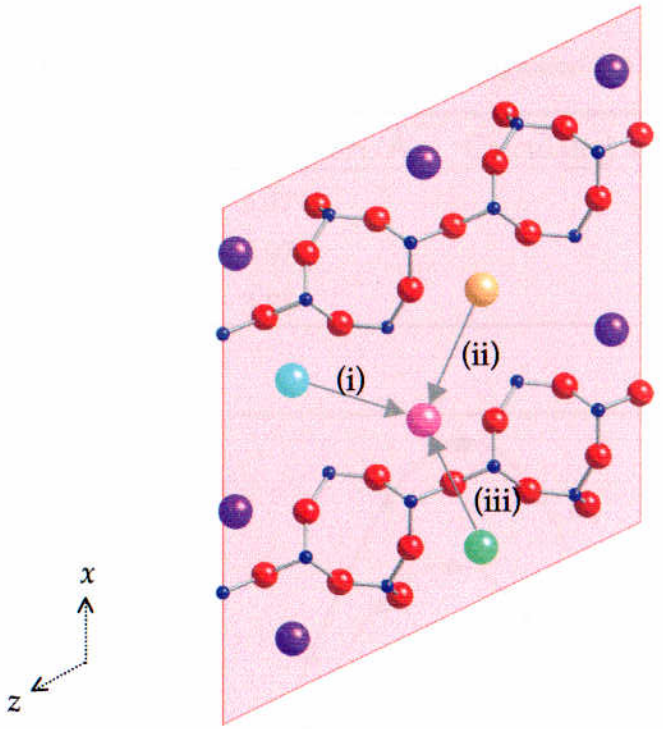

Figure 7.21 View of the (010) migration plane in the sanidine structure showing three possible K^+ ion migration pathways. The migrating ions/ pathways are: (i) turquoise; (ii) orange; (iii) green and the vacant K site is shown in pink..

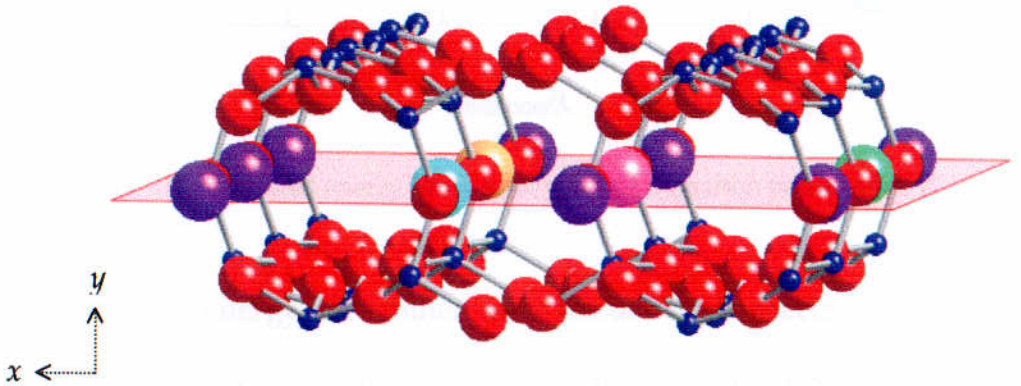

Figure 7.22 View down ~[001] of the sanidine structure showing the three possible K^+ ion migration pathways described above.

Table 7.5 Calculated activation energies for migration of K^+ in the (010) plane in sanidine.

Channel	Bottleneck width/Å	Calculated activation energy/eV
(i)	5.47	0.99
(ii)	3.97	2.29
(iii)	3.88	2.92

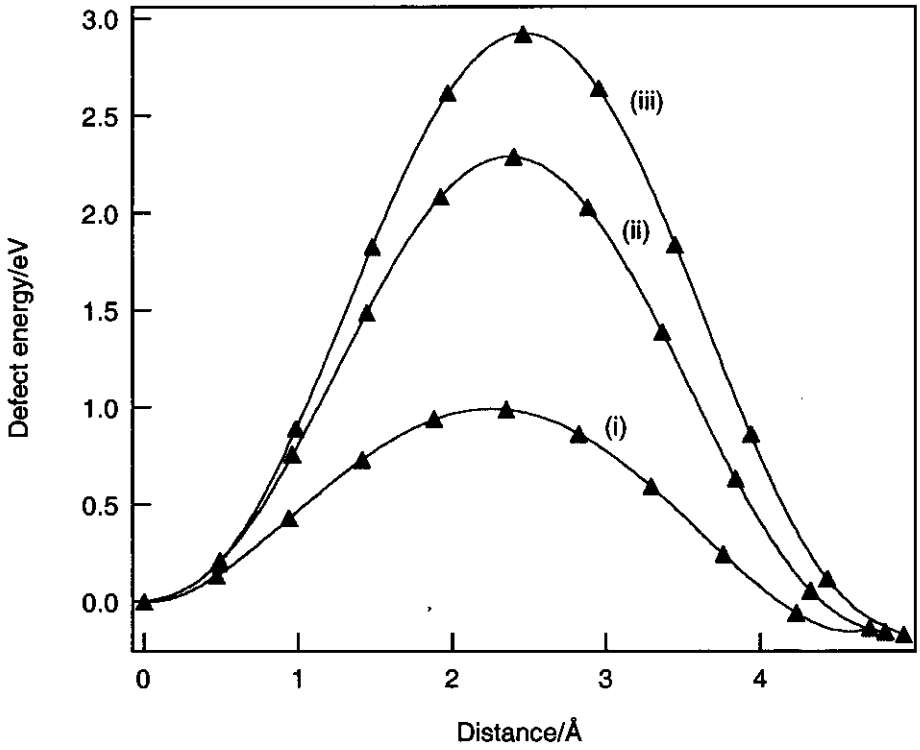

Figure 7.23 The calculated energy profiles for possible migration pathways of K^+ in the (010) plane in sanidine.

The activation energy determined from the dielectric spectroscopy measurements was 1.33 ± 0.03 eV. Although this value does not agree closely with any of the calculated values, this does not necessarily imply that the proposed migration pathway is incorrect. It can be seen from Table 7.5 that a difference in the channel width of ~ 0.1 Å may result in a difference in defect energy of ~ 0.6 eV. The calculated value of the *a* parameter of the simulated structure used for these calculations (Table 7.4 (b)) was 4.4 % higher than the experimentally determined value, i.e. there was a

difference of 0.38 Å between the two values of *a*. This means that the actual channel width for this ion migration pathway in the *ac* plane is ~ 0.13 Å less than the value used for the calculation of the K^+ migration energy. This discrepancy could therefore account for the difference between the calculated and experimentally determined activation energies, and it would still appear that the most likely ion migration pathway for a K^+ ion in the sanidine structure is as described previously.

In view of the fact that the albite and sanidine structures are very similar, it is somewhat surprising to find that the experimentally determined activation energy for the migration of a small Na^+ ion is almost identical to that found for the migration of the much larger K^+ ion in the (010) plane. It can be seen from the lattice parameters given in Table 7.4 that sanidine has a more open structure than albite and the experimentally determined value of the *a* parameter is ~ 2.9 % higher in sanidine. However, this fact alone cannot be used to explain the similarity in the experimentally determined activation energies. Additional calculations were therefore carried out on both structures.

An interstitial K^+ ion was inserted into the albite structure and the defect energy measured at the saddlepoint of the trajectory followed by an Na^+ ion in the same (010) plane. Similarly, the defect energy of an interstitial Na^+ ion was measured at the saddlepoint of the trajectory followed by a K^+ ion in sanidine. The results of these calculations are compared with those of the previously described defect calculations in Table 7.6.

Table 7.6 A comparison of the defect energies of interstitial Na^+ and K^+ ions in albite and sanidine.

Interstitial at saddlepoint	Defect energy/eV
K+ ion in albite	1.86
Na^+ ion in albite	1.31
K^+ ion in sanidine	0.99
Na^+ ion in sanidine	0.70

It can be seen from these results that the more open structure of sanidine facilitates a lower energy migration pathway for either cation compared to albite. Although the bottleneck width of the two structures differ, (4.57 Å in albite compared to 5.47 Å in sanidine), both structures relax around the migrating cation to accommodate it at the saddlepoint as shown in Figures 7.24 and 7.25.

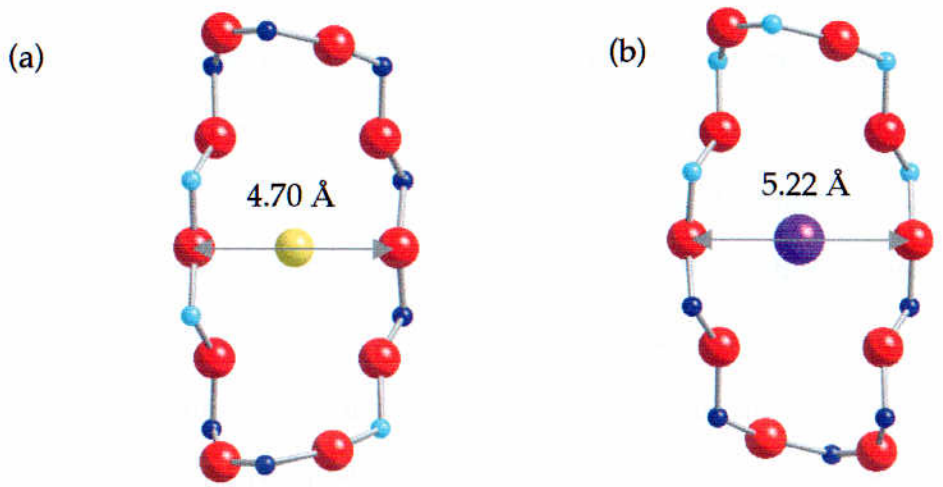

Figure 7.24 Relaxation of the migration channel in albite with the migrating (a) Na^+ ion; (b) K^+ ion at the saddlepoint (viewed down [101]).

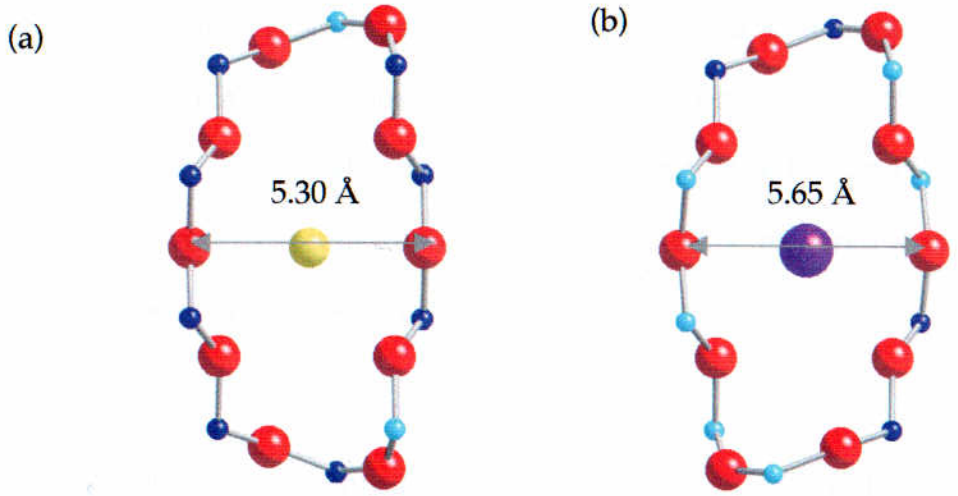

Figure 7.25 Relaxation of the migration channel in sanidine with the migrating (a) Na^+ ion (b) K^+ ion at the saddlepoint (viewed down [101]).

It can be seen from Figure 7.24 that the channel in albite widens by ~ 0.1 Å and ~ 0.7 Å to allow the migration of the Na^+ or K^+ ions, respectively; the corresponding channel in sanidine contracts around the smaller Na^+ ion by ~ 0.17 Å when it is at the saddlepoint, but has to expand by ~ 0.18 Å to allow the migration of larger K^+ ion through the same bottleneck (Figure 7.25). These observations illustrate how the feldspar framework responds to ion movement within the structure. The presence of vacancies and interstitial ions appear to have a significant effect on the dimensions of the interconnecting channels between the cation sites. It may therefore be appropriate to regard the ion migration process which occurs in these feldspars as a cooperative process, involving interstitial cations and framework relaxation, rather than merely a static framework through which ions diffuse. A molecular dynamics study carried out on mixed-alkali silicates (Kieffer, 1999) has suggested that the presence of an alkali cation or a vacancy affects the local structure surrounding it, and that the

migration of cations invokes structural relaxations which go beyond just the widening and closing of the passageway between two stable sites. Kieffer's observations suggest that cation sites are actually created (and recreated) ahead of the migrating ion, which would consequently have an effect on the energetics of the migration process. If this is also the case in the migration of Na^+ and K^+ ions in albite and sanidine, then a molecular dynamics study would be required to establish the likelihood of these processes occurring.

(c) Anorthite

The anorthite structure (Wainwright and Starkey, 1970) used for the assessment of the potential model was pure end-member anorthite. The sample used for the dielectric measurements contained approximately 4% Na in the cation sites. The calculated lattice parameters of a simulated structure containing a partial Ca/Na occupancy in the cation sites varied by an average of 0.58 % from the experimentally determined values, compared to 0.62 % for the pure end member (Table 7.4 (c)). Therefore, as the structures gave similar agreement, all subsequent simulations were done on the pure Ca-anorthite structure. There are 8 cation sites per unit cell of $CaAl_2Si_2O_8$ therefore, in order to simulate the migration of Ca^{2+} within the structure as accurately as possible, a 2*a* supercell was used for the defect calculations. (The ordering in anorthite results in a doubling of the *c* lattice parameter of the unit cell compared to albite and sanidine, therefore it was unnecessary to use a 2*a*2*c* supercell as used for the other feldspar structures.)

A possible migration pathway for a Ca^{2+} ion within the anorthite structure is along a trajectory, similar to that mapped out for albite, in the (010) plane. Such a pathway between an occupied and vacant site would appear to offer the most energetically

favourable route in terms of the proximity of the Ca^{2+} ion to the nearest neighbour oxygens at the saddlepoint position. The migration energy of the Ca^{2+} ion was therefore determined by calculating the defect energy at several points along this pathway in order to identify the saddlepoint configuration and calculate the energy barrier to migration. The calculated energy profile is shown in Figure 7.26, and the energy barrier to migration is calculated to be 2.84 eV. This value is much higher than the experimentally determined activation energy measured using dielectric spectroscopy (1.32 ± 0.03 eV).

One possible reason for this high calculated energy barrier to migration is that the strong Ca-framework interaction in the *ac* plane may account for the contraction of the framework around the cation sites. As a consequence, the width of the migration channel at the bottleneck in the (010) plane is just 3.85 Å ; this is very much narrower than the corresponding channel widths in both albite (4.57 Å) and sanidine (5.47 Å). The results of the simulations would suggest that the Ca^{2+} ions are largely immobilised within the anorthite structure, as appears to be the case for Ca^{2+} ions in yoshiokaite (Chapter 5).

The dielectric measurements suggested that an ion migration process with an activation energy of 1.32 ± 0.03 eV was taking place. The average height of the dielectric loss peaks for anorthite (~ 0.6) was significantly lower than that observed for albite (~ 0.9) or K-feldspar (~ 0.9). It is therefore possible that the observed dielectric process in anorthite can be accounted for by migration of Na^+ ions. Defect calculations were therefore carried out to investigate Na^+ migration in anorthite. An interstitial Na^+ ion was moved along the same trajectory in the (010) plane as had been used for Ca^{2+}. The calculated energy profile is shown in Figure 7.26, and the energy barrier to migration is calculated to be 1.73 eV.

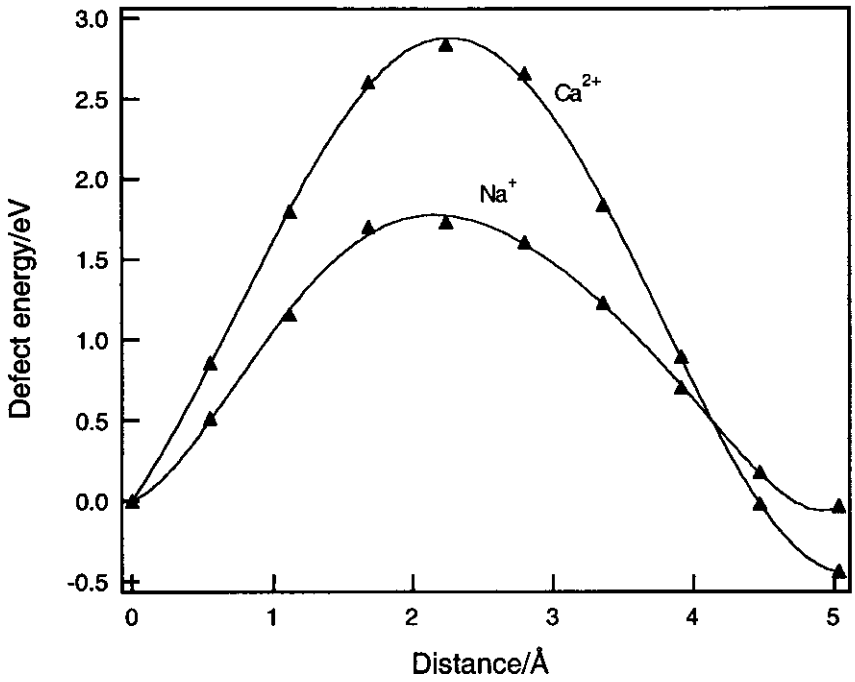

Figure 7.26 The calculated energy profiles for Ca^{2+} and Na^{+} ion migration in the (010) plane in anorthite. The points indicate the calculated defect energies at points along the migration pathway.

There is some evidence from studies of the mixed-alkali effect in silicates (Kieffer, 1999) that when migrating ions arrive at sites previously occupied by dissimilar cations, the consequent structural rearrangements which occur during ion migration may modify the energetics of the process. Although the modelling techniques used in the present study allow relaxation of the lattice surrounding a defect, the dynamic adjustment of the framework during migration may not be effectively modelled. This would clearly affect the magnitude of the calculated energy barrier to the migration of Na^{+} ions in the anorthite structure.

7.6 Conclusions

Although the feldspar structure is a stuffed framework, it is markedly different from the other minerals studied in this work. Ion migration pathways are not immediately apparent as, unlike structures such as nepheline and β-eucryptite, there is no distinct

channel network. Nevertheless, it has been possible to model migration pathways and calculate the energetics for ion migration in albite , K–feldspar and anorthite. The agreement between the calculated and observed activation energies for these processes has not been consistent, but in view of the complexity of the structures and the variable response of the framework to changes in site occupancy the following conclusions can be made:

- The migration of interstitial cations in the feldspar structures occurs in the (010) plane. This is in agreement with the diffusion studies described in section 7.2.2 (Giletti et al., 1974; Petrovic, 1972).
- The most energetically favourable pathway for ion migration in the feldspars is a linear pathway between cation sites in the (010) plane.
- The energy barriers to Na^+ and K^+ ion migration are relatively low compared with Ca^{2+} ions; the possibility of Ca mobility via a similar mechanism as established for Na and K is unlikely.

Although there may not be the scope for long range cooperative ionic motion within the feldspar structure, it is not impossible that short-range cooperative mechanisms, involving clusters of cations and vacancies, may occur. The results of the computer simulations have shown how the presence of vacancies and interstitial ions can have a significant effect on the width of a bottleneck, and hence the energy barrier to migration. Any degree of cooperative motion would therefore have an effect on both the calculated and the experimentally determined activation energies. This could be established if the present work was extended by carrying out a molecular dynamics study on these structures.

Chapter 8

Conclusions

Contents

8.1 Crystal Chemical Systematics

A long-term aim of this investigation was to develop *transferable* crystal-chemical data, relating basic structural features and the nature of inter-framework cations to mobility patterns and activation energies of ion migration processes. By systematically investigating the influence of framework geometry, ion size and ion charge on ion mobility, independently of the other constraints, the data could then be used in a predictive capacity in the study of related framework minerals.

8.1.1 The effect of framework geometry, ionic radius and charge on ion mobility

The activation energies for ion hopping processes will not only be dependent on the characteristics of the migrating ions, but are also likely to have a dependence on the framework geometry and the influence of nearby cationic species. In addition to this, ion migration mechanisms in different structures may change with composition, stoichiometry and temperature. Consideration of all of these crystal-chemical factors may lead to an improved understanding of the relative mobilities of ions and ion migration mechanisms.

A variety of framework topologies has been investigated in the present study. These have included the distorted tridymite framework in nepheline and yoshiokaite and the β-quartz derivative, β-eucryptite. In addition to these minerals, the framework structures of the feldspars have been investigated by focussing on albite, sanidine and anorthite. Although the feldspars do not have a distinct channel structure, they have large irregular cavities which, in common with the stuffed-silica minerals, accommodate cations within the aluminosilicate framework.

In a given structure, the mobility of the ions will be subject to the constraints of geometry - the porosity of the structure compared to the size of the ion (Dowty, 1980). Clearly, very compact structures will not allow the diffusion of large ions and the amount of space in a crystal structure should be an important factor in ion mobility. The anion porosity of a structure is defined as the volume of the unit cell minus the volume of the included anions, divided by the unit cell volume (expressed as a percentage) (Sippel, 1963). It has been suggested (Dowty, 1980) that the relative mobility of a given cation in different minerals is strongly dependent on the porosity. However, the geometry/size of the individual diffusion channels must also play a significant role in the ionic mobility. As this is often determined by the nature (size and charge) of the interstitial cations, (as is seen in the structures of nepheline and kalsilite), the two are inextricably connected. One additional factor which may influence the effect of the framework on ion migration, is the Si/Al ratio in the structure. In stuffed silica derivatives this is dependent on the nature of the cationic stuffing species, as the need to maintain charge balance is satisfied by substitution of Si by Al. However, this effect is not likely to be very significant in a disordered structure.

Many crystal structures are anisotropic with respect to diffusion of interstitial cations. Various studies (Alpen et al., 1977; Follstaedt and Richards, 1976) have demonstrated the anisotropy of diffusion of Li^+ ions in β-eucryptite. While β-eucryptite is considered to be a one-dimensional superionic conductor, other channel structures, such as nepheline, also exhibit strong anisotropy of conductivity and ion transport can occur most easily along the structural channels (Roth and Böhm, 1986). However, there is some evidence (Petrovic, 1974) that alkali feldspars, which do not

have a distinct channel structure, also exhibit anisotropy of diffusion. Petrovic pointed out that possible interstitial sites and large cation vacancies are connected only in the (010) plane and that alkali diffusion must occur by a vacancy mechanism. This observation is in qualitative agreement with both his experimental observations of faster alkali diffusion in this plane, and also with the results of the computer modelling experiments carried out in this investigation, described in Chapter 7.

The principal contribution to the forces holding an atom in a particular site in oxides and silicates is the electrostatic or Madelung energy. The site energy is defined as the work required to bring the ion into the site from an infinite distance and it is usually assumed that there is a rough proportionality between site energy and activation energy. (This activation energy is the difference between the total energy of the crystal when the ion is in its initial position, and that when it is in a high-energy interstitial position.) In a given structure, ions with lower site energies will tend to be more mobile (Dowty, 1980), subject to the constraints of the geometry of the framework compared to the size of the ion. Site energies for cations are strongly correlated with z^2/d, where z is the formal charge on the ion and d is the average cation-anion distance (Ohashi, 1976; Raymond, 1971). There is a large body of evidence (Seifert and Virgo, 1975; Sipling and Yund, 1974; Virgo and Hafner, 1969) suggesting that the mobility of ions very much depends on site energy rather than ionic size. The diffusivities of Li^+, Na^+ and K^+ in quartz have been found to decrease in that order (Verhoogen, 1952), and the diffusivities of Mg^{2+}, Fe^{2+}, Ca^{2+} and Al^{3+} were undetectably small. It would therefore appear from this evidence that although ionic radius has an effect, charge is more important.

8.2 Discussion

The activation energies and ion migration mechanisms for the minerals investigated in this work have been discussed in individual chapters. In order to rationalise these data in a more general manner, consideration of these findings, together with the factors discussed above, will now be made for all of the systems studied.

8.2.1 Systematics

Activation energies, measured from the dielectric experiments, and calculated from the computer simulations of the ion migration mechanisms investigated, are summarised in Table 8.1 together with some structural data on each mineral system.

Table 8.1 A comparison of calculated and experimentally determined activation energies for ion migration processes in stuffed silica minerals

System	Ion	Ionic radius/Å	Approximate channel width/Å	Calculated E_a/eV	Experimentally determined E_a/eV
nepheline	Na^+	1.16	4.1	1.38	1.38
	Na^+	1.16	3.23	1.84	
	Na^+	1.16	5.3	0.28	
	K^+	1.52	4.1	2.5	
	K^+	1.52	5.3	1.15 -1.60	
yoshiokaite	Ca^{2+}	1.14	5.3	1.18	1.35
	Ca^{2+}	1.14	3.0	4.99	
	Ca^{2+}	1.14	4.6	3.56	
β-eucryptite	Li^+	0.90	4.9	1.44	1.08/1.33
	Li^+	0.90	3.6/5.2	0.15	
albite	Na^+	1.16	4.9	1.31	1.26
K-feldspar	K^+	1.52	5.47	0.99 -1.27	1.33
anorthite	Ca^{2+}	1.14	3.85	2.84	1.32
	Na^+	1.16	3.85	1.73	

Where the migration mechanism is assumed to be a simple hopping-type process, there is a pattern of behaviour linking the calculated activation energies to the channel width. Figure 8.1 illustrates this pattern for the migration of Ca^{2+} in yoshiokaite, anorthite and nepheline, and Na^{+} ions in anorthite, nepheline, albite and K-feldspar.

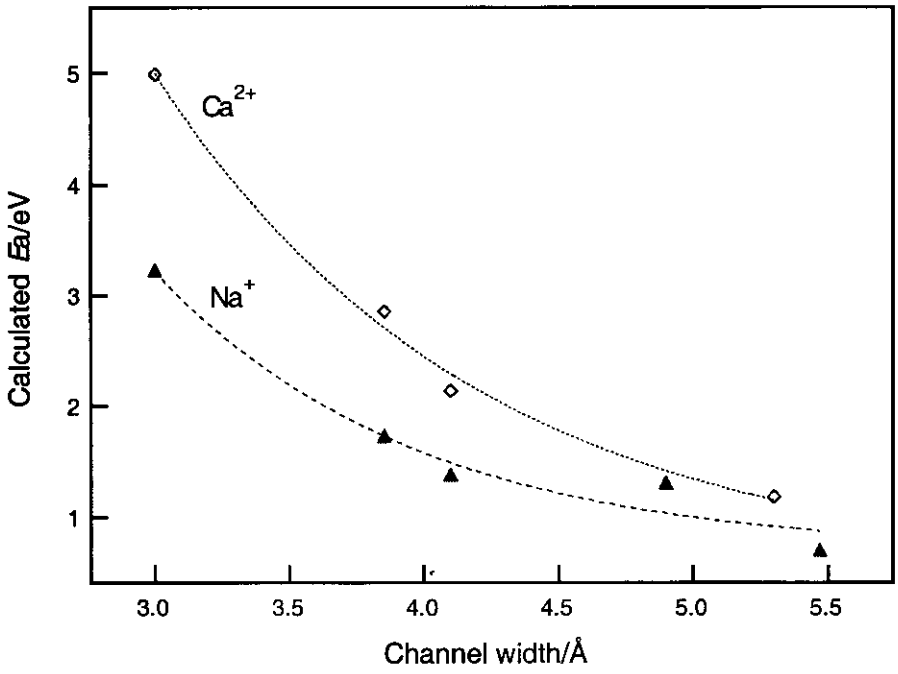

Figure 8.1 The variation of calculated activation energies with channel width for the migration of Ca^{2+} and Na^{+} ions. (The lines are guides to the eye.)

Although there does appear to be a relationship between framework geometry and calculated activation energies, it is not possible to predict exactly how the framework geometry will alter in response to interstitial cation occupation. Frameworks will respond to changes in composition or temperature by tetrahedral tilting in order to optimise the cationic coordination within structural cavities (Megaw, 1974a; Megaw, 1974b). The degree of tilting will necessarily depend on factors such as the charge on the interstitial cations and the ionic radii.

In order to investigate the relationship between ion size, ion charge and activation energy, additional atomic simulations were carried out on the nepheline structure.

8.2.2 A computer probe for ionic mobility

Ion migration in the (001) plane in nepheline

The trajectory which had been established for the migration of Na^+ between the oval and hexagonal channels in nepheline was used as a "model pathway" to examine the effect of ionic size and charge in a typical ion migration mechanism in an aluminosilicate framework structure. Interstitial ions were inserted into the oval channel on a site normally occupied by a sodium ion. Defect calculations were then carried out along the trajectory previously determined for Na^+ ion migration in the (001) plane between the oval and hexagonal sites. The calculated activation energies for this process, compared to the 1.38 eV previously calculated for a Na^+ ion following the same pathway, are shown in Table 8.2 and the energy profiles for these migration processes are shown in Figures 8.2(a) and (b).

Table 8.2 Calculated activation energies for migration of monovalent and divalent ions along a trajectory in the (001) plane in nepheline between a Na-site in the oval channel and a vacancy in the hexagonal channel

Ion	Ionic radius/Å	Activation energy/eV
Li^+	0.90	0.64
Na^+	1.16	1.38
K^+	1.52	2.22
Mg^{2+}	0.86	0.65
Ca^{2+}	1.14	2.23
Sr^{2+}	1.32	2.94
Ba^{2+}	1.49	3.84

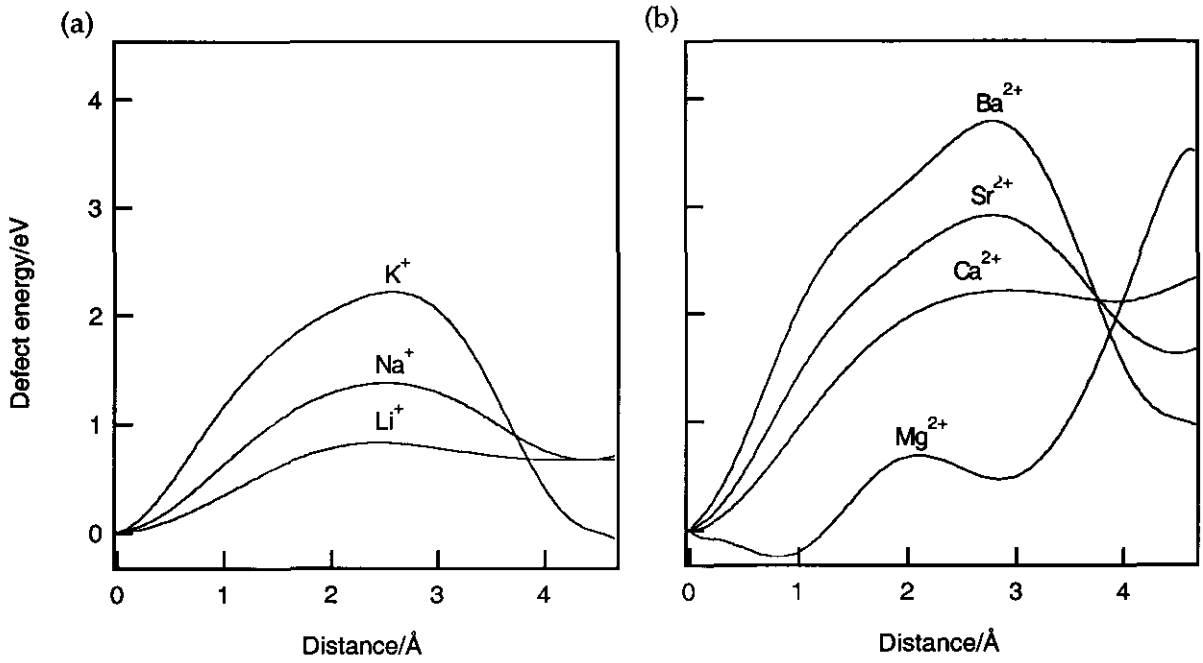

Figure 8.2 Calculated energy profiles for the migration of (a) monovalent; (b) divalent ions along a trajectory in the (001) plane in nepheline between a Na-site in the oval channel and a vacancy in the hexagonal channel. (The lines represent the fits through the calculated points at ~ 0.2 Å intervals.)

The magnitude of the activation energies calculated for divalent ions compared to monovalent ions of comparable size would suggest that the energy barriers to cation migration are not only dependent on the size of the migrating ion, but significantly on the charge. It is also interesting to note here that the defect energies calculated for Li^+, Ca^{2+} and Mg^{2+} ions in the hexagonal channel are higher than those calculated for larger ions of similar charge (Figure 8.2). This is likely to be the result of the poor coordination of a small ion occupying a large site (Flygare and Huggins, 1973; Kieffer, 1999). Figure 8.3 illustrates how the calculated energy barrier is dependent on both ionic size and charge.

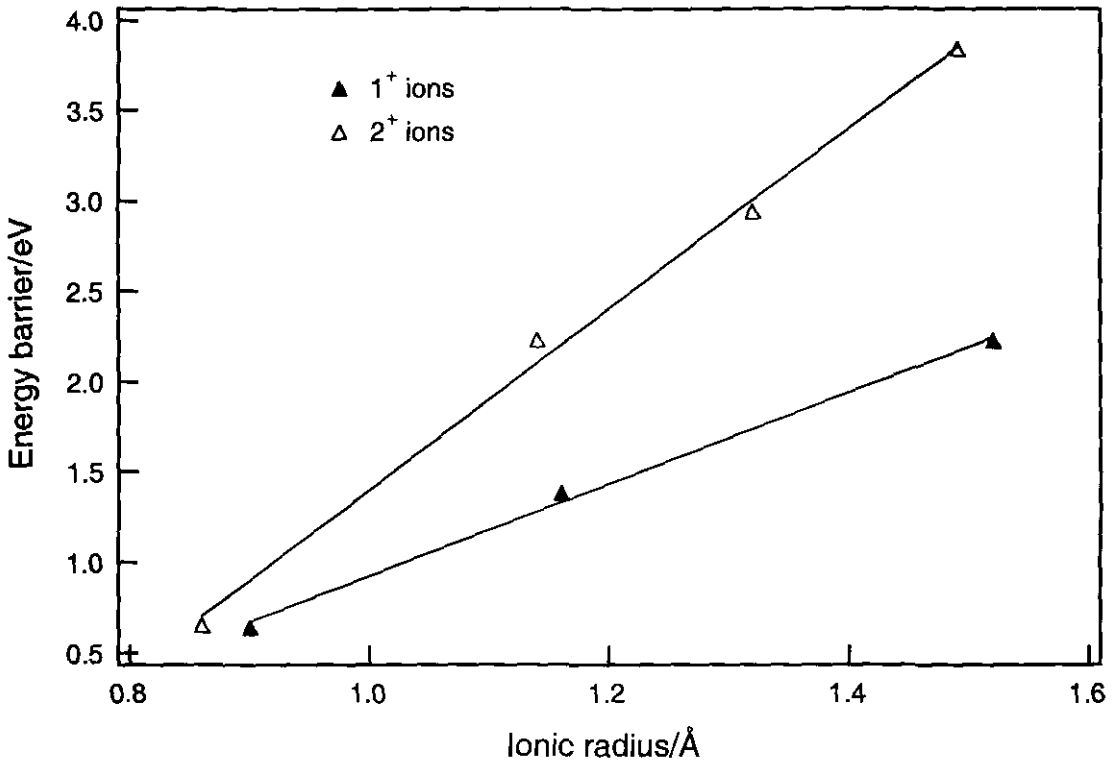

Figure 8.3 Dependence of the energy barrier to migration on ionic charge and ionic radius for ion migration along a trajectory in the (001) plane in nepheline between a Na-site in the oval channel and a vacancy in the hexagonal channel.

It can be seen from Figure 8.3 that the magnitude of the calculated activation energy increases almost linearly with increasing ionic radius for both monovalent and divalent ions. It would appear that ionic charge plays a significantly greater role in the determination of activation energy than ionic radius, and the two effects will therefore be considered independently of each other.

The insertion of interstitial ions into a structure is also going to have an effect on the framework geometry. The local effects of these interstitial defects were examined by measurement of local structural variations around the defects in the relaxed structures. The widths of the oval and the hexagonal channels, as shown in Figure 8.4, were measured and compared with the radius of the occupying cation, as shown in Figures 8.5 (a) and (b).

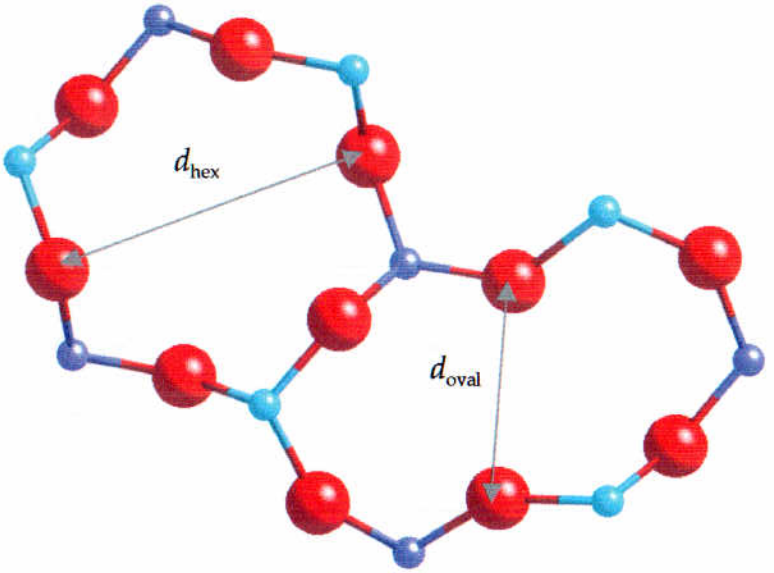

Figure 8.4 View down [001] of the oval and hexagonal channels in nepheline and the measured channel widths d_{hex} and d_{oval}.

It is not surprising to find that the charge on the interstitial defect has a major effect on local structural distortions within the framework, and it would also therefore be expected to alter the conformation of the migration pathway bottleneck. The approximate pathway of the ions as they pass through the interconnecting side channel between the oval and hexagonal sites is shown in Figure 8.6. The widths of the interconnecting side channel, when the migrating ions are at the saddlepoint, are listed in Table 8.3 and the variation with ionic radius and charge is illustrated in Figure 8.7. The subsequent relaxation of the side channel in each case is shown in Figure 8.8.

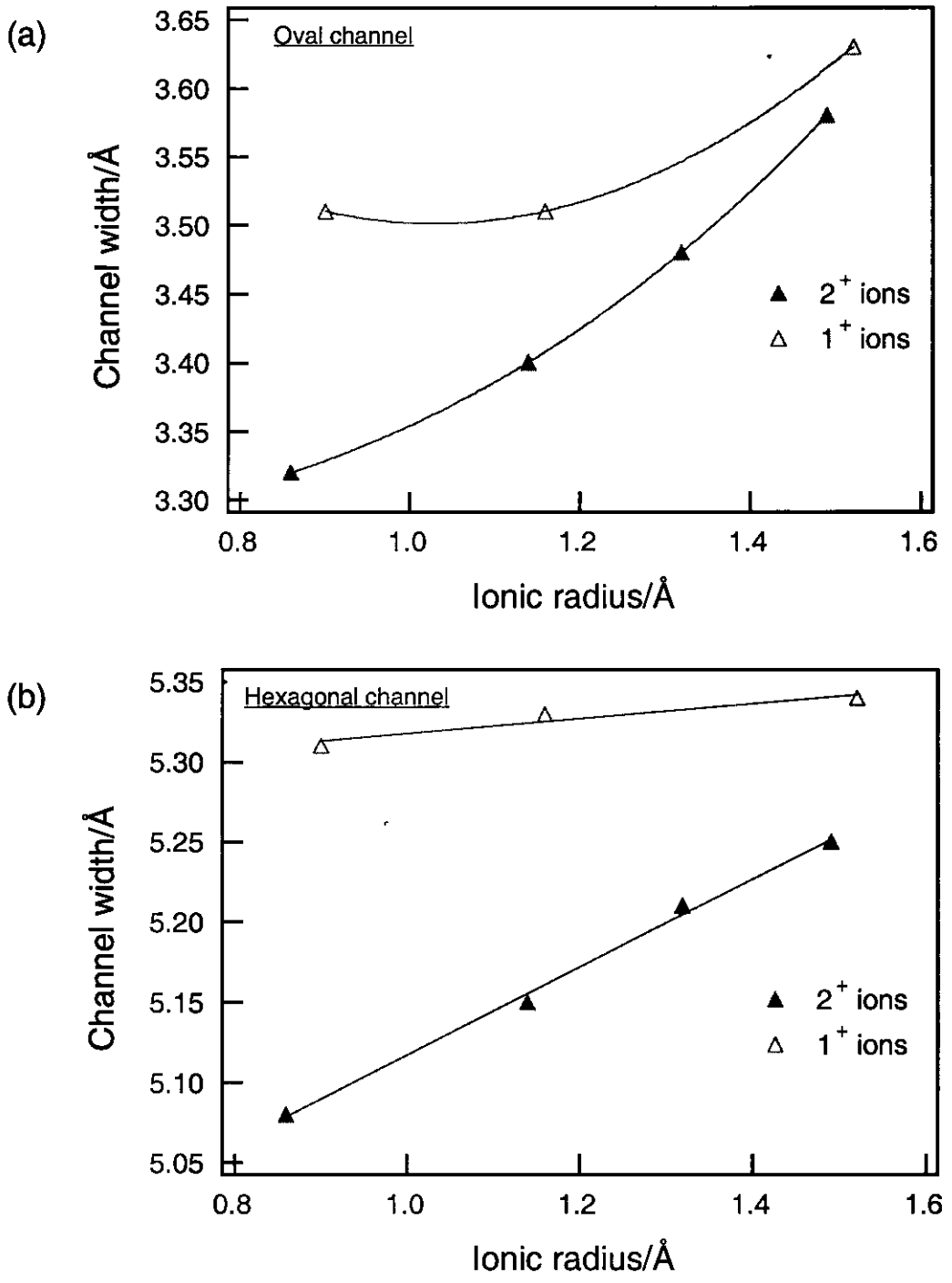

Figure 8.5 The effect of the radius of occupying cations on the width of (a) the oval channel; (b) the hexagonal channel in the nepheline structure.

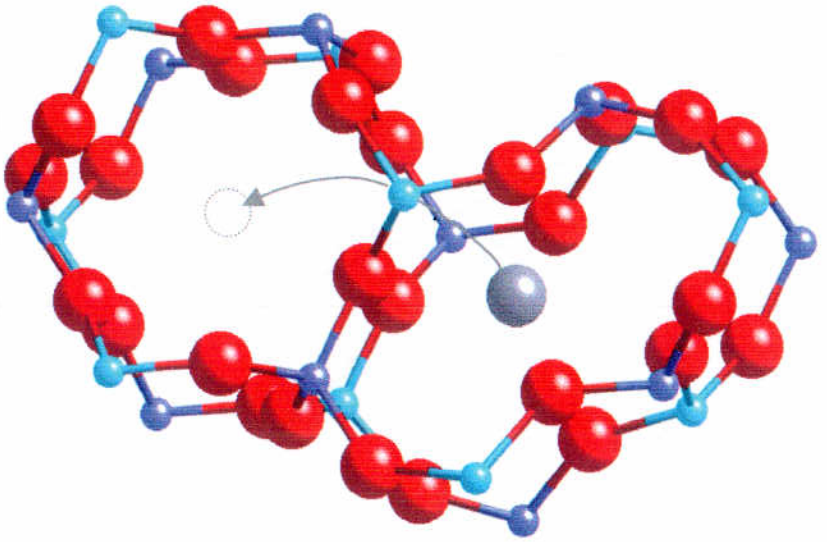

Figure 8.6 The approximate trajectory of an ion migrating between the oval and hexagonal sites in nepheline.

Table 8.3 Calculated width of interconnecting side channel between oval and hexagonal sites in the nepheline structure with the interstitial ions at the saddlepoint position.

Ion	Ionic radius/Å	Channel width/Å
Li^+	0.90	3.63
Na^+	1.16	3.94
K^+	1.52	4.23
Mg^{2+}	0.86	3.21
Ca^{2+}	1.14	3.70
Sr^{2+}	1.32	3.94
Ba^{2+}	1.49	4.28

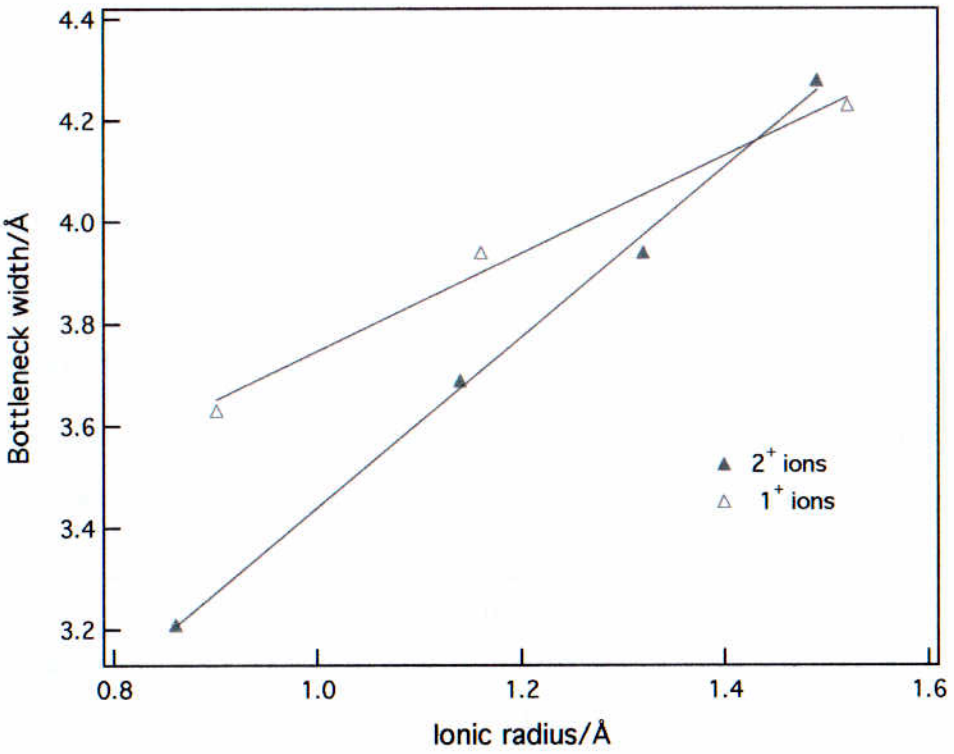

Figure 8.7 Variation of bottleneck width with ionic radius and charge.

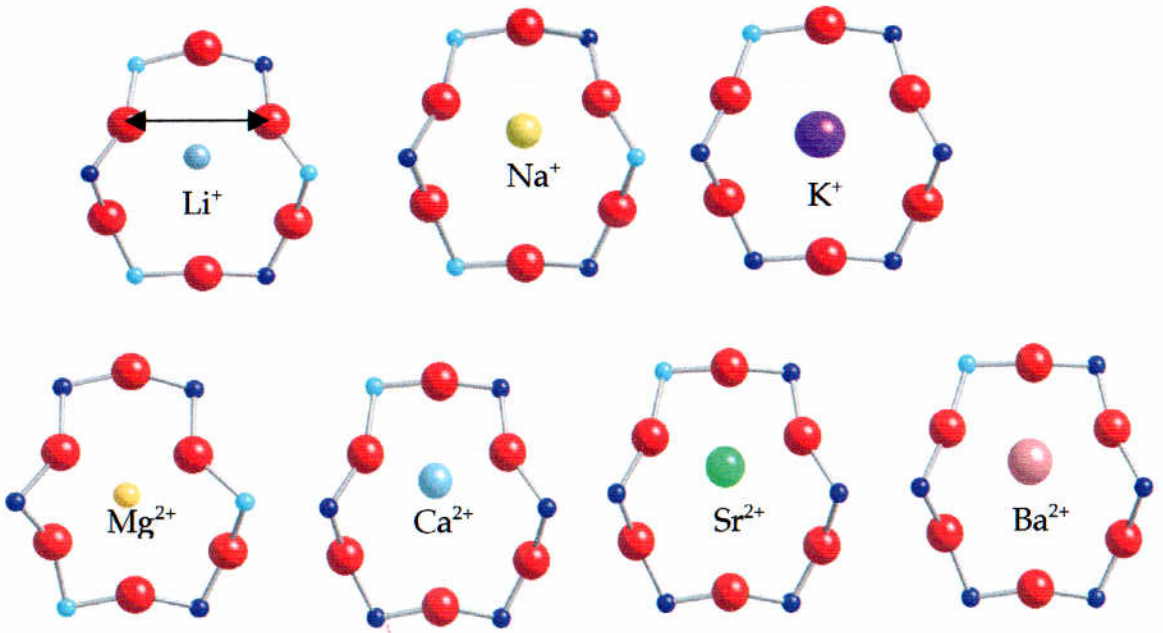

Figure 8.8 Saddlepoint configurations with interstitial ions in the interconnecting side channel in nepheline. The position of the measured bottleneck width is indicated.

Ion migration along [001] in nepheline

In order to determine the activation energy for the migration of cationic species along the hexagonal [001] channel in nepheline, calculations involving the migration of a cation from an occupied to a vacant site were carried out on a 3*c* supercell. Unrealistic results were obtained for the migration of Mg^{2+}, Ca^{2+} and Li^{+} along this channel, probably because of their small size compared to the channel width. The results of the calculations for the other ions are shown in Table 8.4 and Figure 8.8.

Table 8.4 Calculated activation energies for migration of monovalent and divalent ions along [001] in the hexagonal channel in nepheline between an occupied and vacant site in a 3*c* supercell

Ion	Ionic radius/Å	Activation energy/eV
Na^{+}	1.16	0.28
K^{+}	1.52	1.43
Sr^{2+}	1.32	0.92
Ba^{2+}	1.49	2.13

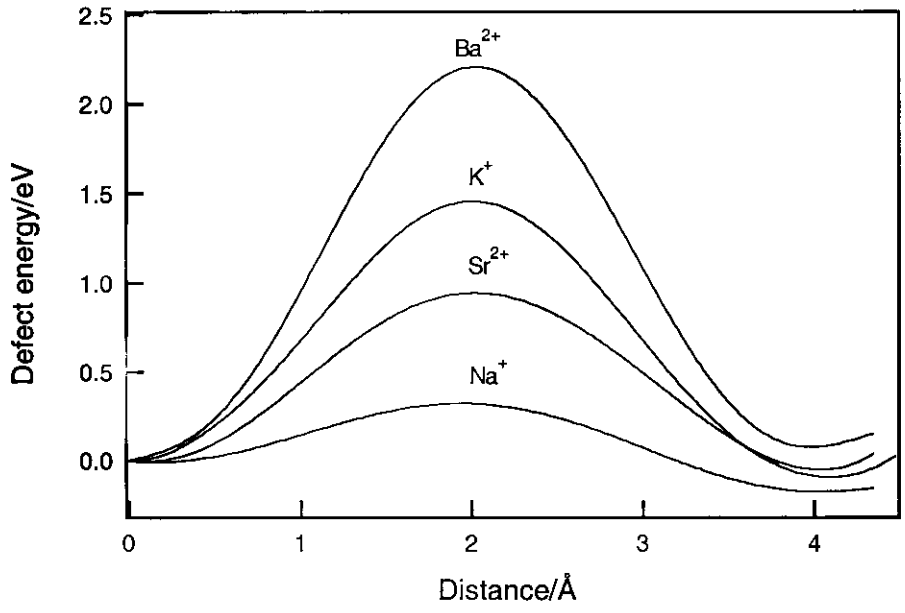

Figure 8.9 Calculated energy profiles for the migration of mono- and divalent ions along [001] in the hexagonal channel in nepheline between an occupied and vacant site in a 3*c* supercell. (The lines represent the fits through the calculated points at ~ 0.25 Å intervals.)

As with the previous set of calculations carried out on the nepheline structure, these results also suggest that ionic charge plays a significantly greater role in the determination of migration energetics than ionic radius, in a given framework.

Summary

The results presented here agree with the conclusions reached in Chapters 5 and 7 regarding the mobility of Ca^{2+} ions in yoshiokaite and anorthite, respectively. Although the radius of the Ca^{2+} ion (1.14 Å) is very similar to that of the Na^{+} ion (1.16 Å), the calculated energy barriers to migration are very different: 2.23 eV and 1.38 eV, respectively, in nepheline, and 2.84 eV and 1.73 eV, respectively, in anorthite. This would suggest that the mobility of the Ca^{2+} ion is severely restricted in comparison to the Na^{+} ion in similar frameworks.

The effect of ion charge on framework configuration influences not only the energetics of ion migration processes, but also the feasibility of particular migration mechanisms. This was apparent in the yoshiokaite structure, where highly distorted side channels (Chapter 5, Figure 5.8), linking Ca sites to [001] hexagonal channels, prevent Ca^{2+} (or Na^{+}) migration. This was also found to be the case for anorthite, where migration of Ca^{2+} was inhibited by a distorted framework; the corresponding migration channels in albite and sanidine allowed migration of Na^{+} and K^{+}, respectively. A major controlling factor on the likelihood of a particular ion migration process occurring is therefore the conformation adopted by the framework around the bottleneck, which in turn is determined by the charge on the interstitial ions.

Figure 8.1 illustrated the variation of *calculated* activation energies with channel width for a variety of mineral systems. Part of Figure 8.1 is reproduced below, together with experimental data for Na^{+} migration in anorthite, nepheline and albite (Figure 8.10).

Although this comparison includes a limited amount of data, the experimentally determined activation energies lie closeto the trend defined by the calculated values.

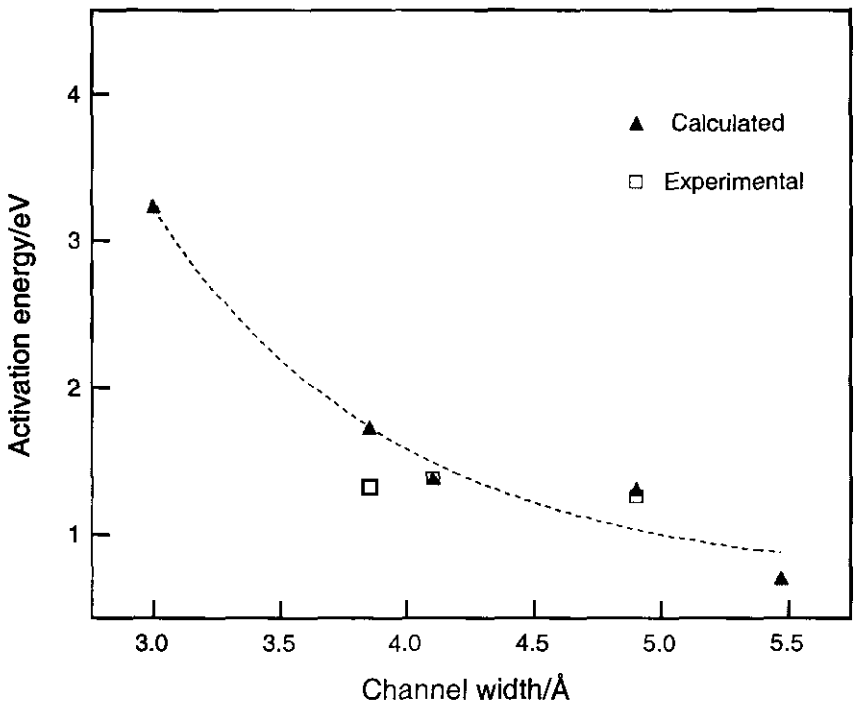

Figure 8.10 Comparison of calculated and experimentally determined activation energies for Na^+ migration in anorthite, nepheline and albite. The error bars for the experimental data are smaller than the plotted points.

By extending this study to include a wider range of ions/mineral systems, one would expect to obtain a closer correlation between calculated and experimental data. These *transferable* data could then be applied as follows:

- Experimentally determined activation energies could be used to determine a migration channel width.
- Knowledge of the crystal structure could then be used to attribute the observed process to a particular ion migration mechanism.
- Alternatively, such a system could be used to predict the energetics, and hence the feasibility, of a particular ion migration process occurring within a structure.

8.3 Final conclusions

This study has demonstrated a novel approach in the use of computer modelling techniques to complement data obtained using dielectric spectroscopy, and thereby elucidate the mechanisms for experimentally observed processes. These methods have been used to investigate diffusion-related processes in different frameworks with different ionic content. By combining knowledge of the local crystal structural environment with a highly specific spectroscopic probe, ionic mobility in a range of minerals has been characterised, and activation energies have been measured for discrete diffusion mechanisms. In order to rationalise the spectroscopy data in the context of actual ionic mobility mechanisms, atomistic simulation techniques have been applied to the systems under study. These have provided a quantitative basis for predicting diffusion energetics and controlling factors underlying the mechanism of processes which occur in a wide range of geologically relevant systems.

By applying the methods used here to a variety of mineral systems, it should be possible to develop a comprehensive body of transferable data relating structural aspects of framework minerals to the systematic prediction of ion migration mechanisms and energetics. The consequences of the use of such a system in a predictive capacity would be far reaching, from both a geological and a technological viewpoint.

Appendix 1

Units, constants and conversion factors

Table 1 (a) Units

Quantity	*Symbol*	Units
current	I	ampère (A)
potential difference	V	volt (V)
resistance	R	ohm (Ω)
impedance	Z	ohm (Ω)
charge	Q	coulomb
capacitance	C	farad (F)
conductance	G	siemens (S)
conductivity	σ	siemens/metre (Sm^{-1})
time	t	second (s)
frequency	f	hertz (Hz)
dipole moment	m	coulomb metres (Cm)
electric field	E	volts/metre (Vm^{-1})
polarisation	P	coulombs/metre^2 (Cm^{-2})
electrical flux density	D	coulombs/metre^2 (Cm^{-2})
temperature	T	kelvin (K)

Table 1 (b) Constants

Quantity	Symbol	Value	Units
permittivity of free space	ε_o	8.854×10^{-12}	Fm^{-1}
Boltzmann constant	K_b	1.38066×10^{-23}	JK^{-1}
gas constant	$R=N_Ak$	8.31451	$JK^{-1}mol^{-1}$
Avogadro constant	N_A	6.02214×10^{23}	mol^{-1}

Table 1 (c) Conversion factors

1 eV	96.485 $kJmol^{-1}$
1 Å	10^{-10} m

Appendix 2

Effective ionic radii

The ionic radii used in the calculations and in the CrystalMaker models (CrystalMaker, 1994-2001) in this thesis are those presented by Shannon and Prewitt (1976; 1969). They include two sets of radii: the first is a set of traditional radii based on $r(^{VI}O^{2-})$ = 1.40 Å; the other set is based on $r(^{VI}O^{2-})$ = 1.26 Å and corresponds to *crystal radii* as defined by Fumi and Tosi (1964). These crystal radii differ from traditional radii only by a constant factor of 0.14 Å and are felt to correspond more closely to the physical size of ions in a solid and are more relevant in the discussion of diffusion in solids (Flygare and Huggins, 1973). However it should be remembered that these values cannot be considered to be absolute values of ionic radii in any particular structure, as these will be dependent on the nature (i.e. degree of covalency) of the bonding and the coordination number of each particular ion. In addition to this, there may be a variation in near-neighbour distances in complex aluminosilicate structures, in which case there may be some uncertainty in the coordination number of the cations in any one particular site. The radii used in this work are presented in Table 2.

Table 2 Crystal radii (Shannon and Prewitt, 1976)

Ion	Coordination number	Crystal radius/Å
Li^+	VI	0.90
Na^+	VI	1.16
K^+	VI	1.52
Mg^{2+}	VI	0.86
Ca^{2+}	VI	1.14
Sr^{2+}	VI	1.32
Ba^{2+}	VI	1.49

Appendix 3

Dielectric data

All the dielectric data presented in this thesis were obtained from measurements of capacitance and conductance as described in Chapter 2. These measurements, for each mineral system studied, are in the attached CD-ROM. A brief summary of the files contained in the CD-ROM is outlined in Table 3.

Table 3 Dielectric data

Folder	Folder contents
Nepheline_1	Isothermal data
Nepheline_2	High temperature data
Yoshiokaite	High temperature data
β-eucryptite_1	High temperature data with *c*-axis parallel to electric field
β-eucryptite_2	High temperature data with *c*-axis perpendicular to electric field
β-eucryptite_3	Repeat measurements of high temperature data with *c*-axis perpendicular to electric field
Albite	High temperature data
K-feldspar	High temperature data
Anorthite	High temperature data

References

Abbot, R.N. (1984) $KAlSiO_4$ stuffed derivatives of tridymite:phase relationships. American Mineralogist, 69, 449-457.

Alpen, U.V., Schulz, H., and Talay, G.H. (1977) One-dimensional cooperative Li-diffusion in beta-eucryptite. Solid State Communications, 23, 911-914.

Andou, Y., and Kawahara, A. (1982) The refinement of the structure of synthetic kalsilite. Mineralogy Journal of Japan, 12, 153-161.

Angel, R.J., Carpenter, M.A., and Finger, L.W. (1990) Structural variation associated with compositional variation and order-disorder behaviour in anorthite rich feldspars. American Mineralogist, 75, 150-162.

Bailey, A. (1971) Comparison of low-temperature with high-temperature diffusion of sodium in albite. Geochimica Cosmochimica Acta, 35, 1073-1081.

Barrer, R.M., and Saxon-Napier, E.A. (1962a) Dielectric properties of basic sodalite and a silver nitrate-zeolite complex. Transactions of the Faraday Society, 58, 145-155.

Barrer, R.M., and Saxon-Napier, E.A. (1962b) Dielectric properties of some ion-exchanged analcites. Transactions of the Farady Society, 58, 156-165.

Beall, G.H. (1994) Industrial applications of silica. Reviews in Mineralogy, Mineralogical Society of America, 29, 469-505.

Böhm, H. (1975) Dielectric properties of beta-eucryptite. Physica Status Solidi, 30, 531-536.

Böhm, H. (1981) Diffuse scattering of two-dimensional clusters in the compound $Li_2Al_2Si_3O_{10}$. Zeitschrift für Krystallographie, 157, 27-37.

Böhm, H. (1983) Modulated structures at phase transitions. American Mineralogist, 68, 11-17.

Brinkman, D., Mali, M., Roos, J., and Schweickert, E. (1981) Dimensionality effects of Li diffusion in beta-eucryptite studied by single crystal Li NMR. Solid State Ionics, 5, 433-436.

Buening, D.K., and Buseck, P.R. (1973) Fe-Mg lattice diffusion in olivine. Journal of Geophysical Research, 65, 735-750.

Buerger, M.J. (1948) Crystals based on the silica structures. American Mineralogist, 33, 751-752.

Buerger, M.J. (1954) The stuffed derivatives of the silica structure. American Mineralogist, 39, 600-614.

Bush, T.S., Gale, J.D., Catlow, C.R.A., and Battle, P.D. (1994) Self-consistent interatomic potentials for the simulations of binary and ternary oxides. Journal of Material Chemistry, 4(6), 831-837.

Carpenter, M.A. (1988) Thermochemistry of aluminium/silicon ordering in feldspar minerals. Physical Properties and Thermodynamic Behaviour of Minerals, 265-323. NATO ASI Series, Kluwer Academic, Dordrecht.

Catlow, C., and Price, G.D. (1990) Computer modelling of solid-state inorganic materials. Nature, 347, 243-248.

Catlow, C.R.A. (1987) Computational techniques and simulation of crystal structures. 231-277 p. Clarendon Press, Oxford.

Catlow, C.R.A. (1989) Mott-Littleton Calculations in Solid-state Chemistry and Physics. Journal of the Chemical Society, Faraday Transactions 2, 85(5), 335-340.

Catlow, C.R.A. (1992a) Can the mechanisms of ion transport in SSIs be determined by computer modelling? Solid State Ionics, 53-56, 955-963.

Catlow, C.R.A., ed. (1992b) Modelling of structure and reactivity in zeolites. Academic, London.

Catlow, C.R.A. (1994) Computer modelling as a technique in inorganic chemistry. Journal of Materials Chemistry, 4(6), 781-792.

Catlow, C.R.A., Ackerman, L., Bell, R.G., Cora, F., Gay, D.H., Nygren, M.A., Pereira, J.C., Sastre, G, Slater, B., and Sinclair, P.E. (1997) Computer modelling as a technique in solid state chemistry. Faraday Discussions, 106, 1-40.

Catlow, C.R.A., Jackson, R.A., and Thomas, J.M. (1990) Computational studies of solid oxidation catalysts. Journal of Physical Chemistry, 94, 7889-7893.

Chan, L.-H., Edmond, J.M., Thomson, G., and Gillis, K. (1992) Lithium isotopic composition of submarine basalts: Implications for the lithium cycle in the oceans. Earth and Planetary Science Letters, 108, 151-160.

Cole, K.S., and Cole, R.H. (1941) Dispersion and Absorption in Dielectrics. Journal of Chemical Physics, 9, 341-351.

CrystalDiffract. (1995-2000) Powder diffraction software for Macintosh computers. CrystalMaker Software, P.O. Box183, Bicester, Oxfordshire, OX6 7BS, UK, http:www.crystalmaker.com.

CrystalMaker. (1994-2001) A crystal structures program for Macintosh computers. CrystalMaker Software, P.O. Box183, Bicester, Oxfordshire, OX6 7BS, UK, http:www.crystalmaker.com.

Darlington, C.N.W., and Knight, K.S. (1999) On the lattice parameters of sodium niobate at room temperature and above. Physica B: Condensed Matter, 266(4), 368-372.

de Dombal, R.F. (1992) Phase transitions in nepheline and tridymite. Ph.D. Thesis University of Cambridge.

de Neufville, J., and Schairer, J.F. (1966) Carnegie Institute of Washington Year Book, 61, 59-68.

De Souza, R., Islam, M.S., and Ivers-Tiffee, E. (1999) Formation and migration of cation defects in the perovskite oxide $LaMnO_3$. Journal of Materials Chemistry, 9, 1621-1627.

Debye, P. (1929) Polar Molecules. Chemical Catalogue Company, New York.

Deer, W.A., Howie, R.A., and Zussman, J. (1992) Nepheline Group. An Introduction to the Rock-Forming Minerals, p. 473-485. Longman.

Deubener, J., Sternizke, M., and Muller, G. (1991) Feldspars $MAlSi_3O_8$ (M = H, Li, Ag) synthesised by low temperature ion-exchange. American Mineralogist, 76, 1620-1627.

Dick, B.G., and Overhauser, A.W. (1958) Theory of the dielectric constants of alkali halide crystals. Physical Review, 112, 90-103.

Dollase, W.A., and Peacor, D. (1971) Si-Al Ordering in nepheline. Contributions to Mineralogy and Petrology, 30, 129-134.

Dove, M.T., Giddy, A.P., and Heine, V. (1993a) Rigid Unit Model of displacive phase transitions in silicates. Transactions of the American Crystallographic Association, 27, 65-74.

Dove, M.T., Heine, V., and Hammonds, K.D. (1993b) Rigid unit modes in framework silicates. Mineralogical Magazine, 59, 629-639.

Downs, R.T., Andalman, A., and Hudacsko, M. (1996) The coordination numbers of Na and K atoms in low albite and microcline as determined from a procrystal electron-density distribution. American Mineralogist, 81, 1344-1349.

Dowty, E. (1980) Crystal-chemical factors affecting the mobility of ions in minerals. American Mineralogist, 65, 174-182.

Ewald, P.P. (1921) Die Berechnung optischer und elektrostatischer Gitterpotentiale. Annalen der Physik, 64, 253.

Ferry, J.M., and Blencoe, J.G. (1978) Subsolidus phase relations in the nepheline-kalsilite system at 0.5, 2.0, and 5.0 kbar. American Mineralogist, 63, 1225-1240.

Fisher, C.A.J., Islam, M.S., and Brook, R.J. (1997) A computer simulation investigation of Brownmillerite-structured $Ba_2In_2O_5$. Journal of Solid State Chemistry, 128, 137-141.

Flygare, W.H., and Huggins, R.A. (1973) Theory of ionic transport in crystallographic tunnels. Journal of the Physics and Chemistry of Solids, 34, 1199-1204.

Follstaedt, D.M., and Richards, P.M. (1976) NMR relaxation in the superionic conductor beta-eucryptite. Physical Review Letters, 37, 1571-1574.

Foreman, N., and Peacor, D. (1970) Refinement of nepheline at several temperatures. Zeitschrift für Kristallographie, 132, 45-70.

Freeman, C.M., and Catlow, C.R.A. (1990) A computer modelling study of defect and dopant states in SnO_2. Journal of Solid State Chemistry, 85, 65-75.

Fumi, F.G., and Tosi, M.P. (1964) Ionic sizes and Born repulsive parameters in the NaCl-type alkali halides - I. Journal of the Physics and Chemistry of Solids, 25, 31-43.

Fyfe, C.A., Thomas, J.M., Klinowski, J., and Gobbi, G.C. (1983) Magic angle spinning NMR (MAS NMR) spectroscopy of the structure of zeolites. Angew. Chem. Int. Ed. Engl., 22, 259-275.

Gale, J.D. (1997) GULP: A computer program for the symmetry adapted simulation. Journal of the Chemical Society, Faraday Transactions, 93(4), 629-637.

Giletti, B.J., Semet, M.P., and Kasper, R.B. (1974) Self-diffusion of potassium in low albite using an ion microprobe. Geological Society of America, Abstracts with Programs 6, 754.

Gillery, F.H., and Bush, E.A. (1959) Thermal contraction of beta-eucryptite ($Li_2O.Al_2O_3.2SiO_2$). Journal of the American Ceramic Society, 42, 175-177.

Gregorkiewitz, M. (1986) Alkali ion diffusion in M'($AlSiO_4$) compounds with frameworks of the tridymite topology and its variants. Solid State Ionics, 18, 19, 534-538.

Guth, H., and Heger, G. (1979) Temperature dependence of the crystal structure of the one-dimensional Li^+-conductor beta-eucryptite ($LiAlSiO_4$). In: Vahista, Mundy and Shenoy (ed.), Fast Ion Transport in Solids, Elsevier North Holland, New York, 499-502.

Haas, C.W. (1973) On the necessity for invoking a free-ion-like model for the super ionic conductors. Journal of Solid State Chemistry, 7, 155-157.

Hahn, T., and Buerger, M.J. (1954) The detailed structure of nepheline. Zeitschrift für Kristallographie, 106, 308-338.

Hammonds, K.D., Dove, M.T., Giddy, A.P., Heine, V., and Winkler, B. (1996) Rigid-unit phonon modes and structural phase transitions in framework silicates. American Mineralogist, 81, 1057-1079.

Harlow, G.E., and Brown, J., G E. (1980) Low albite: an X-ray and neutron diffraction study. American Mineralogist, 65, 986-995.

Harrop, P.J. (1973) Dielectrics. 155 p. Butterworths, London.

Hayward, S.A., Pryde, A.K.A., de Dombal, R.F., Carpenter, M.A., and Dove, M.T. (2000) Rigid Unit Modes in disordered nepheline: a study of a displacive incommensurate phase transition. Physics and Chemistry of Minerals, 27, 285-290.

Heaney, P.J., and Veblen, D. (1991) Observations of the alpha- beta phase transition in quartz: a review of imaging and diffraction studies and some new results. American Mineralogist, 76, 1018-1032.

Heyes, D.M. (1981) Electrostatic potentials and fields in infinite point charge lattices. Journal of Chemical Physics, 74, 1924-1929.

Hippler, B., and Böhm, H. (1989) Structure investigation on sodium nephelines. Zeitschrift für Kristallographie, 187, 39-53.

Holland, T.J.B., and Redfern, S.A.T. (1997) Unit cell refinement from powder diffraction data: the use of regression diagnostics. Mineralogical Magazine, 61, 65-77.

Hovis, G.L., Spearing, D.R., Stebbins, J.F., Roux, J., and Clare, A. (1992) X-ray powder diffraction and ^{23}Na, ^{27}Al and ^{29}Si MAS-NMR investigation of nepheline-kalsilite crystalline solutions. American Mineralogist, 77, 19-29.

Huebner, J.S., and Dillenburg, R.G. (1995) Impedance spectra of hot, dry silicate minerals and rock: qualitative interpretation of spectra. Americam Mineralogist, 80, 46-64.

Islam, M.S. (2000) Ionic transport in ABO_3 perovskite oxides: a computer modelling tour. Journal of Materials Chemistry, 10, 1027-1038.

Islam, M.S., Cherry, M., and Catlow, C.R.A. (1996) Oxygen diffusion in $LaMnO_3$ and $LaCoO_3$ perovskite-type oxides: a molecular dynamics study. Journal of Solid State Chemistry, 124, 230-237.

Islam, M.S., Illett, D.J., and Parker, S.C. (1994) Surface structures and oxygen hole formation on the La_2O_3 catalyst. A computer simulation study. Journal of Physical Chemistry, 98, 9637-9641.

Islam, M.S., Read, M.S.D., and D'Arco, S. (1997) From oxides to oxyhalides: modelling the properties of high T_c superconductors. Faraday Discussions, 106, 1-10.

Jackson, R.A., and Catlow, C.R.A. (1988) Computer simulation studies of zeolite structure. Molecular Simulation, 1, 207-224.

James, R.H., Rudnicki, M.D., and Palmer, M.R. (1999) The alkali element and boron geochemistry of the Escanaba Trough sediment-hosted hydrothermal system. Earth and Planetary Science Letters, 171, 157-169.

Jiménez, R., and Gregorkiewitz, M. (1999) Alkali cation diffusion in the channel system of hexagonal nepheline. Journal of the Electrochemical Society, 146(7), 2620-2630.

Jones, A., Palmer, D., Islam, M.S., and Mortimer, M. (2001) Ion migration in nepheline: a dielectric spectroscopy and computer modelling study. Physics and Chemistry of Minerals, 28, 28-34.

Julien, C., and Stoynov, Z. (2000) Materials for lithium-ion batteries. NATO Science Series, Kluwer Academic, Dordrecht.

Kawahara, A., Andou, Y., Marumo, F., and Okuno, M. (1987) The crystal structure of high temperature form of kalsilite ($KAlSiO_4$) at 950°C. Mineralogy Journal of Japan, 13, 260-270.

Kieffer, J. (1999) Fast relaxations in mixed alkali silicates. Journal of Non-Crystalline Solids, 255, 56-66.

Kihara, K. (1978) Thermal change in unit cell dimensions, and a hexagonal structure of tridymite. Zeitschrift für Kristallographie, 148, 237-253.

Kirkpatrick, R.J., and Steele, I.M. (1973) Hexagonal $CaAl_2SiO_6$: a new synthetic phase. American Mineralogist, 58, 945-946.

Lichtenstein, A.I., Jones, R.O., Xu, H., and Heaney, P.J. (1998) Anisotropic thermal expansion in the silicate beta-eucryptite: a neutron diffraction and density functional study. Physical Review B, 58(10), 6219-6223.

Lidiard, A.B. (1989) The Mott-Littleton method: an introductory survey. Journal of the Chemical Society, Faraday Transactions 2, 85(5), 341-349.

Lin, T.H., and Yund, R.A. (1972) Potassium and sodium self-diffusion in alkali feldspar. Contributions to Mineralogy and Petrology, 34, 177-184.

Loewenstein, W. (1954) The distribution of aluminium in the tetrahedra of silicates and aluminates. American Mineralogist, 39, 92-96.

McConnell, J.D.C. (1962) Electron diffraction study of subsidiary maxima of scattered intensity in nepheline. Mineralogical Magazine, 33, 114-124.

McConnell, J.D.C. (1981) Time-temperature study of the intensity of satellite reflections in nepheline. American Mineralogist, 66, 990-996.

Megaw, H.D. (1974a) The architecture of the feldspars. In McKenzie, W.S. and Zussman, J., Ed. The Feldspars, p. 2-24. Manchester University Press, Manchester.

Megaw, H.D. (1974b) Tilts and tetrahedra in feldspars. In McKenzie, W.S. and Zussman, J., Ed. The Feldspars, p. 87-113. Manchester University Press, Manchester.

Mott, N.F., and Littleton, M.J. (1938) Conduction in polar crystals. I. Electrolytic conduction in solid salts. Transactions of the Faraday Society, 34, 485-509.

Muller, W.F., and Schulz, H. (1976) Antiphase domains in beta-eucryptite. Naturwiss, 63, 294.

Nagel, W., and Böhm, H. (1982) Ionic conductivity studies on $LiAlSiO_4$-SiO_2 solid solutions of the high quartz type. Solid State Communications, 42, 625-631.

Nover, G., Will, G., and Waitz, R. (1992) Pressure induced phase transition in Mg_2GeO_4 as determined by frequency dependent complex electrical resistivity measurements. Physics and Chemistry of Minerals, 19, 133-139.

Ohashi, Y. (1976) Lattice energy of some silicate minerals and the effectof oxygen bridging in relation to crystallization sequence. Carnegie Institute of Washington Year Book, 75.

Ohgushi, T., and Kazuhide, K. (1998) Movements of sodium ions in mordenite and their assignment. Journal of the Chemistry Society, Faraday Transactions, 94, 3769-3775.

Omar, M.A. (1975) Dielectric and Optical Properties of Solids. Elementary Solid State Physics. Addison Wesley.

Palmer, D.C. (1994) Stuffed derivatives of the silica polymorphs. Reviews in Mineralogy, Mineralogical Society of America, 29, 83-117.

Palmer, D.C. (1995) Dielectric spectroscopy: a novel way to measure ionic and molecular mobility in minerals. Terra Abstracts, 7(10), 80.

Palmer, D.C. (1997) Ionic mobility, dehydration and phase transitions in analcime. EOS Transactions of the American Geophysical Union, 78, 753.

Palmer, D.C., Dove, M.T., Ibberson, R.M., and Powell, B.M. (1997) Structural behaviour, crystal chemistry and phase transitions in substituted leucite: High-resolution neutron powder diffraction studies. American Mineralogist, 82, 16-29.

Palmer, D.C., Jones, A., and Welch, M.D. (2001) High-temperature structural behaviour and ionic mobility in a Ca-stuffed tridymite. NERC Research Grant Final Report.

Palmer, D.C., and Salje, E.K.H. (1990) Phase transitions in Leucite: dielectric properties and transition mechanism. Physics and Chemistry of Minerals, 17, 444-452.

Pauling, L. (1960) The Nature of the Chemical Bond. Cornell University Press, Ithaca, New York.

Perotta, A.J., and Smith, J.V. (1965) The crystal structure of kalsilite. Mineralogical Magazine, 35, 588-595.

Petrovic, R. (1972) Alkali ion diffusion in alkali feldspars, p. 131. Yale University, New Haven, Connecticut.

Petrovic, R. (1974) Diffusion of alkali ions in alkali feldspars. In McKenzie, W.S. and Zussman, J., Ed. The Feldspars, p. 174-182. Manchester University Press, Manchester.

Phillips, M.W., and Ribbe, P.H. (1973) The structures of monoclinic potassium-rich feldspars. American Mineralogist, 58, 263.

Pillars, W.W., and Peacor, D.R. (1973) The crystal structure of beta eucryptite as a function of temperature. American Mineralogist, 58, 681-690.

Poole, J.C.P., and Farach, H.A. (1971) Dielectric Relaxation. Relaxation in Magnetic Resonance, p. 319-363. Academic Press, New York.

Press, W., Renker, B., Schulz, H., and Böhm, H. (1980) Neutron Scattering study of the one-dimensional ionic conductor beta-eucryptite. Physical Review B, 21(3), 1250-1257.

Putnis, A. (1995) Introduction to Mineral Sciences. 457 p. Cambridge University Press, Cambridge.

Raymond, M. (1971) Madelung constants for several silicates. Carnegie Institute of Washington Year Book, 70, p. 225-227.

Rice, M.J., and Roth, W.L. (1972) Ionic transport in super ionic conductors: a theoretical model. Journal of Solid State Chemistry, 4, 294-310.

Roth, G., and Böhm, H. (1986) Ionic conductivity of sodium nepheline single crystals. Solid State Ionics, 18, 19, 553-556.

Sahama, T.G. (1962) Order-disorder in natural nepheline solutions. Journal of Petrology, 3, 65-81.

Schulz, H. (1974) Thermal expansion of beta-eucryptite. Journal of the American Ceramic Society, 57, 313-317.

Schulz, H., and Tscherry, V. (1972a) Structural relations between the low and high temperature forms of beta-eucryptite ($LiAlSiO_4$) and low and high quartz. I. Low temperature form of beta-eucryptite and low quartz. Acta Crystallographica, B28, 2168-2173.

Schulz, H., and Tscherry, V. (1972b) Structural relations between the low- and high-temperature forms of beta-eucryptite ($LiAlSiO_4$) and low and high quartz. II. High-temperature form of beta-eucryptite and high quartz. Acta Crystallographica, B28, 2174-2177.

Seifert, F., and Virgo, D. (1975) Kinetics of the Fe^{2+}-Mg, order-disorder reaction in anthophyllites; quantitative cooling rates. Science, 188, 1107-1109.

Shannon, R.D. (1976) Revised effective ionic radii and systematic studies of interatomic distances in halides and chalcogenides. Acta Crystallographica, A32, 751-767.

Shannon, R.D., and Prewitt, C.T. (1969) Effective ionic radii in oxides and fluorides. Acta Crystallographica, B25, 925-946.

Simmons, W.B., and Peacor, D.R. (1972) Refinement of the crystal structure of a volcanic nepheline. American Mineralogist, 57, 1711-1719.

Simonov, M.A., Egorow-Tismenko, Y.K., and Belov, N.V. (1976) Refined crystal structure of chkalovite $Na_2Be[Si_2O_6]$. Soviet Physics Doklady, 20(12), 805–807.

Sipling, P.J., and Yund, R.A. (1974) Kinetics of Al/Si disordering in alkali feldspars. In B.J. Hofmann, H.S. Giletti, H.S. Yoder, and R.A. Yund, Eds. Geochemical Transport and Kinetics, 634, p. 185-194. Carnegie Institute of Washington Publication.

Sippel, R.F. (1963) Sodium self diffusion in natural minerals. Geochimica Cosmochimica Acta, 27, 107-120.

Stebbins, J.F., Farnan, I., Williams, E.H., and Roux, J. (1989) Magic angle spinning NMR observations of sodium site exchange in nepheline at 500°C. Physics and Chemistry of Minerals, 16, 763-766.

Stebbins, J.F., Murdoch, J.B., Carmichael, I.S.E., and Pines, A. (1986) Defects and short range order in nepheline group minerals: a ^{29}Si NMR study. Physics and Chemistry of Minerals, 13, 371-381.

Steele, I.M., and Pluth, J.J. (1990) Crystal structure of synthetic Yoshiokaite, a stuffed derivative of the tridymite structure. American Mineralogist, 75, 1186-1191.

Stefanovich, E.V., Shluger, A.L., and Catlow, C.R.A. (1994) Theoretical-study of the stabilisation of cubic-phase ZrO_2 by impurities. Physical Review B, 49, 11560-11571.

Taylor, D. (1968) The thermal expansion of the sodalite group of minerals. Mineralogical Magazine, 36, 761-769.

Taylor, D. (1972) The thermal expansion behaviour of framework silicates. Mineralogical Magazine, 38, 593-604.

Tscherry, V., and Laves, F. (1970) Synthesis and X-ray reflection pattern of beta-eucryptite. Naturwissen, 57, 194.

Tscherry, V., Schulz, H., and Laves, F. (1972a) Average and super structure of beta-eucryptite. Part 1. Average structure. Zeitschrift für Kristallographie, 135, 161-174.

Tscherry, V., Schulz, H., and Laves, F. (1972b) Average and super structure of beta-eucryptite. Part 2. Superstructure. Zeitschrift für Kristallographie, 135, 175-198.

Tuttle, O.F., and Smith, J.V. (1958) The nepheline-kalsilite system: II. Phase relations. American Journal of Science, 256, 571-589.

Tyburczy, J.A., and Fisler, D.K. (1995) Electrical properties of minerals and melts. Mineral Physics and Crystallography, A Handbook of Physical Constants, p. 185-208. American Geophysical Union.

Vaniman, D.T., and Bish, D.L. (1990) Yoshiokaite, a new Ca, Al-silicate mineral from the moon. American Mineralogist, 75, 676-686.

Vaniman, D.T., Bish, D.L., and Chipera, S.J. (1989) A new Ca, Al-silicate mineral from the moon. Lunar and Planetary Science XX, p. 1150-1151, The Lunar and Planetary Institute, Houston.

Vaniman, D.T., Heiken, G., Warren, P., and Jerde, E. (1988) Glasses and a "HASP"-mimicking mineral or mineral intergrowth in Apollo 14 regolith breccias. Lunar and Planetary Science XIX, p. 1215-1216, The Lunar and Planetary Institute, Houston.

Verhoogen, J. (1952) Ionic diffusivity and electrical conductivity in quartz. American Mineralogist, 37, 637-655.

Vineyard, G. (1957) Frequency factors and isotope effects in solid state rate processes. Journal of Physics and Chemistry of Solids, 3, 157.

Virgo, D., and Hafner, S.S. (1969) Fe^{2+}, Mg order-disorder in heated orthopyroxenes. Mineralogical Society of America Special Papers, 2, 67-81.

Wainwright, J.E., and Starkey, J. (1970) A refinement of the structure of anorthite. Zeitschrift für Kristallographie, 133, 75-84.

West, A.R. (1984) Solid State Chemistry and its Applications, p. 452-552. John Wiley and Sons Ltd., Chichester.

Winch, L.J., and Islam, M.S. (1995) Defects and holes in the mercury-based oxide superconductors - relevance to high T_c behaviour. Journal of the Chemical Society Chemical Communications, 15, 1595-1597.

Winkler, H.G.F. (1948) Synthese und kristallstruktur des eukryptite, $LiAlSiO_4$. Acta Crystallographica, 1(27-34).

Winter, J.K., Okamura, F.P., and Ghose, S. (1979) A high-temperature structural study of high albite, monalbite, and the analbite to monalbite phase transition. American Mineralogist, 64, 409-423.

Withers, R.L., and Thompson, J.G. (1993) Modulation wave approach to the structural parameterization and Rietveld refinement of low carnegieite. Acta Crystallographica, B49, 614-626.

Wittingham, M.S. (1975) Mechanism of fast ion transport in solids. Electrochimica Acta, 20, 575-583.

Xiao, Y., Kirkpatrick, R.J., Hay, R.L., Kim, Y.J., and Phillips, B.L. (1995) Investigation of Al, Si order in K-feldspars using ^{27}Al and ^{29}Si MAS NMR. Mineralogical Magazine, 59, 47-61.

Xu, H., Heaney, P.J., and Beall, G.H. (2000) Phase transitions induced by solid solution in stuffed derivatives of quartz: A powder synchrotron XRD study of the $LiAlSiO_4$-SiO_2 join. American Mineralogist, 85, 971-979.

Xu, H., Heaney, P.J., and Bohm, H. (1999a) Structural modulations and phase transitions in beta-eucryptite: an in-situ TEM study. Physics and Chemistry of Minerals, 26, 633-643.

Xu, H., Heaney, P.J., Navrotsky, A., Topor, L., and Liu, J. (1999b) Thermochemistry of stuffed quartz-derivative phases along the join $LiAlSiO_4$-SiO_2. American Mineralogist, 84, 1360-1369.

Xu, H., Heaney, P.J., Yates, D.M., Von Dreele, R.B., and Bourke, M.A. (1999c) Structural mechanisms underlying near-zero thermal expansion in beta-eucryptite: A combined synchrotron X-ray and neutron Rietveld analysis. Journal of Materials Research, 14, 3138-3151.

Yoshioka, T. (1970) Metastable solid solution with nepheline-type structure in the CaO-Al_2O_3-SiO_2 system. Bulletin of the Chemical Society of Japan, 43, 1981-1987.

Yund, McCallister, and Savin. (1972) An experimental study of nepheline-kalsilite exsolution. Journal of Petrology, 13, 255-72.

Yund, R.A. (1983) Diffusion in Feldspars. Feldspar Mineralogy, Reviews in Mineralogy, 2, 203-222.